
Photoinduced dynamics in photocatalysis:
Mechanistic insights from time-resolved absorption spectroscopy and reaction quantum yield determination

Qi Hu



Dissertation

München 2020

Photoinduced dynamics in photocatalysis:
Mechanistic insights from time-resolved absorption spectroscopy and reaction quantum yield determination

Qi Hu

Dissertation
an der Fakultät für Physik
der Ludwig-Maximilians-Universität
München

vorgelegt von
Qi Hu
aus Yanji, Jilin, China

München, im Juni 2020

Erstgutachter: Prof. Dr. Eberhard Riedle
Zweitgutachter: Prof. Dr. Jürgen Hauer

Tag der mündlichen Prüfung: 29. 07. 2020

Tag der Abgabe: 19. 06. 2020

Kurzfassung

Die Photokatalyse weckt großes Interesse, weil sie als Technik zur Erweiterung des Potenzials der synthetischen organischen Chemie unter milden Bedingungen und zur Gewinnung der unbegrenzten Sonnenenergie durch Nutzung von Wasser verwendet werden kann. Fortschritte in diesem Bereich sind jedoch hauptsächlich auf empirische Erkenntnisse zurückzuführen und weniger auf ein gründliches mechanistisches Verständnis der zugrunde liegenden photoinduzierten Prozesse. Zweifellos wird die detaillierte Kenntnis der mechanistischen Feinheiten eine dominierende Rolle bei der Verbesserung der bestehenden Reaktionseffizienz und dem Entwurf neuer Transformationen spielen. Aus diesem Grund wurden in dieser Arbeit die besten verfügbaren Techniken zur Gewinnung mechanistischer Informationen, d.h. Methoden zur Bestimmung der Quantenausbeute und die Ultrakurzzeit-Spektroskopie, hervorgehoben. Darüber hinaus wurden zwei repräsentative photokatalytische Transformationen mit diesen Methoden untersucht.

Die Experimentellen Methoden werden im ersten Teil der Arbeit beschrieben. Um photoinduzierte Radikalkettenreaktionen zu charakterisieren, wurden der Quantenausbeute-Bestimmungsaufbau (QYDS) und der Lichtpulsgenerator (LED Pulser) kombiniert. Der QYDS erlaubt die einfache und genaue Bestimmung der Reaktions-Quantenausbeute (QY) in einem Syntheselabor. Der LED-Pulser stellt eine geeignete Methode zur Abschätzung der Lebensdauer der Radikalkette dar. Um die Dynamik des angeregten Zustands zu beobachten, wurde das transiente Absorptions- (TA) Spektrometer verwendet. Das TA-Experiment ermöglicht die direkte Beobachtung transientser Zwischenprodukte in mechanistischen Studien.

Die photoinduzierten Prozesse in einer photokatalytischen α -Alkylierung des Aldehyds wurden im zweiten Teil der Arbeit untersucht. Der QY wurde in zeitabhängiger Weise in einem Bereich von niedrigen bis mittleren Lichtleistungen bestimmt. Mit diesem Ansatz konnte gezeigt werden, dass der QY der Alkylierungsreaktion als eine Funktion der Lichtleistung und der Zeit betrachtet werden muss. Daher wurde ein neuer Mechanismus vorgeschlagen: Bei niedriger Lichtleistung dominiert die Radikalkettenreaktion, während bei hoher Leistung die Photokatalyse die Hauptrolle spielt. Die Durchführung der Reaktion unter gepulster Beleuchtung und die Änderung der Frequenz der intermittierenden Beleuchtung lieferten eine Abschätzung der Radikalkettenlebensdauer mit 23 μ s. Die Konkurrenz zwischen der Radikalkettenreaktion und der Photokatalyse wurde ebenfalls direkt beobachtet, indem die Löschung des Triplett-Zustandes des Photokatalysators NDI-A und die Bildung seines radikalischen Anions auf der ns- und μ s-Zeitskala verfolgt wurde. Dieser neuartige Mechanismus wurde bisher bei der Photokatalyse nicht berücksichtigt.

Die photoinduzierten Prozesse in einer photokatalytischen Wasserspaltungsreaktion wurden im dritten Teil der Arbeit untersucht. Die Faktoren wurden untersucht, von denen die Aktivität der photokatalytischen H_2 Produktion abhängt. Eine Reihe von sterisch verwandten Molekülen N_x -Me wurde als Photokatalysatoren verwendet. Die H_2 Produktion konnte als Folge des steigenden Stickstoffgehalts in N_x -Me dramatisch gesteigert werden. Die TA-Experimente zeigten, dass sowohl der QY der Triplett-Zustandsbildung als auch die Triplett-Zustandslebensdauer entlang der Serie N_0 bis N_3 -Me zunimmt. Darüber hinaus zeigten die Berechnungen der freien Energien des Ladungstransfers und die Experimente, dass der Elektronentransfer vom Opfer-Elektronen-Donator in den N_x -Me Triplett-Zustand durch den Anstieg des Stickstoffgehalts thermodynamisch begünstigt wird. Deshalb ist es wichtig, die Eigenschaft der angeregten Zustände und die Antriebskraft für die Elektronentransfer-Schritte bei dem Design von neuen Photokatalysatoren für die photokatalytische Wasserspaltung zu berücksichtigen.

Short summary

Photocatalysis sparks much interest as a technique to expand potential of synthetic organic chemistry and to harvest the unlimited solar energy by splitting water. However, progresses in this area have mainly been driven by empirical findings rather than a thorough mechanistic understanding of the underlying photo-induced processes. Undoubtedly, the detailed knowledge of the mechanistical intricacies will play a dominant role in the improvement of existing reaction efficiency and the design of new transformations. For that reason the best techniques available for acquiring mechanistic information, i.e. quantum yield determination methods and transient absorption spectroscopy, have been highlighted in this thesis. Furthermore, two representative photocatalytic transformations, the photoredox organocatalytic enantioselective α -alkylation of aldehydes and the photocatalytic water splitting have been investigated using these methods.

The experimental and interpretation methods have been delineated in the first part of the thesis. In order to characterize photo-induced radical chain reactions, the quantum yield determination setup (QYDS) and the light pulse generator (LED Pulser) have been used. The QYDS allows the facile and exact determination of the reaction quantum yield in a synthesis laboratory environment. The LED Pulser provides a proper method to estimate the radical chain lifetime. In order to monitor the excited state dynamics of photocatalysts, transient absorption (TA) spectrometers of our own design have been used. The TA experiment enables to observe directly transient intermediates in mechanistic studies of photocatalysis.

The photo-induced processes in a photocatalytic α -alkylation of aldehyde reaction have been investigated in the second part of the thesis. The reaction quantum yield (QY) was determined in a time dependent way at a range of low to medium light powers. With this approach it could be shown that the QY of α -alkylation reaction must be considered as a function of irradiation power and time. Therefore, a new mechanism has been proposed: the radical chain reaction dominates for low light power, whereas the photocatalytic mechanism plays the main role for high power. Running the reaction under pulsed LED illumination and changing the frequency of the intermittent illumination provided an estimate of the radical chain lifetime with 23 μ s. The competition between the radical chain reaction and the photocatalysis was also directly observed through tracking the quenching of the triplet state of the photocatalyst NDI-A and the forming of its radical anion on the ns and μ s time scale. This novel mechanism has not been taken into account for photocatalysis so far.

The photo-induced processes in a photocatalytic water splitting reaction have been investigated in the third part of the thesis. Ultrafast TA spectroscopy has been used to study the factors that dictate the photocatalytic H₂ evolution activity. A series of sterically related molecules N_x-Me was used as photocatalysts. The H₂ evolution could be dramatically enhanced as a consequence of increasing nitrogen content in these photocatalysts. The TA data treatment showed that the QY of the triplet state formation as well as the lifetimes of the triplet state increase gradually along the series N₀ to N₃-Me. In addition, the calculations of charge transfer free energies and the experiments demonstrated that electron transfer from the sacrificial donor to the N_x-Me triplet state becomes thermodynamically favored as a result of the increase in the nitrogen content. Thus, it is important to consider the nature of excited states and the driving forces for charge transfer steps in the photocatalyst's design for photocatalytic water splitting.

Publications

Publication in Journal:

- Determination of reaction quantum yields: LED Based Setup with better 5% precision
H. Volfova, Q. Hu and E. Riedle
EPA Newsletter, 51 (2019).

To be submitted:

- Transient absorption spectroscopy and quantum yield methods offer novel mechanistic insights for the photoredox organocatalytic α -alkylation of aldehyde
Q. Hu, B. Reiß, H.-A. Wagenknecht and E. Riedle
In preparation.
- Understanding photophysics-activity relationships in a triphenylarene platform for photocatalytic water splitting
Q. Hu, V. S. Vyas, E. Riedle and B. V. Lotsch
In preparation.

Contents

Kurzfassung	i
Short summary	iii
Publications	v
1. Introduction and aim of the thesis	1
2. Experimental and interpretation methods	5
2.1. Broadband transient absorption spectroscopy	5
2.2. Transient absorption dataset analysis	12
2.3. Quantum yield determination setup – QYDS	19
2.4. LED light pulse generator – LED Pulser	21
2.5. Fiber-based fluorescence detection setup	28
2.6. Additional chemical and spectroscopic methods	30
3. Light intensity-dependent quantum yield of the photoredox catalytic aldehyde alkylation and a detailed kinetic analysis	31
3.1. Introduction	31
3.2. Kinetic analysis	39
3.2.1. Enamine formation	39
3.2.2. Light power and absorbance	40
3.2.3. Mathematical model	42
3.2.4. Estimation of the rate constants	44
3.2.5. Numerical results	49
4. Effect of intermittent illumination on the photoredox catalytic aldehyde alkylation	55
4.1. Introduction	55
4.2. Theory of intermittent illumination method	56
4.3. Intermittent illumination experiment on α -alkylation	61
5. Ultrafast transient absorption spectroscopy of naphthalene diimide in the photoredox catalytic aldehyde alkylation	63

5.1. Photocatalyst – Naphthalene diimide	64
5.1.1. Structure	64
5.1.2. Photophysics and photochemistry	65
5.2. Observation of the competitive mechanism of aldehyde α -alkylation by synergistic photoredox catalysis with NDI and organocatalysis	87
6. Understanding photophysics-activity relationships in a triphenylarene platform for photocatalytic water splitting	95
6.1. Introduction	95
6.2. Structure and steady-state characterization of N_x -Me	98
6.3. Excited state kinetics of N_x -Me	102
6.4. N_x -Me excited state interactions with TEA	108
7. Summary and outlook	115
8. Reference	123
Nomenclature	135
Appendix	141
A1. Solution to the system of the steady-state equations in Chapter 3	
A2. MathCad code for quantum yield simulation of the photoredox catalytic aldehyde alkylation reaction described in Chapter 3	
A3. MathCad code for estimating the average lifetime of the radical chain in the photoredox catalytic aldehyde alkylation reaction	
A4. Steady-state and TA spectroscopic characterizations of NDI-A in Chapter 5	
A5. Steady-state and TA spectroscopic characterizations of N_x -Me in Chapter 6	
Acknowledgment	179

1. Introduction and aim of the thesis

If anyone asks me “How do you know this?”
I can answer: “I know because we measure.”

Confessions, Book XI, Chapter XXI

— Augustine of Hippo, 354–430

Vast amounts of energy are needed to support rising standards of life in a growing world population. To meet that demand, people make use of the energy released during fossil fuel combustion, thereby producing inevitably emissions, the majority of which are harmful to the environment. The increasing challenges in energy shortages and worsening environmental pollution have invigorated growing awareness of a potential crisis. For the sustainable development of human society, it is mandatory to develop both pollution-free technologies and alternative clean energy supplies for environmental protection.

Solar energy is an inexhaustible, environmentally clean, and geographically widely distributed natural resource. The magnitude of the available solar power striking the earth's surface on an hourly basis exceeds the annual global energy consumption [Gol04, Lew07]. Renewable energy techniques that harvest solar energy work as desirable approaches toward fulfilling the need for clean energy. Among these various renewable energy projects, photocatalysis has gained considerable attention with its diverse potential in energy and environmental applications [Mal02, Cie04, Ess07, Fag07, Pal07, Sch14]. Photocatalysis describes chemical transformations that require light as an energy input to proceed. In addition, photocatalysis also requires an appropriate photocatalyst to carry out the thermodynamically uphill reactions. In a typical photocatalytic reaction, the photocatalysts absorb light energy and are thereby converted into their excited states. The excited photocatalysts are generally more reactive than before in a chemical reaction and can therefore undergo electron transfer processes, i.e. an electron transfer to or from a substrate, generating highly chemically reactive radical anions or cations of the photocatalysts. Through chemical deactivation processes and various physical decay pathways, the ground state of the photocatalyst is finally regenerated and the absorbed light energy is stored in chemical bonds. These processes are also found in natural photosynthesis [Bla14], which fixes solar energy in chemical bonds and provides an indispensable prerequisite for life on earth.

The chemical transformations, that take place by the action of light show many environmental advantages. Photocatalysis features generally mild conditions required for substrate activation and well suits the requirements for “green reactions”, in which the use and production of harmful chemicals are avoided and the quantity of raw material that ends up in the final product are maximized [Fag07, Pal07]. Furthermore, the photocatalytic generation of storable chemical fuels is regarded as one of the lasting solutions to the world’s energy and environmental crises in the future [Ong16].

With all these advantages the field of photocatalysis moves at a very fast pace. A significant part of the photocatalysis studies concerns extending the range of photocatalysis applications and developing of highly efficient and stable while still cost-effective photocatalysts [Kön17]. However, the mechanistic understanding of these complex reactions remains insufficient for different reasons [Kön17, Buz19]. First, some chemical measurements such as the determination of the quantum yield have been long regarded as an important tool to investigate the reaction mechanism [Jul83, Rub10]. However, the detection of these quantities has been challenging due to the absence of easily implemented methods in a synthetic lab [Meg10, Pit15]. Second, all of the photophysical and photochemical processes in photocatalysis, the dissipation of light energy to heat or the photoinduced-electron-transfer reactions occur predominantly on the femtosecond to microsecond timescale. For these more detailed investigations of reaction mechanisms, the use of advanced spectroscopy such as transient absorption spectroscopy is suggested [Kär15, Kön17, Buz19]. Nevertheless, it is widely believed that the photocatalytic reactions are too complex to be studied with these spectroscopic methods [Maj14].

There is no doubt that a detailed knowledge of the reaction mechanism is an important prerequisite for the improvement of the existing reaction efficiency and the development of the next-generation photocatalysts and photocatalytic transformations. In order to gain a better mechanistic understanding of the processes in photocatalysis, effort has been dedicated to developing chemist-friendly devices and practical methods for using transient absorption spectroscopy. First, a LED-based quantum yield determination setup is used to measure the light intensity dependent quantum yield of a photocatalytic reaction. Second, an improved LED light pulse generator is used to characterize radical chain processes in the photocatalysis. Both setups have the advantage that they can be easily implemented in a synthetic lab. In addition to these setups, the excited state dynamics of photocatalysts in the liquid phase are directly monitored by transient absorption spectroscopy. This experimental

approach is a pump-probe experiment, in which a short light pulse is used to excite the sample, and a second delayed light pulse scrutinizes the following dynamics. This enables the observation of the ultrafast photophysical processes of the photocatalyst and a detailed probing of the reaction steps in the photocatalysis.

The main goal of this work is to show that the combination of quantum yield determinations and transient absorption spectroscopy can provide a powerful tool to generate a comprehensive mechanistic picture of the photocatalysis. To this end, two representative photocatalytic transformations, photo-redox organocatalytic enantioselective α -alkylation of aldehydes and photocatalytic water splitting, are investigated. By applying the powerful tools to these photocatalytic chemical transformations, the following anticipations can be formed. First, the experiments using our novel quantum yield determination setup shall provide a window onto determining possible reaction steps, especially onto identifying photochemical reactions that involve radical chains. Second, the transient absorption spectroscopy shall provide spectroscopic evidence that supports or improves the understanding of the concatenated sequence of reaction steps.

The thesis is structured as follows. In Chapter 2 the fundamental aspects of ultrafast pump-probe spectroscopy are briefly introduced from a technical point of view. Moreover, an overview on the experimental transient absorption setup used in this thesis is given in this chapter. Furthermore, the basic aspects of time-resolved spectroscopic data analysis are discussed. Additionally, two LED-based optical setups for the quantification of photocatalysis are described and characterized in this chapter as well.

Chapter 3, 4 and 5 describe the mechanistic studies on the photoredox organocatalytic α -alkylation of aldehydes. The reaction α -alkylation of aldehydes has long been considered as the “holy grail” reaction in the realm of organocatalysis [Alb09, Mel09, Ves12]. In the pioneering work of MacMillan et al., they have accomplished the direct α -alkylation of aldehydes by merging photoredox- and organocatalysis [Nic08]. However, the understanding of the reaction mechanism remained insufficient. The underlying mechanisms are not demonstrated yet and are highly debated in the literature [Meg10, Cis15, Kär15]. For that reason, the reaction mechanism of photoredox catalytic α -alkylation of aldehydes is studied by determining and analyzing the light intensity dependent quantum yield (Chapter 3), characterizing the radical chains in this photocatalysis (Chapter 4) as well as demonstrating the reaction steps with spectroscopic evidence (Chapter 5).

Chapter 6 describes the mechanistic investigation into a photocatalytic water splitting reaction. Direct photocatalytic water splitting is one of the most promising ways to convert solar energy into hydrogen (H_2) as a storable and clean fuel [Che17a]. Among the various photocatalysts used in photocatalytic water splitting, covalent organic frameworks (COFs) have emerged as a new platform due to the fact that their properties can be fine-tuned by synthesis [Ban18]. The area of COFs-based photocatalytic water splitting has evolved rapidly, but it is poorly understood why different COFs show very differing photocatalytic activity. Especially, the reaction mechanism has been proposed to proceed via anionic radicals [Vya15], but direct studies of the electron transfer process are still lacking. In the second part of this thesis (Chapter 6), a series of structurally related photocatalysts with markedly different hydrogen evolution activities is investigated using transient absorption spectroscopy. The focus of this study lies on rationalizing the differences in photocatalytic activity between the photocatalysts in terms of differences in their excited state properties and the nature of their radical anions.

2. Experimental and interpretation methods

The thesis is based on the collaborative work between physical and chemical research groups. Therefore, multifarious methods used in chemical and physical labs have been utilized to characterize samples, to study the excited state dynamics of photocatalysts and to investigate the mechanism of photocatalysis. Only the quantum yield determination system (QYDS) and LED Pulser are built according to our own design, the analytical methods from chemistry are all standard techniques (see section 2.6). Regarding the spectroscopic experiments in the physics group, a fiber based detection setup for fluorescence light has been developed in order to match the specific requirements in the study. Moreover and foremost, the transient absorption (TA) spectroscopy setup in the physical lab is made on our own design and is one of the fundamental methods in this thesis.

The QYDS and TA spectroscopy setup are detailed in several publications [Meg09, Meg10, Mat13, Bra14, Xu18, Vol19]. Therefore, only a brief overview of the experimental setup will be presented in the following.

2.1. Broadband transient absorption spectroscopy

A commonly used and well-developed technique for measuring photoinduced dynamics is TA spectroscopy. This technique is a direct successor to the flash photolysis technique. In the method of flash photolysis, an intense burst of light with millisecond duration was produced to create reaction intermediates, and the absorption spectra of these intermediates were recorded by using other light. By exposing a chemical sample to heat, pressure or an electrical shock, this pump-probe technique allowed researchers to study the kinetics with microsecond temporal resolution [Che17b]. For their contribution, the developers of the flash photolysis – Eigen, Norrish and Porter shared the Nobel Prize in 1967 [Nor49, Eig54]. Instead of light bursts, the modern TA spectroscopy uses laser pulses to trigger ultrafast phenomena. This enables us to investigate the mechanistic and kinetic details of chemical and biological processes with a temporal resolution spanning the range from microseconds (μs) to femtoseconds (fs). In 1999, Zewail was credited with the Nobel Prize in the context of this fs-spectroscopic method [Zew00].

The basic idea of TA spectroscopy is illustrated schematically in Fig. 2.1. A laser pulse, so called pump pulse, is used to excite the sample. The time evolution of the excited sample is then interrogated with the second laser pulse, so-called the probe pulse. The time delay

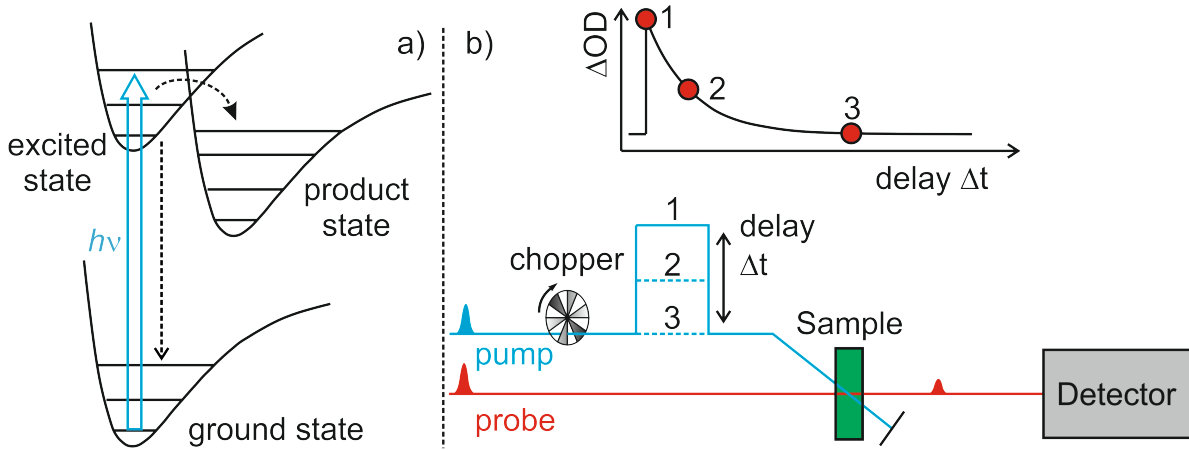


Fig. 2.1: Schematic depiction of the TA spectroscopy principle to measure photoinduced molecular dynamics.

between the pump and the probe pulse is achieved by lengthening the pathway of one of the two pulses. A detector such as photodiode is exploited to record the intensity of the probe light.

Upon absorption of the pump pulse, the molecule system studied is prepared into the respective excited state of interest (see Fig. 2.1a). Because the electronic configuration of the excited state are typically different from that in the ground state, these differences can be measured by the probe pulses which are delayed in time Δt relatively to the pump. The spectral characteristics of the sample can be shown in the optical density $OD(\lambda)$, which is defined by (via the common logarithm due to the Beer-Lambert law [Tur10]):

$$OD(\lambda) = -\log(T(\lambda)) = \varepsilon(\lambda)[J]d \quad (2.1)$$

Here, $T(\lambda)$ is the spectral transmittance, $\varepsilon(\lambda)$ is the molar absorption coefficient, $[J]$ is the molar concentration of the absorbing species J and d is the length of the sample. The comparison of the transmitted probe pulses through the excited sample $T^*(\lambda, \Delta t)$ and the non-excited sample $T_0(\lambda)$ provides the induced changes of the optical density (ΔOD) according to eq 2.2 [Meg09, Bra14]. Generally, this purpose is achieved by blocking every second pump pulse with a chopper in the pump beam for 1 kHz laser systems.

$$\begin{aligned} \Delta OD(\lambda, \Delta t) &= OD_{\text{excited}}(\lambda, \Delta t) - OD_{\text{non-excited}}(\lambda) \\ &= -\log(T^*(\lambda, \Delta t)) + \log(T_0(\lambda)) \\ &= -\log\left(\frac{T^*(\lambda, \Delta t)}{T_0(\lambda)}\right) \end{aligned} \quad (2.2)$$

Therefore, the temporal information of the photophysical or photochemical processes can be studied by analyzing these transient absorbance changes (see Fig. 2.1b).

In contrast to the simple concept of TA spectroscopy, the experimental TA setup used in this thesis is relatively complicated. One reason for the complexity is that many nonlinear optical processes are required for the generation of different wavelengths with fs duration for the pump. Another essential improvement that causes the complexity is the combination of a ns-pulse laser for recording dynamics on the ns- μ s timescale. More details can be found in the following.

The experimental layout of the TA spectrometer is sketched in Fig. 2.2. The TA setup consists of two commercially available laser systems which are fully electronically

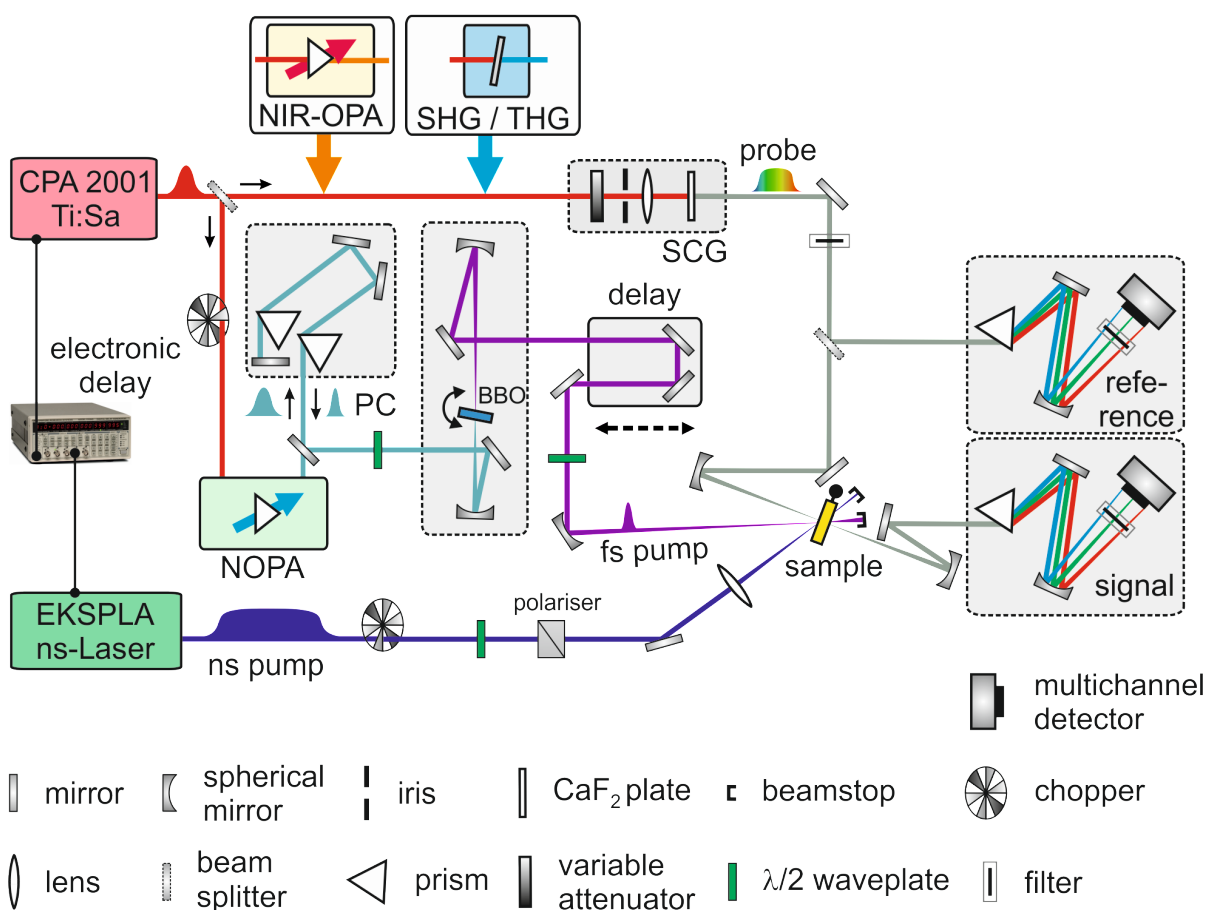


Fig. 2.2: Scheme of the fs and ns broadband transient absorption spectrometer. NIR-OPA: near-infrared optical parametric amplifier; SHG: second-harmonic generation; THG: third harmonic generation; NOPA: non-collinear optical parametric amplifier; PC: prism compressor; BBO: β -barium borate crystal; SCG: supercontinuum generation.

synchronized. One is a Ti:sapphire amplifier system (CPA2001; Clark-MXR) delivering laser pulses centered at 775 nm with 150 fs duration and a repetition rate of 1 kHz. The other is a 1 kHz optical parametric oscillator (OPO) (NT242; EKSPLA) providing nanosecond (ns) light pulses, whose wavelength is tunable from 210 to 2600 nm with 3 ns duration.

To record dynamics on the fs-ps timescale, a fraction of the Ti:sapphire amplifier light is used to operate a non-collinear optical parametric amplifier (NOPA) [Rie00, Cer03], which routinely delivers a pump wavelength in the range from 450 to 740 nm. The NOPA output is then compressed via a fused silica or SF10 prism sequence (prism compressor, PC). After the compression, the pulse duration of about 30 fs is achieved throughout the visible range. To match the absorbance bands of sample molecules in the ultraviolet (UV) range, the compressed pulse is frequency doubled (second harmonic generation, SHG) in a thin β -barium borate (BBO, type-I) crystal. Together with the SHG, the pump wavelength can be adjusted from the region of the fundamental at 775 nm down to about 240 nm. These pulses are routinely characterized by using compact autocorrelators on our own design [Koz04, Hom11]. Subsequently, the pump pulse is mechanically delayed in 20 fs steps using a linear delay stage with sub-10 fs accuracy (M-531 PD; Physik Instrumente GmbH). Before focusing the pump pulse into the sample, a $\lambda/2$ waveplate is used to adjust the polarization of the pump relative to the probe beam. Unless otherwise noted, the polarization between pump and probe beam is set at the magic angle $\theta_{\text{mag}} = 54.7^\circ$ to avoid contributions from the rotational diffusion of molecules in solution [Fle76]. In the end the pump light is focused on to the sample with a FWHM spot size of $\sim 100 \mu\text{m}$ and the energy of these pulses is about 50 – 70 nJ for the fs-ps experiment.

Due to the physical limitation of the mechanical delay stage, the molecular dynamics on the ns and μs time scale are not accessible by changing the optical path length of the pump pulse. Thus, for accessing ns- μs dynamics, the fs pump is replaced by an ns pulse generated by the EKSPLA OPO. The ns pump pulse is electronically delayed by a delay generator (DG645; Stanford Research Inc.). The delay time can be set up to 790 μs with an accuracy of 100 ps. With a set of a $\lambda/2$ waveplate and a polarizer the pump energy is adjusted. At the position of the sample, the FWHM focal size of the pump spot is $\sim 200 \mu\text{m}$ and the energies vary between 200 and 300 nJ for the ns- μs configuration.

As probe pulses, a spectral supercontinuum is generated by focusing the Ti:sapphire amplifier beam into a 5 mm calcium fluoride (CaF_2) crystal. To avoid damage of the crystal, the CaF_2 plate is translated in a circular pattern without changing the orientation. This

supercontinuum generation (SCG) provides a white light ranging from 290 to 710 nm [Hub01, Bra09], which is employed in the present investigations. An appropriate blocking filter is employed in order to reduce the intensity of the CPA fundamental. Thus in the region from 700 to 830 nm the number of counts on the CCD is reduced to 40%, leading to a smaller signal-to-noise ratio. Probing is also possible from 225 up to 1700 nm by using SHG/THG of the fundamental beam or a NIR-OPA before the SCG [Rie13]. The wavelength calibration for the CCD channels is conducted before data collection by using a set of colored glass filters (BG36, Schott AG and short pass filters, Asahi Spectra Inc.) and dielectric mirrors with characteristic transmission oscillations above and/or below the high reflection band (HR355-HT532, Laser Components GmbH).

The method “single-shot referencing” is employed to reduce the noise caused by variations in the light pulse energy so that the sensitivity of the spectrometer is enhanced [Dob10, Bra14]. As shown in Fig. 2.2, the probe pulse is split into two roughly equal parts with a beam splitter: a reference part and a sample part. No sample is placed in the reference arm, whereas the sample part is guided through the sample to be examined. The FWHM focal size on the sample is $\sim 35 \mu\text{m}$ for the pulse. To detect these signals, two prism spectrographs including two identical multichannel CCDs, a reference camera and a signal camera, are installed.

In the case of two cameras referencing the light induced electronic signals on the reference detector $R(\lambda)$ are taken into account in the data acquisition. A transmittance difference $\Delta T_{\text{ref}}(\lambda, \Delta t)$ as a function of wavelength λ and time delay Δt is defined as

$$\Delta T_{\text{ref}}(\lambda, \Delta t) = \frac{R^*(\lambda, \Delta t)}{R_0(\lambda)} \quad (2.3)$$

where the signal with pump is denoted as R^* and the one without pump is R_0 . For the sample light beam the transmittance difference $\Delta T_{\text{sam}}(\lambda, \Delta t)$ is thus calculated according to eq 2.4.

$$\Delta T_{\text{sam}}(\lambda, \Delta t) = \frac{S^*(\lambda, \Delta t)}{S_0(\lambda)} \quad (2.4)$$

Here S^* is the signal with sample excitation recorded on the detector and S_0 shows the one without excitation. The changes of the optical density ΔOD used for the data analysis are calculated according to the following equation [Bra14]:

$$\Delta OD(\lambda, \Delta t) = \Delta A_{\text{sam}}(\lambda, \Delta t) - \Delta A_{\text{ref}}(\lambda, \Delta t) \quad (2.5)$$

$$\begin{aligned} \Delta OD(\lambda, \Delta t) &= -\log(\Delta T_{\text{sam}}) - (-\log(\Delta T_{\text{ref}})) \\ &= -\log\left(\frac{S^*(\lambda, \Delta t)}{S_0(\lambda)} \cdot \frac{R_0(\lambda)}{R^*(\lambda, \Delta t)}\right) \end{aligned} \quad (2.5)$$

To avoid artifacts caused by photodegradation or accumulation of photoproducts, the sample is exchanged between two consecutive light pulses in a flow cuvette including two fused silica windows, each of 200 μm [Meg09]. The path length is adjusted by a Teflon spacer of 100 μm , 250 μm or 1 mm thickness. All experiments are performed under room temperature unless otherwise noted.

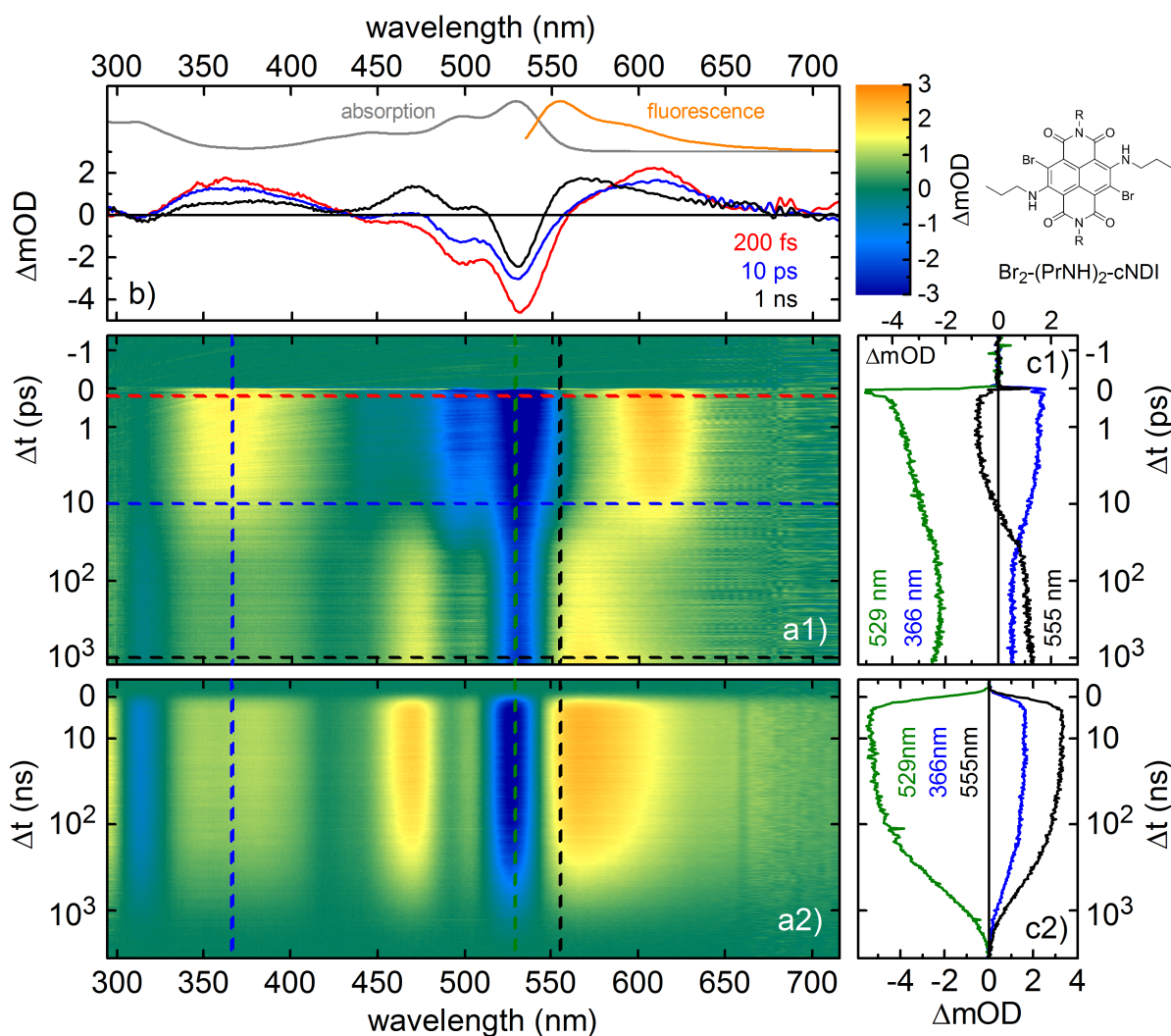


Fig. 2.3: Time-resolved transient absorption measured after 500 nm excitation of $\text{Br}_2\text{-(PrNH)}_2\text{-cNDI}$ in dichloromethane. a) False color representation of the time and wavelength resolved data. b) TA spectra recorded at several time delays. For reference the absorption and fluorescence spectra are shown in addition. c) Kinetics for the dynamics of different species at selected wavelengths.

In Fig. 2.3 the transient absorption after 500 nm excitation of Br₂-(PrNH)₂-cNDI in dichloromethane is shown as an exemplary dataset. The structure of the molecule is shown in the inset of Fig. 2.3. A false color representation of the TA signal is depicted in Fig. 2.3a, in which the warm colors indicate high transient absorption and the cold colors show low absorption. The observed TA spectra consist of various signal contributions caused by different photophysical and photochemical processes:

- Ground state bleach (GSB): a negative signal contribution at the positions of the steady-state absorption bands (see Fig. 2.3b). The ground state is partially depopulated after excitation, which leads to an increased transmitted intensity in the ground state absorption bands because less absorption occurs at these bands.
- Stimulated emission (SE): a negative signal contribution where the sample fluoresces (see Fig. 2.3b). Due to the interaction of the probe photon with the excited molecule a transition from an excited state to the ground state occurs via emission of a photon, which has the same wavelength as the probe photon. Thus, the light intensity at this wavelength is increased on the detector.
- Excited state absorption (ESA): a positive signal contribution corresponding to a transition from an excited state to a higher-lying excited state. The excited state absorption leads to a decrease in the intensity of the probe light.
- Product absorption: a positive signal contribution at the absorption positions of the newly formed photoproduct.

In addition, the nonlinear interaction of pump and probe pulses leads to “coherent artifact (CA)” contributions in the UV-Vis spectral range [Lor02]. These contributions occur about hundred femtoseconds around the time zero and stem mainly from two photon absorption (TPA) and cross phase modulation (XPM) [Bau17]. Generally, these CA contributions are used to determine the time zero by fitting a modulated Gaussian function and/or its first derivative to the CA signals [Bau17]. This approach also offers the effective time resolution of the TA experiments [Meg09]. Because sub-ps molecular dynamics signals can intermingle with the CA and the major part of the CA is generated within the solvent and the cuvette windows, the data for the CA fitting are measured before the actual experiment in the pure solvent with the same cuvette.

2.2. Transient absorption dataset analysis

A 2D dataset obtained from a TA measurement are an absorption difference matrix as functions of time and probe wavelengths $\Delta OD(\lambda, \Delta t)$. The column of the matrix is a time trace for a selected detection wavelength and the row presents a TA spectrum at a delay time. Information about photo induced processes, such as the temporal evolution of excited states, can be achieved from the TA data when an adequate model is numerically fitted to the data. The ubiquitous implemented model fits a sum of exponential functions with different coefficients to the TA data. This is based on the assumption that the complete dynamics can be described as a set of first-order differential equations. Suppose that the population of a state is N_i and the rate of depopulation of this state ($-dN_i/dt$) is proportional to its population:

$$\frac{dN_i}{dt} = -k_i \cdot N_i \quad (2.6)$$

The coefficient k_i is called the rate constant for the process. The reciprocal of the rate constant is defined as the time constant for the process (τ_i), which represents the time required for the population of an intermediate to fall to 1/e of its initial value.

$$\tau_i = \frac{1}{k_i} \quad (2.7)$$

If $N_i(0)$ is the initial population of the state at time zero ($t = 0$), the solution of the differential equation 2.6 is given by

$$N_i(t) = N_i(0) \cdot \exp(-k_i t) = N_i(0) \cdot \exp\left(-\frac{t}{\tau_i}\right) \quad (2.8)$$

For a coupled n-states system, the application of this model is obtained by fitting the TA data at one detection wavelength with a linear combination of exponential functions with different amplitudes A_i and time constants τ_i [Meg09]. The number of the exponential functions equals the number of states in the system. The fit function $F(t)$ is given by

$$F(t) = IRF(t) \otimes \left\{ \theta(t) \left[\sum_i^n A_i \cdot \exp\left(-\frac{t}{\tau_i}\right) \right] \right\} + \text{const.} + CA \quad (2.9)$$

Here the symbol \otimes denotes a convolution integral, $\theta(t)$ is the Heaviside step function, CA is the coherent artifact and $IRF(t)$ is the instrumental response function assumed to be of Gaussian shape with a full width at half maximum of the peak (FWHM) τ_{FWHM} .

$$\text{IRF}(t) = \frac{2\sqrt{\ln 2}}{\sqrt{\pi}} \frac{1}{\tau_{\text{FWHM}}} \exp\left(-4 \ln 2 \frac{t^2}{\tau_{\text{FWHM}}^2}\right) \quad (2.10)$$

This fitting approach is also called “single line analysis”. Because the coherent artifact occurs at different delay times for different probe wavelengths, the single line analysis offers the best fit of the time zero position. However, in the absence of any information of the states in the system, using single line analysis, it is possible to determine more fitting parameters from the data set than required. Furthermore, in the presence of TA band shifts due to solvation or vibrational cooling (an example see Chapter 5), the single line analysis can lead to ambiguities because the obtained rate constants are highly dependent on the probe wavelength [Meg11].

Since the TA dataset consists of kinetics at different probe wavelengths, a “global analysis” can be applied to the TA data in order to take the entire spectrally resolved dataset into consideration [Van04, Fit06, Ruc12]. In global analysis one attempts to extract one common set of time constants τ_i for the kinetics recorded at all probe wavelengths. The fit function is defined as

$$F(t) = \text{IRF}(t) \otimes \left\{ \theta(t) \left[\sum_i^n \text{DADS}_i(\lambda) \cdot \exp\left(-\frac{t}{\tau_i}\right) \right] \right\} + \text{const.} + \text{CA} \quad (2.11)$$

with a predefined number of discrete exponentials. The global analysis yields the decay associated difference spectra (DADS_i) corresponding to its time constant τ_i . A positive contribution in the DADS indicates a decrease in the intensity of ESA or an increase in the intensity of GSB, whereas a negative signal corresponds to recovery of GSB and SE or growth of an ESA band.

The data from the global analysis can then be subjected to a specific “kinetic model”, which is performed according to the literature [Hol96, Cor07]. The kinetic model is a proposed mathematical description of the population dynamics of each observed state: an arbitrarily selected state x is populated from a state y with a rate constant k_{yx} and decays with a rate constant k_{xz} into a state z . The temporal behavior of the state population $N_i(t)$ is described

$$\frac{d}{dt} N_i(t) = \sum_{j=1}^n K_{ij} N_j(t) \quad \text{for } i = 1 \dots n \quad (2.12)$$

$$\begin{pmatrix} \frac{d}{dt} N_1 \\ \frac{d}{dt} N_2 \\ \frac{d}{dt} N_3 \\ \vdots \\ \frac{d}{dt} N_n \end{pmatrix} = \begin{pmatrix} -k_1 & k_{21} & k_{31} & \cdots & k_{n1} \\ k_{12} & -k_2 & k_{32} & \cdots & k_{n2} \\ k_{13} & k_{23} & -k_3 & \cdots & k_{n3} \\ \vdots & \vdots & \vdots & \ddots & \vdots \\ k_{1n} & k_{2n} & k_{3n} & \cdots & -k_n \end{pmatrix} \cdot \begin{pmatrix} N_1(t) \\ N_2(t) \\ N_3(t) \\ \vdots \\ N_n(t) \end{pmatrix} \quad \text{with } k \geq 0 \quad (2.12)$$

by the system of differential equations in matrix formalism (eq 2.12), where K_{ij} is a matrix of rate constants. By solving this differential equation system the mathematical terms for $N_i(t)$ are obtained, if the eigenvalues of K_{ij} (κ_j) are not degenerate (eq 2.13).

$$\begin{aligned} N_i(t) &= \sum_{j=1}^n M_{ij} \cdot \exp(-\kappa_j \cdot t) \\ &= \sum_{j=1}^n M_{ij} \cdot \exp\left(-\frac{1}{\tau_j} \cdot t\right) \quad \text{for } t > 0 \end{aligned} \quad (2.13)$$

Here $\tau_j = 1 / \kappa_j$ are the time constants. The coefficient matrix M_{ij} reflects the rate model and its columns consist of the eigenvectors associated with the eigenvalues κ_j . The M_{ij} is obtained by applying the specific starting condition, namely the population change of the state induced by the excitation $N_i(t=0)$.

In addition, the data matrix produced by the TA measurement $\Delta OD(t, \lambda)$ includes a superposition of different species spectra (which reflect the absorption cross section) weighted by their population $N_i(t)$.

$$\Delta OD(\lambda, t) = \frac{d}{\ln(10)} \sum_{i=1}^n N_i(t) \cdot SADS_i(\lambda) \quad (2.14)$$

Here d is the optical length of the sample. $SADS_i(\lambda)$ denotes species associated difference spectra (SADS). By inserting the rate model (eq 2.13) into the data matrix (eq 2.14) the connection between SADS and DADS ($DADS_i(\lambda)$) is found.

$$\begin{aligned} \Delta OD(\lambda, t) &= \frac{d}{\ln(10)} \sum_{i=1}^n \sum_{j=1}^n M_{ij} \cdot \exp\left(-\frac{t}{\tau_j}\right) \cdot SADS_i(\lambda) \\ &= \frac{d}{\ln(10)} \sum_{j=1}^n \exp\left(-\frac{t}{\tau_j}\right) \sum_{i=1}^n M_{ij} \cdot SADS_i(\lambda) \end{aligned} \quad (2.15)$$

$$\Delta OD(\lambda, t) = \frac{d}{\ln(10)} \sum_{j=1}^n \exp\left(-\frac{t}{\tau_j}\right) \cdot \text{DADS}_i(\lambda) \quad (2.15)$$

Therefore, by applying the M_{ij} to the DADS from the global analysis, the SADS are eventually constructed (eq 2.16).

$$\text{SADS}(\lambda) = (M)^{-1} \cdot \text{DADS}(\lambda) \quad (2.16)$$

In sum, this analysis involves a simultaneous optimization of the rate constants and the spectra in order to optimally describe the data with the proposed model. The results are the rate constants for the kinetic model chosen and the spectra of each species present in the model.

However, there is an important limitation in this procedure, so-called the identifiability problem [Hol96b, Cor07]. In general, the unknown rate constants involved in the kinetic model cannot be uniquely solved only on the basis of global analysis alone, because the given results from global analysis might not contain enough information inquired. An example is shown in Chapter 5, in which three rate constants have to be extracted for the model. Nevertheless, by using global analysis, there exist only two independent time constants. Thus the number of linearly independent equations is not enough (only two) in order to determine three rate constants. In order to find a unique solution, the other one must be fixed on an otherwise determined value. In this case, the purpose is achieved using peak position evolution, provided a wavelength region can be found where only one excited state decays into another state. In general cases, the same purpose can be achieved, if the analysis of the TA data could be linked to another time-resolved measurement data, e.g., fluorescence lifetime data [Hol96a].

It is important to note that in all analysis described above, the number of distinct exponential functions needed to fit the data is chosen by the user's judgement. The fit procedure can become difficult to perform when different processes exhibit similar time constants. Therefore, a mathematical method is needed to estimate the smallest number of the exponential functions which can unambiguously describe a TA dataset. "Maximum entropy analysis" is chosen to achieve this purpose [Dan92, Kut13]. In the maximum entropy analysis, the pre-exponential amplitude is regarded as a probability distribution $p(k)$. This method determines the distribution $p(k)$ in a sum of a large number of exponential functions with fixed rate constants for each probe wavelength independently. For a fixed wavelength, the fit function is shown as

$$F(t) = \int_0^{\infty} f(t, k) p(k) dk \quad (2.17)$$

$$f(t, k) = \int_{-\infty}^t \exp(-k(t - t')) \cdot \text{IRF}(t') dt', \quad k = 1/\tau$$

In order to obtain a distribution $p(k)$ that doesn't contain more information than required to fit the data, the entropy S of the distribution $p(k)$, which is a concept in probability theory and shown in eq 2.18, should be maximized.

$$S = - \sum_{i=1}^m p(k_i) \cdot \ln(p(k_i)) \quad (2.18)$$

The resulting m discrete values $p(k_i)$ represent the distribution function $p(k)$. The result of the maximum entropy analysis is a three-dimensional map $p(\lambda_j, k_i)$ for the probability of the presence of rate constants k_i at wavelength λ_j . Therefore, the rate constant components present in TA data can be depicted from this map. An example of the maximum entropy analysis is shown in Chapter 5.

Another useful analysis technique is a spectral reconstruction method known by the acronym TEM (for Thulstrup, Eggers, and Michl) [Thu68, Thu70, Mic70, Vet17]. A variation of the TEM method is used in this thesis and has been adequately described in the supporting information of ref. [Wil18]. This method allows us to extract species associated spectra (SAS) from TA spectra. It is based on the assumption that at a specific delay time the TA spectra can be exactly described as the sum of one intermediate's absorption spectrum (SAS) and the ground state bleach (GSB) (here the contribution of stimulated emission is ignored). The latter is simply the inverse spectrum of the steady-state absorption (*abs*). Therefore, the SAS can be finally retrieved as a linear combination of the ΔOD at a selected delay time and the absorption spectra.

$$\text{SAS}(\lambda) = \Delta OD(\lambda) + \alpha \cdot \text{abs}(\lambda) \quad (2.19)$$

The linear coefficient α is a scaling factor, indicating the amount of ground state molecules located at the intermediate state. In order to estimate the scaling factor, two constraints are introduced. Firstly the SAS contains only nonnegative spectral signals. Secondly there must be a spectral region of the SAS, which shows insignificant vibronic structure, while the steady-state absorption spectra present a pronounced spectral peak at the same region. This specific band is then applied as an indicator in the reconstruction procedure. In order to show

a prominent difference between the SAS and the steady-state absorption spectra at the indicator band, the second derivative of the band is calculated (eq 2.20) [Art92]. The scaling factor obtained from the reconstruction procedure will be quite rational, when the second derivative of the resulting indicator band is approximately equal to zero.

$$\frac{d^2}{d\lambda^2}(\Delta OD(\lambda) + \alpha \cdot \text{abs}(\lambda)) \approx 0 \quad (2.20)$$

In this thesis, the modified TEM method is used to estimate the quantum yield of intersystem crossing (ISC) process Φ_{ISC} (also used as synonymous with quantum yield of formation of triplet state). The estimation procedure of the Φ_{ISC} of $\text{N}_2\text{-Me}$ (the molecule studied in Chapter 6) after 270 nm excitation is shown as an example in the following.

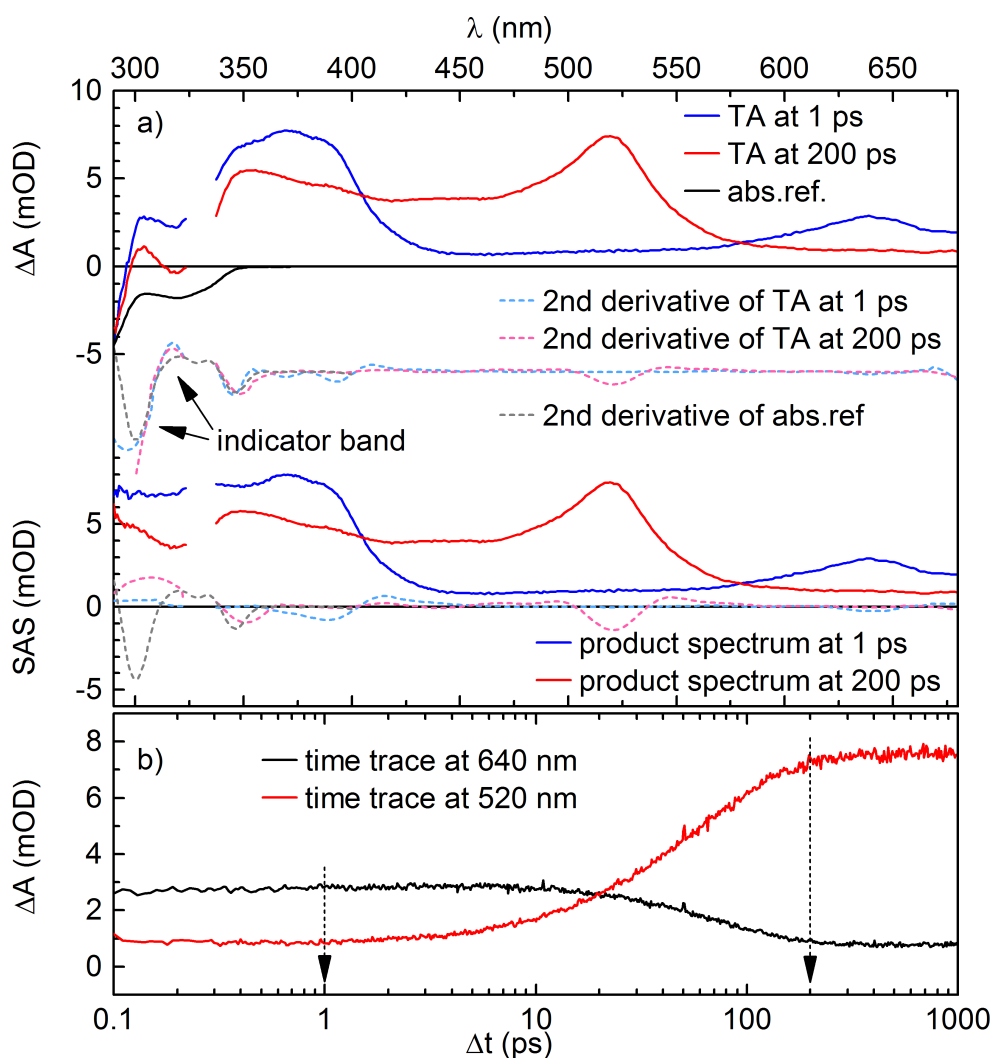


Fig. 2.4: Reconstruction of TA spectra of $\text{N}_2\text{-Me}$ after 270 nm excitation into SAS by adding ground state absorption at selected time delays.

A representation of the procedure is depicted in Fig. 2.4. At the delay time of 1 ps, the contributions of coherent artifact are neglected and the entire excited molecules are assumed in their lowest excited singlet state S_1 . Moreover, at this delay time, the triplet state T_1 has not built up via the ISC process significantly because the lifetime of the S_1 state is 67.40 ps \gg 1 ps. For $\Delta t = 200$ ps the S_1 state has already entirely decayed and the T_1 state is populated. The kinetic traces monitored at 520 and 640 nm show the concomitant growth of the T_1 state with the S_1 state decay.

At the selected delay times 1 ps and 200 ps, the amount of ground state molecules located at these excited states is estimated by applying the reconstruction method. The amplitude of the GSB in the TA spectra is a measure for the number of molecules found in the excited state. Therefore, the comparison of the GSB at these delay times delivers the estimation of the Φ_{ISC} , which is given by

$$\begin{aligned}\Phi_{ISC} &= \frac{\text{The number of molecules in triplet state}}{\text{The number of molecules in singlet state}} \\ &= \frac{\alpha \text{ at } 200 \text{ ps}}{\alpha \text{ at } 1 \text{ ps}} \\ &= 84\%\end{aligned}\tag{2.21}$$

where α is the scaling factor mentioned in eq 2.19.

2.3. Quantum yield determination setup – QYDS

The detection of the reaction quantum yield is often necessary to characterize the photoefficiency of photochemical reactions and to understand their underlying reaction mechanism [Jul83]. The reaction quantum yield describes how many product molecules are produced from one photon absorbed by the sample. Therefore, the fraction of the number of photons absorbed by a sample that are transformed into products is termed the quantum yield of a photochemical reaction $\Phi(\lambda)$ [IUPAC14]:

$$\begin{aligned}\Phi(\lambda) &= \frac{\text{The number of products formed}}{\text{The number of absorbed photons of the particular wavelength}} \\ &= \frac{N_{\text{prod}}}{N_{\text{ph,abs}}(\lambda)}\end{aligned}\quad (2.22)$$

This simple definition should be used with caution. It is strictly speaking only valid for small overall conversion. Any product absorption will falsify the result. For a precise determination of $\Phi(\lambda)$ both of the quantities, N_{prod} and $N_{\text{ph,abs}}$ have to be exactly quantified. N_{prod} can be measured via standard spectroscopic techniques, e.g., NMR spectroscopy [Fel13] or UV/Vis spectrophotometry [Sta18]. $N_{\text{ph,abs}}$ can be determined per time via our quantum yield determination setup (QYDS) [Meg10, Vol19]. Measuring the absorbed radiant power P_{abs} and the illumination time t_{illu} allows the accurate calculation of $N_{\text{ph,abs}}$. The latter quantity is calculated from the relation as follow:

$$N_{\text{ph,abs}} = \frac{\lambda}{h \cdot c} \cdot \frac{1}{N_{\text{A}}} \cdot t_{\text{illu}} \cdot P_{\text{abs}}\quad (2.23)$$

In eq 2.23 λ is the LED peak wavelength, h is Planck's constant, c is the speed of light and N_{A} is the Avogadro constant.

A schematic diagram of the setup is illustrated in Fig. 2.5. As excitation high power LEDs are used. The wavelengths of these light sources are available from 255 to 1050 nm from various manufacturers. Imaging of the LED die into a cuvette is realized by a lens system, which consists of two best form lenses (Bernhard Halle Nachfl. GmbH) with focal lengths of 25 mm and 100 – 150 mm respectively. These result in a high collection efficiency of the LED light power. A mechanical shutter, which is electronically controlled, is used to precisely regulate the illumination time. Since hundreds of μW of light is typically sufficient for some measurements, optical filters can be employed to further control the amount of light.

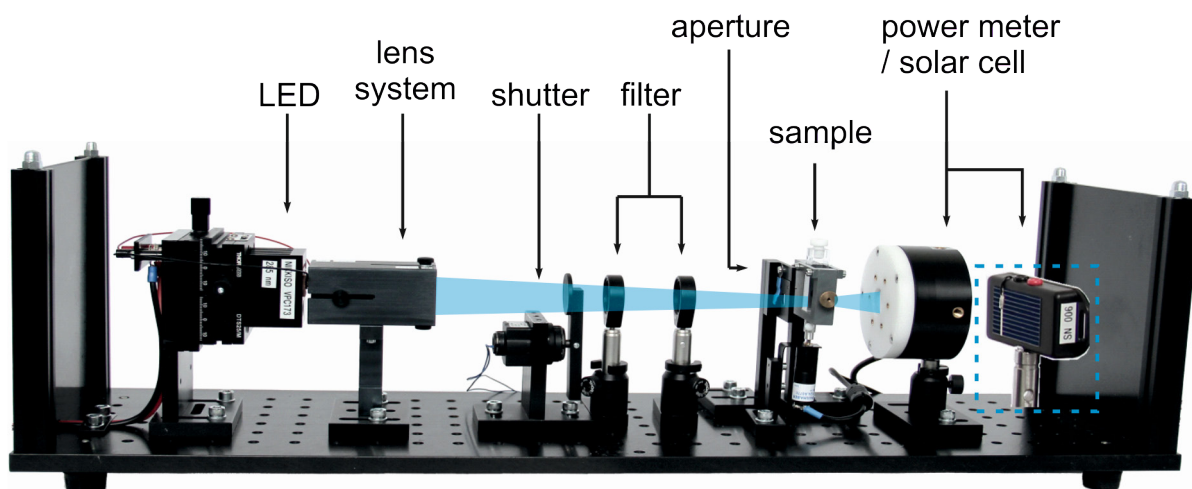


Fig. 2.5: Schematic depiction of the QYDS. The LED light is focused into a sample and the transmitted light is detected either by a commercial available powermeter (for light power > 10 mW) or a calibrated UV sensitive solar cell (for light power < 10 mW).

After an 8×8 mm² aperture, the LED light is imaged into the sample. A 10×10 mm² spectroscopic cuvette is recommended to hold the sample. A magnetic stir bar is used in the cuvette to ensure that the sample is irradiated homogeneously.

The power of light transmitted through the sample is determined by a powermeter (PS19Q, Coherent Inc.) for light power > 10 mW or a solar cell detector of our own design for power < 10 mW. Measuring the power of the transmitted light with sample in the cuvette in comparison to the transmission with a solvent cuvette renders the absorbed illumination power.

For further details on the QYDS, please refer to ref. [Meg10, Rei17, Xu18, Vol19].

2.4. LED light pulse generator – LED Pulser

Free radical chain reactions are recognized as being one of the most important product pathways in the visible-light photoredox catalytic synthesis [Cis15]. In the study of such radical-mediated synthetic transformations it is often necessary to be able to measure the properties of the radical chain reaction, such as radical lifetimes. However, the detection of these radical properties has been challenging due to the absence of easily implemented methods in a synthetic lab [Pit15].

In this section, an accessory of QYDS - a LED light pulse generator will be presented. It is similar to QYDS, the LED light pulse generator can also be easily applied in chemical labs. Making use of this pulse generator, the reaction sample can be irradiated intermittently, which enables us to control the concentration of the free radical generated by light absorption. Furthermore, by combining with kinetic models, the intermittent illumination allows the duration in time of the chain to be measured for a chain reaction.

The idea of the use of intermittent illumination in the studies of photochemical reactions dates back to the 1920s, when Briers, Chapman and Walters initially suggested using this method to measure the lifetime of free radicals [Bri26]. In 1946, Burnett and Melville developed this method with particular reference to photo-polymerization reactions. At the time, a rotating slotted disk was placed in the path of the light for interrupting the light beam. Their study was successful in proving that such intermittent illumination could be used to characterize chain reactions, in particular the rate constants for chain propagation [Bur47]. However, this technique eventually faded from view because another powerful tool - electron spin resonance (ESR) spectroscopy was developed and then widely used to study radical-mediated reactions.

A major disadvantage of the conventional intermittent illumination technique is that the adjustment of the period of irradiation is difficult. Different pulse durations require different sectorized disks. The procurement of a functioning disk can unnecessarily extend the experiment time. This drawback can be easily addressed through using LED technologies. By controlling with an external pulse input, the LED is turned on and off regularly, which produces flat-topped light pulses. The light pulse duration is simply adjusted by tuning the input electric pulse duration. Recently the LED method was demonstrated by Scaiano and the coworkers to be the new generation of the intermittent illumination approach for detection of very short-lived chains [Pit15].

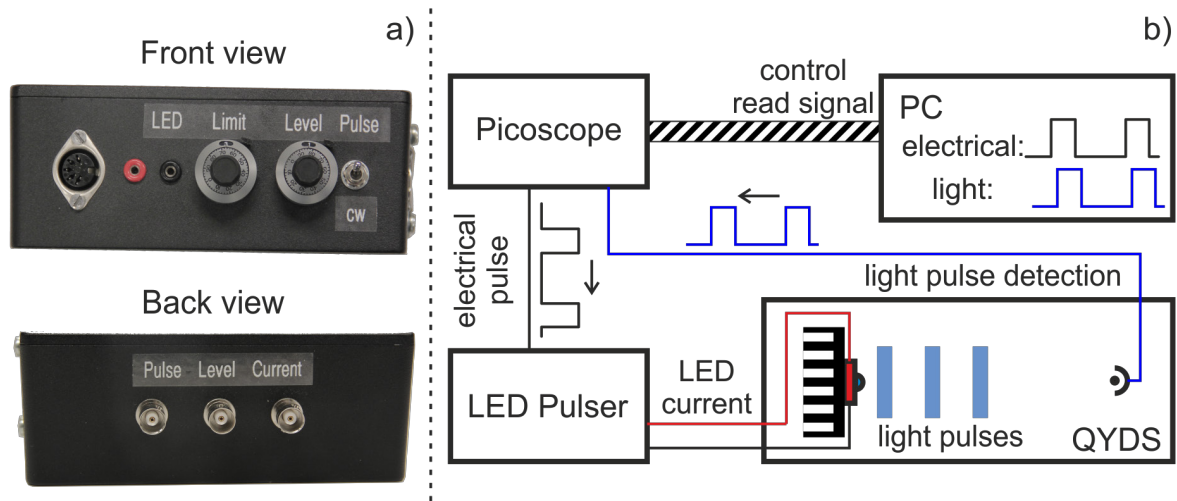


Fig. 2.6: a) LED pulser and b) Schematic diagram of the LED light pulse generation setup.

The LED pulser is able to generate a pulse that is gated by a logic signal (pulse input), and whose amplitude is set separately by using a panel knob. Two photos of the LED pulser and a schematic diagram of the LED pulser combined with the QYDS are shown in Fig. 2.6. The LED pulser receives pulse input signals from a function generator or a digital oscilloscope with arbitrary waveform generator (AWG), by connecting the input cable to the “Pulse” BNC connector on the back side of the box. The parameters of the input, such as pulse duration and pulse repetition frequency, are defined through the oscilloscope software on a computer or adjustment dials. According to the pulse input, the LED pulser establishes the drive current sent to the high power LED in the QYDS. The current maximum is regulated through the “Level” knob on the front side of the box and monitored on the computer. Due to different kinds of LED having distinct current limits the “Limit” knob is used to limit the current to prevent damaging the LED. Finally, the light pulses are detected by a photodiode and the properties of the light pulses are characterized in the oscilloscope software.

The LED pulser is also designed to operate in the “continuous” mode, i.e. the box delivers constant current to the LED. By means of the “Pulse/cw” switch, the operation mode of the box can be easily changed. The circuit diagram of the LED pulser box is shown in detail in Fig. 2.7. A ± 12 V power supply is used to operate the circuit. In term of functions, the circuit is separated into three parts, pulse input modification (a), current level setting (b) and LED current output (c) respectively.

In part (a), a two-stage amplifier is introduced (AD823ANZ, Analog Devices) for the

modification of the pulse input voltage. The first stage is a summing amplifier, whose output voltage is given by

$$V_{out} = -100k\Omega \left(\frac{V_{in}}{10k\Omega} + \frac{-12V}{47k\Omega} \right) \text{ and } V_{out} \in [-12V, 12V] \quad (2.24)$$

The second stage is an inverting amplifier, whose gain is -1.2 (V/V). The output voltage after this two-stage amplifier will eventually drift into the required voltage for controlling the amplifier (OPA548T) in part (c). For instance, a square wave works as input signal, which has the amplitude between 0 and 2 V. The input signal is amplified by the AD823ANZ, which generates an output square wave with the amplitude between -12 V and -6.638 V. This is the control input level needed for the enable/disable input of the OPA548.

In part (b), a potentiometer (10 kΩ) is used as an adjustable voltage divider in order to adjust the current applied on the LED. A Zener diode (1N4737A) is connected in parallel with the potentiometer and acts as a voltage reference. The voltage applied across the series of a 10 kΩ potentiometer and a 130 Ω resistor is regulated to 7.5 V. The output voltage of the voltage divider is fed into an operational amplifier (TL081BCP, Texas Instruments). The amplifier works as a voltage follower in order to prevent the defined voltage from being affected by the load.

After setting the LED current level, the output of the voltage follower is connected to the input pin 1 of the operational amplifier (OPA548T, Texas Instruments) in part (c). This OPA can deliver current pulses of up to 5 A. The input signal is amplified by the OPA548T, which flows through the LED and a resistor (2.4 Ω). The load resistor of 2.4 Ω works as a

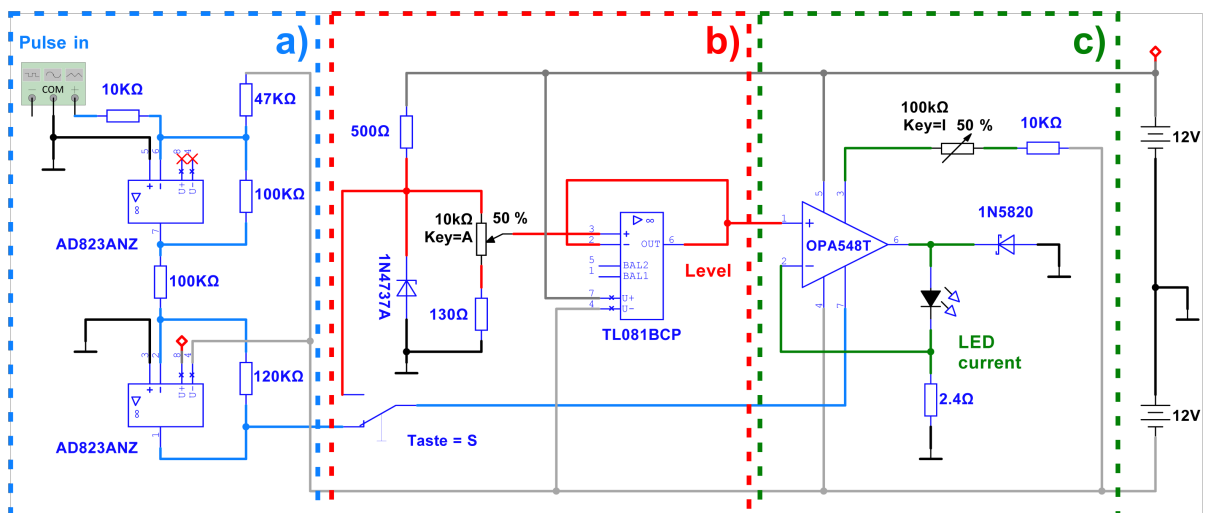


Fig. 2.7: Circuit diagram of the LED pulser.

current gauge for the connected LED. Because of the feedback, the voltage across the load resistor is equal to the input voltage. Thus, the LED drive current is determined by the following equation

$$I_{LED} = \frac{V_{Level}}{2.4\Omega} \quad (2.25)$$

In order to obtain the LED light pulse, the OPA548T output is switched on and off regularly using the voltage on the enable/disable pin 7 (E/S pin). As was stated in the description of part (a), a pulse train with required voltage is fed into the E/S pin. When the voltage of the pulse is no greater than -11.2 V, the OPA548T output is disabled. Thus, no current flows through the LED. When the E/S pin is pulled to at least -9.6 V, the OPA548T output returns to an enabled state. The LED is switched on.

Moreover, the OPA548T features an accurate current limit by controlling the input to the pin 3. Through connecting a potentiometer (100 k Ω) in series with a 10 k Ω resistor between the pin 3 and the negative power supply, the current limit is adjusted according to the equation as follows

$$I_{lim} = \frac{15000 \cdot 4.75V}{13750\Omega + 10k\Omega + R_{100k\Omega}} \quad (2.26)$$

where I_{lim} is the output current limit of the OPA548T and $R_{100k\Omega}$ is the value of the load part of the potentiometer. In this way a maximum current of 4 A can be set. Even LEDs with a lower nominal maximum current can be driven at much higher levels when the current pulse is short and the duty cycle low enough. Some reduction of the lifetime of typically 30.000 hours of the LED might result, but this is irrelevant for the experiments described in this thesis.

The optical properties of the light pulses generated by the LED pulser have been characterized. The characteristics of a representative blue LED (470 nm, Osram) are presented. A photodiode (ET-2020, Electro-Optics Technology) and an oscilloscope (PicoScope 2000, Pico Technology) are used to detect and measure the light pulses. For this purpose the LED light is imaged onto the photodiode with a large aperture aspheric lens. For power measurements the photodiode is replaced by a powermeter (Coherent USB19Q). The pulse repetition frequency is set to 10 kHz. In order to change the pulse duration of the light pulse, the duty cycle of the input pulse is adjusted, which is defined as *pulse duration* \times *pulse repetition frequency* \times 100%.

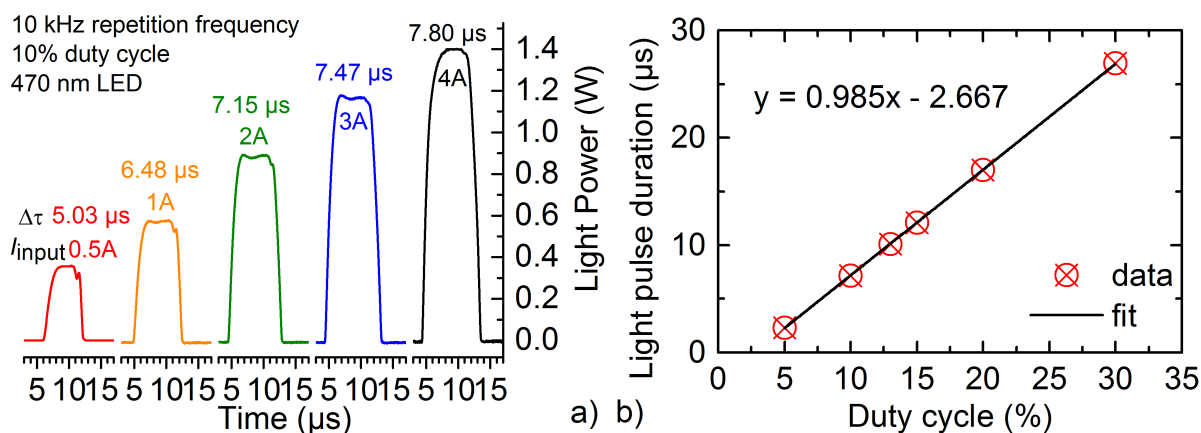


Fig. 2.8: a) Relationship between the light intensity and the drive current, b) Relationship between the pulse duration and the duty cycle of the input pulse.

Table 2.1: Power of 470 nm LED light pulse generated by different LED drive currents.

Input parameters				
Pulse repetition frequency	Duty cycle	LED drive current	Power of light	Peak power
10 kHz	13% (electrical) 10% (optical)	1 A	53.4 mW	0.5 W
		2 A	88.7 mW	0.9 W
		3 A	117.7 mW	1.2 W
		4 A	142.3 mW	1.4 W

The relationship between the light power and the drive current of the LED is established, as shown in Table 2.1 and Fig. 2.8a. The results show that the peak power increases with the increase of the drive current. With 4 A supplied to the LED, the integrated power of light is 142 mW and its peak power is ~ 1.4 W. The reported peak power is available for spectroscopic experiments in a standard 10×10 mm² cuvette in an area that can be made smaller than 2×2 mm².

It is intriguing that, under a fixed drive current, the light pulse duration, which is defined as the interval between the 50% of the amplitude, is not proportional to the duty cycle, but can be described as a linear function of the duty cycle. The linear fit result is shown in Fig. 2.8b. In addition, the light pulse duration is obviously dependent on the drive current. It rises with the increase of the drive current. The relationship between them is summarized in Table 2.2.

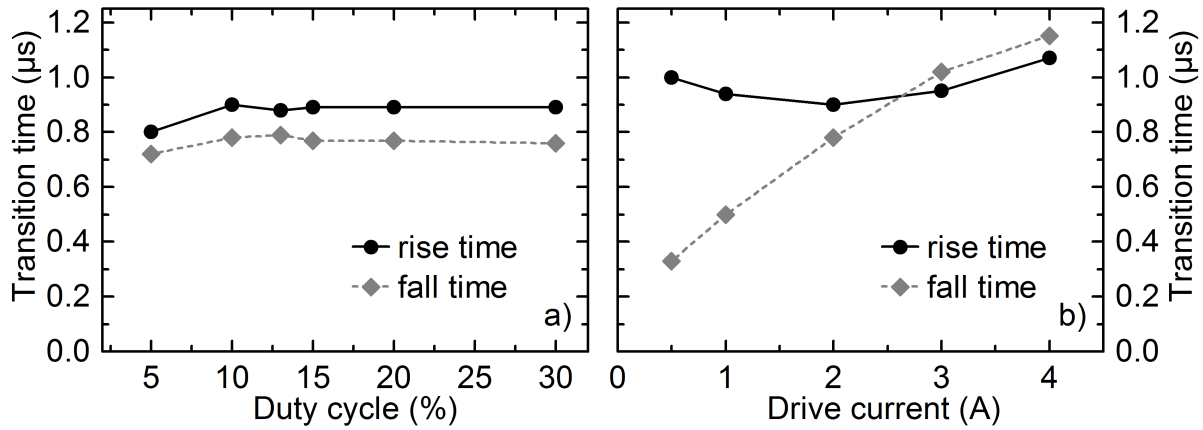


Fig. 2.9: a) Relationship between the pulse rise/fall time and the duty cycle of the input pulse, b) Relationship between the pulse rise/fall time and the drive current.

Table 2.2: Characteristics of 470 nm LED light pulse generated by different LED drive currents.

electrical parameters			light parameters		
pulse repetition frequency	LED drive current (A)	Duty cycle (%)	pulse rise time (μs)	pulse fall time (μs)	pulse duration (μs)
10 kHz	0.5	10	1.00	0.33	5.03
	1		0.94	0.50	6.48
	2		0.90	0.78	7.15
	3		0.95	1.02	7.47
	4		1.07	1.15	7.80

The other two important parameters of the light pulses are the rise and fall time. Pulse rise time is the time taken by a light pulse to change from 20% to 80% of the pulse amplitude maximum. And pulse fall time is the time taken for the pulse amplitude to decrease from 80% to 20% of the maximum value. Fig.2.9b shows that the pulse rise time drops first and then rises with the increase of the drive current. This is an intricate interplay between the current/voltage curve of the LED and the finite slew rate of the OPA548 OpAmp used in the pulser. In addition, the pulse fall time increases with the increase of the drive current. With 4 A supplied to the LED, the fall time of the light pulse is approximately 3.5 times higher than that with 0.5 A. This slowing of the turn-off is due to the large capacitance of the LED and the resulting “after-glow” when the current is turned off. With just a transistor used to switch the LED, a $\sim 50 \mu\text{s}$ after-glow was observed. To avoid this, the charge is thus actively

drawn from the LED. As can be seen in Fig. 2.9a, the influence of the duty cycle on the pulse rise and fall time is negligible. By optimizing the electrical input pulse, a light pulse as short as 2.3 μs can be generated. This leads to a maximum frequency of above 100 kHz.

2.5. Fiber-based fluorescence detection setup

The detection of the fluorescence spectrum of a sample is often necessary to understand its underlying electronic and vibronic properties. Standard lab equipment is sometimes not flexible or sensitive enough to match the specific requirements given by the problem in question. In this section, a home-built fluorescence setup is presented. It can be used to detect the fluorescence of materials from the UV to the NIR spectral region. Fused silica lenses are used to collect the emission signal and a flexible, fiber-based detection scheme is implemented that allows for an easy change of the detector.

The setup consists of a detection scheme based on best form lenses that couple the emitted light into an optical fiber, connecting to a compact grating spectrometer. A schematic is given in Fig. 2.10.

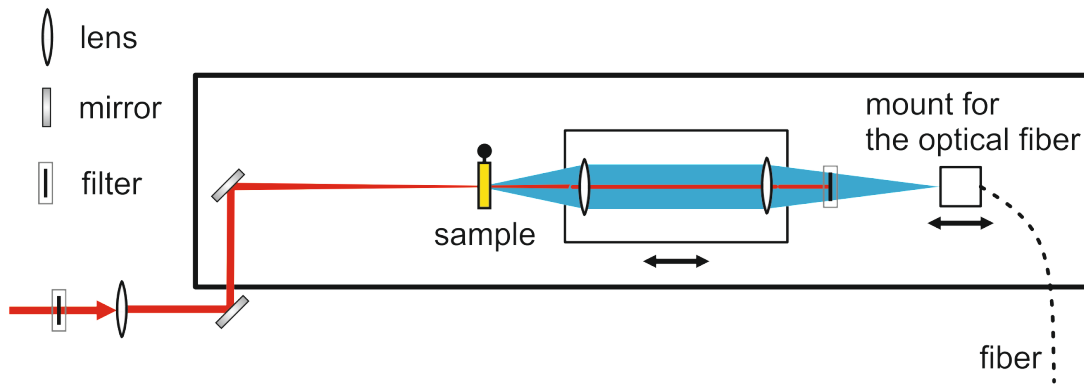


Fig. 2.10: Optical layout of the fluorescence detection setup.

As excitation, an OPO with a 1 kHz repetition rate is used (EKSPLA NT242). A shortpass spectral filter removes unwanted “stray” light from the laser, e.g., the fundamental of the OPO. The beam is focused onto the sample cuvette with a singlet lens $f = 350$ mm to obtain a $150 \mu\text{m}$ spot (FWHM) at a wavelength of 350 nm. This number depends on the wavelength used due to Gaussian beam optics and slightly changed output characteristics of the OPO for the different wavelengths. Signal collection is realized by a front (best form) lens with a diameter of 20 mm and a focal length of 25 mm, resulting in a numerical aperture of $\text{NA} = 0.37$. A second (best form) lens images the emitted light into an optical fiber. The focal length of this lens is 50 mm, giving a twofold magnification of the fluorescence spot to the optical fiber. In the measurement, a FWHM of $316 \mu\text{m}$ was found for 350 nm - without the sample cuvette. In experiments, the excitation beam size should be chosen such that it equals half the diameter of the fiber (or fiber bundle) in order to achieve maximum detection

sensitivity. Residual excitation light is removed by a longpass spectral filter. The optical fiber in use consists of a fiber bundle of 7 individual fibers with a diameter of 200 μm each. These are arranged in a fashion which is optimized for the entrance slit of a spectrometer by going from a round to a linear arrangement, thereby enhancing the total signal yield as compared to a single, larger fiber. As a detector, a compact grating spectrometer (Ocean Optics QE Pro) is used. The baseline of the experiment is detected at blocked excitation but with otherwise unchanged measurement conditions to be subtracted afterwards.

The excitation energy that can be used depends on the absorption coefficient and the concentration of the sample under investigation. To avoid reabsorption it is typically required that the optical density of the sample is around 0.1 OD or lower and no more than 10 % of the molecules should be excited. The excitation volume can roughly be estimated as the product of the cuvette's thickness and a circular spot size with the diameter of the FWHM of the real laser spot [Sai12].

Due to the various components in a spectrometer with wavelength dependent reflection or detection efficiency, an intensity calibration of the spectrometer is required. The intensity calibration allows that an absolute irradiance measurement is performed. That makes a spectrum accurate in both shape and magnitude. The transform from scope mode (counts) into irradiance mode ($\mu\text{W}/\text{cm}^2/\text{nm}$) for each pixel is expressed as follows:

$$I_p = C_p \left(\frac{S_p - D_p}{t_{\text{int}} \cdot \text{Area} \cdot dL_p} \right) \quad (2.27)$$

where I_p is the intensity in $\mu\text{W}/\text{cm}^2/\text{nm}$, C_p is a wavelength dependent calibration factor in $\mu\text{J}/\text{count}$, S_p is sample spectrum in counts, D_p is the baseline in counts, t_{int} is the integration time in seconds, Area is the collection area in cm^2 , specific to the sampling optics, dL_p is how many nanometers each pixel represents.

A NIST-traceable light source (HL-3 plus-CAL-EXT, Ocean Optics) is used to calibrate the absolute spectral response. The output power of the light source has been measured precisely. An optical diffuser (CC-3-UV-T, Ocean Optics) is used as sampling optics, in order to expand the collection of signal to 180° field of view (while a bare fiber has a 25° full angle field of view). The setting of any optics and fibers in the calibration should be maintained during the measurements. Therefore, it is best to calibrate the system prior to the measurement.

The combination of a compact grating spectrometer with a simple, lens based detection

scheme at a high numerical aperture yields an easy to use way to detect the fluorescence spectrum of samples with a low fluorescence quantum yield. Key parameters are the optimization of the signal collection by using best form lenses and a high NA, the use of a rearranged fiber bundle to transmit maximum signal to the spectrometer, and high quality spectral filters to block the excitation light.

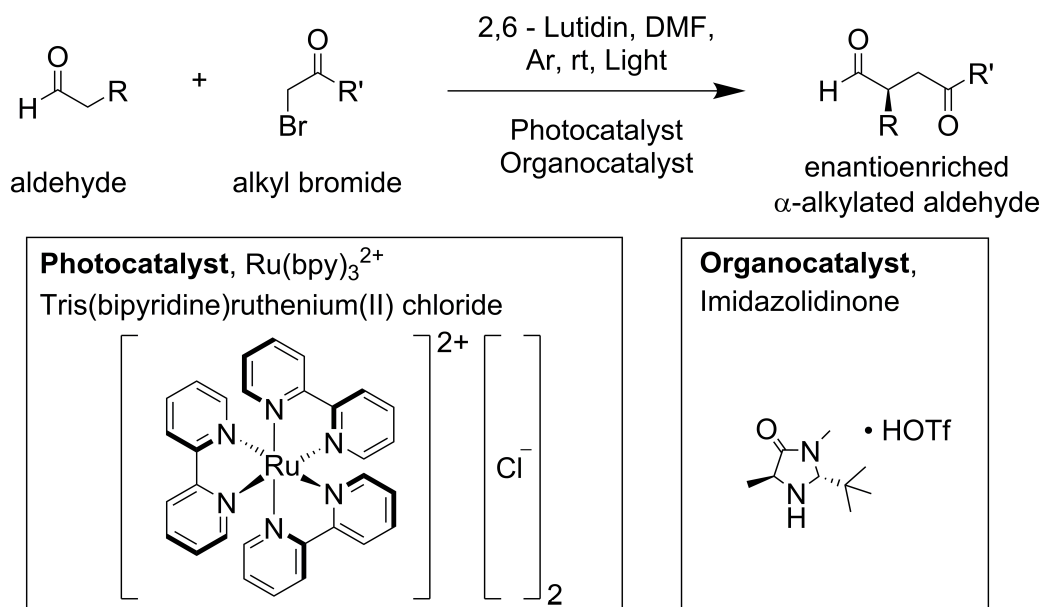
2.6. Additional chemical and spectroscopic methods

For characterizing chemical samples several chemical and spectroscopic methods have been used in this thesis. UV-Vis-NIR steady-state absorption data are measured on a Shimadzu UV-2600 absorption spectrometer. A Horiba Fluorolog fluorescence spectrometer with a 150 W Xe lamp is used for a part of fluorescence measurements. Spectroelectrochemical measurements are performed using an optically transparent thin-layer electrochemical (OTTLE) cells purchased from Hartl Research Group at University of Reading. It is equipped with CaF_2 windows, platinum mini-grid working and auxiliary electrodes and a silver wire reference electrode. During the micro-electrolysis procedures, the electrode potential is controlled by the Gamry Instruments Interface 5000P potentiostat. Solutions containing 0.2 M NBu_4PF_6 as the supporting electrolyte are used.

3. Light intensity-dependent quantum yield of the photoredox catalytic aldehyde alkylation and a detailed kinetic analysis

3.1. Introduction

The α -alkylation of aldehydes (Scheme 3.1) is one of the fundamental carbon-carbon bond forming transformations in organic synthesis. Additionally, this reaction has long been considered as the “holy grail” reaction in the realm of organo-catalysis [Alb09, MeI09, Ves12]. In 2008, Nicewicz and MacMillan reported a pioneering work, in which the direct α -alkylation of aldehydes is accomplished by merging photoredox- and organocatalysis [Nic08]. Their work has helped to initiate a renewed interest in the utility of photoredox catalysis to synthetic organic reaction development [Rom16].



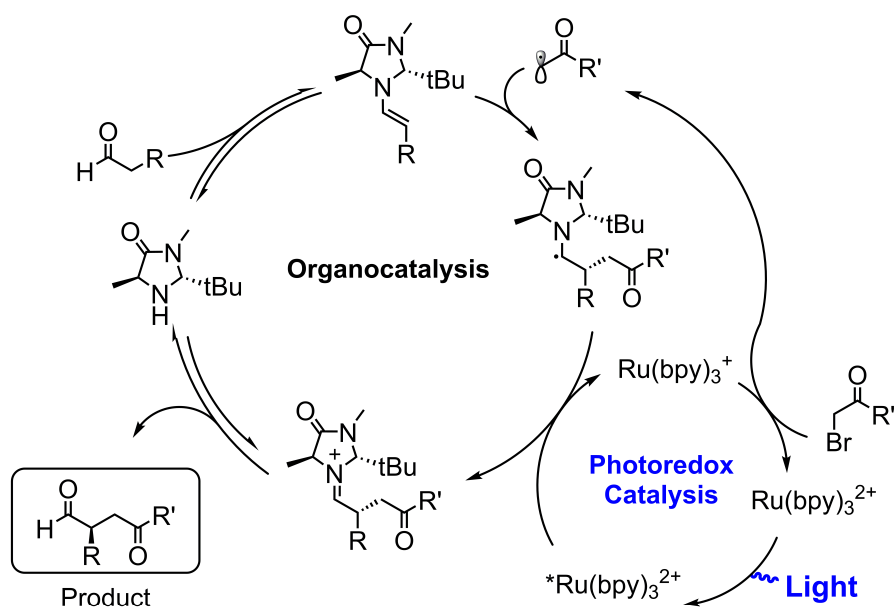
Scheme 3.1: Procedure of photoredox organocatalytic enantioselective α -alkylation of aldehydes [Nic08]. R and R', generic organic substituent; Ar, argon gas; rt, room temperature; HOTf, trifluoromethanesulfonic acid.

In the work, they hypothesized that the dual-catalysis aldehyde alkylation is initiated and terminated through a photoredox catalytic cycle [Nic08]. A detailed description of their proposed mechanism is illustrated in Scheme 3.2. Ruthenium tris(bipyridine) Ru(bpy)₃²⁺ is used as a visible light photoredox catalyst. After accepting a photon from a household 15W (electrical power) fluorescent light bulb, the excited catalyst *Ru(bpy)₃²⁺ removes a single electron from an enamine to initiate the first catalytic cycle by providing the Ru(bpy)₃⁺. This

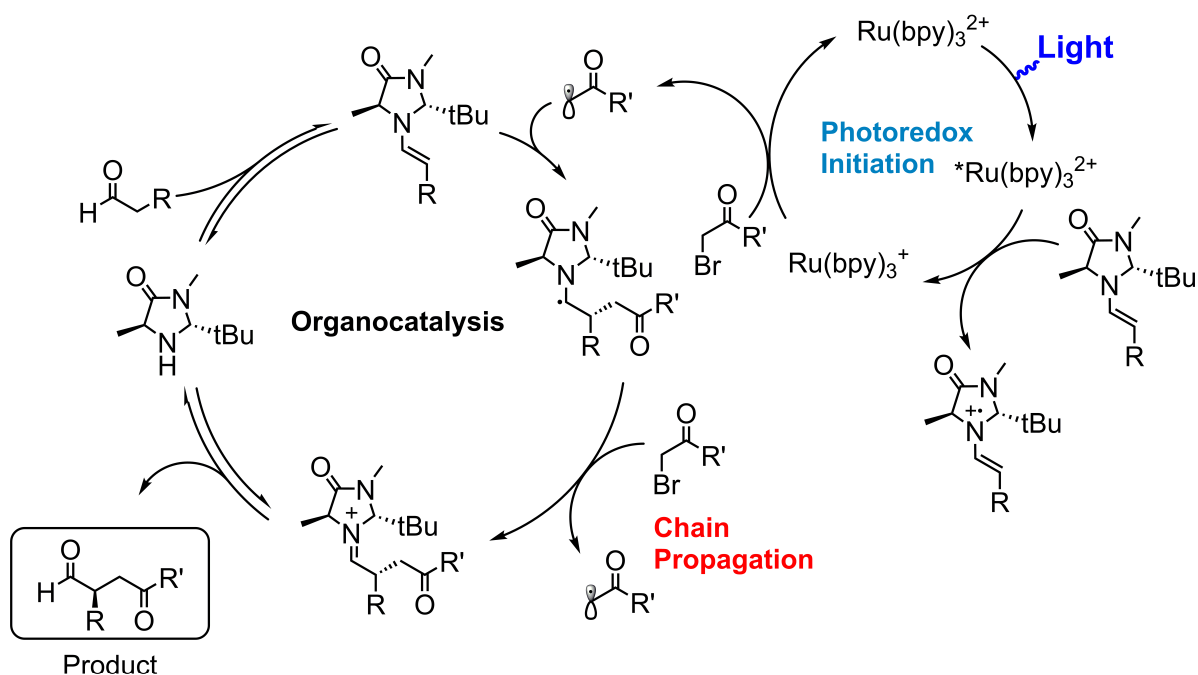
compound is a potent reductant and reacts with the α -bromocarbonyl substrate to deliver the alkyl radical while regenerating the ground state of the photoredox catalyst $\text{Ru}(\text{bpy})_3^{2+}$. The subsequent addition of the alkyl radical to the enamine produces an electron-rich α -amino radical. This species has a low barrier to oxidation and reacts next with the $^*\text{Ru}(\text{bpy})_3^{2+}$ via single electron transfer to furnish the iminium ion, which upon hydrolysis releases the requisite α -alkylated product.

In order to test the validity of their mechanistic proposal, they conducted a series of control experiments and $^*\text{Ru}(\text{bpy})_3^{2+}$ luminescence quenching studies [Nic08]. They confirmed that the excited catalyst $^*\text{Ru}(\text{bpy})_3^{2+}$ participates in the chemical transformation. Moreover, the $^*\text{Ru}(\text{bpy})_3^{2+}$ emission quenching by enamine was observed, which supports their proposed initiation pathway. Unfortunately, they didn't report any reaction quantum yield (Φ^P), which plays a very important role in the mechanistic studies [Jul83, Rub10].

The first quantum yield of the α -alkylation reaction has been determined by the König group and our own lab. Measurements were taken using gas chromatography (GC) and the photon number determination setup of our own design. They reported that, under irradiation with 20.5 mW (optical power) of a 443 nm LED for 60 min, a reaction quantum yield value of 49% was obtained [Meg10]. This result ($\Phi^P \leq 100\%$) is in agreement with the closed catalytic cycle hypothesized by the MacMillan group, as according to the photocatalytic mechanism, every photon absorbed generates one product maximum ($\Phi^P_{\text{max}} = 100\%$).



Scheme 3.2: Mechanistic proposal for photoredox organocatalytic α -alkylation of aldehydes by Nicewicz and MacMillan (Initiation part is not shown) [Nic08].



Scheme 3.3: Mechanistic proposal for photoredox initiated chain propagation manifold α -alkylation of aldehydes by Cismesia and Yoon [Cis15].

In 2015 Cismesia and Yoon have questioned the validity of the photoredox catalysis mechanism [Cis15]. Using NMR and chemical actinometry to determine the reaction quantum yield, they reported a value of 1800% for the same chemical transformation. According to their new value ($\Phi^P \gg 100\%$), they proposed an alternative mechanism in which the free radical chain reaction is the major mechanistic pathway in the α -alkylation reaction.

The mechanism proposed by the Yoon group is shown in Scheme 3.3. It shares several similar features to the one of the MacMillan group. First, the reaction is initiated by reductive quenching of the $^*\text{Ru}(\text{bpy})_3^{2+}$ by enamine. Second, the final α -alkylated product arises upon hydrolysis of the iminium ion, which is the result of one-electron oxidation of the α -amino radical. It was proposed that this final oxidation occurs through the electron transfer from the α -amino radical to the $^*\text{Ru}(\text{bpy})_3^{2+}$ [Nic08]. However, the Yoon group highlighted that this step is more likely a chain propagating reduction of the bromomalonate by the α -amino radical.

Meanwhile, there is great discrepancy between the reaction quantum yield value of Yoon group (1800%) and the one of König and Riedle groups (49%). Cismesia and Yoon attributed this to the different setups used, and especially whether oxygen is removed from

the solution [Cis15]. Indeed, König, Riedle and coworkers performed the measurement through a LED and optical powermeter based setup [Meg10], while Cismesia and Yoon employed chemical actinometry to determine the reaction quantum yield. However, the reaction solution used in the work of König and Riedle groups was also purged by nitrogen gas (N₂), which is the same as the Yoon group did (It is not mentioned in ref. [Meg10]).

When these two inconsistent reaction quantum yield values are evaluated, it is important to have an accurate knowledge of the experimental parameters of the quantum yield measurements. As was mentioned above, there was no significant difference in sample preparation. Moreover, the measurements were conducted in standard cuvettes with the same optical path length (10 mm). In addition, both the reaction solutions were stirred during the irradiation.

The main difference between the two measurements of reaction quantum yield lies in the concentration of the reactants and catalysts, as well as irradiation wavelength, power and time. They are summarized in Table 3.1.

Table 3.1: The difference between reaction quantum yield measurements performed by the König/Riedle groups [Meg10] and by the Yoon group [Cis15].

The amount of the reactants and catalysts						
Group	Octanal (mmol)	Diethyl Br-malonate (mmol)	Ru(bpy)₃Cl₂•6H₂O (mmol)	Organo- catalyst (mmol)	2,6- lutidine (mmol)	DMF (mL)
König, Riedle	1.93 (2 eq)	0.963 (1 eq)	0.0048 (0.5 mol%)	0.193 (20 mol%)	1.93 (2 eq)	2.7
Yoon	1.3 (2 eq)	0.65 (1 eq)	0.0032 (0.5 mol%)	0.13 (20 mol%)	1.3 (2 eq)	1.3
Group	Irradiation wavelength (nm)		Irradiation power (mW)		Irradiation time (hr)	
König, Riedle	443		20.5		1	
Yoon	436		0.183		4	

Table 3.1 shows that the samples were irradiated at slightly different wavelengths. But both of these wavelengths populate the same metal-to-ligand charge transfer (MLCT) excited state of Ru(bpy)₃²⁺ [Kal82]. Especially the molar absorption coefficient of Ru(bpy)₃²⁺ at 443 nm ($1.30 \times 10^4 \text{ M}^{-1}\text{cm}^{-1}$) is almost the same as it is at 436 nm ($1.25 \times 10^4 \text{ M}^{-1}\text{cm}^{-1}$). On

the basis of these data, the absorbance is calculated by the Beer-Lambert's law [Tur10] for the two experiments. The results show that the absorbance in both cases greatly exceeds 4, indicating the irradiation light is absorbed completely. Therefore, the influence of the difference in irradiation wavelength can be excluded.

Table 3.1 also shows that the concentration of the chemicals used by the König and Riedle groups is smaller than that of the Yoon group. But the proportional relations of reactants to the substrate diethyl-bromomalonate are the same for the two measurements. Moreover, a significant difference can be found in the irradiation powers, which differ by two orders of magnitude. Furthermore, the time at which the reaction quantum yield is measured is very important. The substrate consumption in the course of the reaction for longer irradiation time decreases the chemical yield rate of product, and then decreases the reaction quantum yield.

In order to distinguish which parameters could account for the disparity of quantum yield, we have thus performed a series of new quantum yield measurements by using the QYDS. The concentration of the reactants and catalysts were the same as the Yoon group applied. The yield of product was quantified via NMR spectroscopy. The reaction quantum yield was determined in a time dependent way using our device at a range of low to medium light powers (from 30 μ W to 10 mW). Our new results are shown in Fig. 3.4 [Rei17]. The simulation results based on our new mechanism are also shown in Fig. 3.4, which will be discussed in more detail later.

It becomes obvious that the quantum yield of α -alkylation reaction must be considered as a function of irradiation power and time. Our new values are consistent with the reported reaction quantum yield, which are in particular $\Phi^P = 49\%$ for 20.5 mW and $\Phi^P = 1800\%$ for 0.184 mW, respectively (inset spots in Fig. 3.4b2).

Surprisingly, the maximum value of the reaction quantum yield (Φ_{\max}^P) in all measurements is achieved at the lowest irradiation power ($\Phi_{\max}^P = 3500\%$ for 30 μ W). The values of Φ_{\max}^P at each irradiation power are proportional to the reciprocal square root of the irradiation power (panel d in Fig 3.4). Furthermore, the reaction quantum yield is not always higher than 100%. The reaction quantum yields determined at an irradiation power higher than 20 mW are all below 100%. This means that the irradiation power exerts a decisive influence on the proceeding mechanism of the reaction. The chain propagation mechanism dominates for low power, whereas the photocatalytic cycle mechanism plays the main role for high power. Our new proposed mechanism is illustrated in Scheme 3.5 in detail [Rei17].

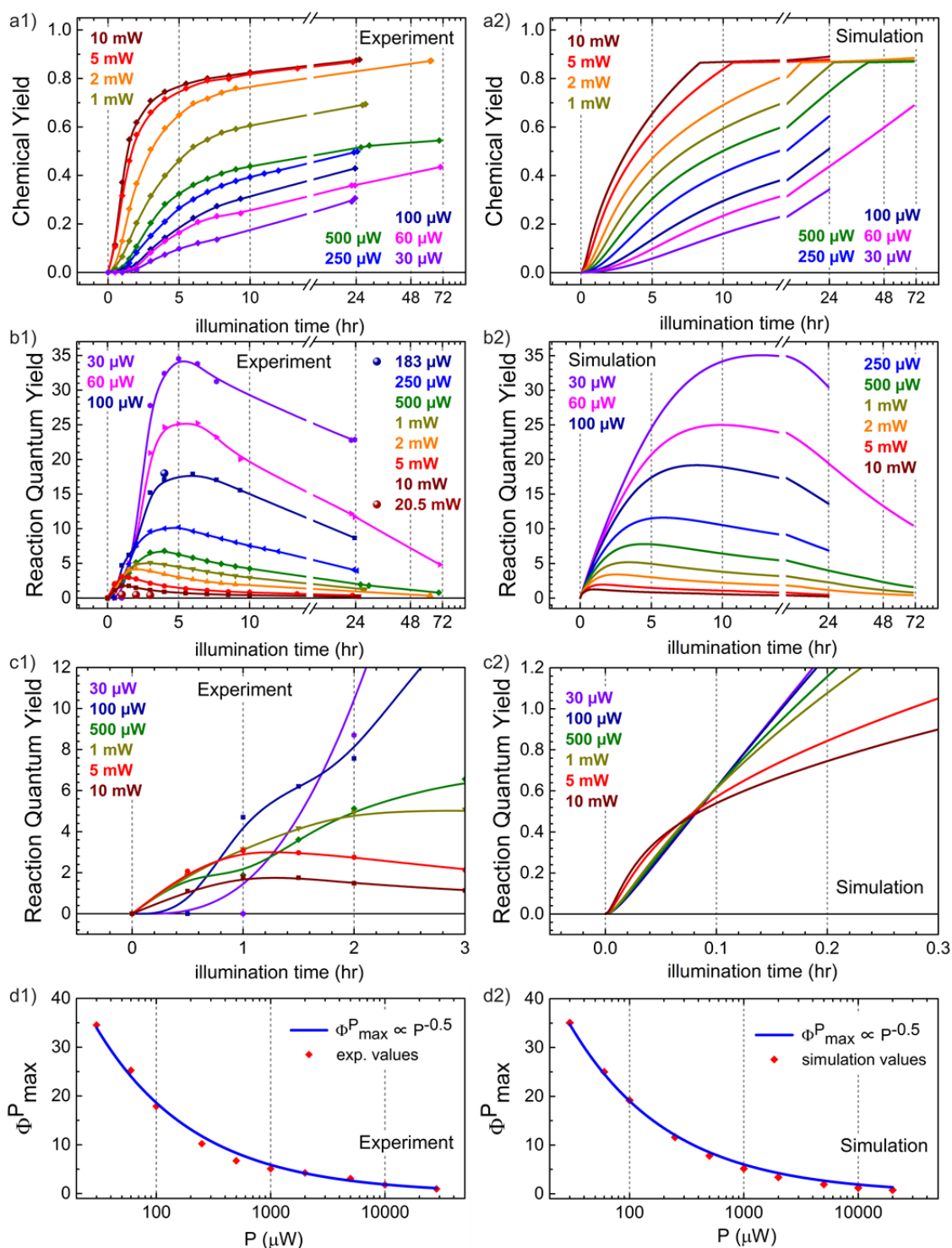
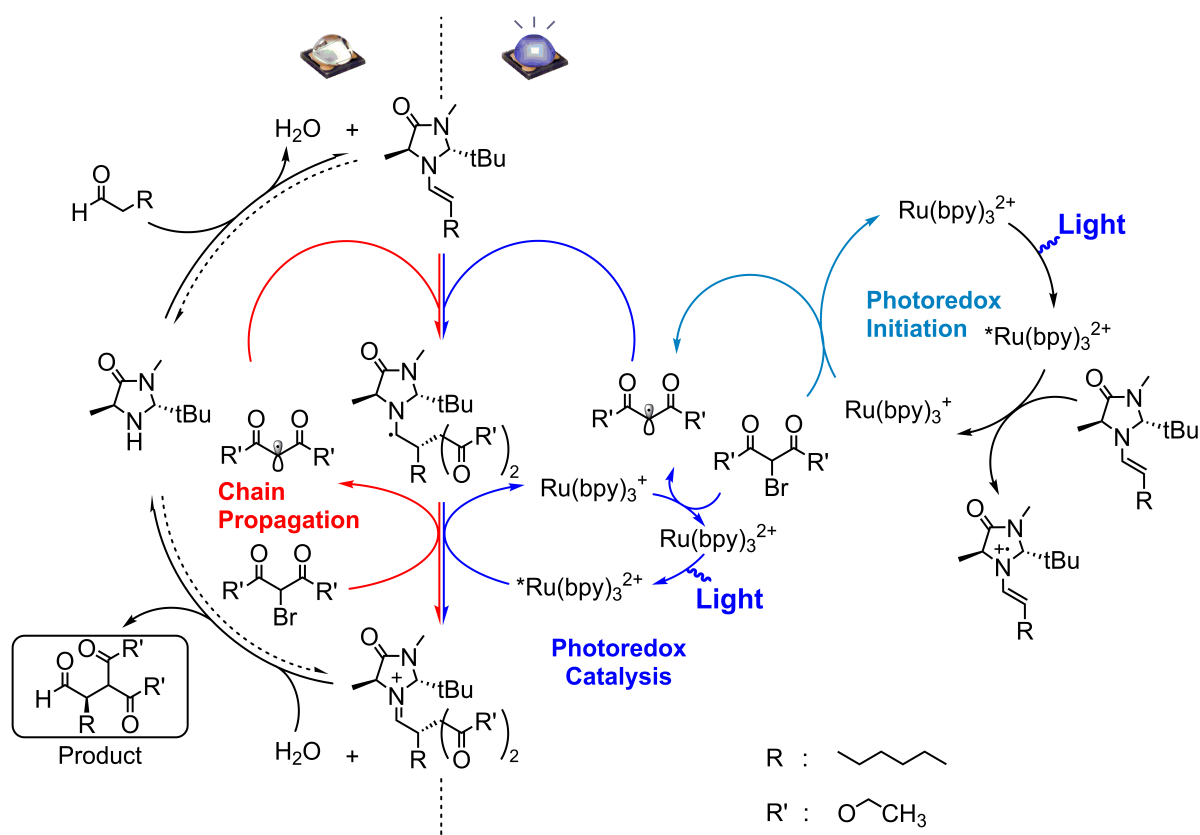
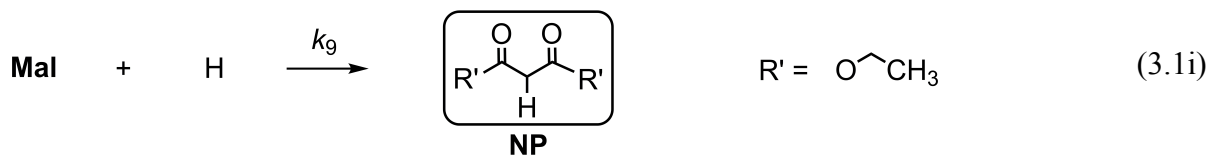
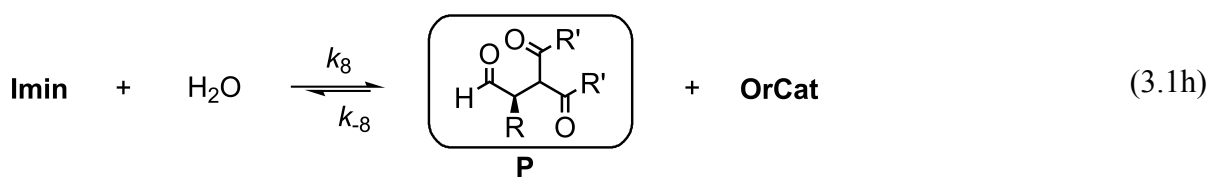
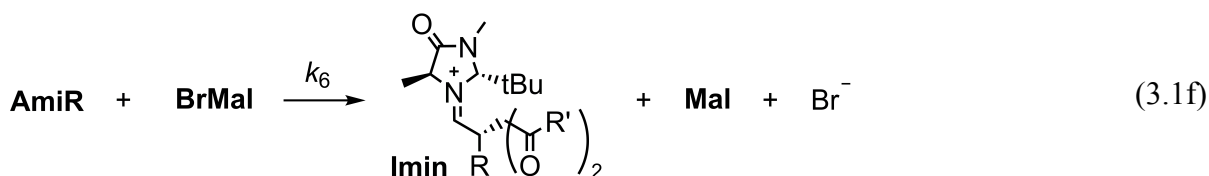
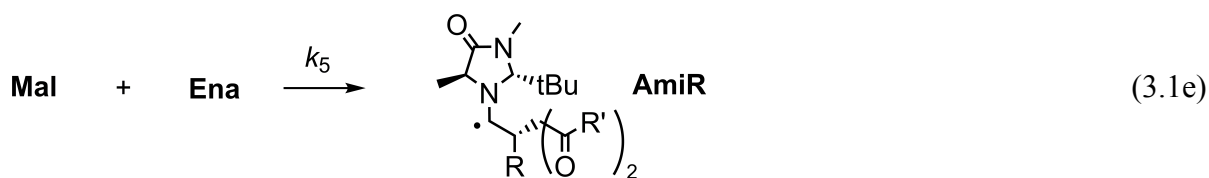
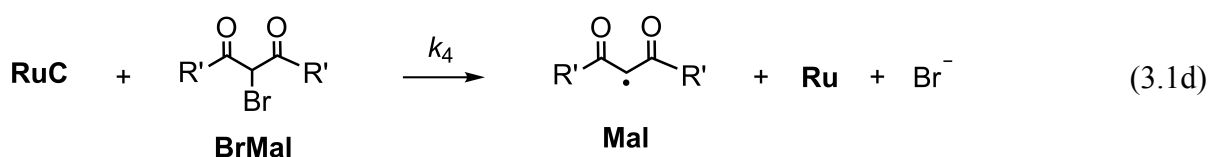
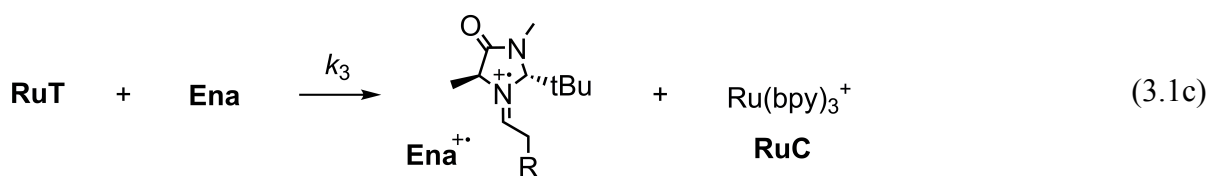
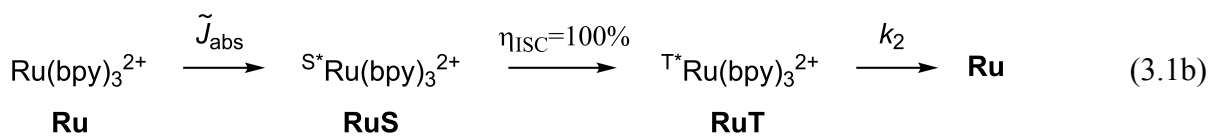
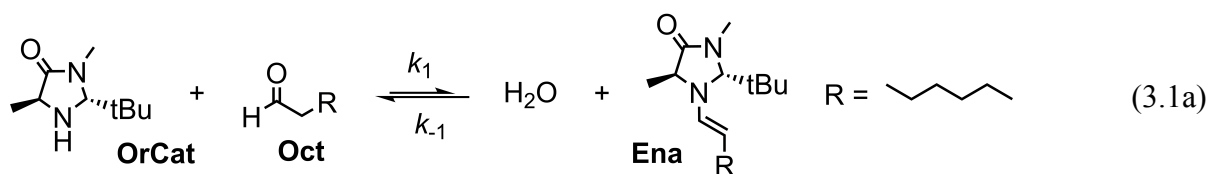


Fig. 3.4: Influence of the light power and the illumination time on the reaction quantum yield results. Left: experimental results (lines in a1, b1 and c1 are added to guide the eye). Right: simulation results. a1,2) Time and light power dependent chemical yield of α -alkylation reaction. b1,2) Φ^P at various excitation light powers. c1,2) The observation of a lag phase at the beginning of the reaction, when the light power is low. d1,2) Maximum values of Φ^P (Φ_{\max}^P) as a function of the light power. The values (red dots) are compared to $P_{\text{abs}}^{-0.5}$ (blue solid line).



Scheme 3.5: Our new mechanistic proposal: Chain propagation in competition with photoredox catalytic production underlying the mechanism of the α -alkylation of aldehydes.

The crucial parameter that decides between the two mechanisms is the occurrence of the malonate radical. Higher concentrations of $*\text{Ru}(\text{bpy})_3^{2+}$ upon higher irradiation power suggest a preferential oxidation of the α -amino radical by the excited photoredox catalyst. This process controls the formation of the malonate radical in a tightly catalytic cycle. And therefore, the determined maximum values of quantum yield are reduced. In contrast, lower concentration of $*\text{Ru}(\text{bpy})_3^{2+}$ upon lower irradiation power results in a favored α -amino radical quenching by bromomalonate. This decouples its photocatalytic production from the organocatalytic reaction by the chain propagation mechanism. Since the latter process is independent on light, a reaction quantum yield significantly higher than 100% is achieved. The occurrence of the two different product formation mechanisms can be controlled by the light power.



Scheme 3.6: The reaction equations for our proposed mechanism in Scheme 3.5. **Oct**, octanal (an aldehyde); **OrCat**, imidazolidinone (organocatalyst); **Ena**, enamine; **RuS**, singlet excited state of $\text{Ru}(\text{bpy})_3^{2+}$; **RuT**, triplet excited state of $\text{Ru}(\text{bpy})_3^{2+}$; **BrMal**, bromomalonate; **Mal**, malonate radical; **AmiR**, α -amino radical; **Imin**, iminium ion; **P**, product; **NP**, by-product.

3.2. Kinetic analysis

In order to have a better understanding of the photocatalytic α -alkylation of aldehydes, a detailed chemical kinetic analysis of our proposed mechanism (Scheme. 3.5) is made based upon the experimental variables. It is convenient to rewrite our mechanism into a set of chemical rate equations, which is summarized in Scheme 3.6.

The kinetic analysis section is divided into five parts. The first part deals with the enamine formation in the dark before the illumination starts. The second part presents the determination of the light amount absorbed by the sample. The third part describes a comprehensive mathematical model for the QY simulation. The fourth part presents a quantitative estimate of the rate constants in the model, which is based on the steady-state assumption. The final part presents the results of the simulation, focusing on the comparison of our mechanism with Yoon's mechanism.

3.2.1. Enamine formation

As all quantum yield determination experiments were performed with a delay of half an hour after mixing, the considerations begin with the dark reaction of the organocatalyst (**OrCat**) with octanal (**Oct**) to form the enamine (**Ena**) (reaction 3.1a). A water molecule (**H₂O**) is split off in addition. The corresponding equilibrium constant (K_{Ena}) has been reported in ref. [Cis15] to be

$$K_{\text{Ena}} = \frac{[\text{Ena}][\text{H}_2\text{O}]}{[\text{Oct}][\text{OrCat}]} = 8.1 \times 10^{-3} \quad (3.2)$$

In our case, a cuvette is initially charged with [**Oct**] of 1 M and [**OrCat**] of 0.1 M. The initial concentration of **H₂O** is estimated to be 1 mM, according to the moisture content in the solvent DMF. On the basis of these data, the initial concentration of **Ena** of 23.9 mM is formed when the reaction reaches a chemical equilibrium status. And the concentration of **H₂O** is increased by the same amount and therefore the assumption of the initial water concentration is not critical.

In addition, the formation speed and the absorption spectrum of **Ena** are determined via steady-state absorption spectroscopy. The absorption spectra of a mixed solution containing 1 M of **Oct** and 0.1 M of **OrCat** are shown in Fig. 3.7. The absorption spectrum remains finally stable after approximately 36 hours, revealing that the formation of **Ena** is complete after 36 hours without the magnetic stirrer. This result highlights that the formation of **Ena** is unfavorable and confirms the reported tiny K_{Ena} by Cismesia and Yoon [Cis15]. However,

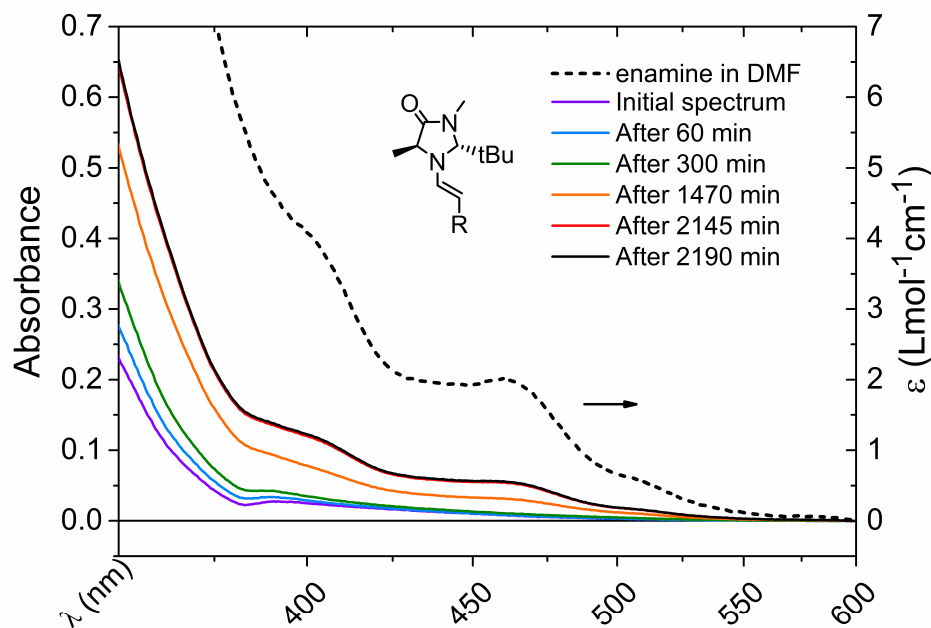


Fig. 3.7: Spectral evolution of the absorption spectrum with time (solid line) and molar absorption coefficient of **Ena** in DMF (dash line). Inset: the structure of **Ena**.

they failed to provide how long the solution was kept in the dark to secure equilibration. In addition, the equilibrium of **Ena** formation has also been investigated by Bahamonde and Melchiorre [Bah16]. They contended that the reaction mixtures were kept in the dark for 30 minutes to assure equilibration. They obtained an equilibrium constant of 0.155 for **Ena** formation in solvent CD_3CN . Their result confirms once again that the equilibrium for **Ena** formation is unfavorable. However, the major defect in their experiments is that they don't verify whether the **Ena** formation reaches the chemical equilibrium status in 30 minutes.

Fig. 3.7 also presents that the **Ena** dissolved in DMF exhibits very weak absorption bands in the visible light region. The maximum of the molar absorption coefficient of **Ena** in the visible range is $\sim 4 \text{ M}^{-1}\text{cm}^{-1}$ at 400 nm.

3.2.2. Light power and absorbance

In general, the reaction quantum yield measurements are conducted in rectangular cuvettes with flat optical windows and 10 mm transmitted optical path length. Thus, the absorption of light by the solution can be described by Beer-Lambert's law [Tur10]. The light flux at time t and a distance z from the front window at which the light enters the cuvette is given by

$$\tilde{J}(z, t) = \tilde{J}_0(z, t) \cdot 10^{-\text{OD}(z, t)} \quad (3.3)$$

where \tilde{J}_0 is the incident light flux ($\text{photons} \cdot \text{cm}^{-2} \cdot \text{s}^{-1}$) and OD is the absorbance, which is

defined by

$$OD(z, t) = \sum_{i=1}^N \varepsilon_i \int_0^z c_i(x, t) dx \quad (3.4)$$

In (3.4), the concentration of species i is denoted by c_i and its corresponding molar absorption coefficient is ε_i . In our experiments, a blue LED (Roithner Lasertechnik GmbH) with center wavelength of 441 nm is used as light source, whose spectrum is shown in Fig. 3.8.

The absorption spectrum for $\text{Ru}(\text{bpy})_3^{2+}$ in DMF solution is also shown in Fig. 3.8. The molar absorption coefficient at 441 nm of $\text{Ru}(\text{bpy})_3^{2+}$ is $\varepsilon_{\text{Ru}} = 1.28 \times 10^4 \text{ M}^{-1}\text{cm}^{-1}$. For the molar absorption coefficient at 441 nm of **Ena**, which could act as an alternative photosensitizer during the QY measurement [Bah16], we use $\varepsilon_{\text{Ena}} \sim 2 \text{ M}^{-1}\text{cm}^{-1}$ based on our absorption measurement (Fig. 3.6). Compared to the $\text{Ru}(\text{bpy})_3^{2+}$ absorbance of 32, the absorbance of **Ena** has been assumed to be sufficiently small (~ 0.05) so that its absorption may be neglected.

As discussed above, the absorbance is greatly in excess of unity. Thus, the distribution of excited photocatalysts (**RuE**) is effectively localized to a thin layer near the front window of the cuvette. In that event, the rate of the reaction would be highly non-uniform.

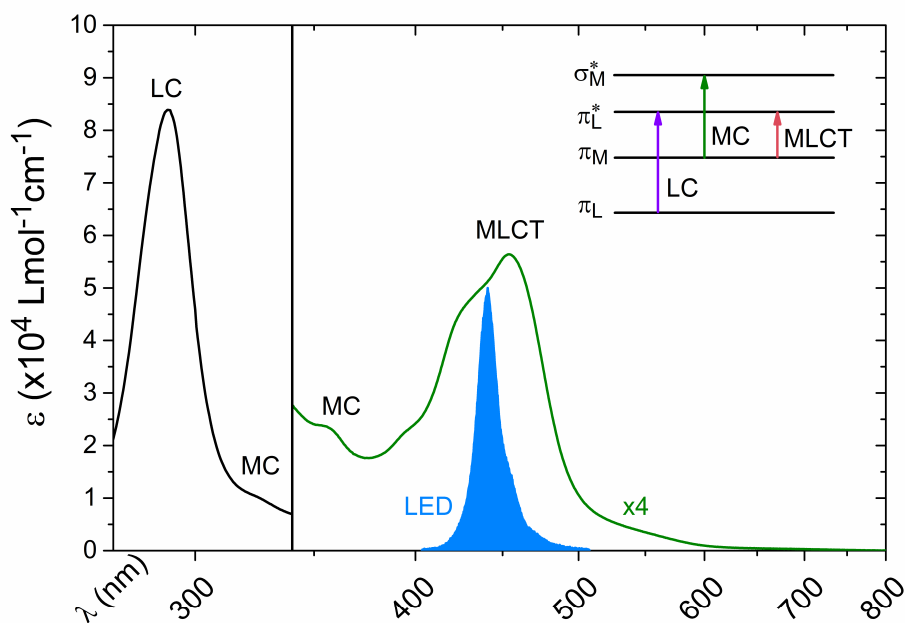


Fig. 3.8: Absorption spectrum for $\text{Ru}(\text{bpy})_3^{2+}$ in DMF at room temperature along with the assignments for the various bands. The inset shows the electronic transitions of $\text{Ru}(\text{bpy})_3^{2+}$. The blue filled curve represents the emission of the LED (nominal 435nm, measured 441nm).

However, the solution was rapidly stirred with a magnetic stirrer bar (8 mm × Ø 3 mm) in the course of the measurement. As a result, it is assumed that the photocatalyst is excited with a uniform rate and the intermediate species have a uniform distribution within the volume. Thus, the volumetric rate of light absorption \tilde{J}_{abs} ($\text{einstein}\cdot\text{L}^{-1}\cdot\text{s}^{-1}$) is given by

$$\tilde{J}_{\text{abs}} = \tilde{J}_0 \cdot \text{Area} \cdot \left(1 - 10^{-\varepsilon_{\text{Ru}} \cdot [\text{Ru}] \cdot d}\right) / V_0 \quad (3.5)$$

where Area is the illuminated area (8×8 mm²), d is the length of cuvette along the optical path, and V_0 is the solution volume.

In our experiments, the absorbed light amount is determined by performing a physical power measurement of the light with and without sample. Thus, the rate of light absorption is calculated by

$$\begin{aligned} \tilde{J}_{\text{abs}} &= P_0 \cdot \frac{\lambda}{h \cdot c} \cdot \frac{1}{N_A} \cdot \frac{\left(1 - 10^{-\varepsilon_{\text{Ru}} \cdot [\text{Ru}] \cdot d}\right)}{V_0} \\ &= P_{\text{abs}} \cdot \frac{\lambda}{h \cdot c} \cdot \frac{1}{N_A} \cdot \frac{1}{V_0} \end{aligned} \quad (3.6)$$

where P_0 is the incident light power, P_{abs} is the absorbed light power and λ is the wavelength of light source. h , c and N_A are the Planck constant, the speed of light in air and the Avogadro constant, respectively.

3.2.3. Mathematical model

In this part a comprehensive mathematical model is described. It includes the reaction steps relevant to our proposed mechanism. Generally, the illumination of an absorbing solution by a light beam directed in any direction other than parallel to the gravity direction must lead to buoyancy-driven fluid motion. However, because a magnetic stirrer is employed in the course of the measurement, it is considered that the stirring speed is fast enough to generate a uniform distribution of reactants and intermediates in the solution. Therefore, the buoyancy-driven fluid motion effect is neglected. The conservation equations derived from reaction 3.1a – 3.1i are

$$\begin{aligned} \frac{d[\text{OrCat}]}{dt} &= -k_1[\text{OrCat}][\text{Oct}] + k_{-1}[\text{Ena}][\text{H}_2\text{O}] + k_8[\text{Imin}][\text{H}_2\text{O}] \\ &\quad - k_{-8}[\text{P}][\text{OrCat}] \end{aligned} \quad (3.7a)$$

$$\frac{d[\text{Oct}]}{dt} = -k_1[\text{OrCat}][\text{Oct}] + k_{-1}[\text{Ena}][\text{H}_2\text{O}] \quad (3.7b)$$

$$\frac{d[\mathbf{H}_2\mathbf{O}]}{dt} = k_1[\mathbf{OrCat}][\mathbf{Oct}] - k_{-1}[\mathbf{Ena}][\mathbf{H}_2\mathbf{O}] - k_8[\mathbf{Imin}][\mathbf{H}_2\mathbf{O}] + k_{-8}[\mathbf{P}][\mathbf{OrCat}] \quad (3.7c)$$

$$\frac{d[\mathbf{Ena}]}{dt} = k_1[\mathbf{OrCat}][\mathbf{Oct}] - k_{-1}[\mathbf{Ena}][\mathbf{H}_2\mathbf{O}] - k_3[\mathbf{Ena}][\mathbf{RuT}] - k_5[\mathbf{Ena}][\mathbf{Mal}] \quad (3.7d)$$

$$\frac{d[\mathbf{Ru}]}{dt} = -\tilde{J}_{\text{abs}} + k_2[\mathbf{RuT}] + k_4[\mathbf{RuC}][\mathbf{BrMal}] \quad (3.7e)$$

$$\frac{d[\mathbf{BrMal}]}{dt} = -k_4[\mathbf{RuC}][\mathbf{BrMal}] - k_6[\mathbf{AmiR}][\mathbf{BrMal}] \quad (3.7f)$$

$$\frac{d[\mathbf{RuT}]}{dt} = \tilde{J}_{\text{abs}} - k_2[\mathbf{RuT}] - k_3[\mathbf{Ena}][\mathbf{RuT}] - k_7[\mathbf{AmiR}][\mathbf{RuT}] \quad (3.7g)$$

$$\frac{d[\mathbf{RuC}]}{dt} = k_3[\mathbf{Ena}][\mathbf{RuT}] - k_4[\mathbf{RuC}][\mathbf{BrMal}] + k_7[\mathbf{AmiR}][\mathbf{RuT}] \quad (3.7h)$$

$$\frac{d[\mathbf{Mal}]}{dt} = k_4[\mathbf{RuC}][\mathbf{BrMal}] - k_5[\mathbf{Ena}][\mathbf{Mal}] + k_6[\mathbf{AmiR}][\mathbf{BrMal}] - k_9[\mathbf{Mal}] \quad (3.7i)$$

$$\frac{d[\mathbf{AmiR}]}{dt} = k_5[\mathbf{Ena}][\mathbf{Mal}] - k_6[\mathbf{AmiR}][\mathbf{BrMal}] - k_7[\mathbf{AmiR}][\mathbf{RuT}] \quad (3.7j)$$

$$\frac{d[\mathbf{Imin}]}{dt} = k_6[\mathbf{AmiR}][\mathbf{BrMal}] + k_7[\mathbf{AmiR}][\mathbf{RuT}] - k_8[\mathbf{Imin}][\mathbf{H}_2\mathbf{O}] + k_{-8}[\mathbf{P}][\mathbf{OrCat}] \quad (3.7k)$$

$$\frac{d[\mathbf{P}]}{dt} = k_8[\mathbf{Imin}][\mathbf{H}_2\mathbf{O}] - k_{-8}[\mathbf{P}][\mathbf{OrCat}] \quad (3.7l)$$

\tilde{J}_{abs} is given by eq 3.6 and the rate constants of the reactions are denoted by k_i (forward reaction) or k_{-i} (backward reaction). Furthermore, the long-lived triplet excited state of $\text{Ru}(\text{bpy})_3^{2+}$ (**RuT**) serves as a single-electron oxidant in the reaction rather than its singlet state (**RuS**). The reason is that the **RuS** relaxes to the **RuT** within 100 fs via intersystem crossing [Dam97], which is significantly shorter than the lifetime of the **RuT** (912 ns at room temperature in DMF [Cas83]). Moreover, the efficiency of intersystem crossing from **RuS** to **RuT** is essentially unity [Cam07]. Thus, the population of the **RuT** upon light absorption is described as $d[\mathbf{RuT}]/dt = \tilde{J}_{\text{abs}}$.

To the conservation eq 3.7a-3.7l, initial conditions are appended. The initial concentration of bromomalonate (**BrMal**) and $\text{Ru}(\text{bpy})_3^{2+}$ (**Ru**) is

$$[\mathbf{BrMal}]_0 = 0.5 \text{ M}, [\mathbf{Ru}]_0 = 2.5 \text{ mM} \quad (3.8)$$

It is assumed that the **Ena** formation reaction (3.1a) reaches the chemical equilibrium status before the illumination starts. Thus, the initial concentration of **OrCat**, **Oct**, **Ena** and **H₂O** is

$$\begin{aligned} [\text{OrCat}]_0 &= 76.1 \text{ mM} , & [\text{Oct}]_0 &= 976.1 \text{ mM}, \\ [\text{Ena}]_0 &= 23.9 \text{ mM} , & [\text{H}_2\text{O}]_0 &= 24.9 \text{ mM} \end{aligned} \quad (3.9)$$

For other intermediates appearing during the reaction and the product, the concentrations are

$$[\text{RuT}]_0 = [\text{RuC}]_0 = [\text{Mal}]_0 = [\text{AmiR}]_0 = [\text{Imin}]_0 = [\text{P}]_0 = 0\text{M} \quad (3.10)$$

Eq 3.6 - 3.10 constitute an initial value problem for a nonlinear system of differential equations. They will be used to calculate time- and light intensity-dependent concentration profiles. Finally, the reaction quantum yield of α -alkylation product is computed by

$$\Phi^{\text{P}} = \frac{[\text{P}](t)}{\tilde{J}_{\text{abs}} \cdot t} \quad (3.11)$$

Eq 3.11 is the time-averaged reaction quantum yield which is determined experimentally. In our case, the illumination power is constant and the light is completely absorbed by the photosensitizer, revealing that \tilde{J}_{abs} is a constant. In addition, after the steady state has become established, the rate of product formation $d[\text{P}]/dt$ can be considered as a constant. Thus

$$\frac{d[\text{P}]}{dt} = \frac{\Delta[\text{P}]}{\Delta t} \quad (3.12)$$

and the reaction quantum yield is expressed as follows:

$$\Phi^{\text{P}}(t) = \frac{\Delta[\text{P}]}{\Delta t} \cdot \frac{1}{\tilde{J}_{\text{abs}}} \quad (3.13)$$

3.2.4. Estimation of the rate constants

The mathematical model in the previous part is highly nonlinear and is unlikely to possess a closed-form solution. Thus, the primary investigation of the quantum yield properties will be conducted numerically in the next part. In this part, the estimation method of the rate constants of the reactions in the model is shown, based on the steady-state assumption and with particular reference to the behavior of the quantum yield in the measurements.

As the time required for establishing the equilibrium is compared to the overall time scale, it suffices for the modelling to ensure that the equilibrium (reaction 3.1a) is maintained. This is also verified by ^1H NMR spectroscopic analysis in ref. [Bah16]. Since this situation corresponds to Arrhenius's concept of an intermediate in equilibrium, the **Ena** is called an Arrhenius intermediate [Lai87]. And the exact condition for this case is

$$\begin{aligned} k_{-1}[\mathbf{Ena}][\mathbf{H}_2\mathbf{O}] &\gg k_3[\mathbf{Ena}][\mathbf{RuT}] \\ k_{-1}[\mathbf{Ena}][\mathbf{H}_2\mathbf{O}] &\gg k_5[\mathbf{Ena}][\mathbf{Mal}] \end{aligned} \quad (3.14)$$

Furthermore, the solutions are always kept in the dark for half an hour after mixing to secure equilibration [Cis15, Bah16, Rei17]. Thus it is assumed that the reversible reaction 3.1a needs at least 30 min to reach the equilibrium state (with magnetic stirrer). Then upon illumination, the **Ena** is consumed through the **RuT** quenching reaction (3.1c) and the **Mal** radical addition reaction (3.1e). The rate of the **RuT** quenching by the **Ena** (3.1c) has been reported in ref. [Cis15].

$$k_3 = 1 \cdot 10^7 \text{ M}^{-1}\text{s}^{-1} \quad (3.15)$$

In addition, according to our quantum yield measurements, the rate of the product formation increases with time before the substrate exhaustion (see Fig. 3.4a). This indicates that the **Mal** addition reaction (3.1e) is more efficient than the quenching reaction (3.1c), because the reaction 3.1e acts as the key step in the product pathway, while the reaction 3.1c merely initiates the organocatalytic cycle. Therefore, the rate with which the **Ena** undergoes reaction 3.1e is assumed to be faster than the quenching rate k_3 .

With these assumptions, the rates k_1 , k_{-1} and k_5 are estimated to be

$$\begin{aligned} k_1 &= 8 \cdot 10^{-4} \text{ M}^{-1}\text{s}^{-1} , \\ k_{-1} &= 0.1 \text{ M}^{-1}\text{s}^{-1} , \\ k_5 &\gg k_3 \end{aligned} \quad (3.16)$$

Another assumption is that the product formation reaction 3.1h remains in equilibrium in the steady state phase. In this case the following equation applies.

$$\frac{[\mathbf{P}][\mathbf{OrCat}]}{[\mathbf{H}_2\mathbf{O}][\mathbf{Imin}]} = K_P \quad (3.17)$$

Since the concentrations of **OrCat** and **H₂O** are assumed to be constant, eq. 3.17 then becomes

$$[\mathbf{P}] = \frac{K_P \cdot [\mathbf{H}_2\mathbf{O}]_{\text{eq}}}{[\mathbf{OrCat}]_{\text{eq}}} \cdot [\mathbf{Imin}] \quad (3.18)$$

With above described assumptions, a steady-state treatment is applied to the equation system (3.7a-3.7l). They are written as

$$\frac{d[\mathbf{RuT}]}{dt} = \tilde{J}_{\text{abs}} - k_2[\mathbf{RuT}] - k_3[\mathbf{Ena}][\mathbf{RuT}] - k_7[\mathbf{AmiR}][\mathbf{RuT}] = 0 \quad (3.19a)$$

$$\frac{d[\mathbf{RuC}]}{dt} = k_3[\mathbf{Ena}][\mathbf{RuT}] - k_4[\mathbf{RuC}][\mathbf{BrMal}] + k_7[\mathbf{AmiR}][\mathbf{RuT}] = 0 \quad (3.19b)$$

$$\begin{aligned} \frac{d[\mathbf{Mal}]}{dt} &= k_4[\mathbf{RuC}][\mathbf{BrMal}] - k_5[\mathbf{Ena}][\mathbf{Mal}] + k_6[\mathbf{AmiR}][\mathbf{BrMal}] \\ &\quad - k_9[\mathbf{H}][\mathbf{Mal}] = 0 \end{aligned} \quad (3.19c)$$

$$\frac{d[\mathbf{AmiR}]}{dt} = k_5[\mathbf{Ena}][\mathbf{Mal}] - k_6[\mathbf{AmiR}][\mathbf{BrMal}] - k_7[\mathbf{AmiR}][\mathbf{RuT}] = 0 \quad (3.19d)$$

The initial concentration of the **BrMal** can be expressed as

$$[\mathbf{BrMal}]_0 = [\mathbf{BrMal}] + [\mathbf{Mal}] + [\mathbf{AmiR}] + [\mathbf{Imin}] + [\mathbf{P}] + [\mathbf{NP}] \quad (3.20)$$

If the initial concentration of the **BrMal** and the concentration of the **Mal** are much greater than that of the intermediates **AmiR**, as well as the amount of the **NP** is negligible, eq 3.19 therefore reduces to

$$\begin{aligned} [\mathbf{BrMal}]_0 &= [\mathbf{BrMal}] + [\mathbf{Imin}] + [\mathbf{P}] + [\mathbf{Mal}] \\ \Rightarrow [\mathbf{BrMal}] &= ([\mathbf{BrMal}]_0 - [\mathbf{Imin}] - [\mathbf{P}]) - [\mathbf{Mal}] \\ \Rightarrow [\mathbf{BrMal}] &\equiv \overline{[\mathbf{BrMal}]} - [\mathbf{Mal}] \end{aligned} \quad (3.21)$$

where $\overline{[\mathbf{BrMal}]}$ is equal to $[\mathbf{BrMal}]_0 - [\mathbf{Imin}] - [\mathbf{P}]$. And the steady-state rate of the product formation is then

$$\begin{aligned} \frac{d[\mathbf{P}]}{dt} &= \frac{K_P \cdot [\mathbf{H}_2\mathbf{O}]_{\text{eq}}}{[\mathbf{OrCat}]_{\text{eq}}} \cdot \frac{d[\mathbf{Imin}]}{dt} \\ &= \gamma \cdot (k_6[\mathbf{AmiR}][\mathbf{BrMal}] + k_7[\mathbf{AmiR}][\mathbf{RuT}]) \end{aligned} \quad (3.22)$$

where the constant γ is equal to $K_P[\mathbf{H}_2\mathbf{O}]_{\text{eq}}/[\mathbf{OrCat}]_{\text{eq}}$. Therefore, the reaction quantum yield is expressed as

$$\begin{aligned} \Phi^P &= \frac{\Delta[\mathbf{P}]}{\Delta t} \cdot \frac{1}{\tilde{J}_{\text{abs}}} \\ &= \gamma \cdot (k_6[\mathbf{AmiR}][\mathbf{BrMal}] + k_7[\mathbf{AmiR}][\mathbf{RuT}]) \cdot \frac{1}{\tilde{J}_{\text{abs}}} \end{aligned} \quad (3.23)$$

The explicit solution of the eq 3.19a - 3.19d, combining with the eq 3.21 and the assumed rate constants in eq 3.15-3.16, is detailed in appendix A1. With this solution, the reaction quantum yield can be finally expressed as

$$\Phi^P = C_0 + C_1 \frac{\overline{[\mathbf{BrMal}]}}{\tilde{J}_{\text{abs}}} + \sqrt{C_2 + C_3 \frac{\overline{[\mathbf{BrMal}]}}{\tilde{J}_{\text{abs}}} + C_4 \left(\frac{\overline{[\mathbf{BrMal}]}}{\tilde{J}_{\text{abs}}} \right)^2} \quad (3.24)$$

where C_0 , C_1 , C_2 , C_3 and C_4 are constants. Moreover, as is described in appendix A1, the constants $C_1 - C_4$ are only dependent on three variables, namely the ratios k_6/k_7 , ratio k_9/k_5 and the constant γ . Therefore, these three variables may be determined through fitting the experimental data to eq 3.24.

It is apparent from Fig. 3.4a and b that the steady-state treatment is valid when the reaction quantum yield reaches its maximum value. Thus, a plot of Φ_{\max}^P vs. $P_{\text{abs}} / [\text{BrMal}]$ should display a curve which can be fitted by eq 3.24. Such behavior is observed and the result is shown in Fig. 3.9. The corresponding data are summarized in Table 3.2.

Table 3.2: Maximum value of the quantum yield of product formation at different pump light power.

$[\text{BrMal}]$ (M)	0.435	0.428	0.395	0.359	0.342	0.317	0.341	0.314
P_{abs} (μW)	60	100	250	500	1000	2000	5000	10000
Φ_{\max}^P	25.24	17.88	10.20	6.72	5.08	4.23	3.07	1.78

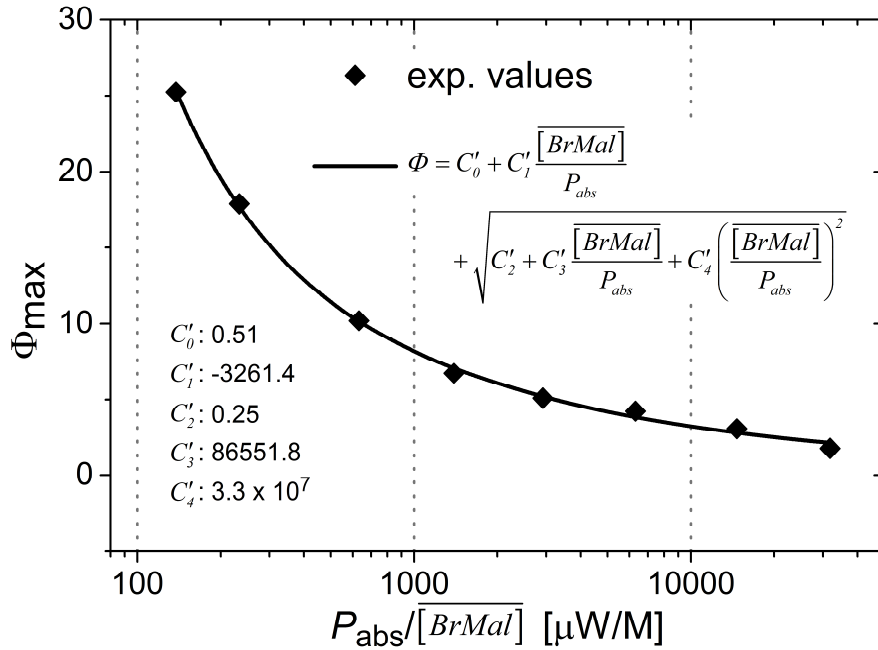


Fig. 3.9: Plot of Φ_{\max}^P vs. $P_{\text{abs}} / [\text{BrMal}]$ for experimental values in Table 3.2 (red dots, the same data are also shown in Fig. 3.4) and the corresponding fit results by using the eq. 3.24 (blue solid line).

What is surprising is the fact that the accurate estimates of the rate constants remain challenging with these fit results. It is plausible that a number of limitations might have influenced the accurate estimation. First, the illumination time at which Φ^P reaches its maximum value is not taken into account in fitting. Another possible source is that some unknown parameters, which are overlooked in the steady-state assumption, may play a role in the quantum yield determination. To sum up, with the fit results and the relationship between P_{abs} and \tilde{J}_{abs} (eq. 3.6), the ratios k_6/k_7 and k_5/k_9 are roughly estimated as follows

$$\begin{aligned} k_6/k_7 &\approx 1 \times 10^{-11} \\ k_9/k_5 &\ll 4 \times 10^{-3} \text{ M} \end{aligned} \quad (3.25)$$

It will be shown in the following section that the kinetics of the product formation process crucially depend on the value of k_7 (or $k_6 = 10^{-11} \times k_7$) and the ratio k_9/k_5 . The simulations described in the following text are performed for several values of rate constants of k_7 less than or equal to the diffusion-limited values and different values of the ratio k_9/k_5 .

The fit results also show that $C'_0 = 0.51$ affords good fits of the calculated value of C_0 ($\sim 0.5\gamma$), if the constant $\gamma = K_P [\text{H}_2\text{O}]_{\text{eq}} / [\text{OrCat}]_{\text{eq}}$ is equal to 1. This indicates that K_P can be assumed to be 3.0, with the value of the $[\text{H}_2\text{O}]_{\text{eq}}$ and $[\text{OrCat}]_{\text{eq}}$ in eq. 3.9. A complete list of the rate constants is given in Table 3.3.

Table 3.3: Summary of the rate constants for the simulation of the QY of α -alkylation product formation. a) diffusion limited rate constant [Mon06], b) [Rei17].

Rate constant	k_1	k_{-1}	k_2	k_3	k_4	k_5
	$K_{\text{Ena}} = k_1/k_{-1}$		[Cas83]	[Cis15]	[Cam07]	$k_3 \ll k_5 \leq 8.3 \times 10^9$ ^a
Value ($\text{M}^{-1}\text{s}^{-1}$)	8×10^{-4}	0.1	$1 \times 10^6 \text{ s}^{-1}$	1×10^7	2.7×10^7	1×10^8
Rate constant	k_6	k_7	k_8	k_{-8}	k_9	
	$\leq k_7 \times 10^{-11}$	$\leq 8.3 \times 10^9$ ^a	$K_P = k_8/k_{-8} = 3.0$ $k_{-8} < k_8$ ^b		$k_9/k_5 \ll 4 \times 10^{-3} \text{ M}$	
Value ($\text{M}^{-1}\text{s}^{-1}$)	≈ 0.08	8×10^9	1	≈ 0.3	$\approx 10^3 \text{ s}^{-1}$	

3.2.5. Numerical results

In the first part of this section, the rate constants $k_5 - k_9$ are estimated via matching the simulated data with the experimental data. The reaction mechanism is discussed with the help of the simulation in the second part. It is important to note that, unless otherwise indicated, the rate constants in Table 3.3 are used in all calculation.

To identify the impact of rate constants on Φ^P , the maximum values of Φ^P (Φ_{\max}^P) and the time (τ_{\max}) at which Φ^P reaches its maximum value are used as a specific quantitative measure of the reaction quantum yield. The simulated values of Φ_{\max}^P and τ_{\max} are generated from the model described in section 3.2.3 with various values of k_5 , k_7 , k_8 and k_9/k_5 .

With $P_{\text{abs}} = 1$ mW, Fig. 3.10a and b show the Φ_{\max}^P and τ_{\max} as a function of k_5 . Within the possible range of k_5 ($1 \times 10^8 \leq k_5 \leq 8.3 \times 10^9$), the predicted values of Φ_{\max}^P and τ_{\max} are independent on k_5 . This is consistent with the result of the steady-state treatment in which the Φ^P is a function of k_9/k_5 , rather than that of k_5 . Therefore, to simplify the following calculations, k_5 is roughly estimated to be $10^8 \text{ M}^{-1}\text{s}^{-1}$.

A similar treatment is made for k_8 in which the rate constants except k_8 and k_{-8} are fixed as well as $P_{\text{abs}} = 1$ mW. The results are shown in Fig. 3.10c and d. When $k_8 < 1 \text{ M}^{-1}\text{s}^{-1}$, the simulated Φ_{\max}^P increases with k_8 , while the value of τ_{\max} decreases. At larger k_8 , the Φ_{\max}^P and τ_{\max} are independent on k_8 . This result can be explained if the steady-state approximation no longer applies when $k_8 < 1 \text{ M}^{-1}\text{s}^{-1}$. Φ^P depends on the ratio $\gamma = k_8/k_{-8}$, rather than that of k_8 . In the simulation, γ remains constant, which means that simulated values of Φ^P should be constant when the steady-state assumption is fulfilled. In addition, the product formation speed is comparable with that of **Ena** formation. Thus, k_8 is estimated to be $1 \text{ M}^{-1}\text{s}^{-1}$.

For the same value of P_{abs} , with the values of the rate constants in Table 3.3 except k_7 , k_9 , Fig. 3.10e and f show the impact of rate constant k_7 and the ratio k_9/k_5 on Φ_{\max}^P and τ_{\max} . The dashed contour lines show the experimental Φ_{\max}^P and τ_{\max} , which are 5.08 and 3.3 hr respectively. Clearly, if the model is correctly specified with k_7 and k_9/k_5 equal to its true value, then the simulated values of Φ_{\max}^P and τ_{\max} will be the same as the values that we observed in the measurement. Working in the reverse order, the best matched simulated values are obtained at the point where the two dashed contour lines intersect, and k_7 and k_9/k_5 are determined to be the values corresponding to the intersection, i.e.

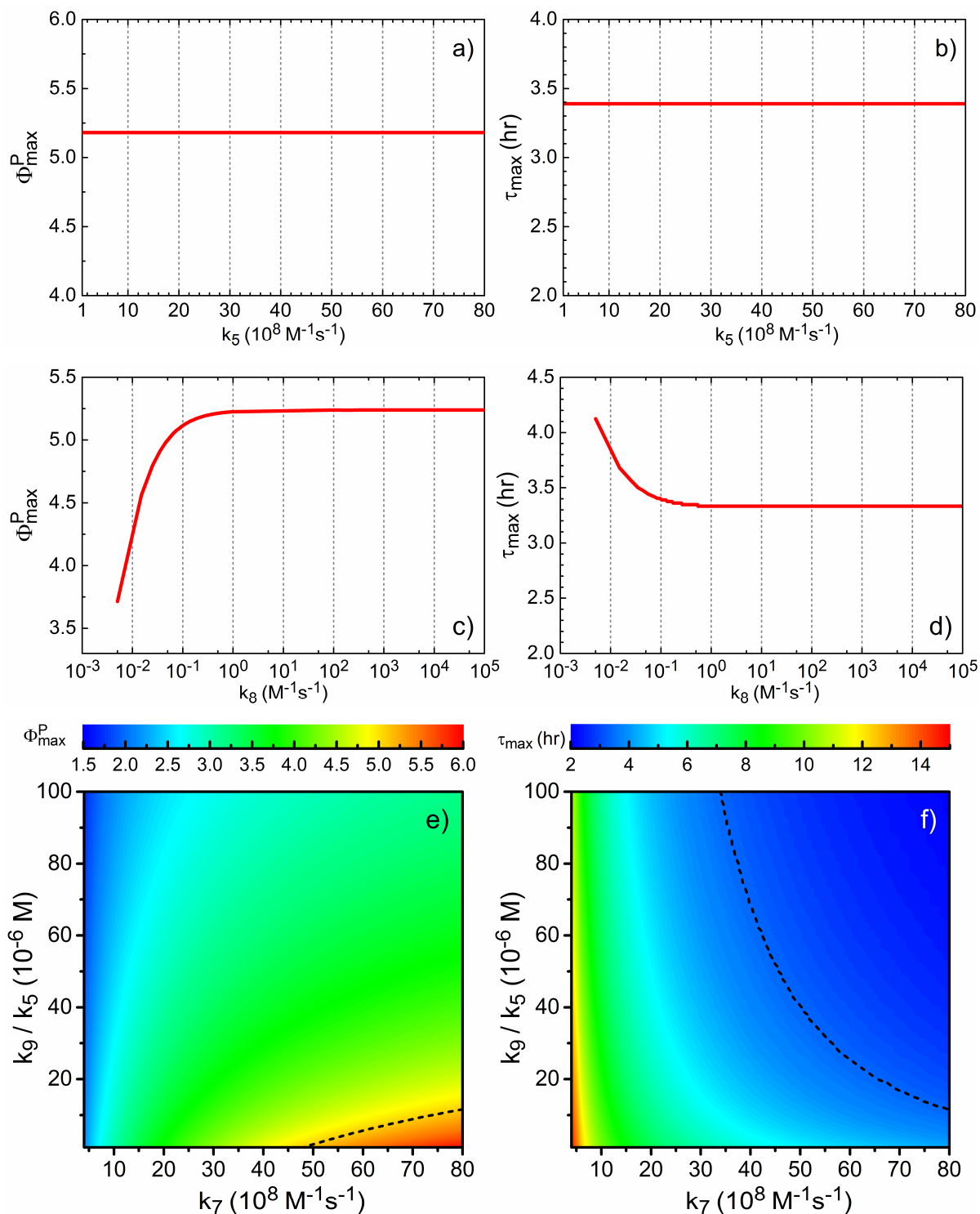


Fig. 3.10: Simulated values of Φ_{\max}^P (left) and τ_{\max} (right) with $P_{\text{abs}} = 1$ mW and the values of rate constants in Table 3.3. a) and b) as function of k_5 ; c) and d) as function of k_8 ; e) and f) as function of k_7 and k_9/k_5 , higher amplitudes are shown in red, and lower amplitudes are shown in blue. The dashed contour lines show the experimental values of $\Phi_{\max}^P = 5.08$ and $\tau_{\max} = 3.3$ hr.

$$\begin{aligned}
 k_7 &\approx 8 \times 10^9 \text{ M}^{-1} \text{ s}^{-1} \\
 \frac{k_9}{k_5} &\approx 1 \times 10^{-5} \text{ M}
 \end{aligned}
 \tag{3.26}$$

Based on the measured values of the reaction quantum yield, all the rate constants are reasonably estimated and summarized in Table 3.3. For initial concentrations described in eq. 3.8-3.10 with these rate constants, the simulation results of reaction quantum yield for a range of values of illumination power are shown in Fig. 3.11a and b. The rapid decrease of Φ^P with increasing P_{abs} is obviously evident. For lower P_{abs} , Φ^P is much greater than 100%, whereas Φ^P remains less than 100% for higher P_{abs} . The results are in good agreement with the experiment (see Fig. 3.4). Furthermore, the behavior of Φ^P as a function of time is also clear. Φ^P rapidly rises to its maximum value before beginning its slow decay to zero.

In addition, the striking lag phase observed in the measurement with low light power also appears in the simulation, which is shown in panel a) of Fig. 3.11. In the experiment, this lag phase is observed as a delayed response of the quantum yield to the light irradiation, when the light power is lower than 0.5 mW. Nevertheless, at the beginning of the irradiation in the simulation, Φ^P is not zero with weak light power. This discrepancy can be attributed to the measuring accuracy of the product concentration. It is very likely that the product concentration is extremely low at the beginning of the irradiation, when the light is weak. And this may lead to the difficulty of the accurate determination of the product concentration. Therefore, the observed lag phase is presented as an initiation phase in the simulation.

In the mechanism suggested by Cismesia and Yoon [Cis15], the chain propagation is the unique product formation pathway in the reaction (Scheme 3.3). This mechanism can be expressed as a model without the photocatalytic oxidation of α -amino radical (without eq 3.1g). In other words, the model is modified for use with $k_7 = 0$. The simulation results of the modified model are shown in Fig. 3.11c and d.

Interestingly, for $k_7 = 0$, the initiation phase disappears (Fig. 3.11c). The simulated Φ^P doesn't show any obvious correlation with P_{abs} at the beginning of the irradiation. This simulation result is not consistent with our experiment. Therefore, the presence of the initiation phase immediately rules out the reaction mechanism proposed by Cismesia and Yoon.

In order to understand why the initiation phase appeared in the measurement, the result with $k_7 = 0$ is compared with that with $k_7 = 8 \times 10^9 \text{ M}^{-1} \text{ s}^{-1}$. In the case of $P_{\text{abs}} = 20 \text{ mW}$, the Φ^P for $k_7 = 0$ reveals a significant deceleration in the rate of product formation (grey dashed line

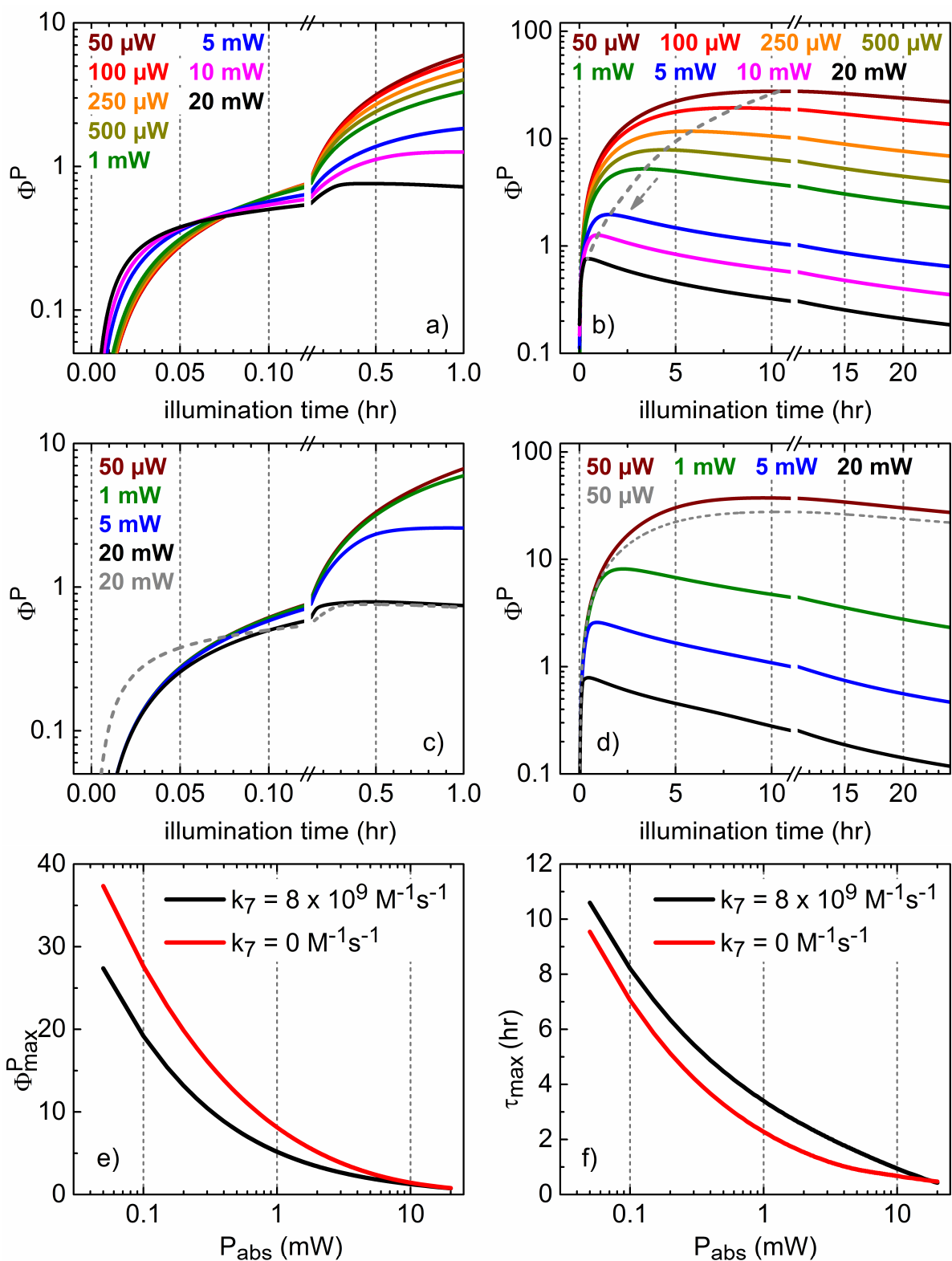


Fig. 3.11: Simulation of Φ^P for the rate constants in Table 3.3 with different values of illumination power. a) and b) results of our mechanism (Scheme 3.5); c) and d) results of Yoon's mechanism (Scheme 3.3), the grey dashed lines show the results based on our mechanism; e) and f) results with the different values of k_7 .

vs. black line in Fig. 3.11c). However, in the case of $P_{\text{abs}} = 50 \mu\text{W}$, no significant difference is found within an hour of irradiation between the results with $k_7 = 0$ and $8 \times 10^9 \text{ M}^{-1}\text{s}^{-1}$. This indicates that the reaction mechanisms are the same for low light power, whereas for high light power the products are formed in different pathways. Furthermore, when the light is strong, this pathway is more efficient than the chain propagation pathway. This is in good agreement with our competitive mechanism. In our explanation, the product formation is dominated by the photocatalytic pathway in the case of high light power. It results in a shorter initiation phase and, consequently, Φ^{P} will reach the steady state faster.

Unexpectedly, for $k_7 = 0 \text{ M}^{-1}\text{s}^{-1}$, Φ^{P} reaches its maximum value faster than that for $k_7 = 8 \times 10^9 \text{ M}^{-1}\text{s}^{-1}$ (Fig. 3.11f). When $P_{\text{abs}} \geq 20 \text{ mW}$, τ_{max} becomes identical in both cases. This finding is consistent with previous experimental results in ref. [Cis15]. Upon addition of *N,N*-dimethyl-*p*-toluidine, which can quench $^*\text{Ru}(\text{bpy})_3^{2+}$ at a very fast rate, they observed a significant increase of the rate of product formation. The reaction conducted with this quencher was complete faster than that without the quencher. In this case, the $^*\text{Ru}(\text{bpy})_3^{2+}$ quenching can be expressed as reduction in the contribution of the photocatalytic pathway to the product formation. If the quenching rate is large enough, the effect of quencher addition is similar to removing the photocatalytic pathway from the mechanism. Therefore, their experiment provides further evidence to support our model.

4. Effect of intermittent illumination on the photoredox catalytic aldehyde alkylation

4.1. Introduction

In order to unambiguously demonstrate the occurrence of the radical-chain processes in the α -alkylation reaction, Cismesia and Yoon performed “light/dark” experiments [Cis15]. The sample was alternatively illuminated with light from a 20W (electrical power) CFL bulb and kept in the dark in 5 minute intervals. The product yield was measured at the start and after each interval. Unfortunately, it was not possible to observe an increase of the product yield in the dark period as expected, the product is only formed during the light periods. Similar results of “light/dark” experiments are also reported in the literature [Miy12, Wal12, Liu13, Sah13, Oh14].

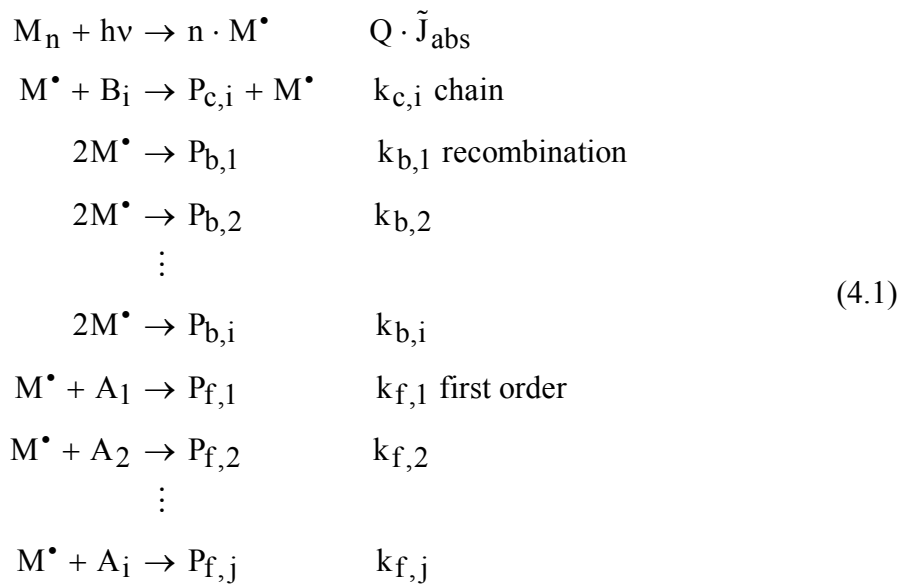
However, since the average lifetime of a radical-chain is generally in the sub- or millisecond range, current attempts to disprove the existence of the radical-chain reaction in a photoredox transformation by performing an intermittent illumination measurement on the time scale of minutes or even longer are futile. The appropriate experiment on the radical-chain reactions is the LED based intermittent illumination measurement, where microsecond to second light pulses can be used.

In this chapter, the intermittent illumination experiments on the photoredox catalytic α -alkylation will be presented. The first section gives a brief overview of the theory of the intermittent illumination method. In the second section the results of the intermittent illumination experiments are presented and discussed.

4.2. Theory of intermittent illumination method

It has been demonstrated that the intermittent illumination method is very useful in the study of photo-initiated radical chain reaction exhibiting bimolecular chain termination [Ing97, Pit15]. Furthermore, the theoretical description of the effect of intermittent light on a chain reaction has been developed with particular reference to photochemical decomposition reactions [Dic41, Ric42, She56, Bow79]. In this section the theoretical treatment of the intermittent illumination method will be briefly reviewed.

Consider a general photo-induced mechanism, which is shown as follows:



In this scheme the first step is known as initiation. Initiating free radicals may be generated by different methods. In photodecomposition the free radical M^\bullet which carries the chain is generated directly from the substrate M_n by exposure to light. In a photocatalytic initiation the substrate M_n doesn't absorb photons, whereas a photocatalyst does. This process produces a long-lived excited state of the photocatalyst that can react with M_n via single-electron transfer. The overall result is the production of free radicals M^\bullet . Regardless of how the free radicals are generated, the rate expression for the formation of M can be given by

$$\frac{d[M^\bullet]}{dt} = n \cdot Q \cdot \tilde{J}_{abs} \tag{4.2}$$

\tilde{J}_{abs} is the volumetric rate of light absorption. Q refers to the probability that absorption of a photon results in the production of radicals. n is a small number depending on the specific process. Then, the radical M^\bullet reacts with B_i to give the products $P_{c,i}$ and this reaction

regenerates M^\bullet . The reproduction of the radical M^\bullet is known as propagation and this reaction will proceed until the termination reactions destroy the chain. In this scheme two chain-breaking steps are considered. One is the recombination of the radicals and the other one is a first order radical reaction.

Suppose that the system studied is illuminated continuously and reaches the steady-state, the expression for the concentration of M^\bullet is expressed by

$$\begin{aligned}\frac{d[M^\bullet]}{dt} &= n \cdot Q \cdot \tilde{J}_{\text{abs}} - [M^\bullet] \sum_j (k_{f,j} \cdot A_j) - 2[M^\bullet]^2 \sum_i k_{b,i} \\ \frac{d[M^\bullet]}{dt} &= 2\Phi - [M^\bullet] K_f - 2[M^\bullet]^2 K_b \\ [M^\bullet]_c &= \sqrt{\frac{\Phi_c}{K_b} \cdot \frac{1}{(1 + \alpha)}}\end{aligned}\quad (4.3)$$

where the summations are over i or j and the subscript c indicates continuous illumination. The parameter α is defined as $K_f / (2K_b[M^\bullet]_c)$, which determines the relative importance of the two chain-breaking steps, i.e. first order reaction and radical recombination.

The rate of destruction of radicals is $2K_b[M^\bullet]_c^2 + K_f[M^\bullet]_c$, so that the average lifetime of M^\bullet (i.e. chain time) during the steady-state condition with continuous illumination is given by

$$\begin{aligned}\tau_0 &= \frac{\text{steady state radical concentration}}{\text{steady state rate of radical disappearance}} \\ &= \frac{[M^\bullet]_c}{2K_b [M^\bullet]_c^2 + K_f [M^\bullet]_c} \\ &= \frac{1}{2K_b [M^\bullet]_c + K_f}\end{aligned}\quad (4.4)$$

In the case of intermittent illumination, each period of light t_L is followed by an light-off period t_D . The dark to light ratio is defined as $p = t_D/t_L$. Apparently, the radical concentration falls during the periods of darkness, so that the average radical concentration is less than that which corresponds to continuous illumination with light of the same intensity. Letting $[M^\bullet]_L(t)$ refer to the change of $[M^\bullet]$ in the light period and $[M^\bullet]_D(t)$ indicate that in the dark period, an average quantity of $[M^\bullet]$ over the entire intermittent illumination is given by

$$\begin{aligned}\overline{[M^\bullet]} &= \frac{\overline{[M^\bullet]}_L + p \overline{[M^\bullet]}_D}{p + 1} \\ &= \left[\frac{1}{t_L} \int \overline{[M^\bullet]}_L(t) dt + \frac{1}{t_L} \int \overline{[M^\bullet]}_D(t) dt \right] \cdot \frac{1}{p + 1}\end{aligned}\quad (4.5)$$

It has been found that the average radical concentration $\overline{[M^\bullet]}$ is a function of t_L/τ_0 [Bow79, Lai87]. As long as the light intensity and total illumination time are kept constant, the average radical concentration $\overline{[M^\bullet]}$ for short and long light durations t_L will differ. The change in concentration occurs apparently when the dark period is approximately equal to the radical lifetime ($t_D \approx \tau_0$).

The theoretical calculation of the behavior of $\overline{[M^\bullet]}$ as a function of t_L/τ_0 has been worked out by Shepp [She56]. If light intensity fluctuations are neglected, Shepp's treatment leads to the result that the ratio $\overline{[M^\bullet]}/[M^\bullet]_c$ for long light period ($t_L \gg \tau_0$) is

$$\lim_{t_L \rightarrow \infty} \frac{\overline{[M^\bullet]}}{[M^\bullet]_c} \rightarrow \frac{1}{p + 1}\quad (4.6)$$

For short illumination period ($t_L \ll \tau_0$) the ratio $\overline{[M^\bullet]}/[M^\bullet]_c$ is

$$\lim_{t_L \rightarrow 0} \frac{\overline{[M^\bullet]}}{[M^\bullet]_c} \rightarrow -\frac{\alpha}{2} + \sqrt{\frac{\alpha^2}{4} + \frac{1 + \alpha}{p + 1}}\quad (4.7)$$

Eqs 4.6 and 4.7 also show that the dispersion of the ratio $\overline{[M^\bullet]}/[M^\bullet]_c$ is reduced with the increase of the parameter α . When the rate of radical recombination is much smaller than the first-order rate so that $\alpha \rightarrow \infty$, the ratio $\overline{[M^\bullet]}/[M^\bullet]_c$ becomes

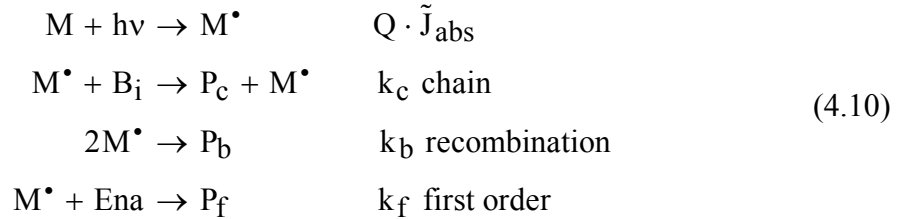
$$\lim_{t_L \rightarrow 0} \frac{\overline{[M^\bullet]}}{[M^\bullet]_c} = \lim_{t_L \rightarrow \infty} \frac{\overline{[M^\bullet]}}{[M^\bullet]_c} \rightarrow \frac{1}{p + 1}\quad (4.8)$$

In a typical experiment, a series of $\overline{[M^\bullet]}/[M^\bullet]_c$ values is measured through the determination of the rate of a first-order termination step for various values of t_L . The equation relating $\overline{[M^\bullet]}/[M^\bullet]_c$ to the experiment is

$$\frac{\overline{[M^\bullet]}}{[M^\bullet]_c} = \frac{\text{rate } \overline{P_{f,j}}}{(\text{rate } P_{f,j})_c} \cdot \frac{[A_j]_c}{[A_j]}\quad (4.9)$$

In eq 4.9 a first-order reaction j is chosen because its reactant A_j is almost constant throughout the experiment. Thus, the ratio $[A_j]_c / \overline{[A_j]}$ can be easily determined with its initial concentrations. Eventually, the behavior of $\overline{[M^\bullet]} / [M^\bullet]_c$ is plotted as the rate ratio of the average product rate $rate \overline{P_{f,j}}$ to the rate corresponding to the radical concentration with continuous illumination $(rate P_{f,j})_c$ against t_L or $\log(t_L)$. The t_L at which the change of $\overline{[M^\bullet]} / [M^\bullet]_c$ takes place is an indication of the radical lifetime.

In order to validate Shepp's theoretical treatment of intermittent illumination experiments, it is important to calculate the ratio $\overline{[M^\bullet]} / [M^\bullet]_c$ with another method. It has been previously shown in the Chapter 3 that the concentrations of reaction intermediates can be estimated by using chemical kinetic analysis. Therefore, the ratio $\overline{[M^\bullet]} / [M^\bullet]_c$ of a test chain reaction will be determined through the simulation of formation and decomposition of radicals M^\bullet . The test chain reaction is a simplified version of the photo-induced chain reaction described in eq 4.1, which is shown as follows:



In this scheme the free radicals M^\bullet are generated from photo-induced initiation reactions in which the substrate M doesn't absorb photons, whereas another molecule does. The quantum efficiency (Q) is included in the rate expression ($Q \times \tilde{J}_{abs}$) to take account of the fact that not all of the absorbed photon produces a radical. Then, the radical M^\bullet can be regenerated by the chain propagation process, which is described with the propagation rate constant k_c . Finally, the radical M^\bullet is terminated by a second order reaction and a first order reaction. Termination by the second order reaction results from the combination of two radicals. And, in the first order reaction, the radical M^\bullet reacts with Ena to give the product P_f . The Ena is assumed to stay constant throughout the reaction.

The conservation equations derived from the test mechanism 4.10 are

$$\frac{d[M^\bullet]}{dt} = Q \cdot \tilde{J}_{abs} - 2 \cdot k_b \cdot [M^\bullet]^2 - k_f \cdot [\text{Ena}] \cdot [M^\bullet] \quad (4.11a)$$

$$\frac{d[P_f]}{dt} = k_f \cdot [\text{Ena}] \cdot [M^\bullet] \quad (4.11b)$$

The light wavelength λ is set to be 441 nm and the light pulse power $P_{\text{abs}} = 5$ mW is selected. Thus, the rate of light absorption is calculated by (the solution volume $V_0 = 1$ mL)

$$\tilde{J}_{\text{abs}} = P_{\text{abs}} \cdot \frac{\lambda}{h \cdot c} \cdot \frac{1}{N_A} \cdot \frac{1}{V_0} \quad (4.12)$$

The quantum efficiency Q is set to be 0.1 because the initiation process is in fact often relatively inefficient [Cis15]. Moreover, the dark to light ratio is fixed with $p = 9$. In addition, the Ena concentration = 23.8 mM, the rate constants $k_b = 8.3 \times 10^9 \text{ M}^{-1}\text{s}^{-1}$ and $k_f = 8.2 \times 10^3 \text{ M}^{-1}\text{s}^{-1}$ are chosen via matching the resulted parameter α with a value of 1.9.

A software code for calculating the temporal evolution of the radical M^\bullet under continuous and intermittent illumination as well as the corresponding ratio $\overline{[M^\bullet]}/[M^\bullet]_c$ is given in appendix A3. The simulation values of ratio $\overline{[M^\bullet]}/[M^\bullet]_c$ against various pulse light periods t_L are plotted in Fig. 4.1.

The simulation results are in good agreement with the values estimated via Shepp's theory. The behavior of the ratio $\overline{[M^\bullet]}/[M^\bullet]_c$ as a function of light durations t_L is clear. The ratios for long and short light durations t_L are different. Furthermore, the maximum and minimum values of the ratio are fully consistent with the estimated values based on Shepp's analysis [She56]. In the limit of low frequency f_{LED} , it is to show that the ratio $\overline{[M^\bullet]}/[M^\bullet]_c \rightarrow (p+1)^{-1} = 0.1$ (eq 4.8). In the limit of high pulse repetition frequency f_{LED} , it is shown that the ratio $\overline{[M^\bullet]}/[M^\bullet]_c \rightarrow 1.42$ by using eq 4.7 with $\alpha = 1.9$.

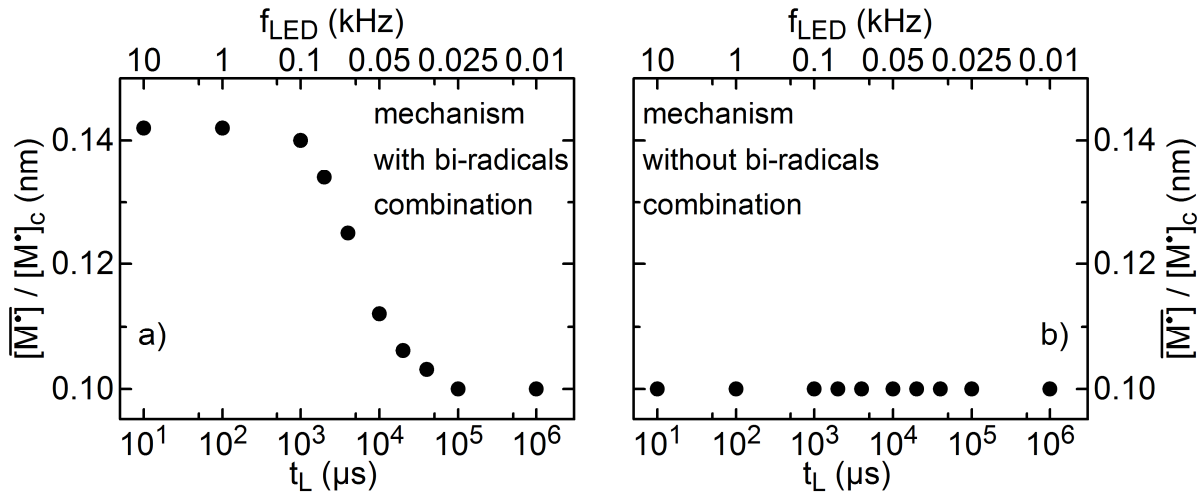


Fig. 4.1: Simulation results: the ratio of the average radical concentration $\overline{[M^\bullet]}$ under intermittent illumination to the stationary state radical concentration $[M^\bullet]_c$ under continuous illumination against t_L and f_{LED} . a) mechanism with bi-radicals combination (eq 4.10); b) mechanism without bi-radicals combination.

In addition, it has been mentioned by Shepp that at large α the dispersion of the plot of ratio $\overline{[M^\bullet]}/[M^\bullet]_c$ is reduced (eq 4.8). This argument can be tested by reducing the recombination rate constant k_b to a very tiny value, whose effect is similar to removing the radical recombination reaction from the mechanism shown in eq 4.10. The simulation results of the mechanism without the termination by combination are shown in Fig. 4.1b. In this case the ratios $\overline{[M^\bullet]}/[M^\bullet]_c$ remain constant with the light durations t_L and their values are equal to $(p+1)^{-1} = 0.1$.

4.3. Intermittent illumination experiment on α -alkylation

To further characterize the radical-chain reaction, the intermittent illumination experiment is performed by using our LED pulse generation setup. The experimental conditions are practically the same as that in our quantum yield determination experiments. The same blue LED (435nm, Roithner Lasertechnik) is employed and the average light power is set to be 500 μ W. The dark to light ratio is fixed with $p = 9:1$ and the pulse repetition frequency is varied, or, what amounts to the same thing, the duration of the light period t_L is changed. Four illumination experiments are conducted, each for a total of 21 hours (light + dark time). In each experiment, aliquots are taken from the chemical solution at 30 min intervals up to 2 hours and then at 1 hour intervals up to 6 hours. The final aliquot is taken after 21 hours intermittent illumination. For further details on the sample preparation and NMR data analysis, please refer to ref. [Rei17].

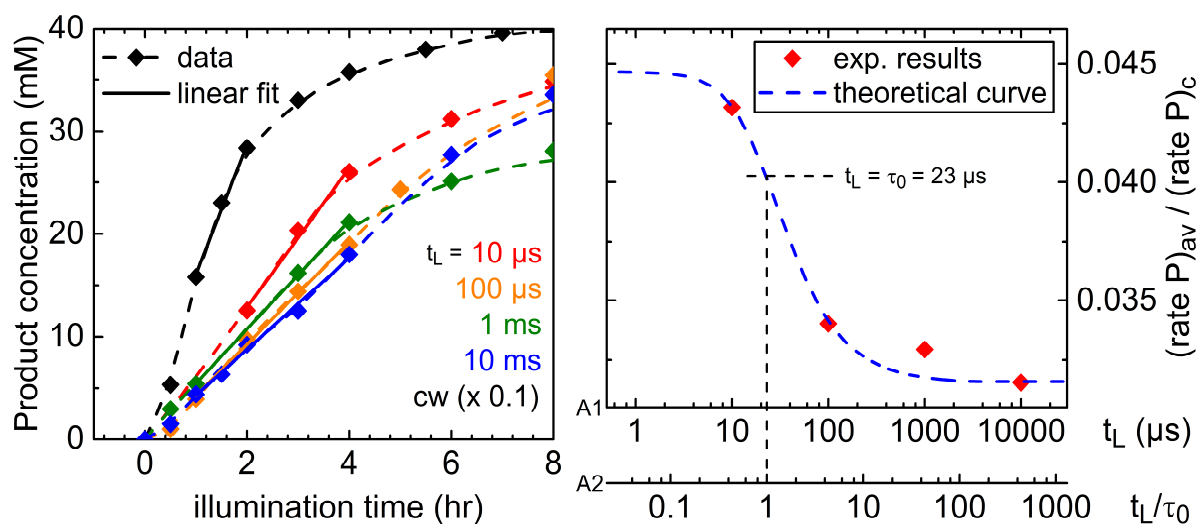


Fig. 4.2: a) Variation with time of the product concentration for the α -alkylation reaction measured with different light pulse durations, cw is continuous wave. b) the rate ratio of the average rate to the rate corresponding to the stationary state radical concentration against t_L (abscissa A1, log scale); and t_L/τ_0 (A2, log scale).

The α -alkylation chemical yields are shown in Fig. 4.2. Due to the large dark to light ratio ($p = 9$), the product yields under intermittent illumination are much smaller than that under continuous illumination (the black curve in Fig. 4.2a). In order to display them in one figure, the product yield under continuous illumination is scaled by a factor of 0.1. The rate of product formation is determined through fitting a linear function to the yield data in the range where the product grows linearly with time.

The rate ratio of the average product rate under intermittent illumination $(rate P)_{av}$ to the product rate under continuous illumination $(rate P)_c$ is plotted as a function of the t_L in Fig. 4.2b). It can be seen from the figure, when the periods of light and dark are long enough (10 ms in this case), the ratio approaches a constant. Moreover, the ratio seems to reveal a rising trend as the light period t_L decreases, which reaffirms that indeed the photoredox catalytic α -alkylation involves a chain propagation mechanism. Based on the theory described in the previous section, the maximum of $(rate P)_{av}/(rate P)_c$ can be estimated by using the first-order radical reaction rate, the radical recombination rate and the dark to light ratio p . However, since the radical recombination side-products have not been observed in the experiments, the recombination rate cannot be measured, leaving the maximum undetermined. This is probably attributed to the much smaller radical recombination rate compared to that of the first-order radical reaction [Ing97]. It also accounts for a large parameter α and an associated small dispersion of the ratio.

Quantitatively, the shape of the $(rate P)_{av}/(rate P)_c$ curve can be calculated theoretically as a function of $(1+\alpha)^{-1}(t_L/\tau_0)$, based on Shepp's analysis [She56]. A software code for estimating the lifetime τ_0 and the value of α is given in appendix A3. The result is shown in Fig. 4.2b. The value of $\alpha = 1.92$ is estimated. The value of τ_0 can be approximated by overlaying the experimental and theoretical curves and determining the displacement of the coordinate that would be required to make both curves coincide [Bow79]. In this experiment the average lifetime corresponds to 23 μ s.

Using our LED-based intermittent illumination setup, the evidence is observed for the occurrence of chain processes in the α -alkylation reaction. In addition, the observed small dispersion of the ratio confirms the observed extremely small radical recombination rate. For more mechanistic details, transient absorption spectroscopic studies of the photoredox catalytic α -alkylation are considered in the next chapter.

5. Ultrafast transient absorption spectroscopy of naphthalene diimide in the photoredox catalytic aldehyde alkylation

From the quantum yield studies in the previous chapters, a reaction mechanism incorporating a competition between the radical-chain process and the photoredox catalysis is highlighted and demonstrated for the photoredox catalytic α -alkylation of aldehyde reaction. However, the quantum yield analysis is a typical “black box approach”, i.e. only the behavior of excitation light intensity (input) and product amount (output) is accounted for. The internal steps of the mechanism are usually inferred, rather than by direct observations of them.

There is no doubt that detailed knowledge of the mechanistical intricacies would benefit the improvement of existing reaction efficiency and the design of new transformations. Therefore, it has been long suggested that the step-by-step mechanism of photoredox catalysis can be anticipated by using transient absorption (TA) spectroscopy [Kär15, Kön17]. Nevertheless, a mechanistic explanation with spectroscopic evidence for photoredox catalytic α -alkylation of aldehydes is still lacking. It is widely believed that the dual catalytic systems are too complex to be studied with the TA spectroscopy [Maj14]. This debate stems from the fact that the interpretation of the TA spectroscopy of transition metal catalysts without reactants is rather ambiguous, not to mention the great complexity added on by numerous reactants [McC03, Wan04, Sta15, Wac15].

This drawback of the transition metal catalysts can be addressed through the use of organic dyes as alternative photoredox catalysts. In contrast to the transition metal catalysts, the organic dyes generally feature spectroscopically observable and distinct intermediates [Rom16]. This enables conveying a clear mechanistic picture of the photoredox catalysis that should convince the community.

In this chapter, a detailed investigation of the photoredox catalytic α -alkylation of octanal with the organic photoredox catalyst NDI-A will be presented. It will start with the photophysical and photochemical properties of NDI-A, which is essential to understand the photochemical processes during the photoredox catalytic cycle. In the second part, the chemical steps in the α -alkylation reaction will be studied by using the TA spectroscopy.

5.1. Photocatalyst – Naphthalene diimide

5.1.1. Structure

Naphthalene diimide, abbreviated as NDI, is the smallest homologue of the rylene diimides. Its structure consists of a rigid polycyclic aromatic scaffold (naphthalene core), with two dicarboxylic acid imide groups substitute at the 1,4- and 5,8-*peri*-positions (see Fig. 5.1).

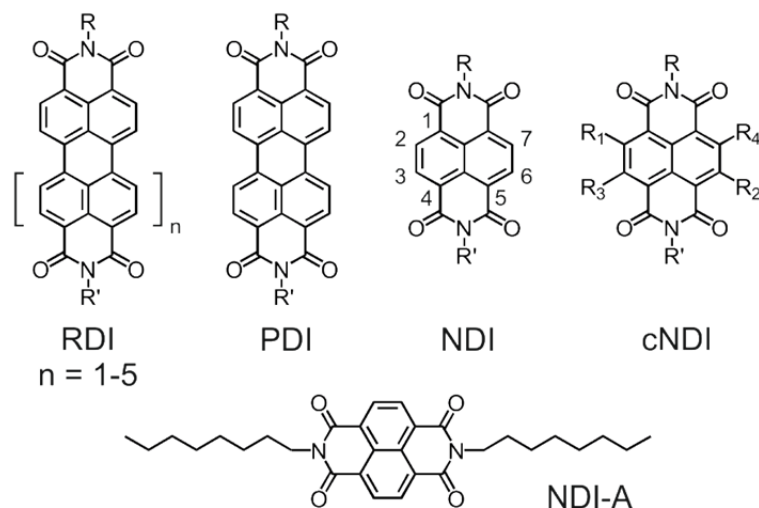


Fig. 5.1: Molecular structure of aromatic diimides. RDI, rylene diimide; PDI, perylene diimide; NDI, naphthalene diimide; cNDI, core-substituted naphthalene diimide; R and R' = H, alkyl or aryl; NDI-A, core-unsubstituted naphthalene diimide under study.

Through introducing substituents selectively at the imide nitrogen positions (N-position) or the 2, 3, 6, 7 positions of the hydrocarbon core (core-position), NDIs with different chemical and physical properties can be readily obtained [Sak10]. It has been long known from PDI studies that the introduction of alkyl substituents at the N-positions has very little effect on the photophysical and electrochemical properties, unless there is a branching at the 1-position to the imide nitrogen [Dem88]. Therefore, the N-position substitution tends to be used to improve the solubility of NDIs [Ert05].

Additionally, the functionalization through core-substitution leads to enormous options for modifying electronic and optical properties of NDI. This ability of NDI was first discovered by Würthner's group in 2002 [Wür02]. Since then, there has been growing interest among researchers in the functionalization of NDI with different substituents, in order to achieve a molecule with desirable electronic and spectroscopic properties. Nowadays, cNDI have been developed into one of the most explored subclasses of the rylene family. Our own group has

investigated the influence of core substituents on the electronic relaxation of NDI via charge transfer processes [Pug10, Pug11]. The properties of cNDI have also been excellently reviewed in ref. [Sak10].

The monomeric NDI in solution can form aggregates upon self-assembly [Mil96, Bar97, AlK16]. The structure of the aggregate shows a slipped face-to-face geometry, according to the X-ray crystal measurement [Cub01, And04]. Their ability to form face-to-face stacking is determined by interacting π -systems of adjacent (planar) aromatic core. This energetically favorable interaction is called π -stacking and is based on several noncovalent forces. Moreover, as Cubberley and Iverson [Cub01] have reported, the hydrophobic interaction plays a dominant role in the NDI π -stacking. They observed that the self-association constants of the NDI increase with increasing solvent polarity ($K_a = 1 \text{ M}^{-1}$ for CDCl_3 and $K_a = 245 \pm 101 \text{ M}^{-1}$ for D_2O). Since the flat surfaces of aromatic molecules are usually considered hydrophobic, the molecules tend to be aromatic stacked in order to minimize the hydrophobic surface area exposed to polar solvents. Therefore, the trend observed in the self-association constants indicates that the hydrophobic effect provides the primary driving force for the NDI π -stacking.

Moreover, cNDI can also produce self-assembled aggregates in solution. This feature is usually used for the creation of supramolecular functional materials. Since the main emphasis of this thesis is on the molecular dynamics in photoredox catalytic reactions, detailed review of the cNDI supramolecular assemblies falls outside the scope of this thesis. Interested readers should refer to the review of Al-Kobaisi et al. [AlK16].

5.1.2. Photophysics and photochemistry

Steady-state characterization

N,N-dioctyl-1,4,5,8-naphthalene diimide, abbreviated as NDI-A (see Fig. 5.1), is used as the photoredox catalyst in the investigation. The steady-state absorption recorded for the NDI-A in different solvents are shown in Fig. 5.2. In all solvents studied (toluene, dichloromethane, acetone, *N,N*-dimethylformamide and methanol), the NDI-A exhibits similar absorption spectra consisting of strong absorbance bands in the UV range. A narrow band at 235 nm is observed in the case of the NDI-A in CH_2Cl_2 and MeOH. This band is not displayed in the measurements of the NDI-A in toluene and DMF, due to the UV cut off of the solvents (284 nm for toluene and 268 nm for DMF). A broad absorbance band composed of a vibronic progression is visible in the UV-A range (315-400 nm). Two distinct maxima of

them vary in the range 358-362 nm and 378-382 nm, and the small shifts do not seem to show any correlation with the polarity of the solvent used (see Table 5.1). The small solvent sensitivity indicates that the NDI-A is a rigid molecule, which doesn't undergo conformational changes when the polarity of the surrounding is altered.

The calculation studies in the literature show that the UV-A absorption band of NDI-A presents the S_0 - S_1 vibronic progression and consists dominantly of two overlapping transitions, each of $\pi\pi^*$ character [Ada95]. Additional $n\pi^*$ transitions caused by lone pairs of the heteroatoms are weak and hardly observable because they may be masked by the $\pi\pi^*$ absorption in the UV-A range [Ave97].

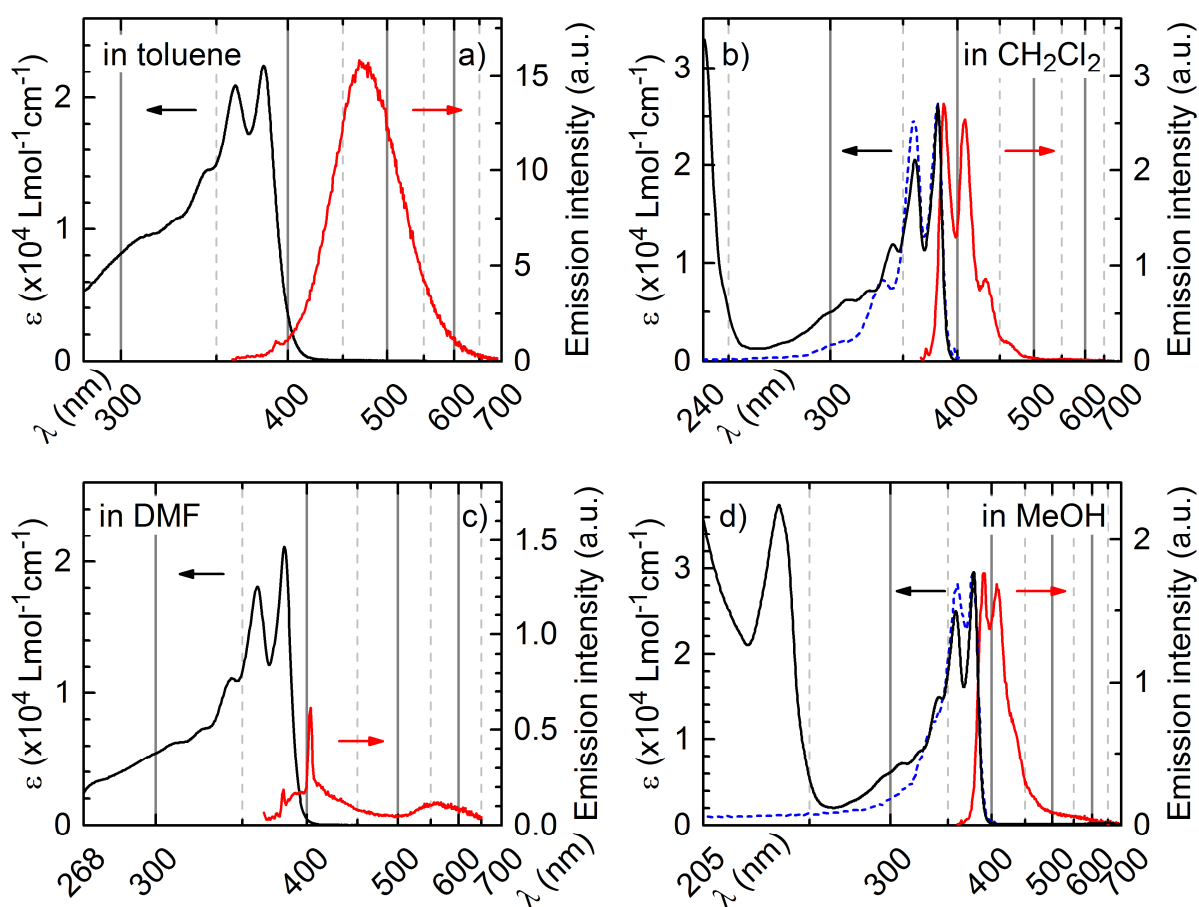


Fig. 5.2: Steady-state absorption and emission spectra of NDI-A in solvents of different polarity at room temperature (the blue dashed curves in b and d show the reflection of the corresponding fluorescence spectrum about the intersection of the absorption and fluorescence spectra). a) 20 μ M in toluene, $\lambda_{\text{exc}} = 350$ nm; b) 20 μ M in dichloromethane (CH_2Cl_2), $\lambda_{\text{exc}} = 360$ nm; c) 20 μ M in *N,N*-Dimethylformamid (DMF), $\lambda_{\text{exc}} = 360$ nm; d) 20 μ M in methanol (MeOH), $\lambda_{\text{exc}} = 350$ nm.

Fig. 5.2 also shows the steady-state emission spectra of NDI-A in the different solvents. The emission spectra recorded in CH_2Cl_2 and MeOH form a mirror image of the corresponding absorption band, with a small Stokes shift (409 cm^{-1} for CH_2Cl_2 and 880 cm^{-1} for MeOH). The deviations from the mirror symmetry on the high-energy side of the absorption spectrum result from superimposed transitions to higher lying electronic states. The form of the fluorescence spectrum is irrespective of the excitation wavelength used (342-380 nm), which indicates that only one fluorescing species exists (Fig. A4.1 in Appendix A4). The transition energies of the lowest singlet state (E_{00}^S) estimated from the intersection of the absorption and fluorescence spectra are 3.25 eV for CH_2Cl_2 and 3.23 eV for MeOH. The slight changes of the emission behavior are observed in the large difference in the polarity of these two solvents. These results provide further evidence for the rigid structure of the NDI-A molecule.

In the case of the NDI-A in toluene, the structured fluorescence band observed in CH_2Cl_2 is replaced by a broad, unstructured, intense emission band, displaying a maximum at approximately 470 nm. The same phenomenon has been observed by Barros et al. [Bar97]. They attribute this emission behavior to direct excitation of a ground state complex, which is composed of a NDI and an aromatic solvent molecule. This excited complex with substantial charge transfer character is referred to as exciplex [Lak06]. The similar emission behavior is also observed by Barros et al. in the measurements of the NDI in other aromatic solvents, such as benzene and p-xylene [Bar97].

The spectral behavior of the NDI-A in DMF is quite distinct to that in other solvents, with a very weak emission. The broad band around 400 nm could be the direct emission from the lowest singlet excited state. The sharp peaks in the spectrum around 400 nm are assigned to the Raman scattering of DMF. In addition, a broad band is observed which has a maximum around 550 nm. This band becomes more obvious when the shorter excitation wavelength of 342 nm is used (Fig A4.2 in Appendix A4). A similar emission spectrum of a NDI analogue has been observed by Ganesan et al. [Gan07]. In their case a charge-transfer emission band centered at approximately 550 nm is observed, which is caused by electron-transfer (ET) between the NDI core and a phenyl ring substituted on the N-position. Likewise, the broad emission band observed in the case of DMF is attributed to an intermolecular charge-transfer transition due to an excited NDI-A dimer, or excimer. This is supported by the fs-ps TA measurements, which will be discussed in more detail later.

Table 5.1: Absorption and emission data for NDI-A in solvents of different polarity.

Solvent	ϵ_r	λ_{abs} (nm)	ϵ ($10^4 \text{ M}^{-1} \text{ cm}^{-1}$)	λ_{emi} (nm)	Stokes shift (cm^{-1})	E_{00}^S (eV)
Toluene	2.4 (25°C)	381.6	2.2	~ 470	-	-
CH ₂ Cl ₂	9.1 (20°C)	380.0	2.6	386	409	3.25
Acetone	20.7 (25°C)	377.4	3.4	387	657	3.25
MeOH	32.6 (25°C)	378.0	3.0	391	880	3.23
DMF	36.7 (20°C)	380.5	2.1	-	-	-

The self-aggregation of the NDI-A in solution is also studied by absorption and emission spectroscopy. The effect of increasing the NDI-A concentration in CH₂Cl₂ is shown in Fig. 5.3. The shape of the NDI-A absorption spectrum and the position of the band maximum do not change in the concentration range 20 μM – 6.7 mM. At a concentration of 13.0 mM, the intensity of the bands at 340 and 360 nm increases slightly. In contrast to the absorption, in the emission experiments a new unstructured band with a maximum at about 500 nm is observed at a concentration of 6.7 mM. This band becomes more intense with increasing concentration of the NDI-A.

The observation in the emission measurements suggests the formation of NDI-A excimers. Due to the short lifetime of the NDI-A singlet state (14 ps in CH₂Cl₂, see TA measurements below) the formation of the excimer cannot be a diffusional process. Thus, it has been concluded by Barros et al. that the excimer must be formed by excitation of a self-

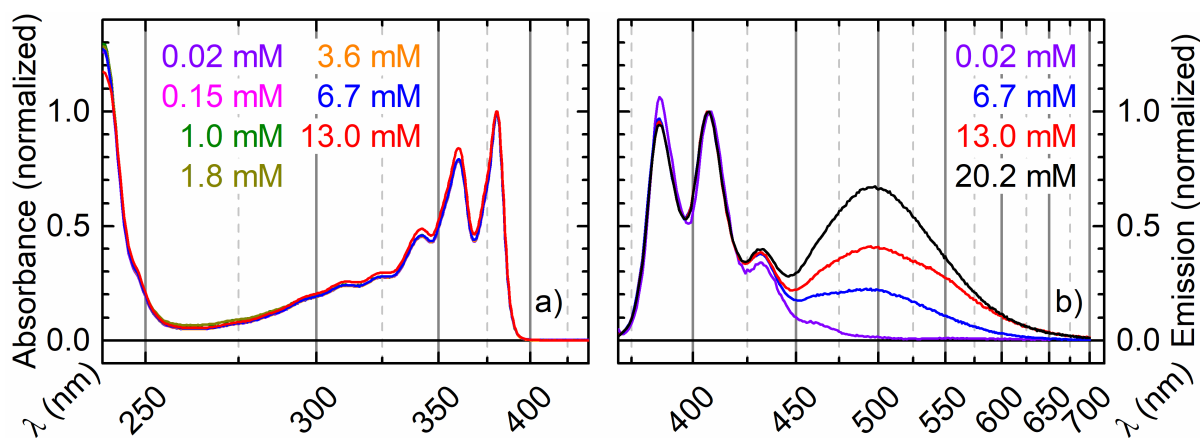


Fig. 5.3: Normalized absorption and emission spectra of the NDI-A in CH₂Cl₂ as a function of the NDI-A concentration. For emission experiment the excitation wavelength is $\lambda_{\text{exc}} = 360 \text{ nm}$.

aggregated dimer in its ground state [Bar97]. Additionally, a characteristic aggregation-induced shift [Kas65] is observed in the absorption spectra at the concentration of 13.0 mM. The change of the absorption spectrum is consistent with the observation in a study of a discrete covalently linked NDI dimer [Wu14], in which the absorption spectrum of the NDI dimer shows a blue-shift of the absorption maximum from 380 nm for the monomeric NDI to 360 nm. It also indicates that the NDI-A in the dimer are arranged in an “side-by-side” H-aggregate (H denotes hypsochromic) fashion [Wu14, Hes18].

The lack of any exciton splitting in the absorption spectra at concentrations below 13.0 mM suggests that the self-association constant K_a of NDI-A in CH_2Cl_2 is minuscule. This confirms previous findings in the ref. [Cub01]. According to their studies, the K_a of NDI-A in CH_2Cl_2 is estimated as 1 M^{-1} . Thus, a tiny concentration of NDI-A dimer of 45 μM is obtained in the 6.7 mM monomeric NDI-A solution. This concentration is over 2 orders of magnitude smaller than that of the monomeric NDI-A.

Excited-state kinetics

Another important feature of the NDI-A is the fluorescence quantum yield. The definition of the fluorescence quantum yield is the ratio between the number of photons emitted and the number of photons absorbed (eq 5.1).

$$\Phi_{\text{fluo}} = \frac{N_{\text{emitted}}}{N_{\text{absorbed}}} \quad (5.1)$$

Excitation of the NDI-A in CH_2Cl_2 at 380 nm results in a very low fluorescence quantum yield ($\Phi_{\text{fluo}} = 0.0016$), which is in strong contrast to its brother compound PDI ($\Phi_{\text{fluo}} \approx 1$) [Wür16]. The low fluorescence quantum yields are also observed for the analogous NDIs in other common solvents ($\Phi_{\text{fluo}} < 0.03$ in [Bar97], $\Phi_{\text{fluo}} \sim 10^{-3}$ in [Yus15]). According to the Strickler-Berg equation [Str62], the radiative lifetime τ_0 of NDI-A in CH_2Cl_2 is estimated from its oscillator strength, yielding a lifetime of 3.5 ns. Then, the fluorescence lifetime τ_{fluo} is calculated from Φ_{fluo} and τ_0 by means of [Lak06]

$$\tau_{\text{fluo}} = \Phi_{\text{fluo}} \cdot \tau_0 \quad (5.2)$$

This simple estimation gives an ultrashort fluorescence lifetime of approximately 5.6 ps, indicating the presence of ultrafast non-radiative deactivation pathways. Further evidence for the ultrafast excited singlet state decay has been provided by the fluorescence decay measurements [Gan07, Yus15]. At room temperature the fluorescence decays of a NDI analogue in CH_2Cl_2 are bi-exponential with 1 and 10 ps for the wavelength monitored

between 420 and 450 nm [Yus15], which supports the estimated fluorescence lifetime.

More details of the excited singlet state dynamics of NDI-A are revealed by fs-ps TA measurements. The first fs-ps TA measurement of a NDI analogue was performed by Ganesan et al. in 2007 [Gan07]. They reported an ultrafast excited singlet state to triplet state intersystem crossing (ISC) process with a time constant of 10 ps. After this publication, a more complex ISC process of the same NDI from the excited singlet state to the triplet manifold was reported by Yushchenko et al. [Yus15]. They confirmed the ultrashort excited singlet state lifetime and found that the ISC process was reversible between the excited singlet state and the triplet state on a few picoseconds timescale. These complex ISC dynamics are also observed in the fs-ps TA measurements of the NDI-A in CH₂Cl₂. Such dynamics are shown in an energy level diagram given in Scheme 5.10.

In the following the results of TA experiments of the NDI-A in CH₂Cl₂, DMF and a CH₂Cl₂/DMF mixture will be discussed in more detail. The NDI-A is excited at 360 or 365 nm for fs-ps measurements and at 380 nm for ns- μ s measurements. The excited state dynamics are observed in the UV and visible region (290-710 nm). The experiments are done under aerated conditions unless otherwise noted. In all TA-spectra, the observed negative bands at 360 nm and 380 nm are due to ground state bleach (GSB) since the absorption bands of NDI-A are located at these positions. In the visible region the TA spectra are dominated by positive bands due to excited state absorption (ESA) or reaction product absorption.

In CH₂Cl₂ there is a negative band with maximum at 409 nm within the first 10 ps after excitation, which is due to stimulated emission (SE). On the same timescale a positive band at 598 nm with a shoulder around 560 nm and a weaker band at 460 nm are clearly visible. The band at 598 nm can be assigned to the absorbance of the lowest excited singlet state (S₁) and the band at 460 nm is supposed to represent the triplet state (T₄) with n π * character. The nature of the T₄ state is confirmed by quantum chemistry calculations in ref. [Yus15]. The ESA of S₁ state loses a part of its intensity within the first picosecond, whereas the ESA of the T₄ state rises. Afterwards, they all decay and give rise to a spectrum with absorption maxima at 452 and 484 nm. This long-lived species hardly decays on the timescale of the fs-ps TA experiment (up to 1.5 ns) and decreases entirely to zero in the ns- μ s TA experiment. This species is identified as the lowest excited triplet state (T₁) of NDI-A, because similar T₁ state spectra have been reported [Gre95, Ave97, Gan07, Yus15]. Moreover, in N₂ purged CH₂Cl₂, the TA spectrum in the ns- μ s TA experiment is identical to that of NDI-A in air-

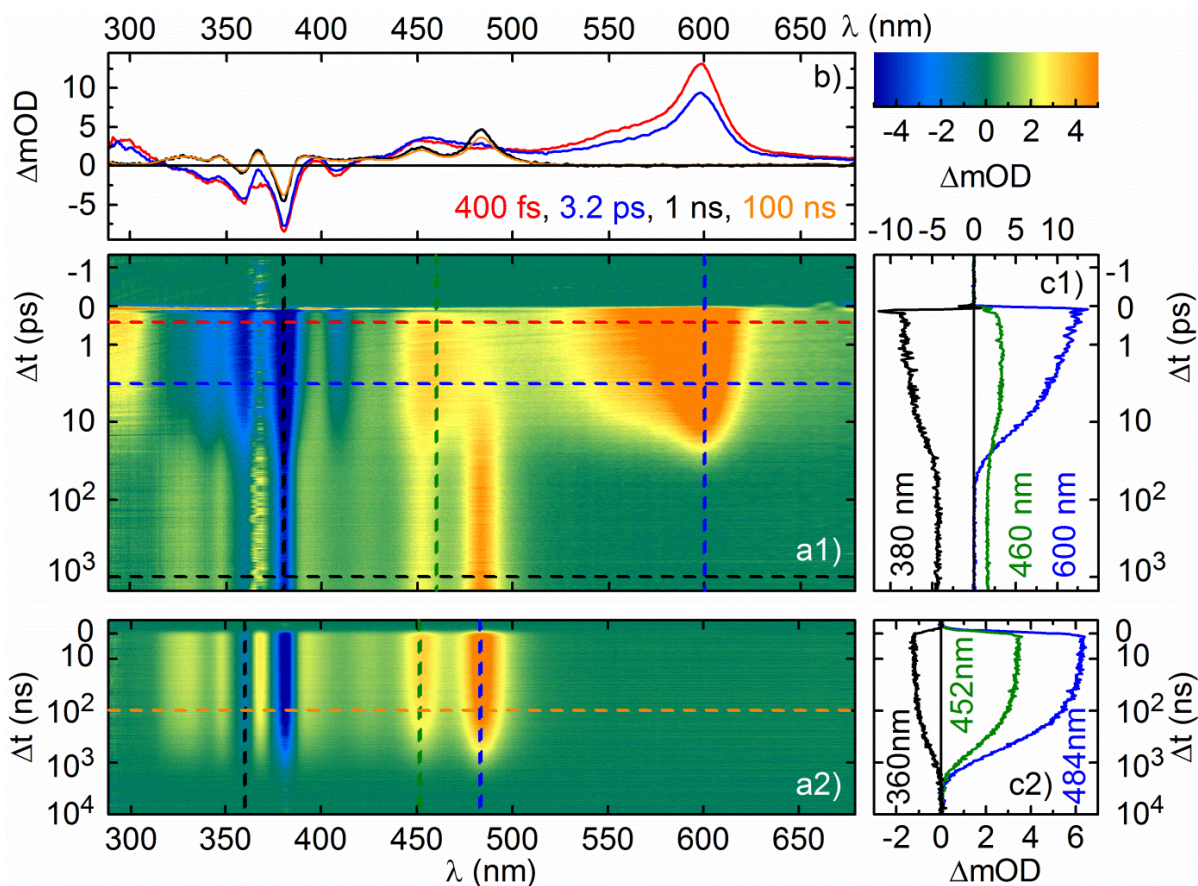


Fig. 5.4: Time-resolved absorption spectra of NDI-A in CH_2Cl_2 at 22 °C. a1) fs-TA: 1 mM NDI-A in 0.1 mm cuvette after 365 nm excitation with pump intensity of 1 mJ/cm^2 ; a2) ns-TA: 1.2 mM NDI-A in 0.1 mm cuvette after 380 nm excitation with pump intensity of 0.6 mJ/cm^2 ; b) Transient absorption spectra recorded at several time delays after excitation; c1, c2) Kinetics for the dynamics of different species at selected wavelengths.

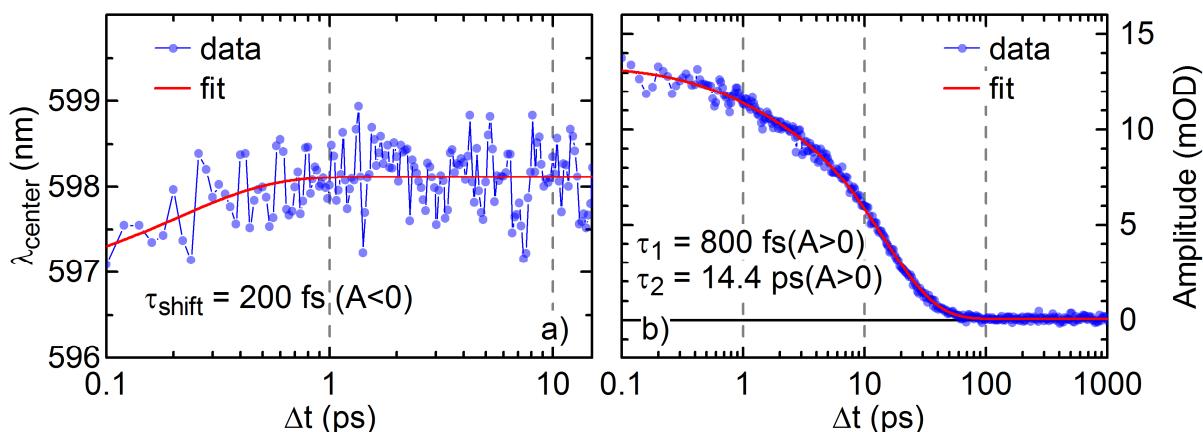


Fig. 5.5: a) Temporal evolution of the S_1 state peak position from the data in Fig. 5.4a and an exponential fit result. b) Kinetics of the peak amplitude after removing the influence of the peak shift and a bi-exponential fit result.

saturated CH_2Cl_2 but the lifetime of the corresponding species in the ns- μs regime is considerably longer. This observation comforts the assignment of the long-lived species to the T_1 state of NDI-A.

In addition, the peak positions of S_1 state are found to shift from 597 to 598 nm within the first picosecond (see Fig. 5.5a). This shift is generally due to differential solvation of the ground and excited state of the chromophore. To determine the temporal evolution of the peak shift, the TA data are parametrized using a Gaussian function. The resulting peak shift is depicted in Fig. 5.5a. The time constant for the peak shift is determined via an exponential fit to the data, which yields a time constant $\tau_{\text{shift}} = \sim 200$ fs. Therefore, the observed red-shift can be assigned to the “initial” solvent relaxation with the similar time constant of 250 fs reported in ref. [Hor95]. After removing the influence of the peak shift, the decay kinetics of S_1 state are measured by the peak amplitude and the result is shown in Fig. 5.5b. The decay of the revised data can be fitted with a bi-exponential function, yielding two time constants of 800 fs and 14.4 ps. This suggests that the dynamics associated with the S_1 state of NDI-A with the time constant of 800 fs is not caused by the solvent relaxation.

In order to retrieve more information from the time-resolved data, the TA data are analyzed using different methods, which have been described in section 2.2. The fs-ps TA data are first analyzed using the maximum entropy method [Kut13]. The resulting matrix of the distribution $p(k, \lambda)$ is shown in Fig. 5.6. The color map reveals three regions along the lifetime axis where TA spectral changes occur. They are indicated by the dashed lines in the color map in Fig. 5.6. Since the peak widths along the lifetime axis measure the uncertainty of lifetimes, the lifetimes are determined by the “peak position” of the distribution: the first lifetime is near 800 fs, the second region shows a lifetime of 14.4 ps and the third lifetime is in the range $\gg 1.5$ ns, which can be measured by the ns- μs TA. Three lifetime density distributions selected at 380, 460 and 600 nm are presented in Fig. 5.6b. At 600 nm (blue in Fig. 5.6b), the decay of S_1 state dominates with two peaks, indicating a bi-exponential decay process. The red (460 nm) and black curve (380 nm) show the same lifetime density distribution around 800 fs and 14.4 ps.

The results of the maximum entropy analysis are confirmed using a single line fit method to the same data. The kinetic traces and fit results at selected wavelengths are shown in Fig. 5.7. Except the GSB region (data at 380 nm as an example), approximately the same three time constants are required for an adequate description of the measured kinetics at all wavelengths (the third time constant is $\gg 1.5$ ns and is not shown in Fig. 5.7).

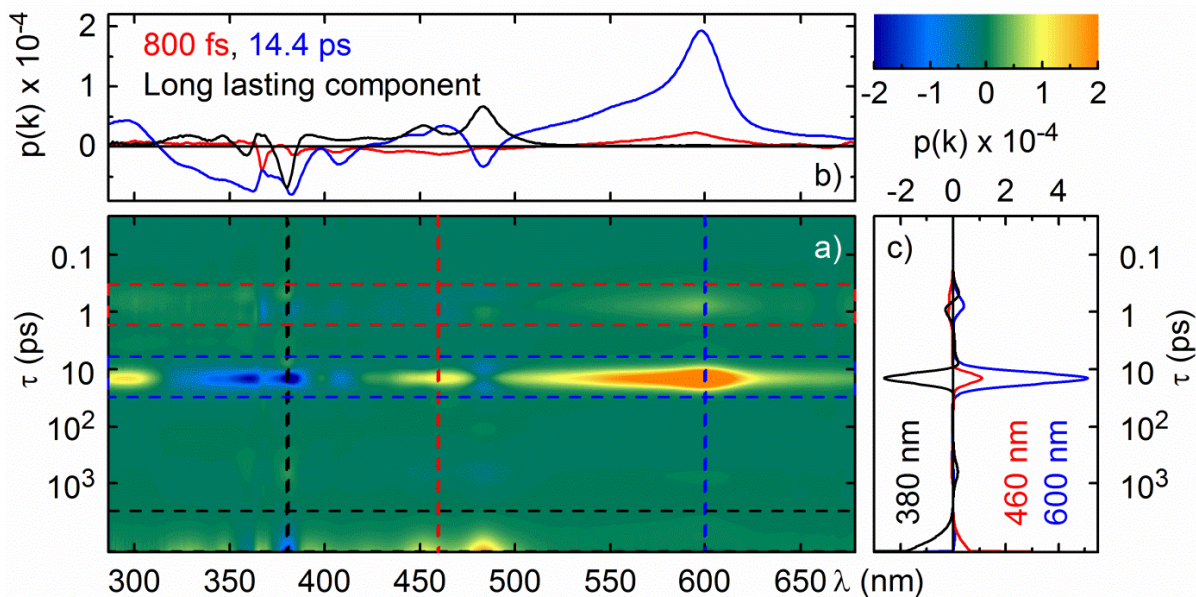


Fig. 5.6: Distribution of rate constants $p(k, \lambda)$ obtained by maximum entropy inverse Laplace transformation [Kut13] for the data matrix in Fig. 5.4a. a) The spectra obtained by integration of $p(k, \lambda)$ over the rate constant intervals indicated. b) The lifetime density distribution at selected wavelengths.

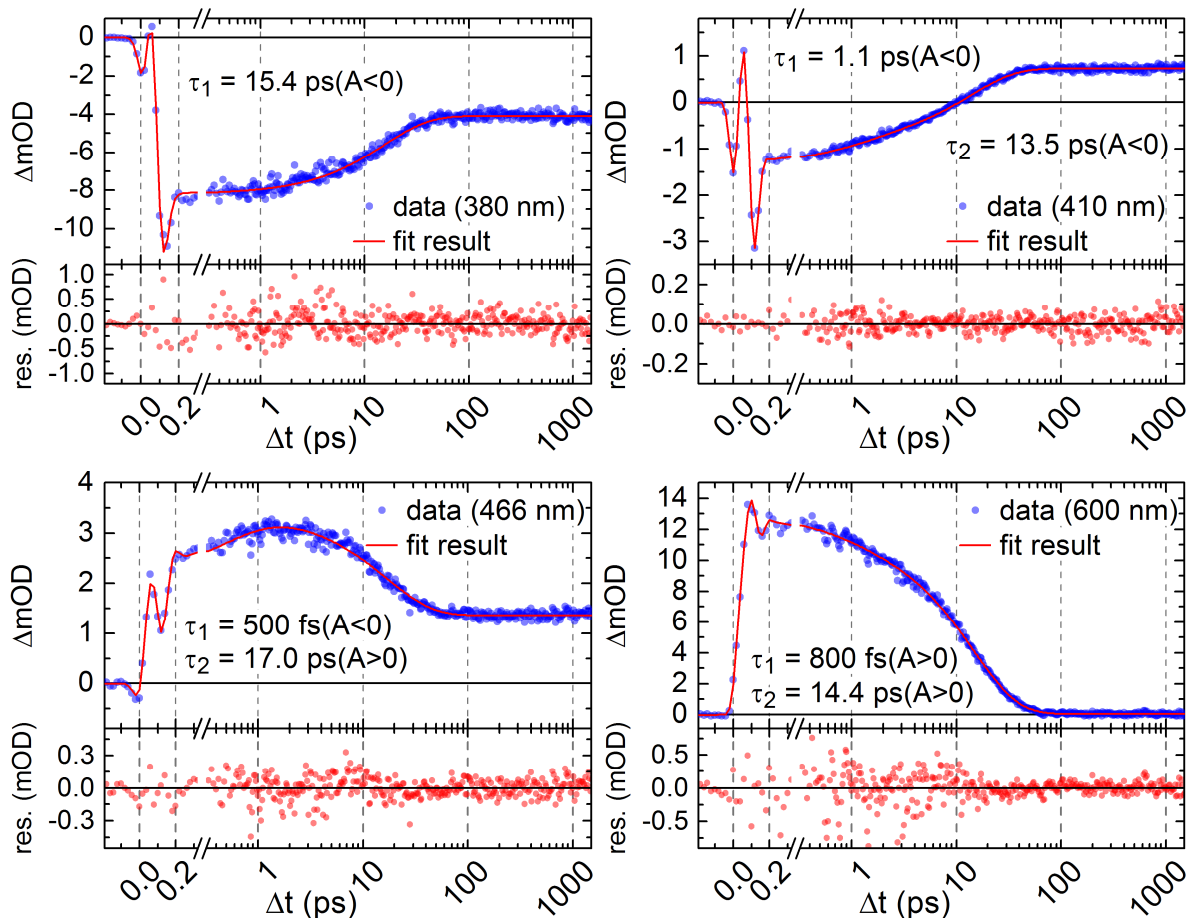


Fig. 5.7: Kinetic traces monitored at selected wavelengths from the data matrix in Fig. 5.4a and the corresponding fit results with a multi-exponential decay model.

The kinetics obtained at 600 nm presents primarily the ESA of the S_1 state and exhibits a decay with the time constants of 800 fs and 14.4 ps. Probing at 466 nm (primarily the ESA of T_4 state) shows a rise with a time constant of 500 fs and a decay with 17.0 ps. The rise of the band at 466 nm and the decay of the band at 600 nm have approximately the same time constant. This result reveals the S_1 to T_4 state transition. The kinetics at 410 nm presents primarily SE and is fitted to a bi-exponential model with the time constants of 1.1 and 13.5 ps, which is in good agreement with the reported time-resolved fluorescence result in ref. [Yus15]. In contrast to the ESA and SE, the dynamics of the GSB monitored at 380 nm is well described with two time constants of 15.4 ps and $\gg 1.5$ ns. The first step with a time constant almost identical to the fluorescence lifetime is assigned to a partial $S_1 \rightarrow S_0$ transition. The reason for the absence of the time constant of near 1 ps is likely due to the tiny fluorescence quantum yield of NDI-A. This leads to a very small ground state recovery within this delay time, which is hardly resolved using the TA setup employed.

Given that, from all above mentioned analysis, two time constants and one long lasting component are needed to fit the fs-ps TA data, these data are globally fitted with two exponentials and a constant offset representing long lasting TA signals from the T_1 state. This global analysis can accurately reproduce the TA data with the time constants and decay associated difference spectra (DADS) in Fig. 5.8. The fast one with a time constant of 800 fs describes the decay of S_1 state due to the positive contribution in the DADS around 600 nm. The negative contribution around 460 nm reflects that the T_4 state grows with the S_1 decay at the same time. In the second step with a time constant of 14.4 ps, the negative peak at 484 nm associated with the S_1 decay with a positive peak at 598 nm and the T_4 decay with a positive peak at 462 nm perfectly matches the known T_1 signature. It reflects that the long-lived T_1 state is populated with the time of 14.4 ps. After these initial transients a long-lasting absorption change persists in the fs-ps TA, which is caused by the T_1 state. The DADS of T_1 state obtained in the fs-ps TA are the same as the one with a time constant of 641 ns gained from the ns- μ s TA. The last DADS (green dash line) from the ns- μ s TA show that the GSB is recovering completely and no characteristic positive bands are observable. It indicates that all excited NDI-A decays back to their ground state and no photoproducts are generated.

Assuming a reversible kinetic model, which is shown in Scheme 5.10, species associated difference spectra (SADS) will be constructed using the DADS from the global analysis. As mentioned in section 2.2, a unique solution of the SADS and rate constants can be obtained,

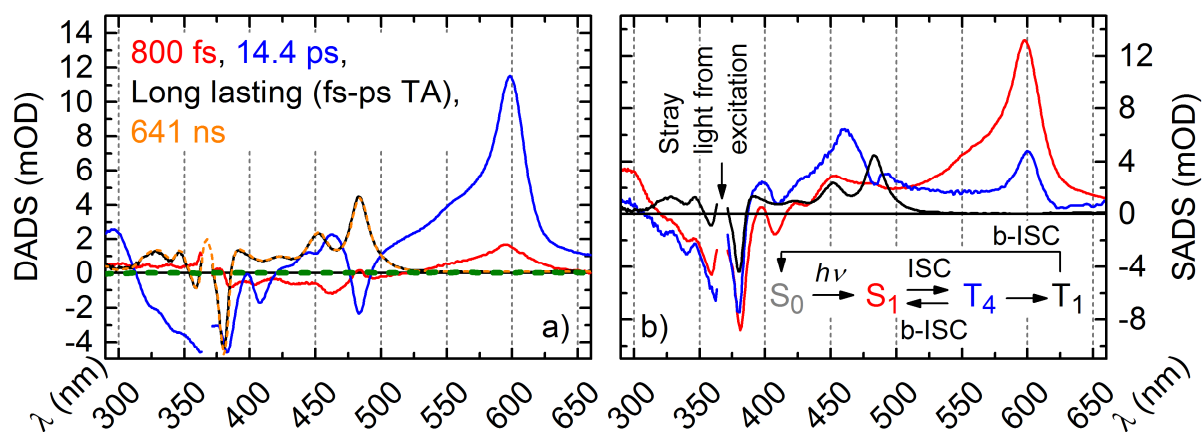


Fig. 5.8: a) Decay associated difference spectra (DADS) of a global fit to the data in Fig. 5.4a. b) Species associated difference spectra (SADS) obtained from the analysis assuming the scheme in the inset (same with the one in Scheme 5.10).

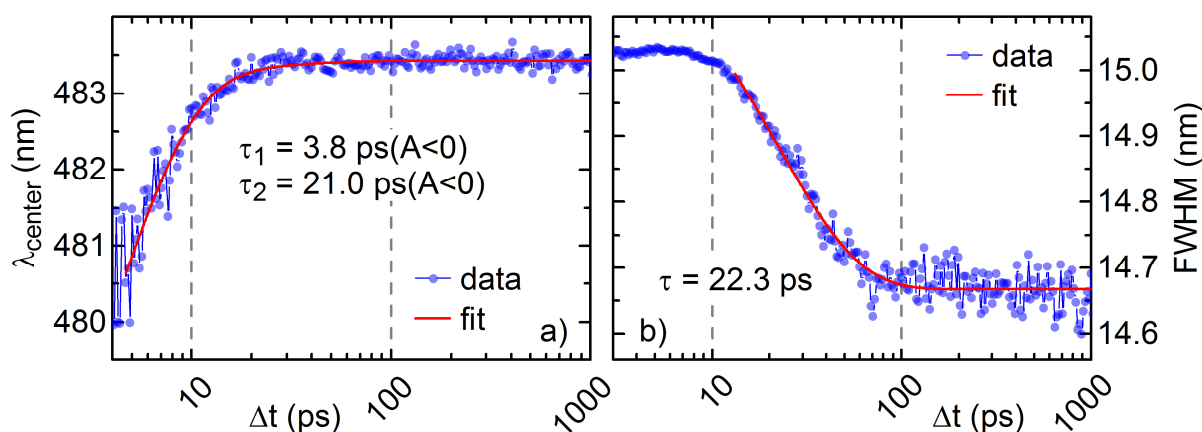
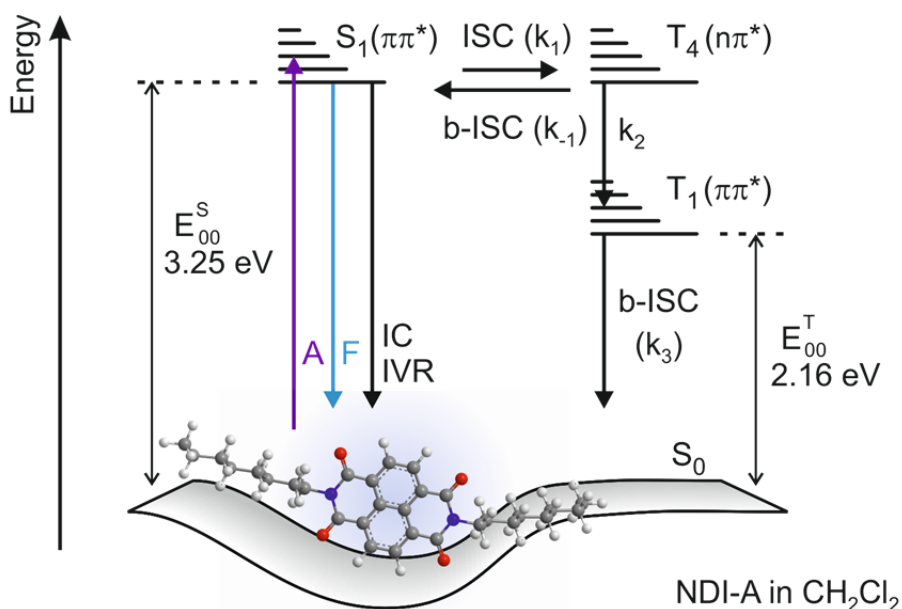


Fig. 5.9: a) Temporal evolution of the peak position (data in Fig. 5.4a) and an exponential fit result. b) Kinetics of the full width at half maximum (FWHM) of the peak after removing the influence of the peak shift and an exponential fit result.

if the analysis of the TA data could be linked to another time resolved data. This purpose is achieved for NDI-A in CH_2Cl_2 using the $T_4 \rightarrow T_1$ transition recorded in the 470-490 nm range. In this spectral range the contribution of the S_1 state absorption spectrum can be treated as background, i.e. it does not contain any spectral peaks in this region. The temporal evolution of the transition from T_4 to T_1 state is determined by tracking the peak shift and band narrowing. The TA data in the 470-490 nm range are thus parametrized using a Gaussian function. The resulting peak shift and band narrowing are depicted in Fig. 5.9. The time constant for the band narrowing is determined via an exponential fit to the data, which yields a time constant of 22.3 ps. This change is generally due to vibrational relaxation [Mon06]. A similar time constant with a value of 21.0 ps is obtained by a bi-exponential fit

to the peak position data (Fig. 5.9a). This time constant is thus also assigned to the vibrational relaxation process. The other time constant of 3.8 ps is assigned to the T_4 to T_1 process, which normally occurs on a few picoseconds time scale [Pig07]. This is also in very good agreement with the 3 ps time constant for the same process reported in ref. [Yus15].

The rate of the $T_4 \rightarrow T_1$ transition ($k_2 = 1/(3.8 \text{ ps}) = 2.6 \times 10^{11} \text{ s}^{-1}$) is linked to the analysis of the TA data and allows a unique solution of the kinetic model. The results are shown in Fig. 5.8b. As expected, the SADS of S_1 state are totally distinct from the SADS of T_4 state. The SADS of the S_1 state is dominated by a band at 598 nm and the distinct feature of the T_4 SADS is the band at 460 nm. Additionally, the bi-exponential decay of the S_1 state is explained by the forward and backward ISC process between the S_1 and T_4 state. The decay and repopulation rate of the S_1 state are described with two rate constants $k_1 = 3.0 \times 10^{11} \text{ s}^{-1}$ and $k_{-1} = 6.2 \times 10^{11} \text{ s}^{-1}$ respectively. The internal conversion from the T_4 state to the lower T_1 state competes with the backward ISC to the S_1 state and possesses a time constant of 3.8 ps. The SADS of the T_1 state of NDI-A can be easily distinguished from the other SADS because of its structured band with the maximum at 484 nm. And a rate constant $k_3 = 1.6 \times 10^6 \text{ s}^{-1}$ is used to characterize the backward ISC process from the T_1 state to the ground state S_0 (it also includes a triplet oxygen quenching contribution).



Scheme 5.10: Energy level scheme of NDI-A in CH_2Cl_2 with the relaxation pathways. The energies E_{00}^S and E_{00}^T estimated as described in the text (A: absorption; F: fluorescence; IC: internal conversion; IVR: intramolecular vibrational redistribution; ISC: intersystem crossing; b-ISC: back intersystem crossing).

In DMF a completely different behavior is observed (see Fig. 5.11). After the pump pulse, a TA band with a maximum at 585 nm and a shoulder around 470 nm is detected, which shows almost the same profile as that of the S_1 state observed in CH_2Cl_2 . Thus, this transient is attributed to the S_1 state of NDI-A in DMF. In contrast to the lifetime of the S_1 state in CH_2Cl_2 of 14.4 ps, the lifetime of the S_1 state in DMF strikingly decreases by a factor of 16, which has a value of 900 fs (global analysis result in Fig. 5.14). The decay of the S_1 state goes along with an apparent rise of a spectrum with the absorption maximum at 474 nm and a weak band around 600 nm. This species decays in 5 ps and its spectral features are in good agreement with the absorption spectrum of the NDI-A radical anion ($\text{NDI-A}^{\bullet-}$) recorded in spectroelectrochemistry (see Fig. 5.12). The appearance of the $\text{NDI-A}^{\bullet-}$ would imply that the singlet state decays via an ET process. This ultrafast S_1 state quenching process also explains why the fluorescence of NDI-A in DMF is extremely weak. Following the decay of $\text{NDI-A}^{\bullet-}$, a very weak residual TA spectrum is observed, whose lifetime is longer than the timescale of the fs-ps TA experiment (up to 1.5 ns). This residual spectrum has a similar profile as that of $\text{NDI-A}^{\bullet-}$. However, because the signal intensity of the residual species is comparable to the intensity resolution of the setup employed, its spectrum is not clearly presented.

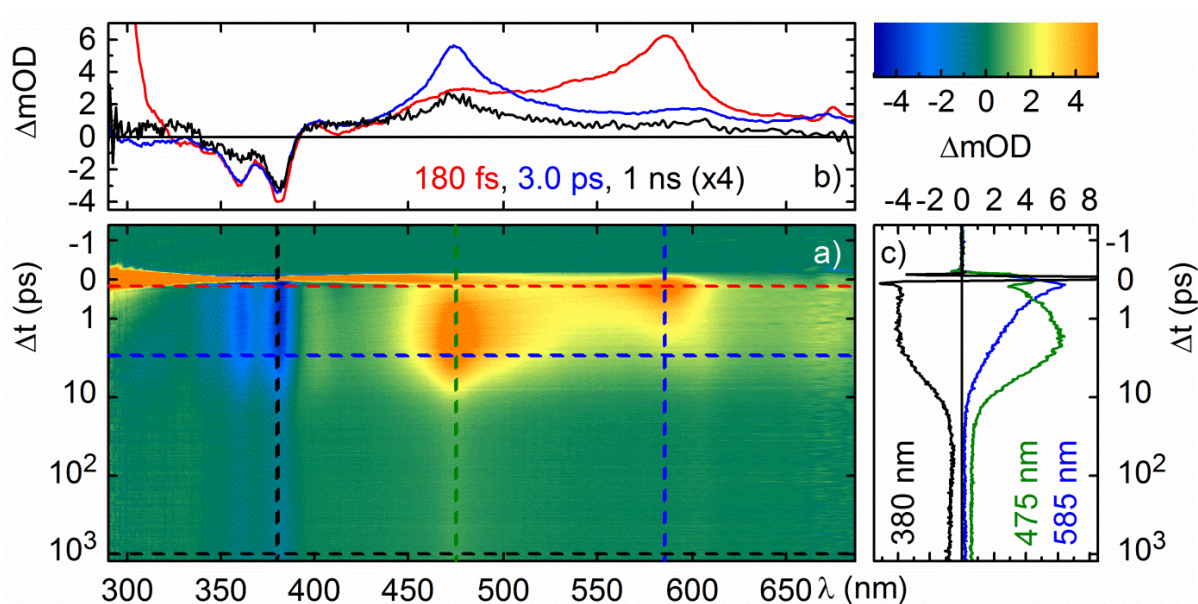


Fig. 5.11: Time-resolved absorption spectra of NDI-A in DMF at 22 °C. a) fs-ps TA: 0.1 mM NDI-A in 1 mm cuvette after 360 nm excitation with pump intensity of 1.8 mJ/cm^2 ; b) Transient absorption spectra recorded at several time delays after excitation (the spectrum at 1 ns is scaled by a factor of 4); c) Kinetics for the dynamics of different species at selected wavelengths.

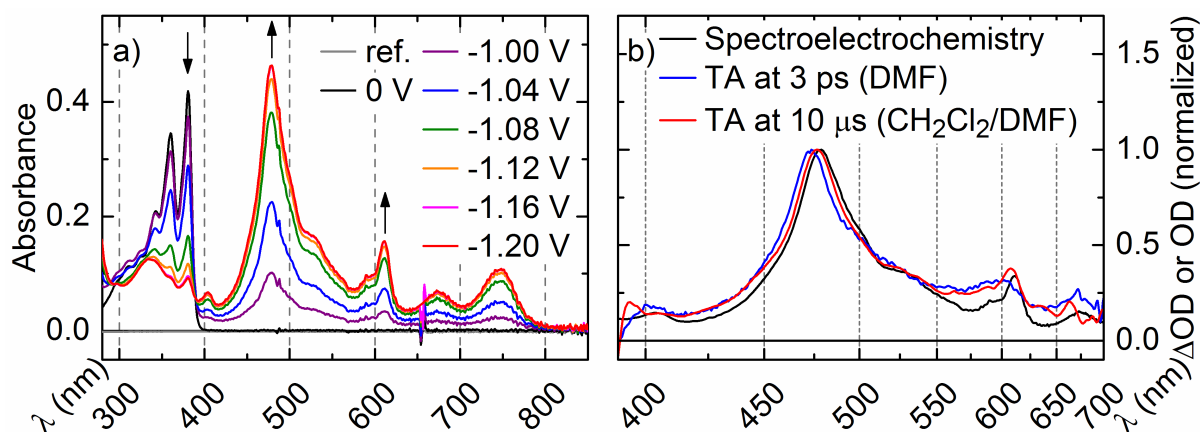


Fig. 5.12: a) UV-Vis spectroelectrochemical response of the transition $\text{NDI-A} \rightarrow \text{NDI-A}^{\bullet-}$ in $\text{CH}_2\text{Cl}_2/0.2 \text{ M TBAH}$ b) Comparison of the TA spectra of NDI-A in DMF at 3 ps delay and in the $\text{CH}_2\text{Cl}_2/\text{DMF}$ mixture at 10 μs delay with the $\text{NDI-A}^{\bullet-}$ absorption spectrum obtained in Spectroelectrochemistry. The spectra have been normalized to the absorption maximum around 470 nm.

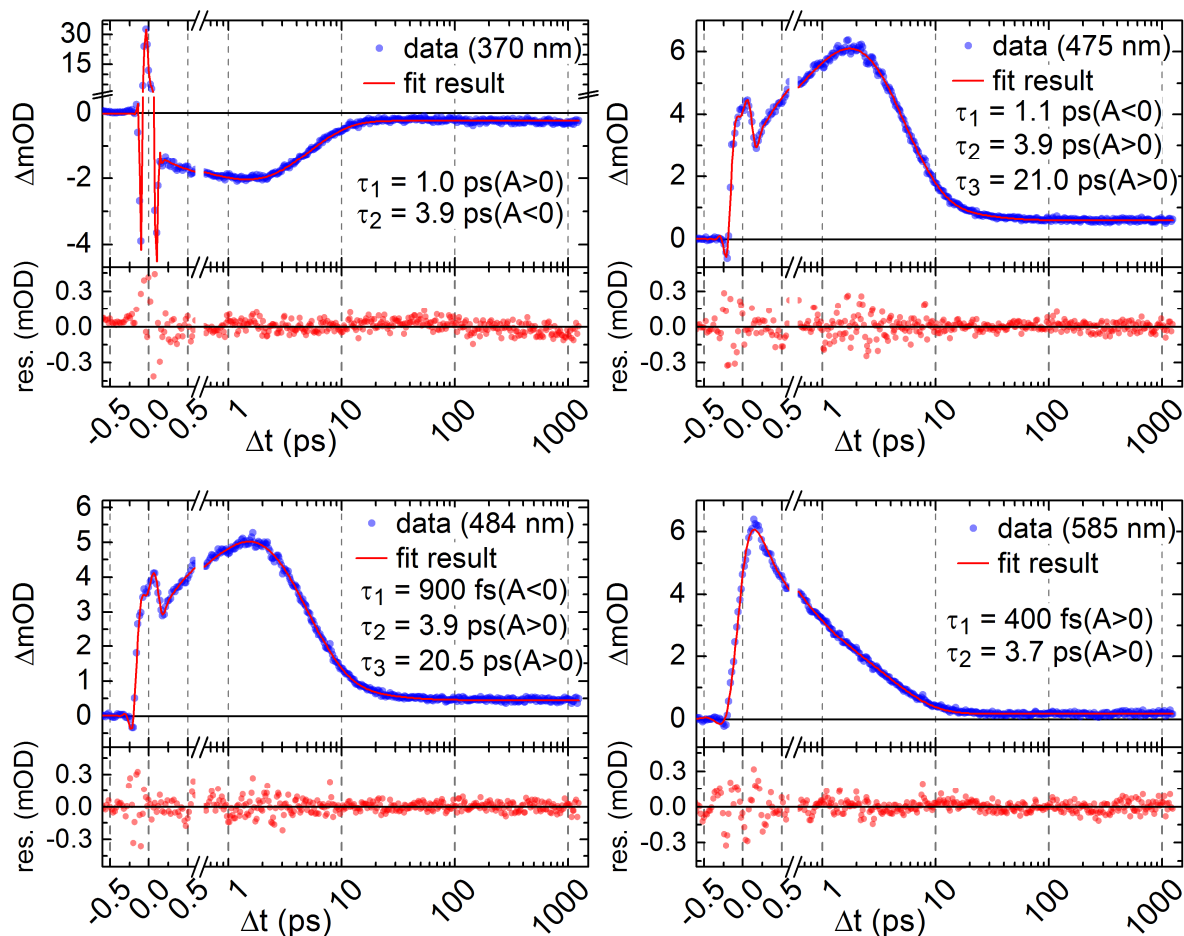


Fig. 5.13: Kinetic traces monitored at selected wavelengths from the data matrix in Fig. 5.11 and the corresponding fit results with a multi-exponential decay model.

The ns- μ s TA measurement for NDI-A in DMF can't resolve any TA spectra and intermediate lifetimes, since the intensity of TA signals are similar to the instrumental intensity resolution. There is only one thing certain and that is that all of the signals decay to the baseline within the observed time window (up to 500 μ s). This indicates a complete deactivation back to the ground state of NDI-A.

To quantify the dynamics observed in DMF, the fs-ps TA data for NDI-A in DMF are analyzed using a single line fit method. Fig. 5.13 presents the kinetic traces and fit results at the selected wavelengths. From the fit results, it can be seen that the same two time constants, i.e. near 1.0 ps and 3.9 ps are required for an adequate description of the measured kinetics at the GSB region (370 nm) and at the absorption of NDI-A^{•-} (475 and 484 nm). The time constant of 1.0 ps describes the population of the NDI-A^{•-} and the time constant of 3.9 ps presents the decay of the NDI-A^{•-} transient. Moreover, there is a marked increase of the GSB (more negative) accompanying the increase of the absorption of NDI-A^{•-}. This finding suggests that the NDI-A in the ground state should participate in the ET reaction. Turning to the data at 585 nm, which present primarily the ESA of the S₁ state and the band of NDI-A^{•-}, the kinetic trace can be well described with two time constants (the third time constant is \gg 1.5 ns and is not shown). The second time constant of 3.7 ps is consistent with the decay time of NDI-A^{•-}, whereas the first time constant of 400 fs, which presents the decay of the S₁ state transient, is much smaller than the rise time of NDI-A^{•-}. The cause of the discrepancy is probable a result of the overlap between the ESA of S₁ and the absorption spectrum of NDI-A^{•-} at the same wavelength. As the increase of the ESA of S₁ is partly countered by the decrease of the absorption of NDI-A^{•-}, the fit of the resulting TA spectra can lead to an erroneous result.

Interestingly, after the second time constant of 3.9 ps the GSB is not recovering completely. Furthermore, an intermediate with a time constant of near 21 ps is observed in the results at 475 and 484 nm, whereas the GSB shows no significant dynamics on this timescale. These observations suggest an unassigned excited state of the NDI-A in DMF with a lifetime of near 21 ps, which is formed from the NDI-A^{•-}.

In order to gain more information of the NDI-A excited state dynamics in DMF, the TA data are globally fitted. The analysis gives four different DADS with the corresponding time constants, which are shown in Fig. 5.14. The first species with an absorption maximum at 585 nm has been assigned to the S₁ state of NDI-A in DMF. It decays with a lifetime of 900 fs. The negative peak at 475 nm associated with the S₁ state decay perfectly matches the

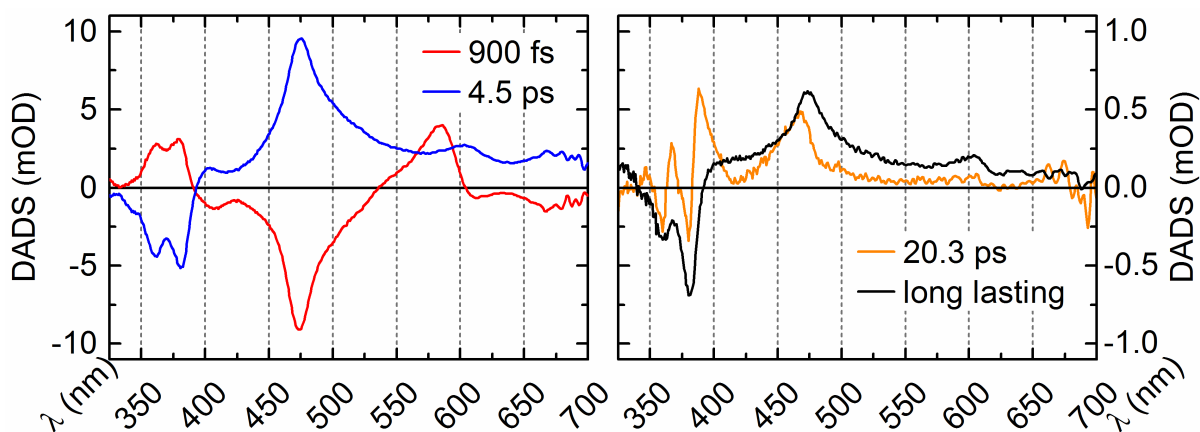
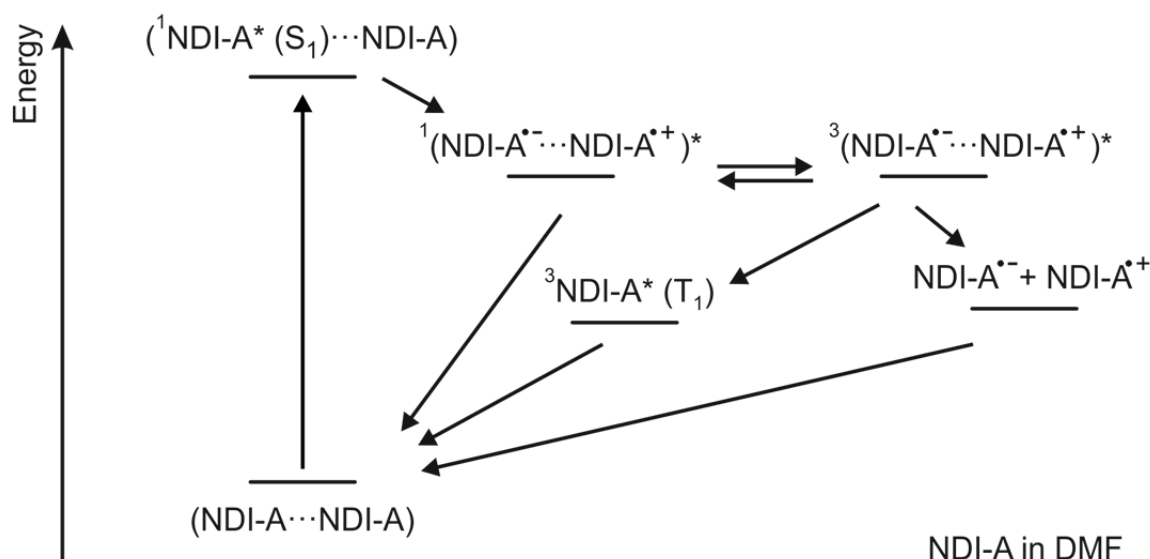


Fig. 5.14: Decay associated difference spectra of a global fit to the data in Fig. 5.11a.

positive part of the second DADS, which has been attributed to the $\text{NDI-A}^{\bullet-}$. This confirms that the S_1 state decays via an ET process. Moreover, a positive band with two maxima at 361 and 381 nm is observed, where the absorption bands of NDI-A are located. This implies that the NDI-A in its ground state is involved in the ET process. Thus, it can be concluded that the $\text{NDI-A}^{\bullet-}$ results from the ET between the ground state and the excited singlet state of the NDI-A, as shown in Scheme 5.15. This reaction also produces simultaneously the NDI-A radical cation ($\text{NDI-A}^{\bullet+}$). However, the similarity of the TA spectra obtained from the ET reaction with the $\text{NDI-A}^{\bullet-}$ absorption spectrum recorded in spectroelectrochemistry suggests that the contribution of the $\text{NDI-A}^{\bullet+}$ to the spectra formed by the ET reaction is negligible. The very weak absorption of the $\text{NDI-A}^{\bullet+}$ is consistent with previous observations in references [Ave97, Yus15].

The $\text{NDI-A}^{\bullet-}$ formed from the singlet state has a lifetime of 4.5 ps. This is followed by a new spectrum with a maximum at 468 nm. This spectrum decays in 20.3 ps, and the spectrum of $\text{NDI-A}^{\bullet-}$ appears again. The spectrum of $\text{NDI-A}^{\bullet-}$ appeared after the unassigned state does not decay on the timescale of the fs-ps TA experiment (up to 1.5 ns). The presence of a long-lived radical anion indicates that the triplet ion pair species is formed since back electron transfer (b-ET) in the triplet ion pair is considerably slower than that in the singlet ion pair [Rom16]. Therefore it seems possible that the unassigned state is the triplet state of NDI-A. A possible mechanism for the formation of the triplet can be through ISC from the singlet ion pair to the triplet ion pair followed by “triplet recombination” producing the NDI-A triplet state [Kav93]. On this basis, the excited state dynamics of the NDI-A in DMF is summarized in an proposed energy level diagram given in Scheme 5.15.



Scheme 5.15: Proposed energy level scheme of NDI-A in DMF with the relaxation pathways.

Due to a high self-association constant in DMF [Cub01], self-aggregated NDI-A dimers are formed at its ground state. It leads not only to a poor solvation of NDI-A in DMF [Rei17], but also to a photoinduced ultrafast forward ET (900 fs) followed by a rapid b-ET (4.5 ps) restoring the NDI-A to the ground state. The latter is a nonproductive cycle because the fast back reaction rules out any further diffusional ET reaction steps needed to convert the substrate to the final product. In addition, the minute amount of the triplet and the long-lived radical anion surviving from the b-ET makes the further analysis very difficult. Thus, to reduce the polarity of solvent, that is to reduce the probability of dimerization, a mixture of DMF and CH_2Cl_2 is used for the study of the NDI-A excited state properties.

In a CH_2Cl_2 /DMF mixture (volume/volume = 4:1) solution, the evolution of the spectra in time is similar to the ones in pure CH_2Cl_2 . As shown in Fig. 5.16 and 5.17, they consist almost of the same signatures, the strong ESA band of the S_1 state around 590 nm at early delay times and the structured band of the T_1 state with the maximum at 484 nm in the ns- μ s range. More information is found by globally fitting the TA data. The global analysis gives four different components (see Fig. 5.16b). The DADS with a time constant of 300 fs has a positive band around 590 nm and a negative contribution around 460 nm, which is very similar to the one with the time constant of 800 fs in pure CH_2Cl_2 . This suggests that the $S_1 \rightarrow T_1$ transition is also observed in the CH_2Cl_2 /DMF mixture. The second DADS with a time constant of 4.4 ps is similar to the one with the time constant of 900 fs in pure DMF. The positive contribution around 600 nm shows the decay of S_1 and the negative band at 476 nm describes the growth of $\text{NDI-A}^{\bullet-}$. The observation of the positive band in the second

DADS with two maxima at 360 and 380 nm demonstrates that the $\text{NDI-A}^{\bullet-}$ results also from the ET between the NDI-A ground state and the S_1 state. Interestingly, in the third step with a time constant of 13.0 ps, not only the $\text{NDI-A}^{\bullet-}$ decay but also the S_1 decay are observed. This can be accounted for by the fact that both the electron transfer step and the ISC process are reversible. After these transients the spectra of the T_1 state persist in the fs-ps TA experiment.

The ns- μs TA data (Fig. 5.17a) are globally fitted with two exponentials and a constant offset and the corresponding DADS are shown in Fig. 5.17b. The DADS with a time constant of 570 ns presents the decay of the T_1 state. Compared with the lifetime of the T_1 state in pure CH_2Cl_2 , the lifetime of the T_1 state in the $\text{CH}_2\text{Cl}_2/\text{DMF}$ mixture is shorter, implying a new T_1 state quenching process.

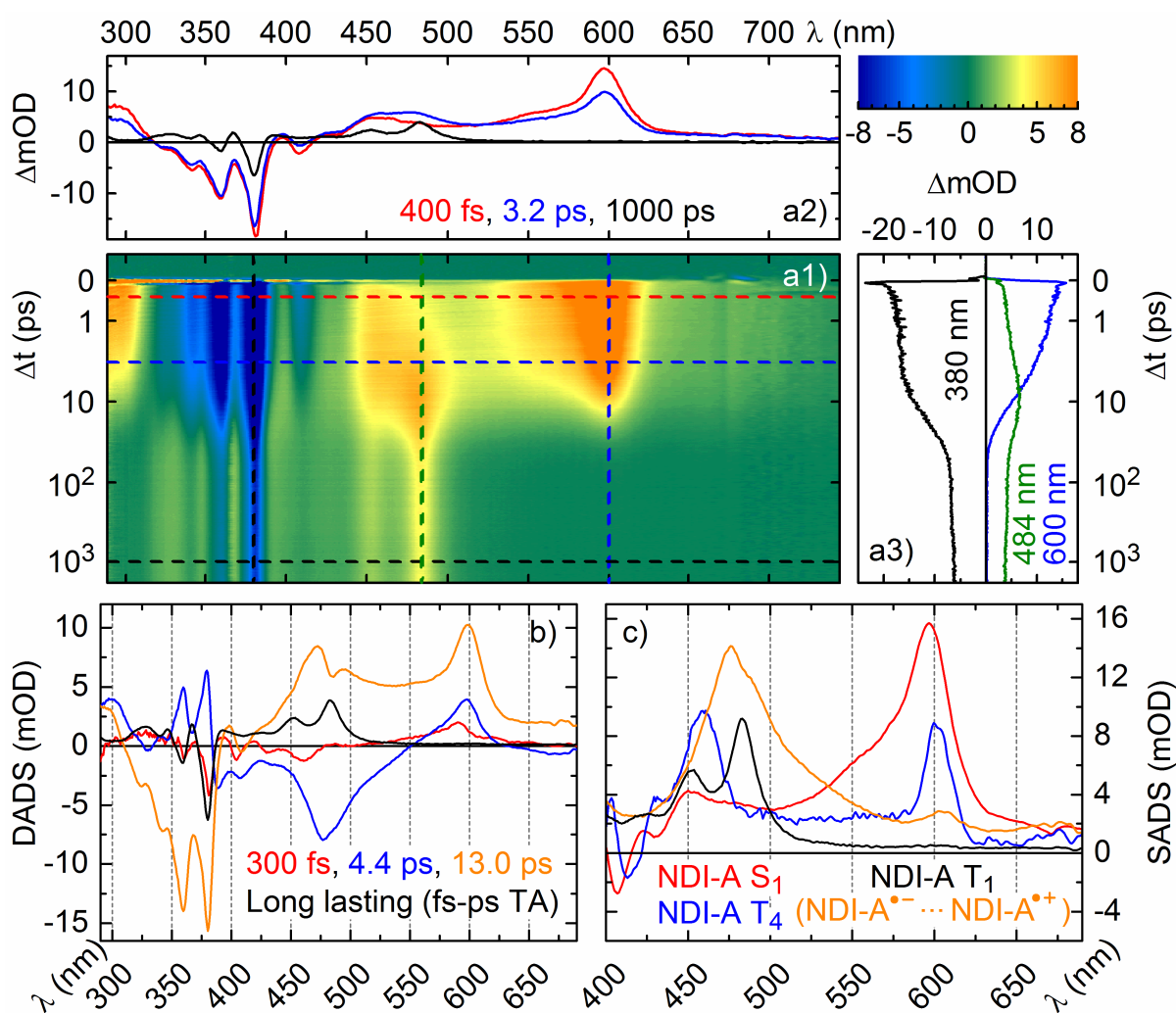


Fig. 5.16: a) fs-ps TA spectra of NDI-A in $\text{CH}_2\text{Cl}_2/\text{DMF}$ (4:1) at 22 °C, and results of (b) global analysis and (c) analysis with the model in Scheme 5.19 (1.2 mM NDI-A in 100 μm cuvette after 360 nm excitation with pump intensity of 1.6 mJ/cm^2).

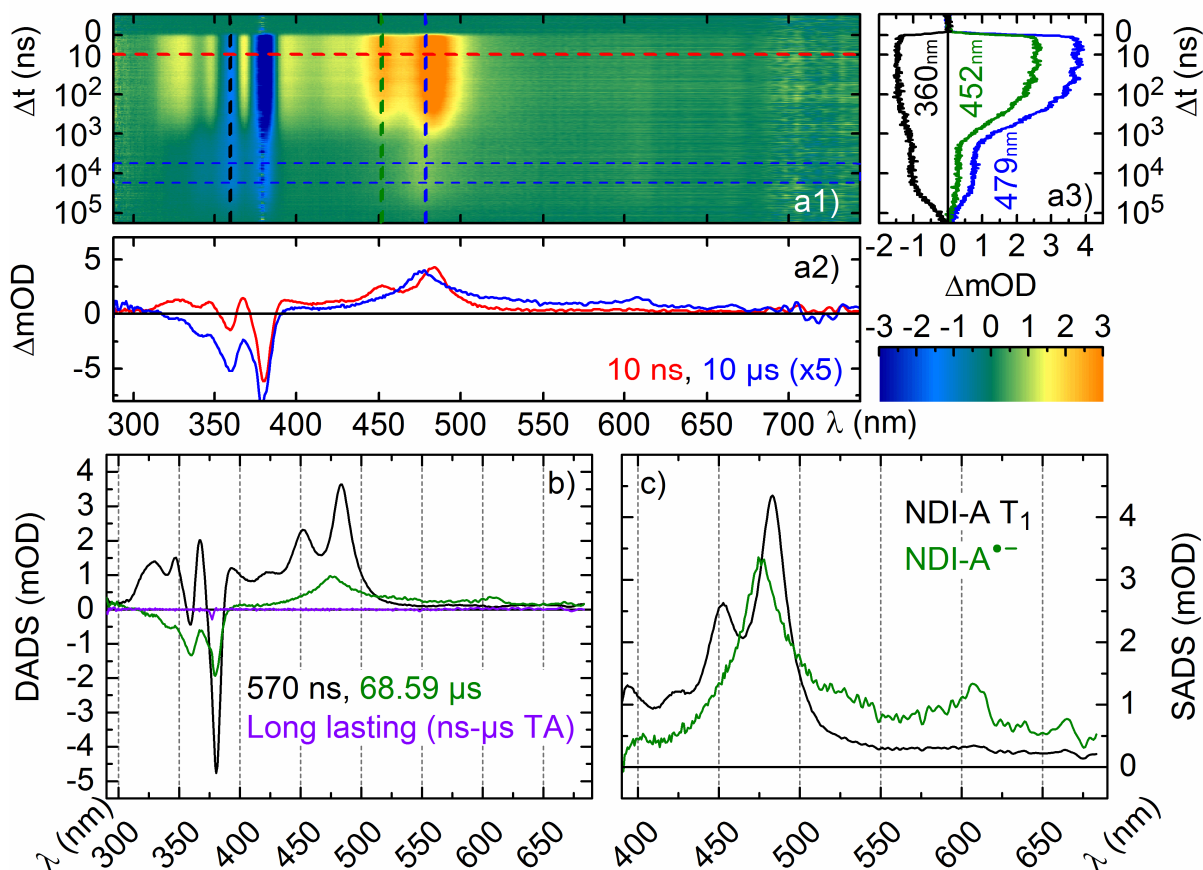
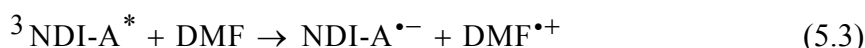


Fig. 5.17: a) ns- μ s TA spectra of NDI-A in $\text{CH}_2\text{Cl}_2/\text{DMF}$ (4:1) at 22 $^\circ\text{C}$, and results of (b) global analysis and (c) analysis with the model in Scheme 5.19 (1.2 mM NDI-A in 100 μm cuvette after 380 nm excitation with pump intensity of 1.0 mJ/cm^2).

In the second step with a time constant of 68.6 μs , the positive part resembles strongly the absorption spectrum of the $\text{NDI-A}^{\bullet-}$ (also shown in Fig. 5.12b). It is concluded that this long-lived species is $\text{NDI-A}^{\bullet-}$. The formation of the radical anion suggests that the quenching of the T_1 state results from a one-electron transfer. Nevertheless, no increase of the GSB is observed accompanying increase of the absorption of $\text{NDI-A}^{\bullet-}$. This indicates that the NDI-A in the ground state should not participate in the ET reaction. Since the NDI-A radical anion is only observed in the presence of DMF, it is inferred that the $\text{NDI-A}^{\bullet-}$ could be formed by electron-transfer from one of the surrounding DMF molecules to the T_1 state of NDI-A, as described by eq 5.3.



Unfortunately, no absorption of the DMF radical cation ($\text{DMF}^{\bullet+}$) is observed in the TA measurements. The reason for this could be that the weak absorption of $\text{DMF}^{\bullet+}$ expected around 415 nm [Mel97] is masked by the much stronger $\text{NDI-A}^{\bullet-}$ absorption. In order to

prove that DMF plays a role in the ET process, the formation of the NDI-A^{•-} is monitored at 484 nm as a function of DMF concentration, which is shown in Fig. 5.18a, and the kinetics of the concomitant decay of the T₁ state is fitted to a dissociative ET model with a pseudo-first-order rate coefficient.

$$k'_{\text{ET}} = \frac{1}{\tau} - \frac{1}{\tau_0} = {}^3k_{\text{ET}} [\text{DMF}] \quad (5.4)$$

Here τ_0 and τ are the lifetimes of the T₁ state in the absence and presence of DMF. The resulting kinetic plot (Fig. 5.18b) is linear, and affords a rate coefficient of ${}^3k_{\text{ET}} = 9.8 \times 10^4 \text{ M}^{-1}\text{s}^{-1}$, which is consistent with Stern-Volmer kinetics [Mon06]. This study confirms that DMF is associated with the charge transfer quenching of the NDI-A T₁ state.

The generation of the NDI-A^{•-} by the ET from DMF is also supported by a sufficiently negative free energy change of -0.97 eV, which is calculated using eq 5.5 (a modified Rehm-Weller equation) [IUPAC14].

$$\Delta G_{\text{ET}}^0 = e \cdot \left[E(\text{DMF}^{\bullet+} / \text{DMF}) - E(\text{NDI-A} / \text{NDI-A}^{\bullet-}) \right] - E_{00}^{\text{T}} + \frac{z(\text{DMF}^{\bullet+})z(\text{NDI-A}^{\bullet-})e^2}{4\pi\epsilon_0\epsilon_r d_{\text{DA}}} \quad (5.5)$$

The oxidation potential of DMF ($E(\text{DMF}^{\bullet+}/\text{DMF}) = 0.38 \text{ V vs. SCE}$) was reported in ref. [Was93]. The reduction potential of NDI-A ($E(\text{NDI-A}/\text{NDI-A}^{\bullet-}) = -0.69 \text{ V vs. SCE}$) was determined in CH₂Cl₂ by the co-worker using cyclic voltammetry [Rei17], consistent with the values reported in the literature [Mon06]. The energy difference between the T₁ state and the ground state ($E_{00}^{\text{T}} = 2.16 \text{ eV}$) is estimated from the short-wavelength band of the phosphorescence spectra. Phosphorescence from NDI-A is not observed at room temperature or in frozen ethanol glasses. Upon addition of 10% ethyl iodide, phosphorescence from NDI is induced via the heavy atom effect [Kas52] and the result is shown in Fig A4.3 in Appendix A4. The last term in eq 5.5 accounts for the effect of the Coulombic attraction in the redox products. Treating the redox products as point charges with the charges located at the center, the distance of the two charged species (d_{DA}) could be estimated to be of the order of 10 Å. Thus, using the estimated dielectric constant with the value $\epsilon_r = 12.1$ for the CH₂Cl₂/DMF (4:1) mixture [Jou04], the electrostatic interaction term is estimated to be 0.12 eV.

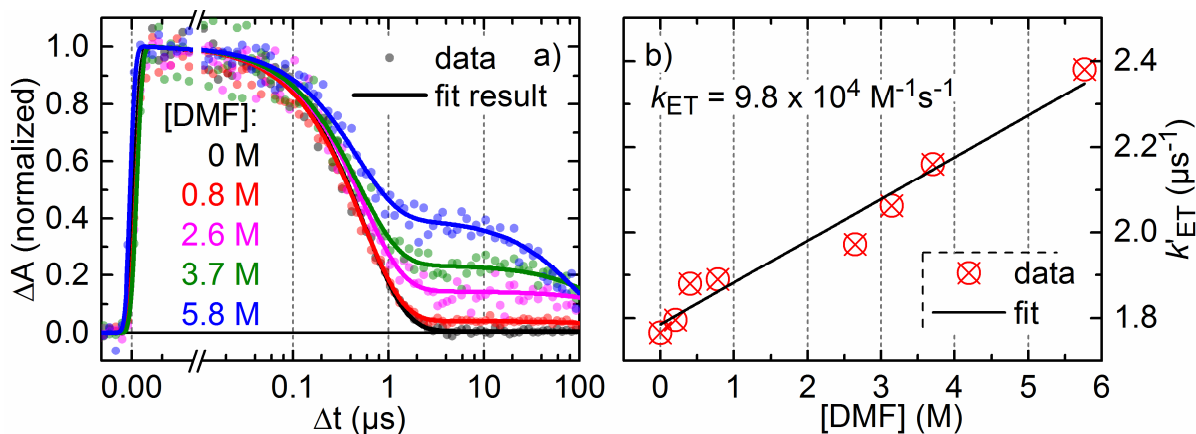
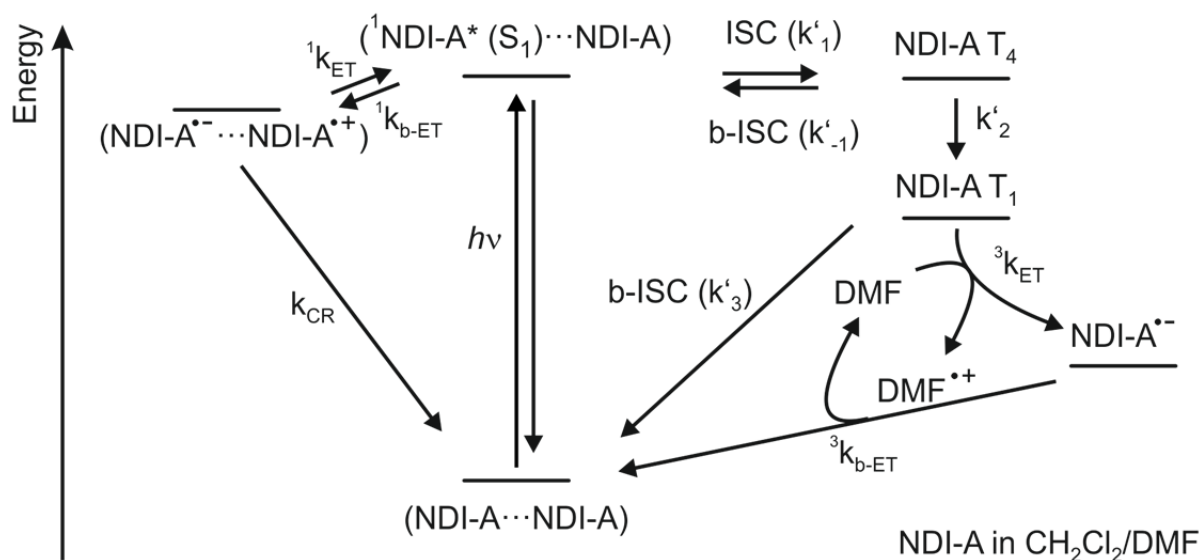


Fig. 5.18: Rate constant of production of NDI-A radical anions by electron transfer from DMF. a) TA concentration dependence study for NDI-A (1.0 mM) and DMF in CH_2Cl_2 . The solid lines represent exponential fits. b) First-order kinetic plot of DMF concentration dependence study.



Scheme 5.19: Proposed energy level scheme of NDI-A in the $\text{CH}_2\text{Cl}_2/\text{DMF}$ mixture with the relaxation pathways.

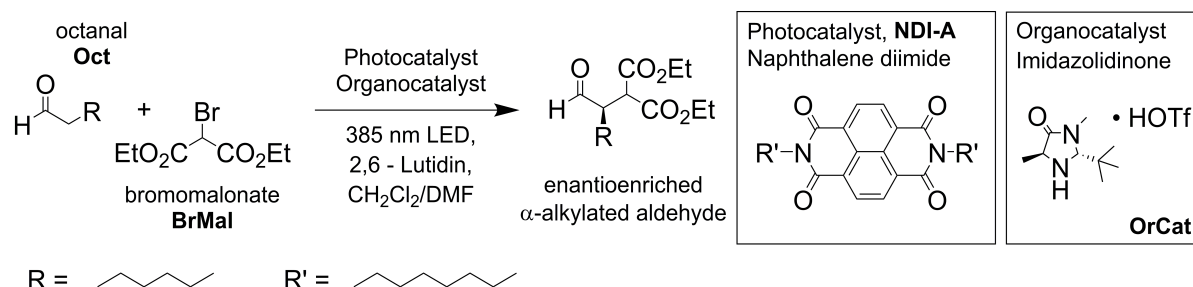
On this basis, the excited state dynamics of the NDI-A in the $\text{CH}_2\text{Cl}_2/\text{DMF}$ mixture is summarized in the energy level diagram (see Scheme 5.19). Self-aggregated NDI-A dimers are formed at its ground state. Upon photoexcitation of NDI-A dimers the S_1 state is formed, which decays rapidly to form the T_4 state via a reversible intersystem crossing process. The decay and repopulation rate of the S_1 state are described with two rate constants $k'_1 = 6.7 \times 10^{11} \text{ s}^{-1}$ and $k'_{-1} = 2.5 \times 10^{12} \text{ s}^{-1}$ respectively, both of them are larger than the values in the measurements for NDI-A in pure CH_2Cl_2 . Meanwhile, the electron transfer connecting the S_1 state and the ion pair occurs and this step is also reversible. The rate constant for this ET

from the equilibrated S_1 state to the ion pair is ${}^1k_{\text{ET}} = 1.1 \times 10^{11} \text{ s}^{-1}$, with a reverse transfer rate of ${}^1k_{\text{b-ET}} = 5.6 \times 10^{10} \text{ s}^{-1}$. The lifetime of these ion pairs is 9 ps. The T_1 state is generated from the T_4 state via internal conversion ($k'_2 = k_2 = 2.6 \times 10^{11} \text{ s}^{-1}$). A fraction of the T_1 state is diffusionally quenched by DMF to form “free” NDI-A radical anions (${}^3k_{\text{ET}} = 9.8 \times 10^4 \text{ M}^{-1} \text{ s}^{-1}$), and some of T_1 repopulates the ground states via b-ISC ($k'_3 = k_3 = 1.6 \times 10^6 \text{ s}^{-1}$). This NDI-A $\dot{\ominus}$ is long lived and repopulates the NDI-A ground state and neutral DMF via back electron transfer to DMF $\dot{\oplus}$. The lifetime of these “free” NDI-A radical anions is 68.6 μs .

According to this model the SADS are constructed (see Fig. 5.16c and 5.17c). As expected, the SADS of the S_1 , T_4 and T_1 state of NDI-A in the $\text{CH}_2\text{Cl}_2/\text{DMF}$ mixture are very similar to the spectra obtained in the TA experiment in pure CH_2Cl_2 . Furthermore, the SADS of the ion pairs and the NDI-A $\dot{\ominus}$ are in line with the NDI-A $\dot{\ominus}$ absorption spectrum obtained in spectroelectrochemistry. So far, all species detected in the TA experiments in CH_2Cl_2 , DMF or the $\text{CH}_2\text{Cl}_2/\text{DMF}$ mixture can be distinguished through their particular spectral features.

5.2. Observation of the competitive mechanism of aldehyde α -alkylation by synergistic photoredox catalysis with NDI and organocatalysis

After the characterization of the ground and excited state properties of NDI-A, the detailed mechanism of the photoredox catalytic α -alkylation will be elucidated by using NDI-A TA spectroscopic studies in combination with the data from synthetic experiments in ref. [Rei17]. In this case, NDI-A is applied as the photoredox catalyst for α -alkylation and the other reactants are the same as that in the $\text{Ru}(\text{bpy})_3^{2+}$ based catalysis described in Chapter 3. The reaction procedure is shown in Scheme 5.20. A commercially available 385 nm LED (Nichia NCSU034B) was used for the synthetic experiments [Rei17] because it fits perfectly the absorption spectrum of NDI-A in CH_2Cl_2 or DMF (see Fig. 5.21).



Scheme 5.20: Application of NDI-A as photoredox catalyst for enantioselective α -alkylation of octanal by bromo-diethylmalonate [Rei17].

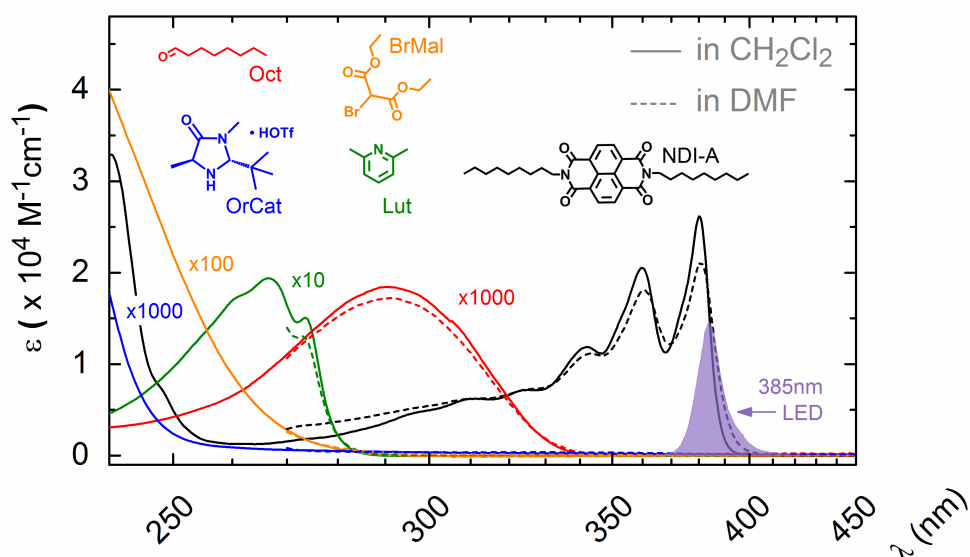


Fig. 5.21: Steady-state absorption spectra of NDI-A and the reactants for α -alkylation of octanal in CH_2Cl_2 or DMF at room temperature. The purple filled curve represents the emission of the 385 nm LED (nominal 385nm, measured 384nm).

It can also be seen from Fig. 5.21 that only the catalyst NDI-A can be excited by the LED light used rather than the other reactants. As was mentioned in the previous Chapter 3, the enamine (**Ena**) also shows an absorption in the emission region of the 385 nm LED (see Fig. 3.7). However, due to the tiny absorption coefficient of **Ena** at 384 nm ($\sim 5 \text{ M}^{-1}\text{cm}^{-1}$) the absorption of **Ena** can be neglected compared to the NDI-A absorption at the same wavelength ($OD_{\text{NDI-A}} = 47 \gg OD_{\text{Ena}} = 0.1$). For the TA spectroscopic studies, the excitation wavelength is set to 380 nm, which thus dominantly excites the catalyst NDI-A in the mixture solution.

Table 5.2 compares the properties of NDI-A and $\text{Ru}(\text{bpy})_3^{2+}$ as well as the results obtained from the synthetic experiments using as catalyst NDI-A or $\text{Ru}(\text{bpy})_3^{2+}$. $\text{Ru}(\text{bpy})_3^{2+}$ can absorb visible light (454 nm) while NDI-A has its absorption maximum in the UV range (380 nm). But the absorption coefficient of NDI-A at 380 nm ($26 \text{ mM}^{-1}\text{cm}^{-1}$) is significantly higher than that of the catalyst $\text{Ru}(\text{bpy})_3^{2+}$ at the corresponding absorption maximum ($14 \text{ mM}^{-1}\text{cm}^{-1}$). This means that NDI-A has greater degrees of opacity. Moreover, these catalysts possess similar triplet state energy and lifetime. Though NDI-A exhibits a triplet yield of 74% and a reduction potential of -0.69 V that are less than those of $\text{Ru}(\text{bpy})_3^{2+}$ ($\Phi_{\text{T1}} = \sim 100\%$ and $E_{\text{red}} = -1.28 \text{ V}$), these values of NDI-A are still large enough to make NDI-A serve as a catalyst for the considered dual catalysis. This view can be supported due to the sufficient product yield (60%) and the ideal substance conversion (99%) using NDI-A as a catalyst for the α -alkylation reaction. Therefore, NDI-A and the catalyst $\text{Ru}(\text{bpy})_3^{2+}$ are comparable in acting as the photoredox catalyst for α -alkylation.

Table 5.2: Yield of the α -alkylation product as well as conversion of **BrMal** in synthetic experiments with NDI-A or $\text{Ru}(\text{bpy})_3^{2+}$. Reported data of NDI-A are in CH_2Cl_2 and the data of $\text{Ru}(\text{bpy})_3^{2+}$ are in aqueous solution [Cam07] unless otherwise noted. λ_{max} : peak of absorption; ϵ_{abs} : absorption coefficient; τ_{exc} : lifetime of triplet state; Φ_{T1} : triplet yield; E_{00}^{T} : triplet state energy; E_{red} : reduction potential (vs. SCE). a) in N_2 purged CH_2Cl_2 ; b) in anoxic DMF [Cas83]; c) in anoxic $\text{CH}_2\text{Cl}_2/\text{DMF}$ (1:1) [Rei17]; d) in anoxic DMF [Nic08].

Catalyst	λ_{max} (ϵ_{abs}) (nm ($\text{mM}^{-1}\text{cm}^{-1}$))	τ_{exc} (ns)	Φ_{T1} (%)	E_{00}^{T} (eV)	E_{red} (V)	Yield (%)	Conversion (%)
NDI-A	380 (26)	1060 ^a	74	2.16	-0.69	60 ^c	99 ^c
$\text{Ru}(\text{bpy})_3^{2+}$	454 (14)	912 ^b	100	2.12	-1.28	92 ^d	$\sim 100^{\text{d}}$

Since NDI-A has comparability with the established catalyst and features intermediates that are spectroscopically much better observable than those of transition metal complexes like $\text{Ru}(\text{bpy})_3^{2+}$, NDI-A is very appropriate for mechanistic studies of photoredox catalytic reactions. Through tracking the generation and quenching of the NDI-A singlet state, triplet state and radical anion under selective influence of the individual reactants in photoredox organocatalytic α -alkylation of octanal, and combining these data with the results from synthetic experiments [Rei17], a comprehensive mechanistic picture can be eventually generated.

In contrast to the catalysis with $\text{Ru}(\text{bpy})_3^{2+}$, in which the reduced form of the photoredox catalyst is initially generated by the enamine initiation step (see scheme 3.5), the NDI-A radical anion $\text{NDI-A}^{\bullet-}$ is already present at the beginning of the light excitation via the ET process from DMF to NDI-A excited states (eq 5.3). Because the electron transfer process between $\text{NDI-A}^{\bullet-}$ and bromomalonate (**BrMal**) represents the decisive step for product formation or reproduction of the chain, the quenching of $\text{NDI-A}^{\bullet-}$ is investigated by tracking its lifetime in a TA quenching study with **BrMal** in different concentrations. Moreover, since the $\text{NDI-A}^{\bullet-}$ arises not only from the NDI-A S_1 state but also from the NDI-A T_1 state, the role of the S_1 and T_1 states of NDI-A in the **BrMal** reduction is elucidated using this experiment. The lifetimes of the NDI-A transient species in the presence of **BrMal** are summarized in Table 5.3.

Table 5.3: Tracking of $\text{NDI-A}^{\bullet-}$ quenching for a series of solutions with different concentrations of **BrMal**. τ_{S1} , $\tau_{\text{ion pair}}$, τ_{T1} and τ_{RA} denote the lifetime of the NDI-A S_1 state, the ion pair ($\text{NDI-A}^{\bullet-} \cdots \text{NDI-A}^{\bullet+}$), the NDI-A T_1 state and $\text{NDI-A}^{\bullet-}$, respectively.

No.	Solution	BrMal (mM)	τ_{S1} (ps)	$\tau_{\text{ion pair}}$ (ps)	τ_{T1} (ns)	τ_{RA} (μs)
#1		0	6.0	11.5	628	62.7
#2	1.2 mM NDI-A	50	7.6	15.9	578	62.5
#3	$\text{CH}_2\text{Cl}_2/\text{DMF}$ (4:1)	100	7.0	16.6	565	59.9
#4		250	7.3	16.9	560	55.3

It is observed that the lifetimes of the NDI-A singlet excited state (S_1) and of the ion pair ($\text{NDI-A}^{\bullet-} \cdots \text{NDI-A}^{\bullet+}$), which results from the ET reaction of the S_1 state, are slightly longer in the presence of **BrMal**, but hardly change with the increase in the **BrMal** concentration. In contrast, the lifetimes of the NDI-A T_1 state and of the $\text{NDI-A}^{\bullet-}$, which are generated from the ET reaction of the T_1 state, decrease significantly with increasing concentration of **BrMal**. It can thus be concluded that **BrMal** undergoes ET only with the $\text{NDI-A}^{\bullet-}$ arising from the T_1 state to generate the important malonate radicals. The rate constant $k_{\text{ET-BrMal}}$ for this $\text{NDI-A}^{\bullet-}$ quenching process can be determined to $8.1 \times 10^3 \text{ M}^{-1}\text{s}^{-1}$ by a Stern-Volmer analysis.

In further TA studies, the individual reactants are added as possible quencher of the NDI-A excited triplet state in order to identify competitive processes (see Table 5.4). In the presence of octanal (**Oct**), **BrMal**, 2,6-lutidine (**Lut**) and organocatalyst (**OrCat**) respectively, the lifetime of NDI-A T_1 state is reduced, but no $\text{NDI-A}^{\bullet-}$ signal is observed, meaning that no ET process takes place between these substances and the T_1 state (#1 - #5 in Table 5.4). DMF reacts with the T_1 state to form the radical anion (#8 in Table 5.4), but only with a yield of 8.9%.

Table 5.4: Temporal data on the dynamics of NDI-A in different reactant mixtures of the photoredox organocatalytic α -alkylation of octanal. $\Phi_{\text{RA}(T_1)}$ is determined by dividing the radical anion concentration by the triplet concentration.

No.	Solution	Oct (mM)	BrMal (mM)	Lut (mM)	OrCat (mM)	τ_{T_1} (ns)	τ_{RA} (μs)	$\Phi_{\text{RA}(T_1)}$ (%)
#1	1.2 mM NDI-A CH_2Cl_2	-	-	-	-	641	-	-
#2		500	-	-	-	634	-	-
#3		-	250	-	-	555	-	-
#4		-	-	500	-	512	-	-
#5		-	-	-	50	574	-	-
#6		-	-	500	50	493	45.0	20.1
#7		500	-	500	50	234	65.5	41.2
#8		-	-	-	-	572	68.6	8.9
#9		-	-	500	50	296	17.1	52.5
#10		500	-	500	50	173	39.4	56.4

Furthermore, **Lut** acts as a base in the reaction and activates the **OrCat** by deprotonation. The observation of quenching of the T_1 state and formation of the $\text{NDI-A}^{\bullet-}$ in the presence of **Lut** and **OrCat** in pure CH_2Cl_2 (#6 in Table 5.4) suggests the availability of an ET process between the activated **OrCat** and the $\text{NDI-A } T_1$ state. Addition of **Oct** to this mixture (#7 in Table 5.4) causes the formation of enamine (**Ena**), which can quench the T_1 state to the $\text{NDI-A}^{\bullet-}$ (initiation in Scheme 5.22). In the additional presence of DMF in both mixtures (#9 and #10 in Table 5.4), the ET process from the T_1 state to $\text{NDI-A}^{\bullet-}$ becomes more effective with a yield of $> 50\%$. In addition, the lifetimes of $\text{NDI-A}^{\bullet-}$ in these cases are also reduced, indicating a reaction of the $\text{NDI-A}^{\bullet-}$ with the **Ena** or the activated **OrCat**.

More than one of the initially added reactants can quench the T_1 state of NDI-A . The formation of the $\text{NDI-A}^{\bullet-}$ is concomitant with this T_1 state decay. In order to determine which reactant dominates largely the T_1 state quenching process, the rate constant of each quenching process is determined. The T_1 state quenching and the $\text{NDI-A}^{\bullet-}$ formation are tracked for a series of solutions with different concentrations of **Ena** in the presence and absence of DMF (see Table 5.5). The measurements were performed 20 minutes after mixing the reactants to ensure equilibrium on the enamine side (**Ena** formation see Chapter 3). It is observed that in both cases the lifetime of the T_1 state decreases with increasing concentration of **Ena**. The bimolecular rate constant for ET from **Ena** to the $\text{NDI-A } T_1$ state, obtained from the slope of the Stern-Volmer plot, is given as $2.1 \times 10^8 \text{ M}^{-1}\text{s}^{-1}$ for pure CH_2Cl_2 solution and $3.3 \times 10^8 \text{ M}^{-1}\text{s}^{-1}$ for the $\text{CH}_2\text{Cl}_2/\text{DMF}$ mixture solution. The results clearly suggest that the formation of the $\text{NDI-A}^{\bullet-}$ can be facilitated by adding DMF in the solution.

Table 5.5: Tracking of the $\text{NDI-A } T_1$ state quenching for a series of solutions with different concentrations of **Ena** in the absence or presence of DMF. 2,6-lutidine with a concentration of 0.5 M is added to the solution.

No.	Solution	Oct (mM)	OrCat (mM)	Ena (mM)	τ_{T1} (ns)	τ_{RA} (μs)	$\Phi_{RA(T1)}$ (%)
#7	1.2 mM NDI-A CH_2Cl_2	500	50	11.8	234	65.5	41.2
#11		800		14.5	218	54.4	40.9
#12		1200		17.2	199	49.4	38.8
#10	1.2 mM NDI-A $\text{CH}_2\text{Cl}_2/\text{DMF}$ (4:1)	500	50	11.8	173	39.4	56.4
#13		800		14.5	149	30.6	52.3
#14		1200		17.2	136	30.2	52.6

In addition, the quenching of the T_1 state by **Ena** is significantly faster than the quenching by DMF (2.1 or $3.3 \times 10^8 \text{ M}^{-1}\text{s}^{-1}$ for **Ena** \gg $9.8 \times 10^4 \text{ M}^{-1}\text{s}^{-1}$ for DMF), which is why the initiation of the catalysis is essentially caused by the quenching of the excited photocatalyst by **Ena** in the sense of a singly occupied molecular orbital (SOMO) catalysis, although the **Ena** is consumed. This mechanism of initiation was proposed in the mechanistic work on the same dual photoredox organocatalytic α -alkylation [Nic08, Cis15, Bah16].

Under the conditions of synthetic catalysis, i.e. all the reactants with the same concentrations for the α -alkylation are added in the solution, the TA studies are carried out in the presence and absence of DMF (Table 5.6). It is observed that in both cases the electron transfer path to the $\text{NDI-A}^{\bullet-}$ is active. This means that in both solvents the conversion to the product, either via a radical chain or via a catalytic cycle, is possible. Nevertheless, no turnover has been detected synthetically using pure CH_2Cl_2 . The formation of products is only observed in the presence of DMF [Rei17]. It is likely that there may be a solubility problem in pure CH_2Cl_2 due to the observations during the TA studies. In the TA measurements it was observed that the intensity of the ESA decreases with each run in the case of using pure CH_2Cl_2 (Fig A4.4 in Appendix A4). However, this phenomenon is not observed in the presence of DMF. A component, which is generated as a result of the light excitation and is involved in product formation pathway, obviously fails in CH_2Cl_2 . This reduces the pump pulse power and gives rise to the intensity decrease of the ESA. This observation explains why the conversion to product falls in synthetic experiments using pure CH_2Cl_2 . The co-worker Reiß has assumed that this component is a derivative of the **OrCat** [Rei17].

Table 5.6: TA spectroscopic study of NDI-A under synthetic conditions in the presence and absence of DMF. 2,6-lutidine with a concentration of 0.5 M is added to the solution.

No.	Solution	Oct (mM)	BrMal (mM)	OrCat (mM)	τ_{T1} (ns)	τ_{RA} (μs)	$\Phi_{RA(T1)}$ (%)
#15	1.2 mM NDI-A CH_2Cl_2	500	250	50	214	8.85	47.7
#16	1.2 mM NDI-A $\text{CH}_2\text{Cl}_2/\text{DMF}$ (4:1)	500	250	50	150	6.26	69.9

Table 5.7: TA spectroscopic study of NDI-A under conditions of synthetic experiments with different concentrations of **BrMal**. 2,6-lutidine with a concentration of 0.5 M is added to the solution.

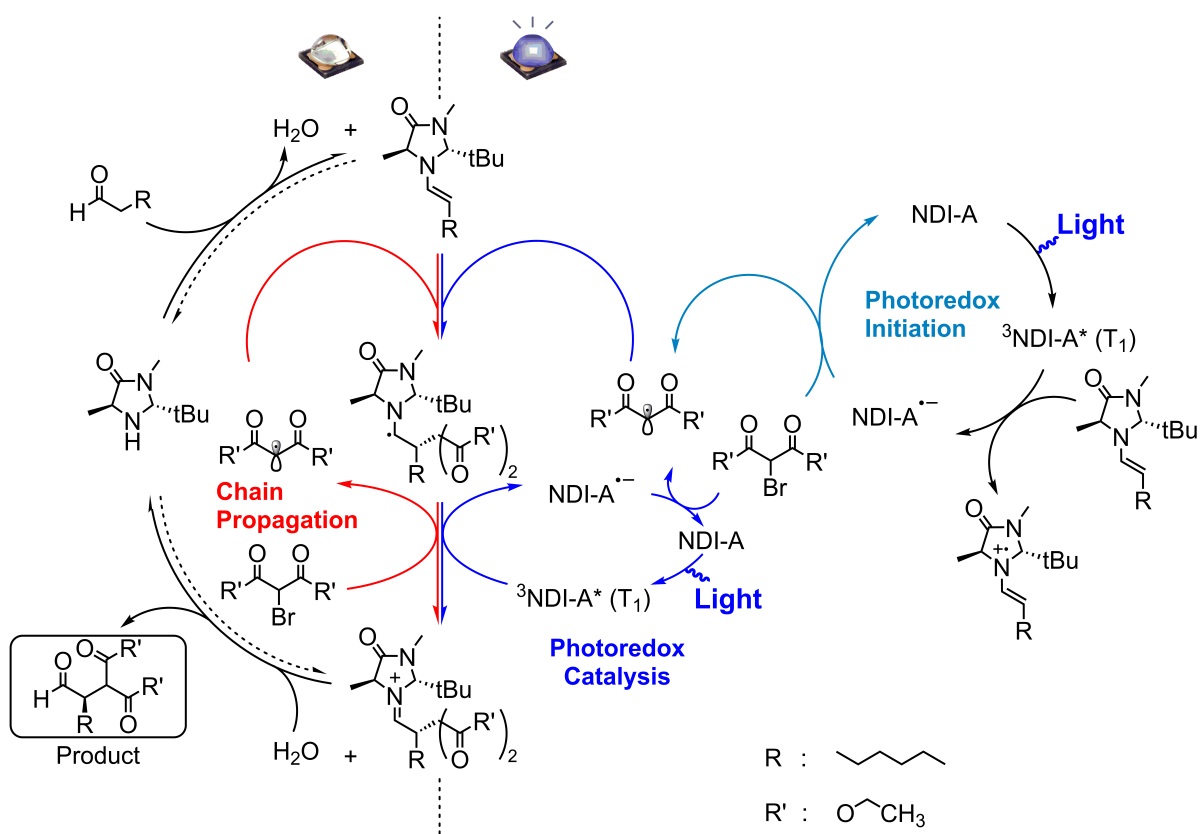
No.	Solution	Oct (mM)	BrMal (mM)	OrCat (mM)	τ_{T1} (ns)	τ_{RA} (μ s)	$\Phi_{RA(T1)}$ (%)
#16	1.2 mM NDI-A CH ₂ Cl ₂ /DMF (4:1)	500	250	50	150	6.26	69.9
#17		500	500	50	166	4.98	63.1
#18		500	800	50	178	3.42	56.2

For a more precise study of the boundary between radical chain and catalysis cycle on the way to the reaction product, the concentration of **BrMal** is varied in TA measurements under the conditions of synthetic catalysis (Table 5.7). It is observed that with increasing concentration of **BrMal** the lifetime of the NDI-A T₁ state increases, while the lifetime of the NDI-A^{•-} and the radical anion yield decreases. As described above, in a mixture of NDI-A and **BrMal** without the other reactants (Table 5.3), a reduction in triplet lifetime is observed with increasing concentration of **BrMal**. This can be explained by the mechanism proposed in this thesis for Ru(bpy)₃²⁺ (Chapter 3, Scheme 3.5), in which the radical chain is inhibited by the excited photocatalyst. The **BrMal** and the T₁ state of NDI-A compete for the oxidation of the amino radical (**AmiR**). The increase in the **BrMal** concentration leads to higher probability of the oxidation of **AmiR** by **BrMal**, which is reflected equally in the increase in the lifetime of the T₁ state and in the lower radical anion yield. The increase in the concentration of **BrMal** also has a direct influence on the lifetime of the NDI-A^{•-}, because the **BrMal** can be reduced by the NDI-A^{•-} to repopulate the neutral NDI-A. This gives rise to the decrease of the NDI-A^{•-} lifetime in the TA measurements of synthetic mixture of all reactants.

According to Yoon's mechanism [Cis15, also shown in Scheme 3.3 in Chapter 3], the lifetime of the excited NDI-A and the radical anion yield should remain unaffected by the increase in the concentration of **BrMal**. The high turnover observed in the *N,N*-dimethyl-*p*-toluidine experiment by Yoon is therefore not as they interpreted due to an improvement in the efficiency of chain initiation, rather than the concentration of the excited photocatalyst decreases in consequence of the presence of the efficient quencher *N,N*-dimethyl-*p*-toluidine. As a result of this, the **AmiR** predominantly reacts with **BrMal** rather than the excited photocatalyst, whereby the product formation pathway is primarily carried by radical chain

propagation. Therefore, the observation in the TA studies provides further evidence to support the kinetic studies in Chapter 3.

The pathways shown in Scheme 5.22 summarize the insights from thorough mechanistic investigations on the photoredox catalytic α -alkylation of octanal using NDI-A as the photoredox catalyst.



Scheme 5.22: Mechanism of the α -alkylation of octanal using NDI-A as the photoredox catalyst: the chain propagation in competition with the photoredox catalytic production.

6. Understanding photophysics-activity relationships in a triphenyl-arene platform for photocatalytic water splitting

6.1. Introduction

Photocatalytic water splitting is one of the most promising ways to convert solar energy into hydrogen (H_2), which can be used as a storable, environmentally benign and renewable fuel [Che17a]. Among the various photocatalysts used in light-induced water splitting, covalent organic frameworks (COFs) gain significant attention as highly promising H_2 evolution photocatalysts due to their unique properties: First, they possess high structural porosity and high crystallinity, which facilitates charge transport. Second, the covalent bonds in COFs provide very good chemical stability to the photocatalysts. In particular, the most remarkable advantage of COFs is that they possess chemical tunability down to the molecular level by engineering their building blocks [Ban18]. This was exemplified in the recent work undertaken by Lotsch and co-workers [Vya15]. They synthesized a series of azine-linked COFs from N_x -aldehydes with a varying number of nitrogen atoms (see Fig. 6.1). As a consequence of the increasing nitrogen content in the frameworks, H_2 evolution is dramatically enhanced from $23 \mu\text{mol h}^{-1}\text{g}^{-1}$ for N_0 -COF to $1703 \mu\text{mol h}^{-1}\text{g}^{-1}$ for N_3 -COF. They demonstrated that the optoelectronic and steric variations in the precursors can be transferred to the resulting COFs, thus leading to enhanced photocatalytic activity.

To understand why different N_x -COFs show very different photocatalytic activities, Lotsch and co-workers investigated the structure, optical and electronic properties of N_x -COFs and their precursors. They found that substitution of the C-H moiety with N atoms gradually decreased the dihedral angle between the central aryl ring and the peripheral phenyl rings. This results in a progressive increase of planarity in the COF building blocks, thus leading to a gradual increase in crystallinity with increasing N content. As a consequence of the improved crystallinity, more facile exciton migration is obtained not only within the COF plane but also along the axial direction. This interpretation agrees with the observed trend in photocatalytic activity.

In addition, based on the steady-state absorption spectra, they found that the N_x -COFs had essentially identical optical band gaps of 2.6 – 2.7 eV. They attributed this observation to the increase in electron-deficient character of the central aryl ring (red shift) acting against the increase in the degree of electronic conjugation (blue shift) along the series N_0 to N_3 .

Moreover, they performed calculation to obtain the change in band gaps and band positions for the N_x -COF series. They inferred that the photocatalytic pathway was likely reductive quenching of the photo-excited COFs, i.e. the sacrificial electron donor quenched the hole on the COFs, thus leading to a radical anionic state for the COFs. And the increase in the electron-poor character of the central aryl ring along the N_x series results in the increase of the stability of the radical anion, which supports the observed trend in the H_2 evolution activity of the COFs.

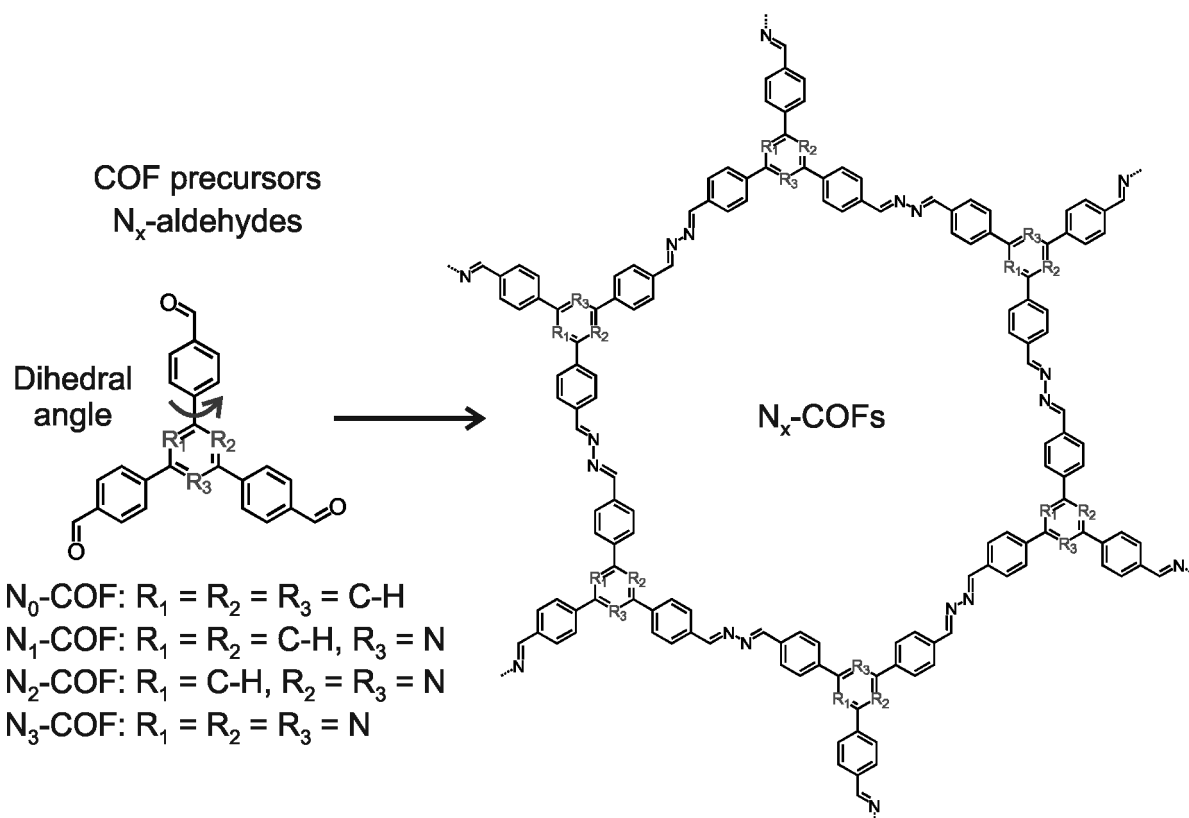


Fig. 6.1: Molecular structure of the N_x -COFs and their organic precursors N_x -aldehydes [Vya15].

Although several attempts to rationalize activity trends along the N_x -COF series have been made, there are still questions in need of further investigations. First, little is known about the photophysical properties of N_x -COFs, which is essential to understand the photoinduced processes during the photocatalytic water splitting. Second, the experimental evidence for the reductive quenching pathway in photocatalytic H_2 production is still lacking. The main challenge is that the time-resolved spectroscopic methods, which are usually employed in studying photophysics and photoinduced electron transfer processes, is limited to clear solutions (as opposed to the turbid solutions used in H_2 production) due to the problem with

light scattering. In order to overcome this difficulty and to gain insight into excited state dynamics of N_x -COFs, especially their role in the photocatalytic H_2 evolution, the N_x -COF building blocks are investigated in this work. They are organic compounds and can be well dissolved in solvents for preparing optically clear solutions. In addition, Lotsch and co-workers have demonstrated that the optoelectronic variation in the building blocks can be transferred to the resulting frameworks [Vya15]. Therefore, an adequate understanding of the excited state dynamics of the building blocks can provide a reliable way to infer the photophysics of N_x -COFs. A similar approach can be found in a theoretical study of the mechanism of light induced water splitting [Dom19].

In this chapter, a detailed spectroscopical investigation of the N_x -COF building blocks (N_x -Me) will be presented. It will start with the photophysical and photochemical properties of N_x -Me. In the second part, the properties of the N_x -Me radical anion generated via photoinduced electron transfer will be studied by using TA spectroscopy and energetics analysis.

6.2. Structure and steady-state characterization of N_x -Me

The molecular structure of the N_x -COF building blocks (N_x -Me) is shown in Fig. 6.2. As described before, the central aryl ring of N_x -Me is substituted progressively by nitrogen atoms, that is, the number of N atoms is $x = 0$ (phenyl), $x = 1$ (pyridyl), $x = 2$ (pyrimidyl) and $x = 3$ (triazine). In addition, Fig. 6.2 shows four structural analogues of N_x -Me, which are called N_x -TP. Instead of p-tolyl groups on the central ring, phenyl groups are used on the peripheral for N_x -TP. Due to the negligible change in the structure, many properties of N_x -Me are nearly the same as their analogues N_x -TP. The photophysical and redox properties of N_x -Me and N_x -TP are summarized in Table 6.1.

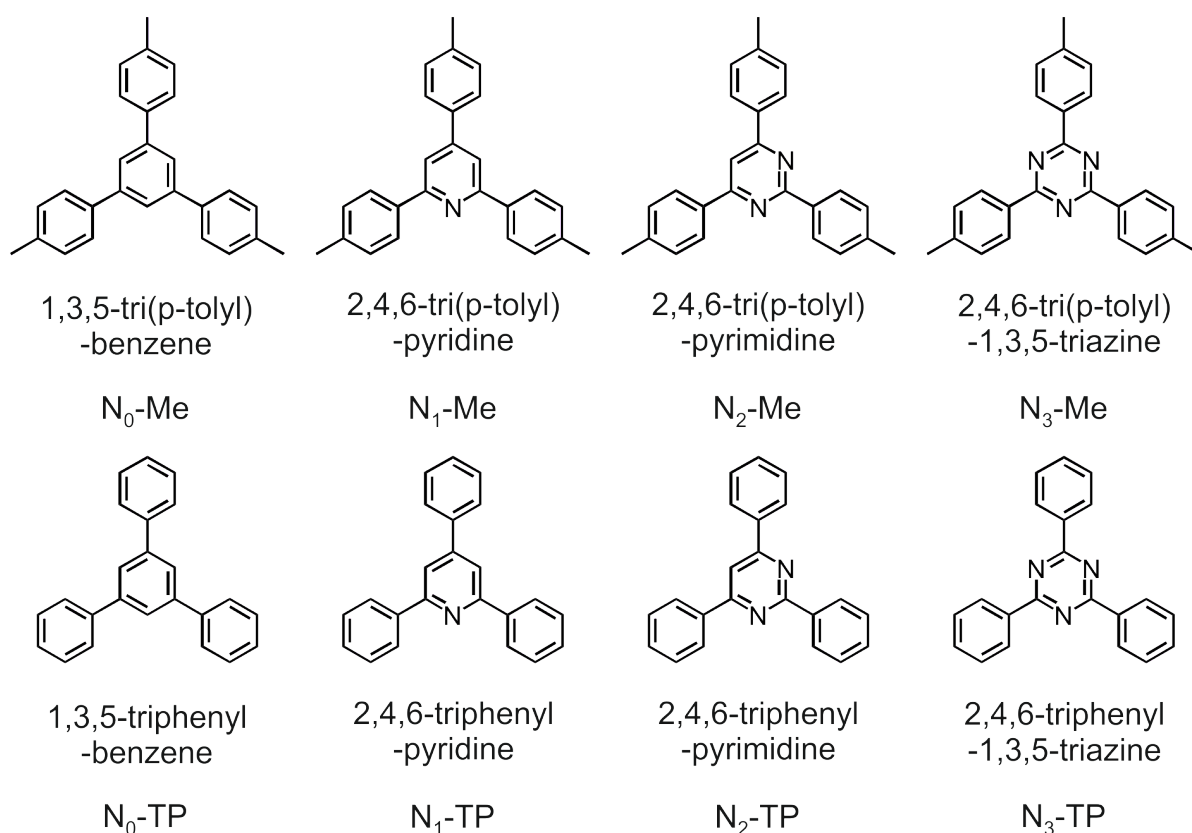


Fig. 6.2: Molecular structure of the N_x -COF building blocks (N_x -Me) and their structural analogues N_x -TP.

The steady-state absorption and emission spectra for the four compounds N_x -Me in the solvent dichloromethane (CH_2Cl_2) are shown in Fig. 6.3. Obviously, their UV-Vis absorption spectra are dependent on the structural symmetry of the molecule. The symmetrical N_0 and N_3 -Me show a dominate absorption band with the peak at 260 and 286 nm respectively, whereas the asymmetrical N_1 and N_2 -Me show two bands in their absorption spectra: a lower energy transition around 320 nm ($\epsilon_{\text{max}} \approx 1 - 1.5 \times 10^4 \text{ M}^{-1}\text{cm}^{-1}$)

and a more allowed transition around 270 nm ($\epsilon_{\max} \approx 5 \times 10^4 \text{ M}^{-1}\text{cm}^{-1}$). The similar absorption features are also observed in the absorption spectra of their analogues $\text{N}_x\text{-TP}$ (see Table 6.1).

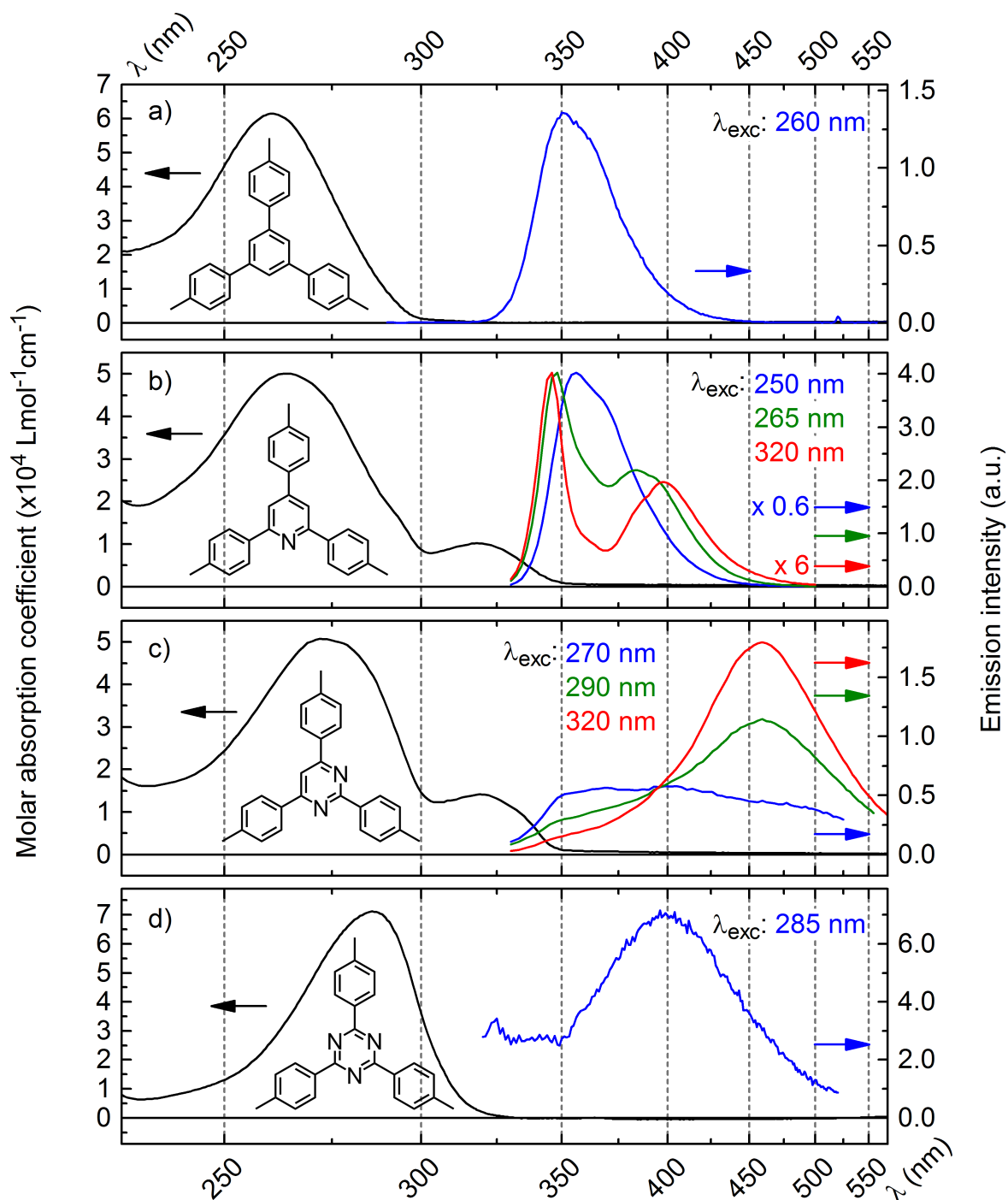


Fig. 6.3: Steady-state absorption and emission spectra of $\text{N}_x\text{-Me}$ in CH_2Cl_2 at room temperature. λ_{exc} shows the excitation wavelength for emission measurements. a) $10 \mu\text{M}$ $\text{N}_0\text{-Me}$ in 1 cm cuvette, b) $100 \mu\text{M}$ $\text{N}_1\text{-Me}$ in 1 mm cuvette, c) $100 \mu\text{M}$ $\text{N}_2\text{-Me}$ in 1 mm cuvette, d) $10 \mu\text{M}$ $\text{N}_3\text{-Me}$ in 1 cm cuvette.

From the emission spectra the dependence on the symmetry is also observed. The emission spectra of the symmetric N_0 and N_3 -Me show a mirror image of the corresponding absorption band. The form of the spectrum is irrespective of the excitation wavelength used (250-320 nm, see Fig A5.1 and A5.2 in Appendix A5). In contrast, the emission spectra of the asymmetric N_1 and N_2 -Me show an excitation wavelength dependent behavior. In the case of N_1 -Me, for an excitation wavelength at 250 nm, an emission band with a peak at 356 nm and a shoulder around 370 nm is observed. With increase of the excitation wavelength, the emission maximum is found to shift toward shorter wavelength while the shoulder appears red-shifted. When excited at higher wavelength (320 nm), a structured emission band with a peak at 346 nm and a shoulder around 400 nm becomes prominent. In the case of N_2 -Me, a two component emission is detected. For an excitation wavelength at 270 nm, a weak, unstructured emission band is observed. But when excited at 320 nm corresponding to the weak absorption band, a second emission band with a maximum at 460 nm becomes obvious. These observations in the case of N_1 and N_2 -Me don't fit with the well-established Kasha's rule, according to which the emission occurs irrespective of excitation band, always from the lowest electronic and vibrational state of the same multiplicity [Tur10]. The exception to this rule implies complex emission dynamics. These dynamics of N_1 and N_2 -Me will be discussed in more detail later.

The excited state energy of the first singlet excited state (E_{00}^S) of N_x -Me is estimated from the intersection of the fluorescence and absorption spectra (see Table 6.1). Like the N_x -COFs they show similar optical band gaps, all four N_x -Me have essentially identical E_{00}^S of around 3.7-3.9 eV. These results are very similar to those of N_x -TP reported in the literature. In addition, no significant difference between the N_0 -TP triplet energy and N_3 -TP triplet energy is found ($E_{00}^T = 2.8$ and 3.0 eV respectively). Thus, it is assumed that the E_{00}^T of N_0 and N_3 -Me are also essentially identical. And the E_{00}^T of N_0 and N_3 -TP are used to estimate the E_{00}^T of N_0 and N_3 -Me respectively.

The reduction potential (E_{red}) of N_3 -Me is almost identical to that of N_3 -TP (-1.67 V for N_3 -Me and -1.69 V for N_3 -TP). Furthermore, the E_{red} gradually decreases along the series N_0 to N_3 -TP, which emphasizes the increase in the electron-deficient character of the central aryl ring. In addition, in line with the molecular orbitals for the model systems of N_x -COF, the highest occupied molecular orbital (HOMO) and the lowest unoccupied molecular orbital (LUMO) energy show a decrease from N_0 to N_3 -TP. This trend is likewise found by comparing the HOMO and LUMO energy of N_0 -Me with those of N_3 -Me. All these results

support once more the hypothesis that the properties of N_x -TP provide a reliable estimate for those of N_x -Me.

Another important feature of the N_x -building blocks is the fluorescence quantum yield (Φ_{fluo}). With the increase in the N content, excitation of N_x -TP results in a lower and lower Φ_{fluo} from 26% to a value smaller than 0.1%. The decrease in the Φ_{fluo} along the series N_0 to N_3 corresponds to a decrease in the lifetime of the emitting state, indicating an enhancement of the efficiency of ultrafast non-radiative deactivation pathways. Further evidence for the ultrafast emitting state decay will be provided by the fluorescence decay measurements and the TA measurements.

Table 6.1: Photophysical and redox properties of N_x -Me and N_x -TP

Compd.	λ_{abs} (nm)	$\lambda_{\text{emi}} (\lambda_{\text{exc}})$ (nm)	E_{00}^S (eV)	E_{00}^T (eV)	E_{red} (V)	HOMO (eV)	LUMO (eV)	Φ_{fluo}
N_0 -Me	260	350 (260)	3.87	-	-	-5.8 ^a	-0.7 ^a	-
N_0 -TP	252 ^b	350 ^b	3.89 ^c	2.79 ^c	-2.68 ^c	-5.61	-1.72	26% ^d
N_1 -Me	264 318	348 (265)	3.67	-	-	-	-	-
N_1 -TP	265 318 ^e	359 (263) ^e	3.72 ^e	-	-2.16	-6.36	-2.64 ^e	25% ^f
N_2 -Me	272 319	~ 355 (270) 460 (320)	3.66	-	-	-	-	-
N_2 -TP	265 318 ^g	381 ^g	-	-	-2.21 ^g	-	-2.59	0.14% ^g
N_3 -Me	286	400 (285)	3.72	-	-1.67 ^h	-6.4 ^a -6.85	-1.6 ^a -3.13	-
N_3 -TP	271 ⁱ	-	4.07 ^j	3.02 ^j	-1.69 ^k	-6.62 ^j -6.78	-1.79 ^j -2.71	< 0.1%

λ_{abs} : absorption peaks; λ_{emi} : emission peaks; λ_{exc} : excitation wavelength; E_{00}^S : energy of the first singlet excited state; E_{00}^T : energy of the first triplet excited state; E_{red} : reduction potential against saturated calomel electrode (SCE); LUMO: from LUMO = -4.8 eV - E_{red} (Fc) and $E_{\text{Fc}} = E_{\text{SCE}} - 0.40$ V; HOMO: from HOMO = LUMO - E_{00}^S ; Φ_{fluo} : fluorescence quantum yield; a. obtained from DFT calculation; b. [Uda92]; c. [Cai04]; d. [Nij95]; e. [Ran16]; f. [Kur89]; g. [Ita04]; h. [Gar09]; i. [Wan18a]; j. [Sha17]; k. [Fin97].

6.3. Excited state kinetics of N_x -Me

To gain a better insight into the excited state dynamics of N_x -Me, fs- μ s TA measurements of N_x -Me are performed. Fig. 6.4 shows the TA spectra probed at times from 20 fs to 10 μ s after 270 nm excitation for N_x -Me in CH_2Cl_2 under aerated condition. In addition, the decay-associated difference spectra (DADS), obtained by global analysis of the corresponding data, are depicted in Fig. 6.5, together with the decay constants.

Immediately after excitation, the TA spectra of N_0 -Me consist of a broad excited state absorption (ESA) band with a peak at 468 nm. The corresponding species appears to decay rapidly within 200 fs and can be assigned to the S_2 excited state. The decay of the S_2 state is accompanied by the concomitant growth of an absorption which shows a peak at 310 nm and a broad band around 600 nm. This ESA band can be assigned to the S_1 - S_n absorption. In addition to the population of the S_1 state, a weak red-shift of its ESA band is observed within the first picosecond. Furthermore, the rising time of the S_1 state population is considerably longer than the lifetime of the S_2 state. Using global analysis, it is shown that the S_1 - S_n band (peaking at 310 nm) rises with a time constants of 17.6 ps, while the S_2 state exhibits a much shorter lifetime of \sim 200 fs. These results can be explained in terms of two parallel pathways of S_2 state depopulation: a minor part decays to form the S_1 state, while another major pathway leads to population of a new state, which then also decays to form the S_1 state. The new state lying between the S_1 and S_2 state can be assigned to a transition from the vibrationally hot singlet state populated by the S_2 - S_1 internal conversion. A similar observation was previously reported in the studies of carotenoids [Pol04, Ant10].

The ESA band of the S_1 state does not decay on the timescale of the fs-ps TA experiment (up to 1.5 ns). In the ns- μ s TA experiment, the S_1 state decays with a lifetime of 16 ns and gives rise to a TA spectrum with maxima at 350 and 510 nm. A slightly negative band is observed below 300 nm, which is due to ground state bleaching. Using global analysis, the resulting DADS associated with the 16 ns decay shows a negative part from 350 to 510 nm, indicating a direct transition between these two transients. Therefore, this species is assigned to the T_1 state of N_0 -Me, which has a lifetime of 475 ns. No residual spectrum is observed after the decay of the T_1 state.

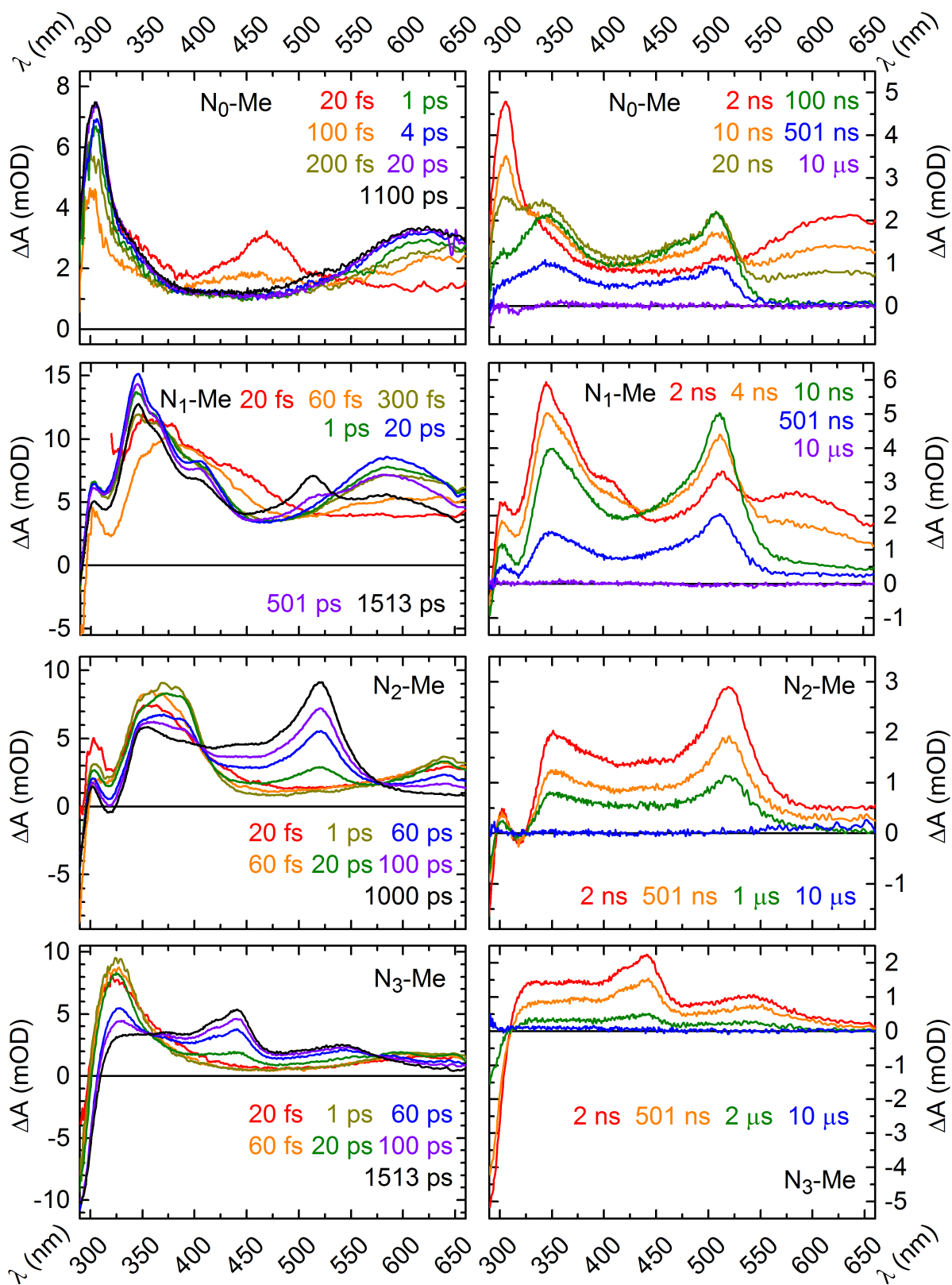


Fig. 6.4: Spectral signatures of photo-generated intermediates on the fs-μs timescale. Transient absorption spectra obtained from N₀, N₁, N₂ and N₃-Me (from top to bottom) in CH₂Cl₂ using an excitation wavelength of 270 nm. (The experiment conditions are detailed in Table A5.1 and A5.2 in Appendix A5.)

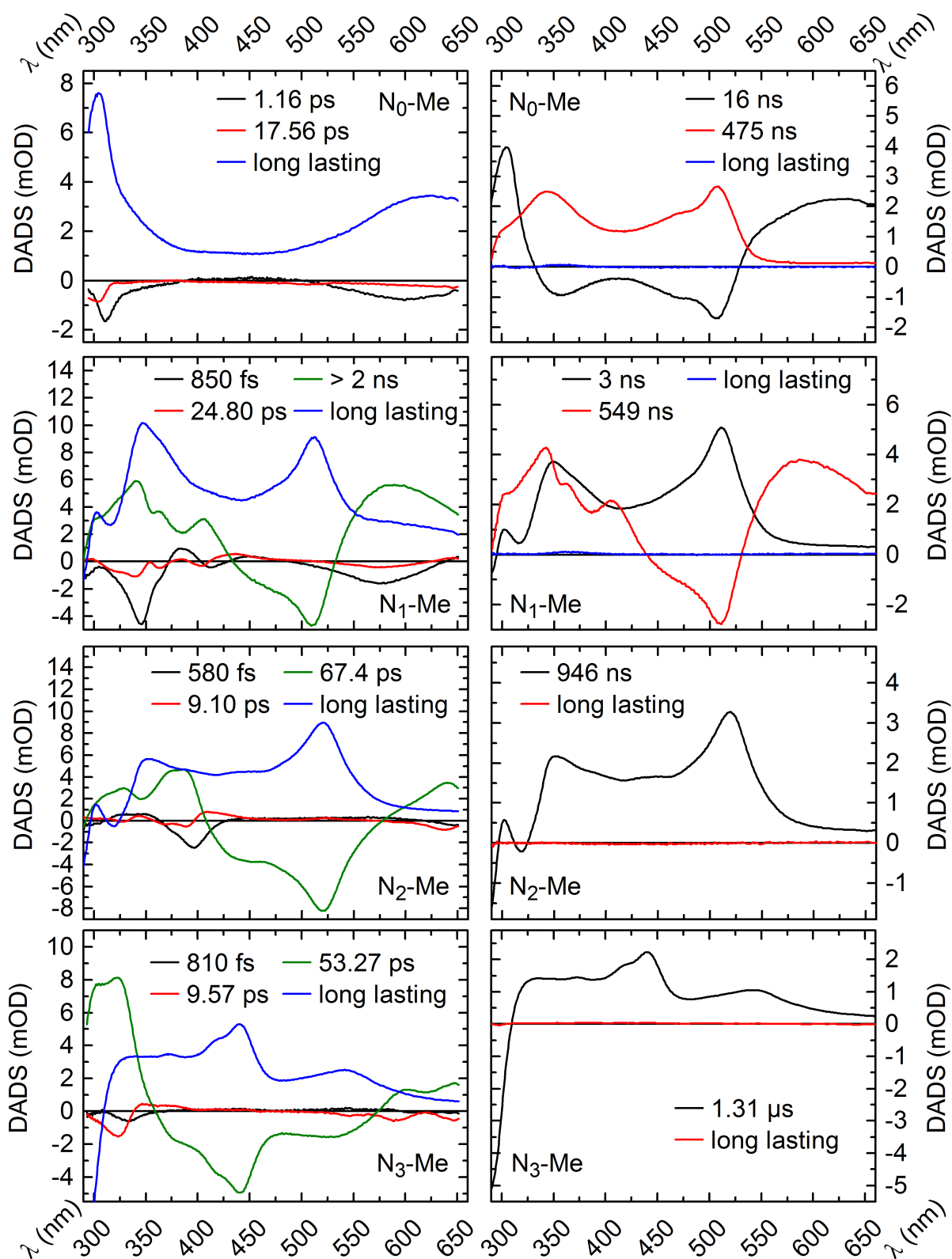


Fig. 6.5: Decay associated difference spectra (DADS) of a global fit to the TA data of N_0 , N_1 , N_2 and N_3 -Me (from top to bottom) in Fig. 6.4.

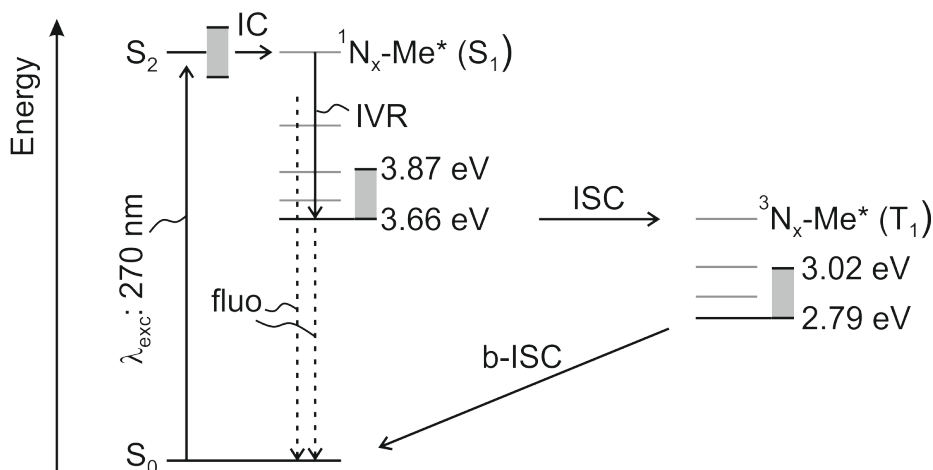


Fig. 6.6: Energy diagram with a range of excited state energies extending from N_0 to N_3 -Me. The energies estimated as described in the text and Table 6.1 (λ_{exc} : absorption; fluo: fluorescence; IC: internal conversion; IVR: intramolecular vibrational redistribution; ISC: intersystem crossing; b-ISC: back intersystem crossing).

Compared with the TA measurement results for N_0 -Me, the TA data for N_1 , N_2 and N_3 -Me show the same relaxation pathways after 270 nm excitation but distinct differences in excited state lifetimes. The excited state dynamics of N_x -Me are summarized in an energy level diagram given in Scheme 6.6. Upon photoexcitation of N_x -Me the S_2 state is formed, which decays rapidly to form the S_1 state and the vibrationally hot singlet state. Then the hot singlet state also populates the S_1 state with a time constant of ~ 10 -20 ps. Afterwards the T_1 state is generated via intersystem crossing (ISC) from the S_1 state. No long-lived species is observed after the decay of the T_1 state.

The lifetimes of the N_x -Me excited states are summarized in Table 6.2. What can be clearly seen in this table is the significant decrease in the lifetimes of the S_1 state along the N_x series. The S_1 state lifetimes decrease from 16 ns for N_0 -Me to 3 ns, 67.4 ps, and finally to 53.3 ps for N_1 , N_2 , and N_3 -Me, respectively. This trend is in line with the experimentally observed fluorescence lifetimes. Further analysis shows that there is a gradual increase in the efficiency of ISC (Φ_{ISC}) and the ISC rate constants (k_{ISC}) along the series N_0 to N_3 . On the one hand this finding indicates that the increased k_{ISC} contributes to the decrease in the S_1 state lifetimes. On the other hand the increase in Φ_{ISC} underlines the fact that more molecules in their T_1 state are populated along the N_x series. As mentioned in the Chapter 5, the charge recombination after the triplet state electron transfer (ET) process is significantly

Table 6.2: Results of the analysis to the TA data for N_x-Me after excitation at different wavelengths. τ_{fluor} : lifetime of fluorescence, τ_{S_1} : lifetime of S₁, τ_{T_1} : lifetime of T₁, Φ_{ISC} : quantum yield of intersystem crossing (also used as synonymous with quantum yield of formation of T₁), k_{ISC} : intersystem crossing rate constants obtained from $\Phi_{\text{ISC}}/\tau_{\text{S}_1}$.

Compd.	τ_{fluor}	$\tau_{\text{S}_1} (\lambda_{\text{exc}})$ (air)	$\tau_{\text{T}_1} (\lambda_{\text{exc}})$ (air)	τ_{T_1} (deaerated)	Φ_{ISC}	k_{ISC} (s ⁻¹)
N ₀ -Me	15.4ns	16ns	475ns	4.2 μ s	~50%	3.1 $\times 10^7$
N ₁ -Me	2.9ns	3ns (270nm) 3ns (320nm)	549ns (270nm) 554ns (320nm)	no data	63% 65%	2.1 $\times 10^8$
N ₂ -Me	-	67.4ps (270nm) 63.0ps (330nm)	946ns (270nm) 971ns (320nm)	no data	84% 87%	1.3 $\times 10^{10}$
N ₃ -Me	< 62.5ps	53.3ps	1.3 μ s	5.8 μ s	92%	1.7 $\times 10^{10}$

slowed down due to the spin forbidden rule, and then the efficiency of the next reaction step is enhanced. Thus, the increase in the population of the T₁ state indicates that the ET quenching of the excited N_x-Me by the sacrificial electron donor becomes more and more efficient along the series N₀ to N₃. This trend is fully consistent with the reported increase in the H₂ evolution activity [Vya15].

In addition, a significant increase in the lifetimes of the T₁ state is observed along the N_x series. Under deaerated conditions, the lifetimes of the T₁ state are considerably longer than that observed in air-saturated solutions. Compared with the change of N₃-Me triplet state lifetime from 1.3 to 5.8 μ s, the increase of N₀-Me triplet state lifetime is larger, which is from 475 ns to 4.2 μ s. This finding suggests that quenching of the N₀-Me triplet state by oxygen is more efficient than that for N₃-Me. These observations indicate that non-product pathways such as quenching by oxygen are more efficient for N₀-Me than for N₃-Me, which is also in line with the reported trend in N_x-COF photocatalytic activity [Vya15].

Interestingly, no significant differences in the lifetimes of the S₁ and T₁ state are found between the excitation wavelength at 270 and 320/330 nm for N₁ and N₂-Me. Especially, there is no evidence that these different excitation wavelengths (270 and 320/330 nm) have a significant influence on the quantum yield of triplet state Φ_{ISC} . Thus, the excitation wavelength dependent fluorescence observed in the steady-state measurements is not caused by the S₁ state emission behavior. Due to the observation of the higher excited singlet states

in the TA experiments, it is inferred that the N_1 and N_2 -Me fluorescence spectra for excitation at different wavelengths could result from the combination of the S_0 - S_1 and S_0 - S_2 electronic relaxation. Such ultrafast emitting dynamics could be investigated in detail by using femtosecond time-resolved fluorescence spectroscopy. Since the main interest is on the lifetimes of the S_1 and T_1 state of the molecules under study, detailed determinations of the nature of the S_n fluorescence fall outside the scope of this thesis.

According to the proposed kinetic model given in Fig 6.6, species associated difference spectra (SADS) are constructed using the DADS from the global analysis (see Fig. 6.7). As expected, the SADS of S_1 state of N_x -Me can be easily distinguished from their SADS of T_1 state because of the particular spectral features. The spectra of the N_x -Me excited states will be employed in the further studies on the ET process between the excited N_x -Me and the sacrificial electron donor for accurate identification of them. And the lifetimes of these N_x -Me excited states will be used for the further analysis in the ET process studies.

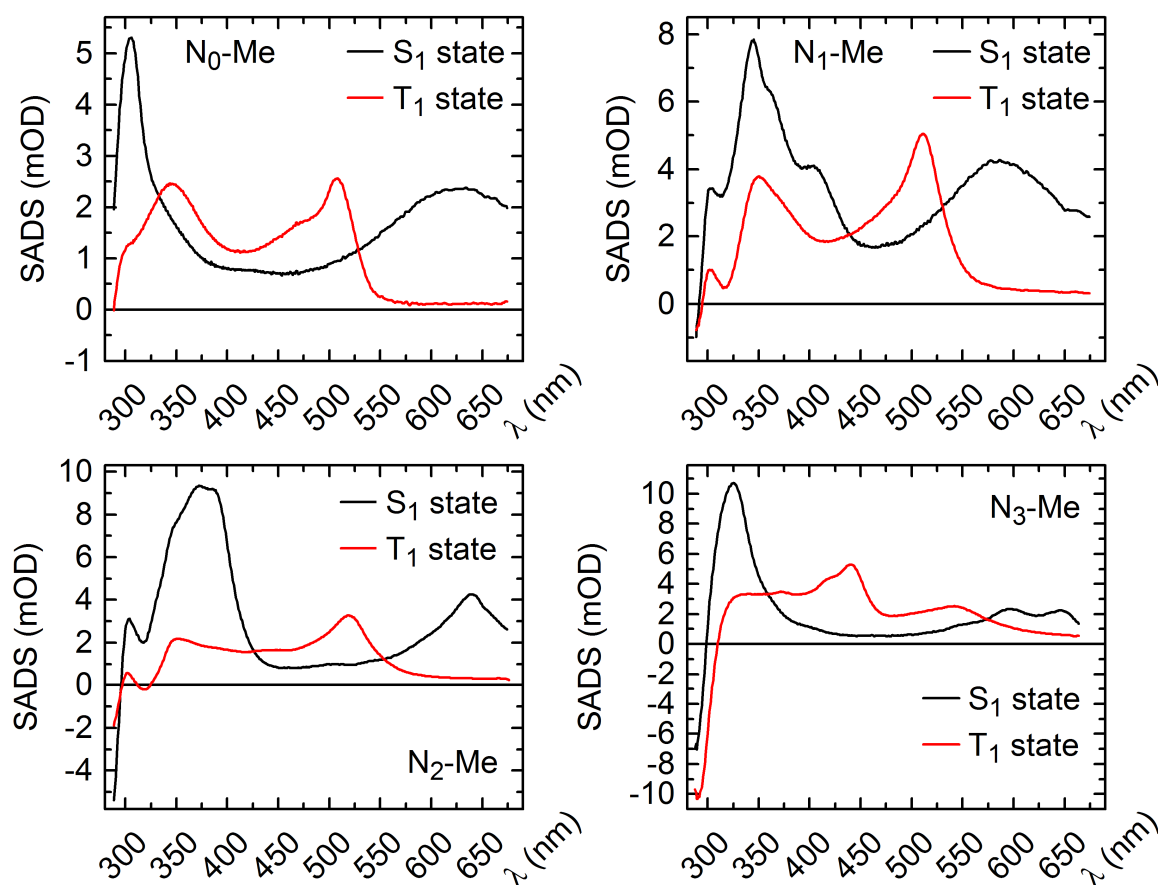


Fig. 6.7: Species associated difference spectra (SADS) obtained from the analysis assuming the kinetic model given in Fig. 6.6.

6.4. N_x -Me excited state interactions with TEA

After the characterization of the ground and excited state properties of N_x -Me, the ET processes between an excited N_x -Me and a sacrificial electron donor are investigated. To aid in the generation of radical anions of N_x -Me, *N,N*-diethylethanamine (TEA) is used as sacrificial electron donor [Wan13]. According to the historical results [Mon06], the quenching with TEA primarily occurs via a reductive electron transfer mechanism. The absorption of TEA at the pump wavelength of 270 nm is negligible (with a molar absorption coefficient of $\sim 7 \text{ M}^{-1}\text{cm}^{-1}$) and does not pester the optical excitation of N_x -Me.

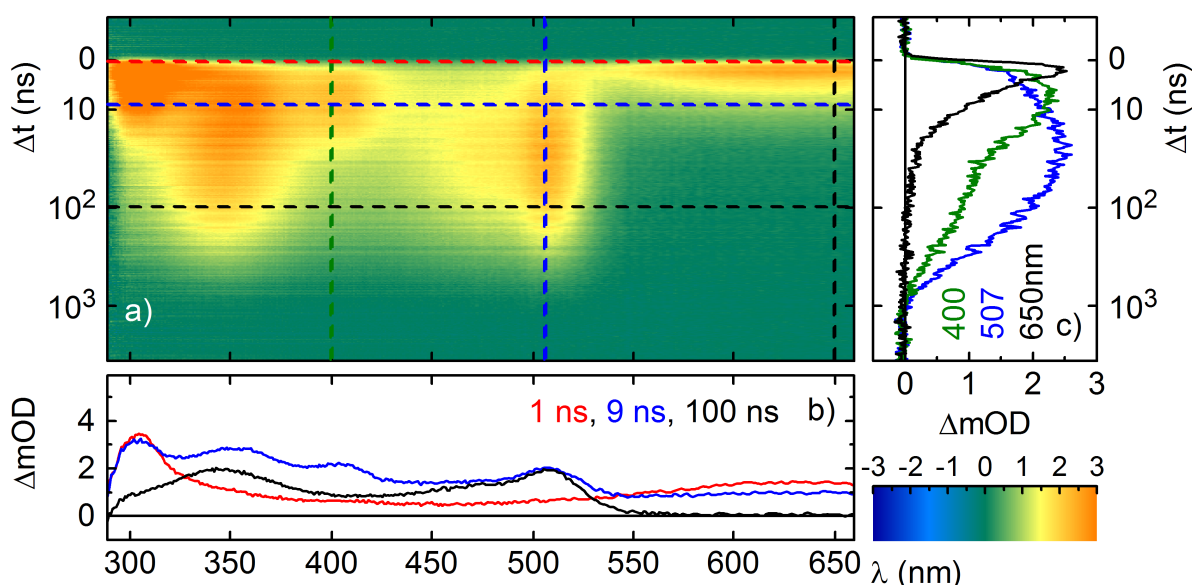


Fig. 6.8: Time-resolved absorption spectra of a N_0 -Me solution in the presence of TEA. a) ns- μ s TA: 1 mM N_0 -Me and 50 mM TEA in a 0.1 mm cuvette after 270 nm excitation with pump intensity of 0.4 mJ/cm^2 ; b) TA spectra recorded at several time delays after excitation; c) Kinetic for the dynamics of different species at selected wavelengths.

Upon 270 nm excitation of a N_0 -Me solution in the presence of TEA, the S_1 state is found to be quenched, whereas no quenching process of the T_1 state is observed. Shown in Fig. 6.8 are the ns- μ s TA spectra observed upon excitation at 270 nm of a N_0 -Me solution containing 50 mM TEA. Concomitant with the decay of the S_1 state at 650 nm, a new transient at 400 nm is observed to grow in. Fig 6.8c shows the concomitant growth of this transient with the S_1 state decay. Meanwhile, the T_1 state of N_0 -Me is populated via ISC from the S_1 state, which could compete with the reaction between the S_1 state and TEA. Following the decay of the T_1 state, no characteristic ESA bands and GSB signals are observable, indicating that

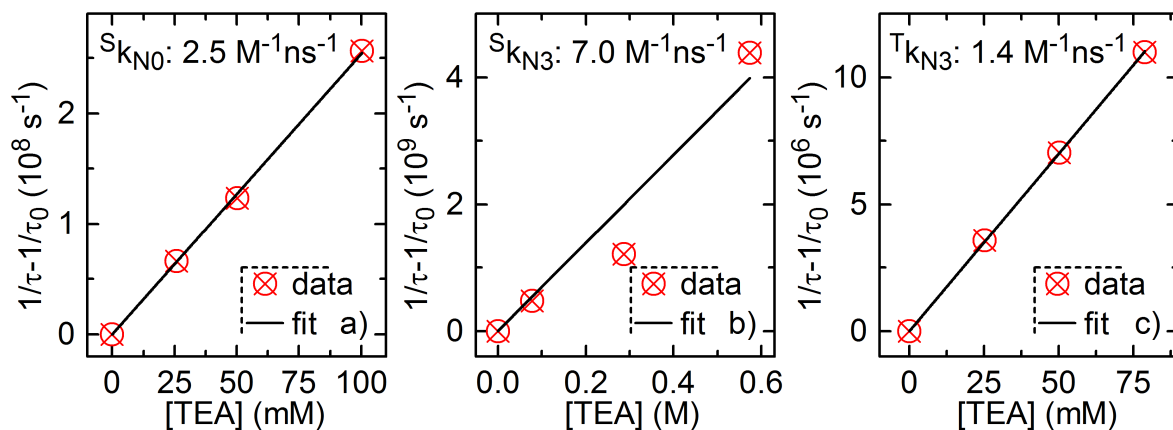


Fig. 6.11: First-order kinetic plots of the TEA concentration dependence study for a) 1.0 mM N_0 -Me and b, c) 1.2 mM N_3 -Me. The solid lines represent linear fits.

the spectra obtained in the TA experiments in the absence of TEA. As the SADS of the second species resembles strongly the absorption spectrum of the radical anion of N_0 -TP generated by radiolysis [Shi88], this species is interpreted as the radical anion ($N_0\text{-Me}^{\bullet-}$) of N_0 -Me.

Having located the spectroscopic signature of $N_0\text{-Me}^{\bullet-}$, its formation is tracked for a series of solutions with different concentrations of TEA. The observed first-order growth of the product or concomitant decay of the singlet is linear with TEA concentration (see Fig. 6.11), consistent with Stern-Volmer kinetics (eq 6.1, [Mon06])

$$\frac{1}{\tau} - \frac{1}{\tau_0} = S_{k_{N_0}} [\text{TEA}] \quad (6.1)$$

with τ_0 and τ being the lifetimes of the S_1 state of N_0 -Me in the absence and presence of TEA. The bimolecular rate constant ($S_{k_{N_0}}$) for ET from TEA to the S_1 state of N_0 -Me, obtained from the slope of this plot, is given as $S_{k_{N_0}} = 2.5 \times 10^9 \text{ M}^{-1}\text{s}^{-1}$.

In contrast to the case of N_0 -Me, the T_1 state quenching is observed upon 270 nm excitation of a N_3 -Me solution in the presence of TEA. Fig. 6.12a1, a2 shows the fs-ps and ns- μ s TA spectra observed upon excitation at 270 nm of a N_3 -Me solution containing 79 mM TEA. The fs-ps TA spectra are almost the same as those detected in the absence of TEA. In the ns- μ s TA spectra, the formation of a new transient is concomitant with the T_1 state decay. This product of N_3 -Me quenching by the TEA is attributed to the one electron reduced form of the N_3 -Me ($N_3\text{-Me}^{\bullet-}$). Its formation is also tracked for a series of solutions with different concentrations of TEA and the kinetics are fitted to a dissociative ET model with a first-order rate constant $T_{k_{N_3}}[\text{TEA}]$. The resulting bimolecular quenching plot is linear (see

Fig. 6.11c), and affords a bimolecular rate constant of $^T k_{N_3} = 1.4 \times 10^9 \text{ M}^{-1} \text{ s}^{-1}$.

For $N_3\text{-Me}$, a slight S_1 state quenching is observed when high concentrations of TEA are employed. At the TEA concentration of 0.57 M, the S_1 state has a lifetime of 43 ps, and it decays simultaneously to the triplet state and to another unassigned state with a lifetime of 300 ps (see Fig. 6.14). Following the decay of the triplet state, the $N_3\text{-Me}^{\bullet-}$ spectrum is observed. Because this unknown species is not observed in the absence of TEA, it might be a complex generated by the ET process from TEA to the S_1 state of $N_3\text{-Me}$. By fitting the kinetics to a first-order model $S_{k_{N_3}}[\text{TEA}]$, the bimolecular rate constant is given as $S_{k_{N_3}} = 7.0 \times 10^9 \text{ M}^{-1} \text{ s}^{-1}$ (see Fig. 6.11b).

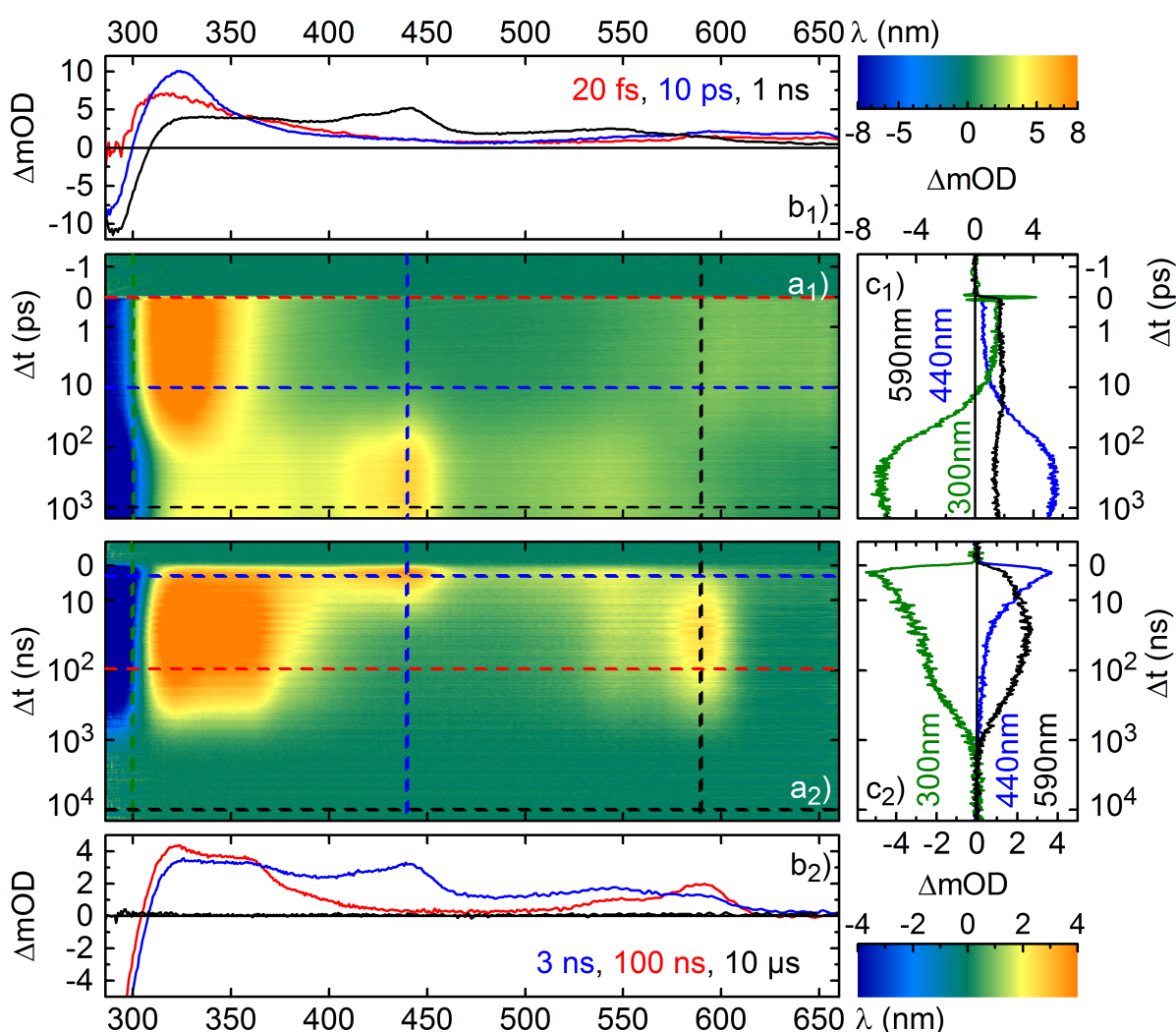


Fig. 6.12: Time-resolved absorption spectra of a $N_3\text{-Me}$ solution in the presence of TEA. a1,a2) fs- μs TA: 1.2 mM $N_3\text{-Me}$ and 79 mM TEA in a 0.1 mm cuvette after 270 nm excitation with pump intensity of 0.4 mJ/cm^2 ; b1,b2) TA spectra recorded at several time delays after excitation; c1,c2) Kinetic for the dynamics of different species at selected wavelengths.

Compared with the ISC rate constant of $N_3\text{-Me}$, the rate constant of the singlet state electron transfer is ~ 4 times smaller (in the case of $[\text{TEA}] = 0.57 \text{ M}$), indicating that most of the $N_3\text{-Me}$ in the S_1 state decays to its T_1 state via ISC. It is also supported by the triplet yield estimate, in which the triplet yield is found in the case of 0.57 M TEA employed ($\sim 83\%$) compared with that without TEA (92%).

A proposed kinetic model including the singlet and triplet ET processes is represented in Fig 6.13 based on the observation in the TA experiments. In Fig. 6.13, singlet excited states of $N_3\text{-Me}$ are produced upon light excitation. A fraction of the S_1 state is diffusionally quenched by TEA to form solvated ion pairs, and some of S_1 populates the T_1 state via ISC. These ion pairs are susceptible to charge recombination and repopulate the ground states of $N_3\text{-Me}$ and neutral TEA. The T_1 state can also be quenched by TEA to form “free” $N_3\text{-Me}^{\bullet-}$ radical anions and TEA radical cations. Without further reactions in which $N_3\text{-Me}^{\bullet-}$ is consumed, the $N_3\text{-Me}^{\bullet-}$ regenerates its ground state via back electron transfer to the TEA radical cation.

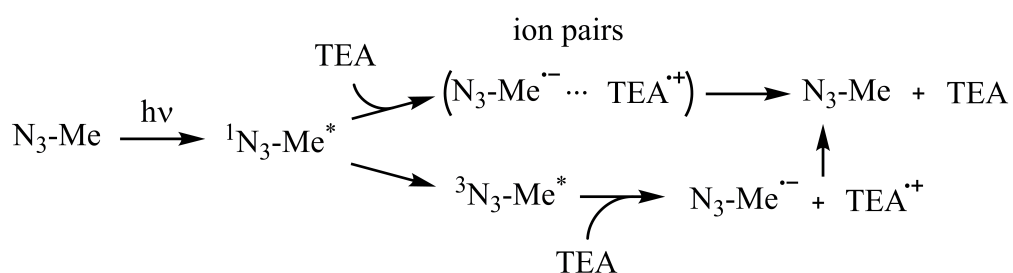


Fig. 6.13: Scheme of the reduction mechanism of the excited $N_3\text{-Me}$ in the presence of TEA.

According to the proposed kinetic model given in Fig. 6.13, SADS are constructed and shown in Fig. 6.14 (the rate constants are summarized in Table A5.4 in Appendix A5). The SADS of the S_1 and T_1 state are consistent with the spectra obtained in the TA experiments in the absence of TEA. Moreover, the SADS of $N_3\text{-Me}^{\bullet-}$ can be easily distinguished from their SADS of S_1 and T_1 because of the particular spectral features at 360 and 590 nm. Compared with the SADS of S_1 , the SADS of ion pairs appearing after S_1 also shows a distinct spectral feature around 360 nm, which is similar to the SADS of the free radical anion.

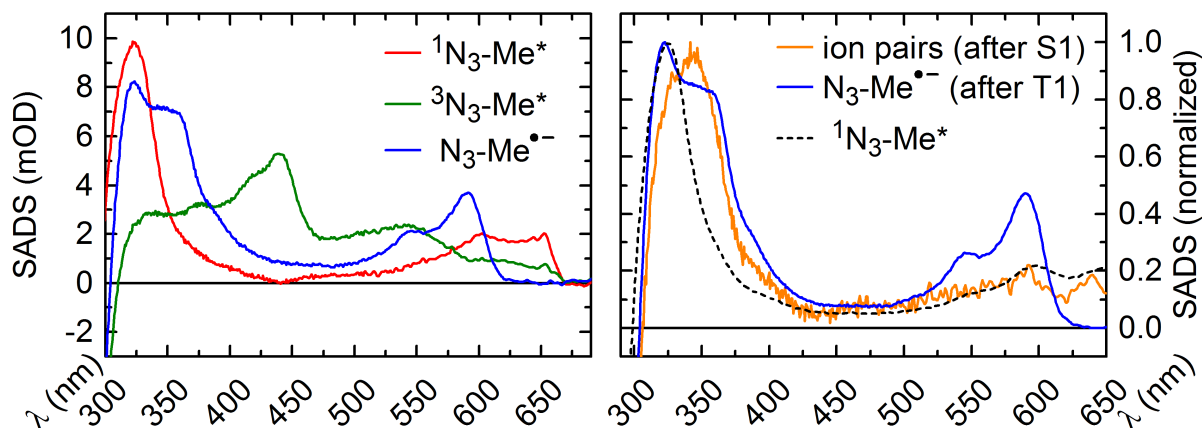


Fig. 6.14: a) Species associated difference spectra (SADS) resulting from the proposed model in Fig. 6.13. b) Difference in SADS between the N_3 -Me singlet excited state ($^1N_x\text{-Me}^*$), ion pairs obtained after the S_1 state and N_3 -Me radical anion. The spectra have been normalized to the ESA maximum.

The rate constants for N_0 and N_3 -Me ($S_{k_{N_0}}$, $S_{k_{N_3}}$ and $T_{k_{N_3}}$) are slower than the diffusion-controlled rate coefficient, estimated to be $\sim 1.6 \times 10^{10} \text{ M}^{-1}\text{s}^{-1}$ in CH_2Cl_2 [Mon06]. This indicates that the rate-limiting step is the electron transfer process itself. To understand the thermodynamics of the ET reactions, the energy needed for the ET processes is calculated. Using the oxidation potentials reported in ref. [Mon06] with 0.96 V and the redox potentials of $N_x\text{-Me}$ listed in Table 6.1, the thermodynamic driving force for forward electron transfer from the TEA to the excited state can be estimated from the eq 6.2.

$$\Delta G_{\text{ET}}^0 = e \cdot \left[E\left(\text{TEA}^{\bullet+} / \text{TEA}\right) - E\left(N_x\text{-Me} / N_x\text{-Me}^{\bullet-}\right) \right] - E_{00} + \frac{z\left(\text{TEA}^{\bullet+}\right)z\left(N_x\text{-Me}^{\bullet-}\right)e^2}{4\pi\epsilon_0\epsilon_r a} \quad (6.2)$$

In eq 6.2, the first two terms are the standard electrode potential of TEA radical cation and $N_x\text{-Me}$ radical anion, respectively. E_{00} shows the energy of the excited state who takes part in the reaction. The last term accounts for the effect of Coulombic attraction in the redox products. Treating the redox products as point charges with the charges located at the center, the distance of the two charged species (a) could be estimated to be of the order of 10 Å. Thus, the electrostatic interaction term is estimated to be 0.16 eV. By using this estimate, the free energy change for the forward ET from the TEA to the $N_x\text{-Me}$ excited state is approximated and summarized in Table 6.3.

Table 6.3: Energetics and rate constants for photoinduced electron transfer.

Compd.	E_{00}^S (eV)	E_{00}^T (eV)	ΔG_{ET}^S (eV)	ΔG_{ET}^T (eV)	S_k ($M^{-1}s^{-1}$)	T_k ($M^{-1}s^{-1}$)
N ₀ -Me	3.87	2.79	-0.07	1.01	2.5×10^9	-
N ₃ -Me	3.72	3.02	-0.93	-0.23	7.0×10^9	1.4×10^9

As can be seen from the Table 6.3, the trend of increasing rate constants for ET reaction (S_k) with increasing free energy change ($-\Delta G_{ET}^S$) of N₀-Me < N₃-Me is consistent with ET in the Marcus normal region [Mon06]. And it is apparent from this table that the reduction of the T₁ state of N₀-Me by TEA should be endothermic ($\Delta G_{ET}^T = 1.01$ eV > 0) and is therefore unfavorable. This explains the fact that the ET reaction between the T₁ state of N₀-Me and TEA is not observed in the TA experiment. In addition, the ET process from TEA to the T₁ state of N₃-Me is thermodynamically feasible, but this process is quite slow due to a small free energy change value ($\Delta G_{ET}^T = -0.23$ eV).

The observed N_x-Me excited state electron transfer processes can also rationalize the trend in the photocatalytic activity across the series of N_x-COFs in ref. [Vya15]. In the study of N_x-COFs photocatalysis, triethanolamine (TEoA) was used as sacrificial electron donor. Compared with the oxidation potential of TEA, the potential of TEoA is slightly smaller with 0.90 V [Mon06]. Thus, the driving force for forward electron transfer from the TEoA to the excited N_x-Me nodes in COFs is almost the same as that for TEA summarized in Table 6.3. This indicates that the ¹N₀-Me* (S₁) rather than ³N₀-Me* (T₁) is indeed responsible for electron acceptor, because the reduction of ³N₀-Me* (T₁) is endothermic. In contrast, the ³N₃-Me* (T₁) rather than ¹N₃-Me* (S₁) produces the radical anionic state for the COF. And as mentioned above, the spin flip required for charge recombination processes within triplet derived ionic state is expected to slow this process down, thus favoring the competitive diffusion process of the exciton generated in N₃-COF. This finding is fully in line with the observed trend in H₂ evolution activity and provides important evidence of the radical anion pathway inferred in ref. [Vya15].

7. Summary and Outlook

Photocatalysis, which utilizes light as a “reagent” in combination with photocatalysts, is more and more attractive for developing previously unattainable chemical transformations with mild conditions and for harvesting the “unlimited” solar energy by splitting water. Advances in this area have mainly been guided by empirical findings rather than a thorough mechanistic understanding of photophysical and photochemical processes [Kön17, Buz19]. One reason is that easily implemented experimental techniques are lacking in synthetic laboratories [Meg10, Pit15]. In addition, it is widely believed that the spectroscopic techniques relevant to mechanistic investigations are only proper to study processes under idealized conditions rather than under synthetically relevant conditions [Maj14, Buz19].

Thus, in this thesis the effort has been dedicated to developing chemist-friendly devices (QYDS and LED pulser) and practical methods for using transient absorption (TA) spectroscopy in the investigation of synthetic reactions. QYDS and LED pulser can be easily implemented in a synthetic laboratory. TA spectroscopic quenching experiments can provide a detailed insight into the photoinduced processes occurring after light absorption. In order to highlight how mechanistically relevant information can be acquired by using these setups, two representative photocatalytic transformations, the photoredox organocatalytic enantioselective α -alkylation of aldehydes and the photocatalytic water splitting were investigated. This thesis has highlighted that the combination of quantum yield determination methods and transient absorption spectroscopy can provide a powerful tool to generate a comprehensive mechanistic picture of these two photocatalytic reactions. Undoubtedly, the detailed knowledge of the mechanistical intricacies will benefit the improvement of existing reaction efficiency and the design of new transformations.

Experimental and interpretation methods

In order to probe a chain-propagating mechanism, the quantum yield determination setup (QYDS) and its accessory, the LED Pulser have been described. The QYDS allows the facile and exact determination of the quantum yield for photochemical reactions in a synthesis laboratory environment. The commercially available LEDs used in the QYDS cover the desired wavelength regions (from 255 to 1050 nm) and have already been widely used in many photochemical laboratories [Kög13]. Moreover, the use of LED light sources allows us to easily control irradiation conditions, for instance, modification of light power by

changing the LED drive current. In addition, besides the LED, the QYDS consists of a lens system, an electronically controlled shutter and a commercially available powermeter (or a calibrated solar cell). These carefully selected optical, electronic and mechanical components are easily learned how to use. And this ensures that chemists with little experience in optics can also perform a precise measurement.

The use of LEDs provides the additional possibility to easily irradiate a sample intermittently. A simple extension of the QYDS turns it into a proper tool, i.e. a LED light pulse generator (LED Pulser) for light-off / light-on experiments. The LED Pulser allows detection of very short-lived chains, which are generally terminated in micro- or milliseconds when the illumination is turned off [Pit15]. The LED Pulser is gated by a logic signal, which is generated by a digital oscilloscope. Thus, the pulse duration and repetition frequency can be easily modified through the oscilloscope software. Moreover, the pulse power can be adjusted by the LED drive current knob. As well as the operation mode between “continuous wave” and pulsed light can be simply changed by means of a switch on the box. A 470 nm LED was used to characterize the LED Pulser. With 4 A supplied to the LED, the peak power of light reached ~ 1.4 W. By optimizing the electrical input pulse, a light pulse as short as 2.3 μs was generated.

In order to detect and characterize transient intermediates in photocatalysis, fs and ns transient absorption spectrometers of our own design have been described. Using single-shot referencing to cancel fluctuations of the probe light, the sensitivity of our TA spectrometer was increased by at least a factor of five down to 20 μOD [Bra14]. This allows for the recording of species with small transition strengths. Moreover, by using SHG/THG of the fundamental beam or a NIR-OPA before the supercontinuum stage, the spectral range of the probe light became tunable from 225 up to 1700 nm [Rie13]. The ultrabroad probing range makes it possible to follow, in a single measurement and in real time, the dynamics of the GSB recovery as well as the redox state, since these species of interest present transitions in this accessible probing range. In addition, the overall temporal resolution of sub-50 fs allows us to resolve ultrafast molecular processes [Meg09]. Furthermore, by using an ns pulse generated by the EKSPLA OPO, the temporal range was extended up to about 1 millisecond [Mat13]. This allows us to record TA spectra in the nano- to microsecond regime, in which many relevant photochemical processes show extensive dynamics.

The analysis methods of TA spectral data have been presented and some of their limitations

have been pointed out in this thesis. Questions are often asked in the data analysis procedures: How many kinetic components can be separated in a TA measurement, how can you prove that you don't resolve too many components? These questions reveal a fact that the analysis in terms of the number of kinetic components involves the unreliable guess. In order to minimize the influence of the contrived judgement, the maximum entropy method [Kut13] has been applied in this thesis to obtain a reasonable estimate of the component number and the relevant lifetimes. Similar analysis procedures, such as lifetime density method [Cro01] and logarithmic differentiation of the absorption changes method (LDAC) [Sat03], have also been applied in the other research groups to achieve the same purpose.

It has been shown that the application of the data analysis methods depends on the system under study and on the details of experiments. Therefore, it is advantageous to conduct "due diligence" before the experiments. "Due diligence" refers to the research done before performing TA measurements in order to collect information from external sources, e.g., reviewing literature, evaluating light-absorbing species by other spectroscopic methods, or determining the excited state energy of chromophores computationally. This knowledge can be used in the planning of a TA experiment in order to ensure optimal results for the data analysis.

Mechanistic studies on the photoredox organocatalytic α -alkylation of aldehydes

A detailed mechanistic investigation of the photoredox organocatalytic α -alkylation of aldehydes has been carried out by combining the quantum yield measurements and the TA spectroscopy. Using our QYDS, the reaction quantum yield has been determined in a time dependent way at the light powers from 30 μ W to 10 mW. The results presented that the quantum yield of α -alkylation reaction must be considered as a function of irradiation power and time. The maximum value of the reaction quantum yield in all measurements was achieved at the lowest light power with a value of 3500%. The values of the maximum reaction quantum yield at each light power were proportional to the reciprocal square root of the light power. Furthermore, the reaction quantum yield was not always higher than 100%. The reaction quantum yields determined at a light power higher than 20 mW were all below 100%.

This new observation thus provided a convincing explanation for previous reported quantum yield of the same reaction by the Yoon group with a value of 1800% [Cis15] and by the

König/Riedle groups with a value of 49% [Meg10]. In the previous studies the measurements of the reaction quantum yield were performed with a constant light power and for a fixed irradiation time. Because they employed different light powers and their results were measured at distinct time, they observed only the individual part of our new reaction quantum yield results.

Light power-dependent QY measurements suggested the proceeding mechanism of this reaction depends on the light power. Therefore, a new mechanism has been proposed: the radical chain reaction dominates for low light power, whereas the photocatalytic mechanism plays the main role for high power. A detailed chemical kinetic analysis of our new mechanism has been carried out. Based on the measured values of the reaction quantum yield, all the rate constants were reasonably estimated. The simulation results were in good agreement with the experiments. In addition, the lag phase observed in the measurements with low light power also appeared in the simulation with our mechanism. Nevertheless, using the mechanism suggested by the Yoon group, this initiation phase disappeared in the simulation. Therefore, the reaction mechanism proposed by the Yoon group can be ruled out due to the presence of the initiation phase in our measurements. The most surprising aspect of the simulation was that the addition of a photocatalyst-quencher could result in a significant increase of the rate of product formation. This finding was also observed in the experiment reported in ref. [Cis15].

In order to demonstrate the occurrence of the radical chain processes in the α -alkylation reaction, the intermittent illumination experiments have been performed by using our LED-Pulser. The rate ratio of the average product rate under intermittent illumination to the product rate under continuous illumination has been determined. Based on the theory described by Shepp [She56], the average lifetime of the radical (i.e. chain time) has been estimated as 23 μ s. In addition, the small dispersion of the measured ratio indicated that the radical recombination rate is much smaller than the rate of the first-order radical reaction. This was consistent with the observation in the experiments.

Using a naphthalene diimide (NDI-A) as the photocatalyst, the photophysical and photochemical dynamics in the α -alkylation reaction have been probed with transient absorption spectroscopy.

Firstly, the ground and excited state properties of NDI-A have been characterized, which is essential to understand the photochemical processes during the photoredox catalytic cycle.

Very similar absorption spectra of the NDI-A have been observed in different solvents, while the emission spectra show solvent-dependence. Especially, the emission of the NDI-A in DMF was very weak, indicating an ultrafast emission quenching process. In addition, the H-aggregation of the NDI-A in CH₂Cl₂ has been detected by the emission measurements when the concentration of the NDI-A was high. After the characterization of the ground state properties of NDI-A, its excited-state kinetics have been studied in CH₂Cl₂, DMF and CH₂Cl₂/DMF mixture. In CH₂Cl₂, a forward and backward intersystem crossing process between the singlet (S₁) and triplet state (T₄) has been observed, which is consistent with the observation reported in ref. [Yus15]. The recovery of the NDI-A ground state accounts completely for the decay of the triplet state (T₁). In DMF, the lifetime of the NDI-A singlet state is particularly short compared with that in CH₂Cl₂. The NDI-A radical anion was detected after the decay of the singlet state, indicating that the electron transfer quenching of the singlet state gives rise to the weak fluorescence of NDI-A in DMF. In CH₂Cl₂/DMF mixture, a bimolecular photoinduced electron transfer from DMF to the NDI-A triplet state has been demonstrated. Studies of the DMF concentration dependence with NDI-A in CH₂Cl₂ afforded a bimolecular rate coefficient of $9.8 \times 10^4 \text{ M}^{-1}\text{s}^{-1}$. In the absence of a quencher of the radical anion, the lifetime of the NDI-A radical anion is 68.6 μs .

Secondly, the reaction steps in the photoredox catalytic α -alkylation reaction have been investigated through tracking the forming and quenching of the NDI-A singlet state, triplet state and radical anion under selective influence of the individual reactants. The investigation of the NDI-A excited state quenching process in the presence of the individual reactants has shown that the enamine possesses the largest quenching rate constant. This finding clearly indicates that the initiation of the catalysis is essentially caused by the quenching of the excited photocatalyst by enamine, which was also suggested in the literature [Nic08, Cis15, Bah16]. The major finding was that, under the same condition of synthetic catalysis, with increasing concentration of bromomalonate the lifetime of the NDI-A triplet state increased and the radical anion yield decreased. The increase in the bromomalonate concentration results in a higher probability of the oxidation of the amino radical by bromomalonate, which is reflected equally in the increase of the lifetime of the NDI-A triplet state and in the lower radical anion yield. Therefore, this observation in the TA studies provides further evidence to support our mechanism containing the competition between the radical-chain process and the photoredox catalysis.

Taken together, these results provide a new understanding of the fundamental mechanism of photocatalysis. A complex relationship between different product-forming reaction pathways was revealed. On the one hand, the radical chain propagation requires a continuous photoinduced initiation. On the other hand, the chain process is also inhibited by a photoinduced competitive pathway with increasing light power. This inhibition process also represents a product formation pathway which could be a closed photoredox catalysis cycle. These results are of fundamental importance for photocatalysis and would encourage the development of new excited-state reactivities in the field of organic synthesis that are enabled by light harvesting.

Mechanistic studies on COFs based photocatalytic water splitting

Four structurally related building blocks of covalent organic frameworks (COFs), which show tunability in photocatalytic hydrogen evolution from water, have been investigated. The previous studies by my co-workers indicated that the photocatalytic hydrogen evolution increases progressively with the increase in the nitrogen content in the aryl ring of the COFs. An in-depth understanding of the factors responsible for this trend has been developed in this thesis.

Using transient spectroscopy, the generation of the photoactive species from femtoseconds to microseconds after light absorption was monitored and their yields and lifetimes were correlated with the photocatalytic activity. Four building blocks N_x -Me show almost the same relaxation pathways after light excitation. Upon photoexcitation their higher singlet excited state (S_2) is formed. Then the lowest singlet excited state (S_1) is populated. Afterwards the lowest triplet state (T_1) is generated via intersystem crossing (ISC) from the S_1 state. No long-lived species were observed after the decay of the T_1 state. The analysis of TA data showed that the quantum yield of T_1 formation, the ISC rate constants as well as the lifetimes of T_1 state increase gradually along the series N_0 to N_3 . The more molecules at their T_1 state are populated and the longer their T_1 lifetimes are, the more efficient the next electron transfer quenching of the excited N_x -Me by the sacrificial electron donor can be. Therefore, these trends are fully consistent with the increase in the H_2 evolution activity.

In addition, the electron transfer processes between the excited N_x -Me and the sacrificial electron donor – *N,N*-diethylethanamine (TEA) – have been investigated. The observation of the radical anion of N_0 and N_3 -Me provided direct spectroscopic evidence for the reductive quenching pathway in the photocatalytic H_2 production. A notable result was that the N_0 -Me

singlet excited state (S_1) is the responsible electron acceptor, whereas the N_3 -Me triplet excited state (T_1) produces the major part of radical anions. Calculations of redox potentials and charge transfer free energies demonstrated that the reduction of the N_0 -Me triplet excited state (T_1) by TEA is endothermic, while the ET process from TEA to the N_3 -Me triplet excited state (T_1) is thermodynamically feasible. The reduction of the triplet manifold leads to the production of long-lived radical anions, which also rationalizes the observed difference in the H_2 evolution activity along the series N_0 to N_3 .

Overall, these studies suggested that multiple factors influence the efficiency of photo-induced proton reduction in the COFs in this series. The considerations such as steady-state spectral absorption as well as structure properties have been the dominant paradigm to date in the photocatalyst design. In this thesis other important factors that dictate the photocatalytic activity have been highlighted. To design photocatalysts for water splitting, it is also important to consider the nature of the excited states of photocatalysts and the driving forces for photoinduced electron transfer steps. For this purpose transient absorption spectroscopy has been demonstrated to be an appropriate tool.

In future, the technical difficulty in the quantum yield determination of the COF-based photocatalytic water splitting reaction should be resolved. Because the COFs are insoluble in water, the solutions used in H_2 production are turbid. The unclear solutions lead to strong light scattering, which so far significantly decreases the high degree of precision in the determination of the absorbed photon number by using our QYDS. Therefore, further developments of the QYDS are required. The difficulty may be overcome with the use of a spherical detector. This detector consists of a spherical cavity with an aperture for the incident light. Mounted on the inside structure are solar cells that detect light from the scattering. Measuring the power of the incident light in comparison to the power of the light scattered could render the absorbed illumination power.

8. References

- [Ada95] M. Adachi, Y. Murata and S. Nakamura, "*Spectral similarity and difference of naphthalenetetracarboxylic dianhydride, perylenetetracarboxylic dianhydride, and their derivatives*," J. Phys. Chem. **99**, 14240-14246 (1995).
- [AlK16] M. Al Kobaisi, S. V. Bhosale, K. Latham, A. M. Raynor and S. V. Bhosale, "*Functional naphthalene diimides: synthesis, properties, and applications*," Chem. Rev. **116**, 11685-11796 (2016).
- [Alb09] A. N. Alba, M. Viciano and R. Rios, "*The Holy Grail of Organocatalysis: Intermolecular α -Alkylation of Aldehydes*," ChemCatChem **1**, 437-439 (2009).
- [And04] G. Andric, J. F. Boas, A. M. Bond, G. D. Fallon, K. P. Ghiggino, C. F. Hogan, J. A. Hutchison, M. A.-P. Lee, S. J. Langford and J. R. Pilbrow, "*Spectroscopy of naphthalene diimides and their anion radicals*," Aust. J. Chem. **57**, 1011-1019 (2004).
- [Ant10] M. R. Antognazza, L. L uer, D. Polli, R. L. Christensen, R. R. Schrock, G. Lanzani and G. Cerullo, "*Ultrafast excited state relaxation in long-chain polyenes*," Chem. Phys. **373**, 115-121 (2010).
- [Art92] T. Arthen-Engeland, T. Bultmann, N. P. Ernsting, M. Rodriguez and W. Thiel, "*Singlet excited-state intramolecular proton transfer in 2-(2'-hydroxyphenyl) benzoxazole: spectroscopy at low temperatures, femtosecond transient absorption, and MNDO calculations*," Chem. Phys. **163**, 43-53 (1992).
- [Ave97] B. M. Aveline, S. Matsugo and R. W. Redmond, "*Photochemical mechanisms responsible for the versatile application of naphthalimides and naphthal-diimides in biological systems*," J. Am. Chem. Soc. **119**, 11785-11795 (1997).
- [Bah16] A. Bahamonde and P. Melchiorre, "*Mechanism of the stereoselective α -alkylation of aldehydes driven by the photochemical activity of enamines*," J. Am. Chem. Soc. **138**, 8019-8030 (2016).
- [Ban18] T. Banerjee, K. Gottschling, G. k. Savasci, C. Ochsenfeld and B. V. Lotsch, "*H₂ evolution with covalent organic framework photocatalysts*," ACS Energy Lett. **3**, 400-409 (2018).
- [Bar97] T. C. Barros, S. Brochsztain, V. G. Toscano, P. Berci Filho and M. J. Politi, "*Photophysical characterization of a 1,4,5,8-naphthalenediimide derivative*," J. Photochem. Photobiol. A **111**, 97-104 (1997).

- [Bau18] "Time resolved broadband spectroscopy from UV to NIR." B. Baudisch doctoral thesis at the LMU Munich (2018), https://edoc.ub.uni-muenchen.de/21902/1/Baudisch_Bastian.pdf
- [Bla14] "Molecular mechanisms of photosynthesis," R. E. Blankenship, (John Wiley & Sons, 2014).
- [Bow79] M. J. Bowden, "Formation of macromolecules," In "Macromolecules, an Introduction to Polymer Science," F. A. Bovey and F. H. Winslow(eds.), (Academic Press, Inc., 1979), pp 23-202.
- [Bra09] M. Bradler, P. Baum and E. Riedle, "Femtosecond continuum generation in bulk laser host materials with sub- μ J pump pulses," Appl. Phys. B **97**, 561 (2009).
- [Bra14] M. Bradler and E. Riedle, "Temporal and spectral correlations in bulk continua and improved use in transient spectroscopy," J. Opt. Soc. Am. B **31**, 1465-1475 (2014).
- [Bri26] F. Briers, D. L. Chapman and E. Walters, "LXXVII.—The influence of the intensity of illumination on the velocity of photochemical changes. The determination of the mean life of a hypothetical catalyst," J. Chem. Soc. (Resumed) **129**, 562-569 (1926).
- [Bur47] G. Burnett and H. W. Melville, "Determination of the velocity coefficients for polymerization processes.-I. The direct photopolymerization of vinyl acetate," Proc. R. Soc. A **189**, 456-480 (1947).
- [Buz19] L. Buzzetti, G. E. M. Crisenza and P. Melchiorre, "Mechanistic Studies in Photocatalysis," Angew. Chem. Int. Ed. **58**, 3730 – 3747 (2019).
- [Cai04] X. Cai, M. Sakamoto, M. Hara, S. Tojo, K. Kawai, M. Endo, M. Fujitsuka and T. Majima, "Transient phenomena of polyphenyls in the higher triplet excited state," J. Phys. Chem. A **108**, 9361-9364 (2004).
- [Cam07] S. Campagna, F. Puntoriero, F. Nastasi, G. Bergamini and V. Balzani, "Photochemistry and photophysics of coordination compounds: ruthenium," Top. Curr. Chem. **280**, 117-214 (2007).
- [Cas83] J. V. Caspar and T. J. Meyer, "Photochemistry of tris(2,2'-bipyridine) ruthenium ion ($Ru(bpy)_3^{2+}$). Solvent effects," J. Am. Chem. Soc. **105**, 5583-5590 (1983).
- [Cer03] G. Cerullo and S. De Silvestri, "Ultrafast optical parametric amplifiers," Rev. Sci. Instrum. **74**, 1-18 (2003).
- [Che17a] S. Chen, T. Takata and K. Domen, "Particulate photocatalysts for overall water splitting," Nat. Rev. Mater. **2**, 1-17 (2017).

- [Che17b] M. Chergui and J. M. Thomas, "From structure to structural dynamics: Ahmed Zewail's legacy," *Struct. Dyn.* **4**, 043802 (2017).
- [Cie04] P. Cieřła, P. Kocot, P. Mytych and Z. Stasicka, "Homogeneous photocatalysis by transition metal complexes in the environment," *J. Mol. Catal. A: Chem.* **224**, 17-33 (2004).
- [Cis15] M. A. Cismesia and T. P. Yoon, "Characterizing chain processes in visible light photoredox catalysis," *Chem. Sci.* **6**, 5426-5434 (2015).
- [Cro01] R. Croce, M. G. Müller, R. Bassi and A. R. Holzwarth, "Carotenoid-to-Chlorophyll Energy Transfer in Recombinant Major Light-Harvesting Complex (LHCII) of Higher Plants. I. Femtosecond Transient Absorption Measurements," *Biophys. J.* **80**, 901-915 (2001).
- [Cub01] M. S. Cubberley and B. L. Iverson, "¹H NMR investigation of solvent effects in aromatic stacking interactions," *J. Am. Chem. Soc.* **123**, 7560-7563 (2001).
- [Dam97] N. H. Damrauer, G. Cerullo, A. Yeh, T. R. Bousie, C. V. Shank and J. K. McCusker, "Femtosecond dynamics of excited-state evolution in [Ru(bpy)₃]²⁺," *Science* **275**, 54-57 (1997).
- [Dan91] G. J. Daniell, "Of maps and monkeys: an introduction to the maximum entropy method," In "Maximum entropy in action," B. Buck and V. A. Macaulay(eds.), (Oxford University Press, Oxford, 1991), pp 1-18.
- [Dem88] S. Demmig and H. Langhals, "Leichtlösliche, lichtechte Perylen-Fluoreszenzfarbstoffe," *Chem. Ber.* **121**, 225-230 (1988).
- [Dic41] "Photochemistry of gases," R. G. Dickinson, (Reinhold Pub. Corp., 1941).
- [Dob10] A. Dobryakov, S. A. Kovalenko, A. Weigel, J. L. Pérez-Lustres, J. Lange, A. Müller and N. Ernsting, "Femtosecond pump/supercontinuum-probe spectroscopy: Optimized setup and signal analysis for single-shot spectral referencing," *Rev. Sci. Instrum.* **81**, 113106 (2010).
- [Dom19] W. Domcke, J. Ehrmaier and A. L. Sobolewski, "Solar Energy Harvesting with Carbon Nitrides and N-Heterocyclic Frameworks: Do We Understand the Mechanism?," *ChemPhotoChem* **3**, 10-23 (2019).
- [Eig54] M. Eigen, "Methods for investigation of ionic reactions in aqueous solutions with half-times as short as 10⁻⁹ sec. Application to neutralization and hydrolysis reactions," *Discuss. Faraday Soc.* **17**, 194-205 (1954).
- [Ert05] Ş. Erten, Y. Posokhov, S. Alp and S. İçli, "The study of the solubility of naphthalene diimides with various bulky flanking substituents in different solvents by UV-vis spectroscopy," *Dyes. Pigm.* **64**, 171-178 (2005).

- [Ess07] A. J. Esswein and D. G. Nocera, "*Hydrogen production by molecular photocatalysis*," Chem. Rev. **107**, 4022-4047 (2007).
- [Fag07] M. Fagnoni, D. Dondi, D. Ravelli and A. Albini, "*Photocatalysis for the Formation of the C–C Bond*," Chem. Rev. **107**, 2725-2756 (2007).
- [Fel13] C. Feldmeier, H. Bartling, E. Riedle and R. M. Gschwind, "*LED based NMR illumination device for mechanistic studies on photochemical reactions–Versatile and simple, yet surprisingly powerful*," J. Magn. Reson. **232**, 39-44 (2013).
- [Fin97] R. Fink, C. Frenz, M. Thelakkat and H.-W. Schmidt, "*Synthesis and characterization of aromatic poly(1,3,5-triazine-ether)s for electroluminescent devices*," Macromolecules **30**, 8177-8181 (1997).
- [Fit06] P. Fita, E. Luzina, T. Dziembowska, C. Radzewicz and A. Grabowska, "*Chemistry, photophysics, and ultrafast kinetics of two structurally related Schiff bases containing the naphthalene or quinoline ring*," J. Chem. Phys. **125**, 184508 (2006).
- [Fle76] G. R. Fleming, J. M. Morris and G. W. Robinson, "*Direct observation of rotational diffusion by picosecond spectroscopy*," Chem. Phys. **17**, 91-100 (1976).
- [Gan07] P. Ganesan, J. Baggerman, H. Zhang, E. J. Sudhölter and H. Zuilhof, "*Femtosecond time-resolved photophysics of 1, 4, 5, 8-naphthalene diimides*," J. Phys. Chem. A **111**, 6151-6156 (2007).
- [Gar09] A. I. García, B. Insuasty, M. A. n. Herranz, R. Martínez-Álvarez and N. Martín, "*New building block for C₃ symmetry molecules: synthesis of S-triazine-based redox active chromophores*," Org. Lett. **11**, 5398-5401 (2009).
- [Gol04] "*World Energy Assessment: Update of the Overview to Energy and the Challenge of Sustainability in 2000*," J. Goldemberg and T. B. Johansson(eds.), (United Nations Development Programme, New York, 2004).
- [Gre95] S. Green and M. A. Fox, "*Intramolecular photoinduced electron transfer from nitroxyl radicals*," J. Phys. Chem. **99**, 14752-14757 (1995).
- [Hes18] N. J. Hestand and F. C. Spano, "*Expanded theory of H- and J-molecular aggregates: the effects of vibronic coupling and intermolecular charge transfer*," Chem. Rev. **118**, 7069-7163 (2018).
- [Hol96a] A. Holzwarth and M. G. Müller, "*Energetics and kinetics of radical pairs in reaction centers from Rhodobacter sphaeroides. A femtosecond transient absorption study*," Biochemistry **35**, 11820-11831 (1996).

- [Hol96b] A. R. Holzwarth, "Data analysis of time-resolved measurements," In "Biophysical techniques in photosynthesis," J. Amesz and A. J. Hoff(eds.), (Springer, 1996), pp 75-92.
- [Hom11] C. Homann, N. Krebs and E. Riedle, "Convenient pulse length measurement of sub-20-fs pulses down to the deep UV via two-photon absorption in bulk material," Appl. Phys. B **104**, 783 (2011).
- [Hor95] M. Horng, J. Gardecki, A. Papazyan and M. Maroncelli, "Subpicosecond measurements of polar solvation dynamics: coumarin 153 revisited," J. Phys. Chem. **99**, 17311-17337 (1995).
- [Hub01] R. Huber, H. Satzger, W. Zinth and J. Wachtveitl, "Noncollinear optical parametric amplifiers with output parameters improved by the application of a white light continuum generated in CaF₂," Opt. Commun. **194**, 443-448 (2001).
- [Ing97] K. Ingold, "Kinetic and mechanistic studies of free radical reactions in the 21st century," Pure Appl. Chem. **69**, 241-244 (1997).
- [Ita04] K. Itami, D. Yamazaki and J.-i. Yoshida, "Pyrimidine-core extended π -systems: general synthesis and interesting fluorescent properties," J. Am. Chem. Soc. **126**, 15396-15397 (2004).
- [IUPAC14] "IUPAC. Compendium of chemical terminology - the Gold Book, Version 2.3.3," 2005 - 2014, <https://goldbook.iupac.org/files/pdf/goldbook.pdf>
- [Jou04] A. Jouyban, S. Soltanpour and H.-K. Chan, "A simple relationship between dielectric constant of mixed solvents with solvent composition and temperature," Int. J. Pharm. **269**, 353-360 (2004).
- [Jul83] M. Julliard and M. Chanon, "Photoelectron-transfer catalysis: its connections with thermal and electrochemical analogs," Chem. Rev. **83**, 425-506 (1983).
- [Kal82] K. Kalyanasundaram, "Photophysics, photochemistry and solar energy conversion with tris(bipyridyl) ruthenium (II) and its analogues," Coord. Chem. Rev. **46**, 159-244 (1982).
- [Kär15] M. D. Kärkäs, B. S. Matsuura and C. R. Stephenson, "Enchained by visible light-mediated photoredox catalysis," Science **349**, 1285-1286 (2015).
- [Kas52] M. Kasha, "Collisional perturbation of spin-orbital coupling and the mechanism of fluorescence quenching. A visual demonstration of the perturbation," J. Chem. Phys. **20**, 71-74 (1952).
- [Kas65] M. Kasha, H. R. Rawls and M. A. El-Bayoumi, "The exciton model in molecular spectroscopy," Pure Appl. Chem. **11**, 371-392 (1965).

- [Kav93] *"Fundamentals of photoinduced electron transfer,"* G. J. Kavarnos, (VCH Publishers, 1993).
- [Kön13] *"Chemical Photocatalysis,"* B. König(ed. (Walter de Gruyter GmbH & Co. KG, 2013).
- [Kön17] B. König, *"Photocatalysis in organic synthesis—past, present, and future,"* Eur. J. Org. Chem. **2017**, 1979-1981 (2017).
- [Koz04] I. Z. Kozma, P. Baum, U. Schmidhammer, S. Lochbrunner and E. Riedle, *"Compact autocorrelator for the online measurement of tunable 10 femtosecond pulses,"* Rev. Sci. Instrum. **75**, 2323-2327 (2004).
- [Kur89] A. Kurfürst, P. Lhoták, M. Petrú and J. Kuthan, *"Oligophenylene 2,4,6-tri-arylpyridines and analogous diaza-p-terphenyls, diaza-p-quaterphenyls and diaza-p-quinquephenyls with luminiscent activity,"* Collect. Czech. Chem. Commun. **54**, 462-472 (1989).
- [Kut13] R.-J. Kutta, T. Langenbacher, U. Kensy and B. Dick, *"Setup and performance of a streak camera apparatus for transient absorption measurements in the ns to ms range,"* Appl. Phys. B **111**, 203-216 (2013).
- [Lai87] *"Chemical kinetics,"* K. J. Laidler, (Prentice Hall, 1987).
- [Lak13] *"Principles of fluorescence spectroscopy,"* J. R. Lakowicz, (Springer Science & Business Media, 2013).
- [Lew07] N. S. Lewis, *"Toward cost-effective solar energy use,"* Science **315**, 798-801 (2007).
- [Liu13] Q. Liu, H. Yi, J. Liu, Y. Yang, X. Zhang, Z. Zeng and A. Lei, *"Visible-Light Photocatalytic Radical Alkenylation of α -Carbonyl Alkyl Bromides and Benzyl Bromides,"* Chem.: Eur. J. **19**, 5120-5126 (2013).
- [Lor02] M. Lorenc, M. Ziolk, R. Naskrecki, J. Karolczak, J. Kubicki and A. Maciejewski, *"Artifacts in femtosecond transient absorption spectroscopy,"* Appl. Phys. B **74**, 19-27 (2002).
- [Maj14] M. Majek, F. Filace and A. J. von Wangelin, *"On the mechanism of photocatalytic reactions with eosin Y,"* Beilstein J. Org. Chem. **10**, 981-989 (2014).
- [Mal02] S. Malato, J. Blanco, A. Vidal and C. Richter, *"Photocatalysis with solar energy at a pilot-plant scale: an overview,"* Appl. Catal. B **37**, 1-15 (2002).
- [Mat13] M. M. Maturi, M. Wenninger, R. Alonso, A. Bauer, A. Pöthig, E. Riedle and T. Bach, *"Intramolecular [2+2] Photocycloaddition of 3-and 4-(But-3-enyl) oxyquinolones: Influence of the Alkene Substitution Pattern, Photophysical*

- Studies, and Enantioselective Catalysis by a Chiral Sensitizer*," Chem.: Eur. J. **19**, 7461-7472 (2013).
- [McC03] J. K. McCusker, "Femtosecond absorption spectroscopy of transition metal charge-transfer complexes," Acc. Chem. Res. **36**, 876-887 (2003).
- [Meg09] U. Megerle, I. Pugliesi, C. Schrieffer, C. F. Sailer and E. Riedle, "Sub-50 fs broadband absorption spectroscopy with tunable excitation: putting the analysis of ultrafast molecular dynamics on solid ground," Appl. Phys. B **96**, 215-231 (2009).
- [Meg10] U. Megerle, R. Lechner, B. König and E. Riedle, "Laboratory apparatus for the accurate, facile and rapid determination of visible light photoreaction quantum yields," Photochem. Photobiol. Sci. **9**, 1400-1406 (2010).
- [Meg11] "Photoinduced molecular dynamics in increasingly complex systems: From ultrafast transient absorption spectroscopy to nanoscopic models." U. Megerle doctoral thesis at the LMU Munich (2011), https://edoc.ub.uni-muenchen.de/13044/1/Megerle_Uwe.pdf
- [Mel97] M. Y. Melnikov, V. Belevskii, S. Belopushkin and O. Melnikova, "Photochemical reactions of radical cations of dimethylformamide in freon matrices at 77 K," Russ. Chem. Bull. **46**, 1245-1247 (1997).
- [Mic70] J. Michl, E. W. Thulstrup and J. H. Eggers, "Polarization spectra in stretched polymer sheets. Physical significance of the orientation factors and determination of π - π^* transition moment directions in molecules of low symmetry," J. Phys. Chem. **74**, 3878-3884 (1970).
- [Mel09] P. Melchiorre, "Light in Aminocatalysis: The Asymmetric Intermolecular α -Alkylation of Aldehydes," Angew. Chem. Int. Ed. **48**, 1360-1363 (2009).
- [Mil96] L. L. Miller and K. R. Mann, " π -Dimers and π -Stacks in Solution and in Conducting Polymers," Acc. Chem. Res. **29**, 417-423 (1996).
- [Miy12] Y. Miyake, K. Nakajima and Y. Nishibayashi, "Visible-light-mediated utilization of α -aminoalkyl radicals: addition to electron-deficient alkenes using photoredox catalysts," J. Am. Chem. Soc. **134**, 3338-3341 (2012).
- [Mon06] "Handbook of photochemistry," M. Montalti, A. Credi, L. Prodi and M. T. Gandolfi, (CRC press, 2006).
- [Nic08] D. A. Nicewicz and D. W. MacMillan, "Merging photoredox catalysis with organocatalysis: the direct asymmetric alkylation of aldehydes," Science **322**, 77-80 (2008).

- [Nij95] N. Nijegorodov and W. Downey, "The influence of symmetrical substitution on fluorescence parameters and the intersystem crossing rate constant in aromatic molecules," *Spectrochim. Acta. A* **51**, 2335-2346 (1995).
- [Nor49] R. G. W. Norrish and G. Porter, "Chemical reactions produced by very high light intensities," *Nature* **164**, 658-658 (1949).
- [Oh14] S. H. Oh, Y. R. Malpani, N. Ha, Y.-S. Jung and S. B. Han, "Vicinal difunctionalization of alkenes: chlorotrifluoromethylation with CF_3SO_2Cl by photoredox catalysis," *Org. Lett.* **16**, 1310-1313 (2014).
- [Ong16] W.-J. Ong, L.-L. Tan, Y. H. Ng, S.-T. Yong and S.-P. Chai, "Graphitic carbon nitride (g- C_3N_4)-based photocatalysts for artificial photosynthesis and environmental remediation: are we a step closer to achieving sustainability?," *Chem. Rev.* **116**, 7159-7329 (2016).
- [Pal07] G. Palmisano, V. Augugliaro, M. Pagliaro and L. Palmisano, "Photocatalysis: a promising route for 21st century organic chemistry," *Chem. Commun.*, 3425-3437 (2007).
- [Pig07] A. Pigliucci, G. Duvanel, L. M. L. Daku and E. Vauthey, "Investigation of the Influence of Solute– Solvent Interactions on the Vibrational Energy Relaxation Dynamics of Large Molecules in Liquids," *J. Phys. Chem. A* **111**, 6135-6145 (2007).
- [Pit15] S. P. Pitre, C. D. McTiernan, W. Vine, R. DiPucchio, M. Grenier and J. C. Scaiano, "Visible-light actinometry and intermittent illumination as convenient tools to study $Ru(bpy)_3Cl_2$ mediated photoredox transformations," *Sci. Rep.* **5**, 16397 (2015).
- [Pol04] D. Polli, G. Cerullo, G. Lanzani, S. De Silvestri, K. Yanagi, H. Hashimoto and R. Cogdell, "Conjugation length dependence of internal conversion in carotenoids: role of the intermediate state," *Phys. Rev. Lett.* **93**, 163002 (2004).
- [Pug10] I. Pugliesi, P. Krok, S. Lochbrunner, A. Blaszczyk, C. von Hänisch, M. Mayor and E. Riedle, "Variation of the Ultrafast Fluorescence Quenching in 2,6-Sulfanyl-Core-Substituted Naphthalenediimides by Electron Transfer," *J. Phys. Chem. A* **114**, 12555-12560 (2010).
- [Pug11] I. Pugliesi, U. Megerle, S.-L. Suraru, F. Würthner, E. Riedle and S. Lochbrunner, "Influence of core-substitution on the ultrafast charge separation and recombination in arylamino core-substituted naphthalene diimides," *Chem. Phys. Lett. A* **504**, 24-28 (2011).

- [Ran16] Q. Ran, J. Ma, T. Wang, S. Fan, Y. Yang, S. Qi, Y. Cheng and F. Song, "Synthesis and fluorescence study of conjugated polymers based on 2,4,6-triphenylpyridine moieties," *New J. Chem.* **40**, 6281-6288 (2016).
- [Rei17] "Photoredoxkatalyse – Eine neue Dimension in Reaktionsquantenausbeuten, Mechanismen und anpassbare, organische Katalysatoren." B. Reiß doctoral thesis at the Karlsruher Institut für Technologie (2017), <https://dnb.info/1141792516/34>
- [Ric42] O. Rice, "The Effect of Intermittent Light on a Chain Reaction with Bimolecular and Unimolecular Chain-Breaking Steps," *J. Chem. Phys.* **10**, 440-444 (1942).
- [Rie00] E. Riedle, M. Beutter, S. Lochbrunner, J. Piel, S. Schenkl, S. Spörlein and W. Zinth, "Generation of 10 to 50 fs pulses tunable through all of the visible and the NIR," *Appl. Phys. B* **71**, 457-465 (2000).
- [Rie13] E. Riedle, M. Bradler, M. Wenninger, C. F. Sailer and I. Pugliesi, "Electronic transient spectroscopy from the deep UV to the NIR: unambiguous disentanglement of complex processes," *Faraday Discuss.* **163**, 139-158 (2013).
- [Rom16] N. A. Romero and D. A. Nicewicz, "Organic photoredox catalysis," *Chem. Rev.* **116**, 10075-10166 (2016).
- [Rub10] M. B. Rubin and S. E. Braslavsky, "Quantum yield: the term and the symbol. A historical search," *Photochem. Photobiol. Sci.* **9**, 670-674 (2010).
- [Ruc12] C. Ruckebusch, M. Sliwa, P. d. Pernot, A. De Juan and R. Tauler, "Comprehensive data analysis of femtosecond transient absorption spectra: A review," *J. Photochem. Photobiol. C* **13**, 1-27 (2012).
- [Sah13] B. Sahoo, M. N. Hopkinson and F. Glorius, "Combining gold and photoredox catalysis: visible light-mediated oxy- and aminoarylation of alkenes," *J. Am. Chem. Soc.* **135**, 5505-5508 (2013).
- [Sai12] "Tracking the short life of highly reactive carbocations." C. Sailer doctoral thesis at the LMU Munich (2012), https://edoc.ub.uni-muenchen.de/15211/1/Sailer_Christian.pdf
- [Sak10] N. Sakai, J. Mareda, E. Vauthey and S. Matile, "Core-substituted naphthalenediimides," *Chem. Commun.* **46**, 4225-4237 (2010).
- [Sat03] H. Satzger, W. Zinth, "Visualization of transient absorption dynamics - towards a qualitative view of complex reaction kinetics," *J. Chem. Phys.* **295**, 287-295 (2003).

- [Sch14] D. M. Schultz and T. P. Yoon, "Solar synthesis: prospects in visible light photocatalysis," *Science* **343**, 1239176 (2014).
- [She56] A. Shepp, "Rate of recombination of radicals. I. A general sector theory; a correction to the methyl radical recombination rate," *J. Chem. Phys.* **24**, 939-943 (1956).
- [Sta18] E. Stadler, A. Eibel, D. Fast, H. Freißmuth, C. Holly, M. Wiech, N. Moszner and G. Gescheidt, "A versatile method for the determination of photochemical quantum yields via online UV-Vis spectroscopy," *Photochem. Photobiol. Sci.* **17**, 660-669 (2018).
- [Sta15] C. W. Stark, W. J. Schreier, J. Lucon, E. Edwards, T. Douglas and B. Kohler, "Interligand electron transfer in heteroleptic ruthenium (II) complexes occurs on multiple time scales," *J. Phys. Chem. A* **119**, 4813-4824 (2015).
- [Str62] S. J. Strickler and R. A. Berg, "Relationship between absorption intensity and fluorescence lifetime of molecules," *J. Chem. Phys.* **37**, 814-822 (1962).
- [Thu68] E. W. Thulstrup and J. H. Eggers, "Moment directions of the electronic transitions of fluoranthene," *Chem. Phys. Lett.* **1**, 690-692 (1968).
- [Thu70] E. W. Thulstrup, J. Michl and J. H. Eggers, "Polarization spectra in stretched polymer sheets. II. Separation of π - π^* absorption of symmetrical molecules into components," *J. Phys. Chem.* **74**, 3868-3878 (1970).
- [Tur10] "Modern Molecular Photochemistry of Organic Molecules," N. J. Turro, V. Ramamurthy and J. C. Scaiano, (University Science Books, 2010).
- [Uda92] B. Udayakumar and G. B. Schuster, "Photoisomerization of 2,2'-ethano-bridged *m*-terphenyl derivatives: ring constraint activates an unreactive chromophore," *J. Org. Chem.* **57**, 348-352 (1992).
- [Van04] I. H. Van Stokkum, D. S. Larsen and R. Van Grondelle, "Global and target analysis of time-resolved spectra," *Biochim. Biophys. Acta* **1657**, 82-104 (2004).
- [Ves12] J. Vesely and R. Rios, "Organocatalytic Enantioselective α -Alkylation of Aldehydes," *ChemCatChem* **4**, 942-953 (2012).
- [Vet17] Ľ. Vetráková, V. Ladányi, J. Al Anshori, P. Dvořák, J. Wirz and D. Heger, "The absorption spectrum of *cis*-azobenzene," *Photochem. Photobiol. Sci.* **16**, 1749-1756 (2017).
- [Vol19] H. Volfova, Q. Hu and E. Riedle, "Determination of Reaction Quantum Yields: LED Based Setup with Better 5% Precision," *EPA Newsletter*, 51-69 (2019).

- [Vya15] V. S. Vyas, F. Haase, L. Stegbauer, G. Savasci, F. Podjaski, C. Ochsenfeld and B. V. Lotsch, "*A tunable azine covalent organic framework platform for visible light-induced hydrogen generation*," *Nat. Commun.* **6**, 1-9 (2015).
- [Wäc15] M. Wächtler, J. Guthmuller, S. Kupfer, M. Maiuri, D. Brida, J. Popp, S. Rau, G. Cerullo and B. Dietzek, "*Ultrafast Intramolecular Relaxation and Wave-Packet Motion in a Ruthenium-Based Supramolecular Photocatalyst*," *Chem.: Eur. J.* **21**, 7668-7674 (2015).
- [Wal12] C.-J. Wallentin, J. D. Nguyen, P. Finkbeiner and C. R. Stephenson, "*Visible light-mediated atom transfer radical addition via oxidative and reductive quenching of photocatalysts*," *J. Am. Chem. Soc.* **134**, 8875-8884 (2012).
- [Wan13] C. Wang, S. Cao and W.-F. Fu, "*A stable dual-functional system of visible-light-driven Ni (II) reduction to a nickel nanoparticle catalyst and robust in situ hydrogen production*," *Chem. Commun.* **49**, 11251-11253 (2013).
- [Wan04] X.-Y. Wang, A. Del Guerzo and R. H. Schmechl, "*Photophysical behavior of transition metal complexes having interacting ligand localized and metal-to-ligand charge transfer states*," *J. Photochem. Photobiol. C* **5**, 55-77 (2004).
- [Wan18] X. Wang, Y. Xu, L. Yang, X. Lu, H. Zou, W. Yang, Y. Zhang, Z. Li and M. Ma, "*Synthesis, spectra, and theoretical investigations of 1,3,5-triazines compounds as ultraviolet rays absorber based on time-dependent density functional calculations and three-dimensional quantitative structure-property relationship*," *J. Fluoresc.* **28**, 707-723 (2018).
- [Was93] S. Wasmus and W. Vielstich, "*The electro-oxidation of formic acid, formamide and dimethylformamide in aqueous acid solution — a comparative study using on-line MS*," *Electrochim. Acta* **38**, 185-189 (1993).
- [Wil18] R. Wilcken, M. Schildhauer, F. Rott, L. A. Huber, M. Guentner, S. Thumser, K. Hoffmann, S. Oesterling, R. de Vivie-Riedle and E. Riedle, "*Complete mechanism of hemithioindigo motor rotation*," *J. Am. Chem. Soc.* **140**, 5311-5318 (2018).
- [Wu14] Y. Wu, M. Frasconi, D. M. Gardner, P. R. McGonigal, S. T. Schneebeli, M. R. Wasielewski and J. F. Stoddart, "*Electron Delocalization in a Rigid Cofacial Naphthalene-1,8,4,5-bis(dicarboximide) Dimer*," *Angew. Chem. Int. Ed.* **53**, 9476-9481 (2014).
- [Wür02] F. Würthner, S. Ahmed, C. Thalacker and T. Debaerdemaeker, "*Core-Substituted Naphthalene Bisimides: New Fluorophors with Tunable Emission Wavelength for FRET Studies*," *Chem.: Eur. J.* **8**, 4742-4750 (2002).

- [Wür16] F. Würthner, C. R. Saha-Möller, B. Fimmel, S. Ogi, P. Leowanawat and D. Schmidt, "*Perylene bisimide dye assemblies as archetype functional supramolecular materials*," Chem. Rev. **116**, 962-1052 (2016).
- [Xu18] J. Xu, H. Volfova, R. J. Mulder, L. Goerigk, G. Bryant, E. Riedle and C. Ritchie, "*Visible-light-driven "on"/"off" photochromism of a polyoxometalate diarylethene coordination complex*," J. Am. Chem. Soc. **140**, 10482-10487 (2018).
- [Yus15] O. Yushchenko, G. Licari, S. Mosquera-Vazquez, N. Sakai, S. Matile and E. Vauthey, "*Ultrafast intersystem-crossing dynamics and breakdown of the Kasha–Vavilov’s rule of naphthalenediimides*," J. Phys. Chem. Lett. **6**, 2096-2100 (2015).
- [Zew00] A. H. Zewail, "*Femtochemistry: atomic-scale dynamics of the chemical bond using ultrafast lasers (Nobel Lecture)*," Angew. Chem. Int. Ed. **39**, 2586-2631 (2000).

Nomenclature

List of abbreviations

2D	2-dimensional
AmiR	α -amino radical
Ar	Argon gas
AWG	arbitrary waveform generator
BBO	β -barium borate
b-ISC	back intersystem crossing
BrMal	bromomalonate
CA	coherent artifact
CaF ₂	calcium fluoride
CCD	charge-coupled device
CH ₂ Cl ₂	dichloromethane
cNDI	core-substituted naphthalene diimide
COF	covalent organic frameworks
const.	constant
CPA	chirped pulse amplification
cw	continuous wave
DADS	decay associated difference spectra
DMF	dimethylformamide
Ena	enamine
ESA	excited state absorption
ESR	electron spin resonance
FWHM	full width at half maximum
GC	gas chromatography
GSB	ground state bleach
H ₂	hydrogen
H ₂ O	water
HOMO	highest occupied molecular orbital
HOTf	trifluoromethanesulfonic acid
IC	internal conversion
Imin	iminium ion
IRF	instrumental response function

ISC	intersystem crossing
IVR	intramolecular vibrational redistribution
LED	light-emitting diode
LUMO	lowest unoccupied molecular orbital
Lut	2,6-Lutidin
Mal	malonate radical
MLCT	metal-to-ligand charge transfer
N ₂	nitrogen gas
NA	numerical aperture
NBu ₄ PF ₆	tetrabutylammonium hexafluorophosphate
NDI	naphthalene diimide
NIR	near infrared
NMR	Nuclear magnetic resonance
NOPA	non-collinear optical parametric amplifier
NP	by-product
Oct	octanal
OD	optical density
OPA	optical parametric amplifier
OPO	optical parametric oscillator
OrCat	imidazolidinone (organocatalyst)
OTTLE	optically transparent thin-layer electrochemical
P	product
PC	prism compressor
PDI	perylene diimide
QY	quantum yield
QYDS	quantum yield determination system
RDI	rylene diimide
rt	Room temperature
Ru / Ru(bpy) ₃ ²⁺	Ruthenium tris-(bi-pyridine)
RuE	excited photocatalyst Ru(bpy) ₃ ²⁺
RuS	singlet excited state of Ru(bpy) ₃ ²⁺
RuT	triplet excited state of Ru(bpy) ₃ ²⁺
SADS	species associated difference spectra
SAS	species associated spectra

SCG	supercontinuum generation
SE	stimulated emission
SHG	second harmonic generation
TA	transient absorption
TEA	<i>N,N</i> -diethylethanamine
TEoA	triethanolamine
THG	third harmonic generation
TPA	two photon absorption
UV	ultraviolet
Vis	visible
XPM	cross phase modulation

Most frequently used parameters

$[J]$	molar concentration of the absorbing species J
\tilde{J}_0	incident light flux
A	amplitude
$abs(\lambda)$	steady-state optical density
c	speed of light in air
d	optical length of the sample
d_{DA}	distance of the two charged species D and A
E_{00}^S	transition energies of the lowest singlet state
E_{00}^T	transition energies of the lowest triplet state
$F(t)$	fit function
h	Planck constant
k	rate constant
K_a	self-association constants
K_{Ena}	equilibrium constant of the enamine formation process
K_{ij}	rate constant matrix
K_p	equilibrium constant of the product formation process
M_{ij}	coefficient matrix which reflects the rate model
N_A	Avogadro constant
N_i	population of states
$N_{ph,abs}(\lambda)$	Number of absorbed photons of the particular wavelength
N_{prod}	Number of products formed
OD	absorbance
$p(k)$	probability distribution
P_{abs}	absorbed light power
R^*	reference camera signal with pump pulses
R_0	reference camera signal without pump pulses
S	entropy
S^*	sample camera signal with pump pulses
S_0	sample camera signal without pump pulses
T^*	transmittance with pump pulses

T_0	transmittance without pump pulses
V_0	solution volume
ΔG_{ET}^0	free energy change in the electron transfer process
ΔOD	changes of the optical density
Δt	delay time
Φ	quantum yield
Φ_{fluor}	fluorescence quantum yield
Φ_{ISC}	quantum yield of intersystem crossing (ISC) process
Φ^{P}	reaction quantum yield
ε	molar absorption coefficient
ε_{r}	dielectric constant
λ	wavelength
$\theta(t)$	Heaviside step function
τ	time constant

Appendix A1

Solution to the system of the steady-state equations in Chapter 3

For estimating the rate constants based on the steady-state assumption.

According to the assumptions described in Chapter 3, the steady-state treatment can be written as

$$\frac{d[\mathbf{RuT}]}{dt} = \tilde{J}_{\text{abs}} - k_2[\mathbf{RuT}] - k_3[\mathbf{Ena}][\mathbf{RuT}] - k_7[\mathbf{AmiR}][\mathbf{RuT}] = 0 \quad (\text{A1.1a})$$

$$\frac{d[\mathbf{RuC}]}{dt} = k_3[\mathbf{Ena}][\mathbf{RuT}] - k_4[\mathbf{RuC}][\mathbf{BrMal}] + k_7[\mathbf{AmiR}][\mathbf{RuT}] = 0 \quad (\text{A1.1b})$$

$$\begin{aligned} \frac{d[\mathbf{Mal}]}{dt} = k_4[\mathbf{RuC}][\mathbf{BrMal}] - k_5[\mathbf{Ena}][\mathbf{Mal}] + k_6[\mathbf{AmiR}][\mathbf{BrMal}] \\ - k_9[\mathbf{H}][\mathbf{Mal}] = 0 \end{aligned} \quad (\text{A1.1c})$$

$$\frac{d[\mathbf{AmiR}]}{dt} = k_5[\mathbf{Ena}][\mathbf{Mal}] - k_6[\mathbf{AmiR}][\mathbf{BrMal}] - k_7[\mathbf{AmiR}][\mathbf{RuT}] = 0 \quad (\text{A1.1d})$$

which are the same as the equations (3.19a-d). The concentration of the **BrMal** can be expressed as

$$[\mathbf{BrMal}] \equiv \overline{[\mathbf{BrMal}]} - [\mathbf{Mal}] \quad (\text{A1.2})$$

where $\overline{[\mathbf{BrMal}]}$ is a function of the initial concentration of the **BrMal** and **P**. Furthermore, the concentration of **Ena** and the rate constants k_2 , k_3 and k_4 are known, which are

$$\begin{aligned} [\mathbf{Ena}] &= 23 \text{ mM}, \\ k_2 &= 1 \cdot 10^6 \text{ s}^{-1}, \\ k_3 &= 1 \cdot 10^7 \text{ M}^{-1} \text{ s}^{-1}, \\ k_4 &= 2.7 \cdot 10^7 \text{ M}^{-1} \text{ s}^{-1}. \end{aligned} \quad (\text{A1.3})$$

The quantum yield for the product formation is given by

$$\begin{aligned} \Phi^{\text{P}} &= \frac{\Delta[\mathbf{P}]}{\Delta t} \cdot \frac{1}{\tilde{J}_{\text{abs}}} \\ &= \gamma \cdot (k_6[\mathbf{AmiR}][\mathbf{BrMal}] + k_7[\mathbf{AmiR}][\mathbf{RuT}]) \cdot \frac{1}{\tilde{J}_{\text{abs}}} \end{aligned} \quad (\text{A1.4})$$

Combining eq. A1.1 – 1.4 affords eq. 1.5, since the negative solution can be neglected when $\Phi^{\text{P}} \geq 0$, which is always the case.

$$\begin{aligned}
\Phi^P = & -\frac{\gamma}{M} \left(4.3 \cdot 10^4 \cdot k_5 + 1.2 \cdot 10^5 \cdot k_6 - 1.2 \cdot 10^{12} \cdot \frac{k_6}{k_7} - 2.2 \cdot 10^{-3} \cdot k_5 k_7 \right. \\
& \left. - 4.9 \cdot 10^2 \cdot \frac{k_5 k_6}{k_9} + 5.0 \cdot 10^6 \cdot k_9 - 0.5 \cdot k_9 k_7 \right) \\
& - \frac{\gamma}{M} \cdot \frac{[\text{BrMal}]}{\tilde{J}_{\text{abs}}} \left(2.6 \cdot 10^3 \cdot k_5 k_6 + 6.2 \cdot 10^5 \cdot k_9 k_6 - 6.2 \cdot 10^{12} \cdot \frac{k_9 k_6}{k_7} \right) \\
& + \frac{\gamma}{M} \left[\left(2.4 \cdot 10^5 \cdot \frac{k_5^2 k_6^2}{k_9^2} - 2.1 \cdot \frac{k_5^2 k_6 k_7}{k_9} + 4.6 \cdot 10^{-6} \cdot k_5^2 k_7^2 \right) \right. \\
& \left. + \frac{[\text{BrMal}]}{\tilde{J}_{\text{abs}}} \left(9.7 \cdot 10^{-2} \cdot \frac{k_5^3 k_6 k_7}{k_9} - 2.6 \cdot 10^6 \cdot \frac{k_5^2 k_6^2}{k_9} + 11.5 \cdot k_5^2 k_6 k_7 \right) \right. \\
& \left. + \left(\frac{[\text{BrMal}]}{\tilde{J}_{\text{abs}}} \right)^2 \left(6.9 \cdot 10^6 \cdot k_5^2 k_6^2 \right) \right]^{0.5} \\
M = & k_9 k_7 + 4.3 \cdot 10^{-3} \cdot k_5 k_7 - 2.3 \cdot 10^5 \cdot k_6
\end{aligned} \tag{A1.5}$$

Because γ , k_5 , k_6 , k_7 and k_9 are constant, the quantum yield can be expressed as

$$\Phi^P = C_0 + C_1 \frac{[\text{BrMal}]}{\tilde{J}_{\text{abs}}} + \sqrt{C_2 + C_3 \frac{[\text{BrMal}]}{\tilde{J}_{\text{abs}}} + C_4 \left(\frac{[\text{BrMal}]}{\tilde{J}_{\text{abs}}} \right)^2} \tag{A1.6}$$

where C_0 , C_1 , C_2 , C_3 and C_4 are constant and can be written as functions of γ , k_5 , k_6 , k_7 and k_9 . From the analysis in Chapter 3, it is known that $k_5 \gg k_3 = 10^7 \text{ M}^{-1} \text{ s}^{-1}$. In addition, as the light intensity becomes large, the quantum yield will become increasingly smaller and eventually will be smaller than 100%. Therefore, a reasonable assumption is $k_7 \gg k_6$. Moreover, the product concentration is always much larger than the by-product concentration. Thus, it is assumed that $k_7 \gg k_9$. The constants C_i in eq. A1.5 and A1.6 therefore reduces to

$$C_0 = \frac{0.5\gamma}{1 + \frac{k_9}{(4.3 \cdot 10^{-3} \cdot k_5)}} + \frac{0.5\gamma}{1 + \frac{4.3 \cdot 10^{-3} \cdot k_5}{k_9}} \tag{A1.7}$$

$$C_1 = 6.0 \cdot 10^5 \frac{k_6}{k_7} \frac{\gamma}{1 + \frac{k_9}{(4.3 \cdot 10^{-3} \cdot k_5)}} + 6.2 \cdot 10^5 \frac{k_6}{k_7} \frac{\gamma}{1 + \frac{4.3 \cdot 10^{-3} \cdot k_5}{k_9}} \tag{A1.8}$$

$$C_2 = \frac{0.25\gamma^2}{\left(1 + \frac{k_9}{4.3 \cdot 10^{-3} \cdot k_5}\right)^2} \quad (\text{A1.9})$$

$$C_3 = 5.2 \cdot 10^3 \frac{k_6}{k_7} \frac{k_5}{k_9} \frac{\gamma^2}{\left(1 + \frac{k_9}{4.3 \cdot 10^{-3} \cdot k_5}\right)^2} \quad (\text{A1.10})$$

$$C_4 = 3.7 \cdot 10^{11} \left(\frac{k_6}{k_7}\right)^2 \frac{\gamma^2}{\left(1 + \frac{k_9}{4.3 \cdot 10^{-3} \cdot k_5}\right)^2} \quad (\text{A1.11})$$

From A1.7-A1.11, the constants depend on the ratio k_6/k_7 , the ratio k_9/k_5 and the value of γ .

Appendix A2

MathCad Code for the chemical kinetics analysis

For simulation of the light intensity-dependent quantum yield of the photoredox catalytic aldehyde alkylation reaction described in Chapter 3.

Quantum yield simulation of photoredox catalytic aldehyde alkylation

1. Unit definition: ORIGIN := 1 $eV := e_c \cdot 1 \text{ V} = (1.602 \cdot 10^{-19}) \text{ J}$

$$M := \frac{\text{mol}}{L} \quad mM := 10^{-3} \frac{\text{mol}}{L} \quad \mu M := 10^{-6} \frac{\text{mol}}{L} \quad fs := 10^{-15} \text{ s}$$

2. Reaction Mechanism:

see Scheme 3.6 and the text in Chapter 3

3. Simulation of the reactions in the solution before the excitation with light:

The initial conditions: $conc_{OrCat} := 100 \text{ mM}$ $conc_{Oct} := 1000 \text{ mM}$

$$conc_{H_2O} := 1 \text{ mM} \quad conc_{Ena} := 0 \text{ mM}$$

Rate constants: $K_{eq} := 0.008$ $k_1 := 8 \cdot 10^{-4} \frac{1}{M \cdot s}$ $k_{n1} := \frac{k_1}{K_{eq}} = 0.1 \frac{1}{M \cdot s}$

Time scale: $dt1 := 10 \mu s$ $t_{start1} := 0 \mu s$ $t_{end1} := 10^4 \mu s$

$$dt2 := 10^3 \mu s \quad t_{start2} := t_{end1} \quad t_{end2} := 1 \text{ s} = 0.017 \text{ min}$$

$$dt3 := 0.5 \text{ s} \quad t_{start3} := t_{end2} \quad t_{end3} := 1800 \text{ s} = 30 \text{ min}$$

$$t1 := t_{start1}, t_{start1} + dt1 .. t_{end1} = \begin{bmatrix} 0 \\ \vdots \end{bmatrix} \mu s \quad \#t1 := \text{length}(t1) = 1001$$

$$t2 := t_{start2}, t_{start2} + dt2 .. t_{end2} = \begin{bmatrix} 10 \\ \vdots \end{bmatrix} ms \quad \#t2 := \text{length}(t2) = 991$$

$$t3 := t_{start3}, t_{start3} + dt3 .. t_{end3} = \begin{bmatrix} 1 \\ \vdots \end{bmatrix} s \quad \#t3 := \text{length}(t3) = 3599$$

$$t_{sim} := \text{stack}(t1, t2, t3) = \begin{bmatrix} 0 \\ \vdots \end{bmatrix} ms \quad \#t := \text{length}(t_{sim}) = 5591$$

Set up rate model for the enamine euqilibration:

$$\text{start values:} \quad n_{start} := \begin{bmatrix} conc_{OrCat} \\ conc_{Oct} \\ conc_{H_2O} \\ conc_{Ena} \end{bmatrix} \quad K_{enaeq} := \begin{bmatrix} k_1 \\ k_{n1} \end{bmatrix}$$

Nebenbedingungsschätzwerte

$$OrCat(0 \text{ s}) = n_start_1 \quad Oct(0 \text{ s}) = n_start_2$$

$$H2O(0 \text{ s}) = n_start_3 \quad Ena(0 \text{ s}) = n_start_4$$

$$\frac{d}{dt} OrCat(t) = -K_1 \cdot OrCat(t) \cdot Oct(t) + K_2 \cdot H2O(t) \cdot Ena(t)$$

$$\frac{d}{dt} Oct(t) = -K_1 \cdot OrCat(t) \cdot Oct(t) + K_2 \cdot H2O(t) \cdot Ena(t)$$

$$\frac{d}{dt} H2O(t) = K_1 \cdot OrCat(t) \cdot Oct(t) - K_2 \cdot H2O(t) \cdot Ena(t)$$

$$\frac{d}{dt} Ena(t) = K_1 \cdot OrCat(t) \cdot Oct(t) - K_2 \cdot H2O(t) \cdot Ena(t)$$

Gleichungslöser

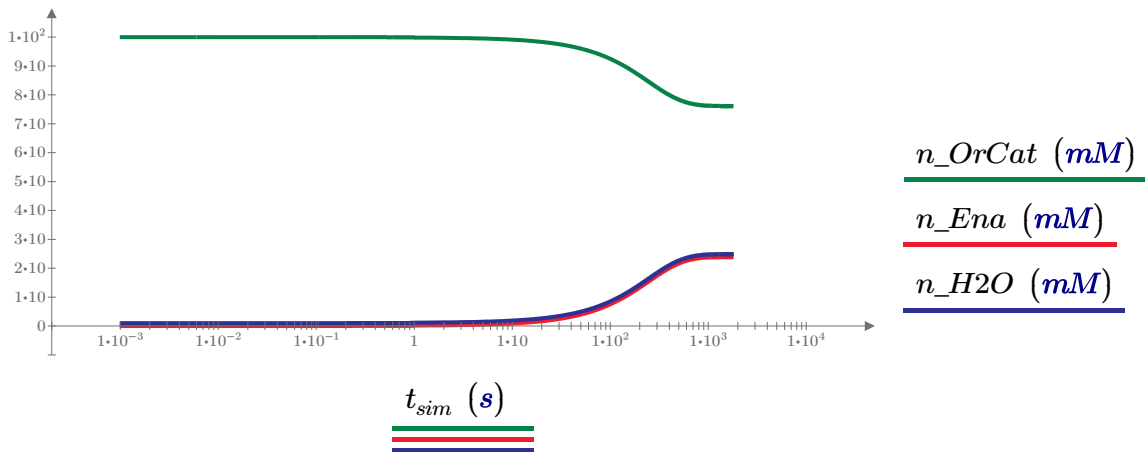
$$enaeq(t_start, t_end, n_start, K) := \text{odesolve} \left(\begin{bmatrix} OrCat(t) \\ Oct(t) \\ H2O(t) \\ Ena(t) \end{bmatrix}, t_end \right)$$

Visualization:

$$n_OrCat := \text{enaeqout}^{(1)} \quad n_Oct := \text{enaeqout}^{(2)}$$

$$n_H2O := \text{enaeqout}^{(3)} \quad n_Ena := \text{enaeqout}^{(4)}$$

$$scale := \frac{\max(n_OrCat, n_H2O, n_Ena)}{mM} = 100$$



The concentration of compounds before the excitation:

$$conc_{OrCat} := n_OrCat_{\#t} = 76.116 \text{ mM}$$

$$conc_{Oct} := n_Oct_{\#t} = 976.116 \text{ mM}$$

$$conc_{H2O} := n_H2O_{\#t} = 24.884 \text{ mM}$$

$$conc_{Ena} := n_Ena_{\#t} = 23.884 \text{ mM}$$

4. Simulation of the reaction in the solution after the excitation with light :

Parameters for light: $V := 1.7 \text{ mL}$ $\lambda := 441 \text{ nm}$

The initial conditions: $\text{conc}_{BrMal} := 500 \text{ mM}$ $\text{conc}_{Ru} := 2.5 \text{ mM}$

Rate constants:

1. Diffusion rate in DMF: $\eta_{DMF} := 0.794 \cdot 10^{-3} \text{ Pa} \cdot \text{s}$ $\varepsilon_{DMF} := 38$

$d_{cc} := 10 \text{ Angstrom}$ $T := 298 \text{ K}$

$$D_{DMF} := \frac{k \cdot T}{6 \cdot \pi \cdot \eta_{DMF} \cdot \frac{d_{cc}}{2}} = (5.498 \cdot 10^{-6}) \frac{\text{cm}^2}{\text{s}}$$

$$k_{diff} := 4 \cdot \pi \cdot N_A \cdot 2 \cdot D_{DMF} \cdot d_{cc} = (8.321 \cdot 10^9) \frac{1}{\text{M} \cdot \text{s}}$$

2. ET rate in DMF: $\lambda_{re_DMF} := 1.83 \text{ eV}$ $\Delta G_{BrMal_Ru1} := -0.85 \text{ eV}$

$H_{AB} := 1 \cdot 10^{-3} \text{ eV}$

$$k_{et} := \frac{2 \cdot \pi}{\hbar} \cdot H_{AB}^2 \cdot \frac{1}{\sqrt{2 \cdot \pi \cdot \lambda_{re_DMF} \cdot k \cdot T}} \cdot \exp\left(\frac{1}{k \cdot T} \cdot \frac{-(\lambda_{re_DMF} + \Delta G_{BrMal_Ru1})^2}{4 \cdot \lambda_{re_DMF}}\right)$$

3. Dissociation rate in DMF:

$$w_{ip} := \frac{(-1) \cdot (1) \cdot e_c^2 \cdot N_A}{\varepsilon_0 \cdot \varepsilon_{DMF} \cdot d_{cc} \cdot 4 \cdot \pi \cdot R \cdot T} = -1.476$$

$$k_{dis} := \frac{D_{DMF}}{(d_{cc})^2} \cdot \frac{w_{ip}}{1 - \exp(-w_{ip})} = (2.405 \cdot 10^8) \frac{1}{\text{s}}$$

4. Others:

$$k_2 := 1 \cdot 10^6 \frac{1}{\text{s}} \quad k_3 := 1 \cdot 10^7 \frac{1}{\text{M} \cdot \text{s}} \quad k_4 := 2.7 \cdot 10^7 \frac{1}{\text{M} \cdot \text{s}}$$

$$k_5 := 1 \cdot 10^8 \frac{1}{\text{M} \cdot \text{s}} \quad k_6 := \frac{0.08}{\text{M} \cdot \text{s}} \quad k_7 := 8 \cdot 10^9 \frac{1}{\text{M} \cdot \text{s}}$$

$$k_8 := 1 \frac{1}{\text{M} \cdot \text{s}} \quad k_{n8} := \frac{k_8}{3 \cdot 1} = 0.333 \frac{1}{\text{M} \cdot \text{s}}$$

$$k_9 := 1 \cdot 10^{-5} \text{ M} \cdot k_5 = (1 \cdot 10^3) \frac{1}{\text{s}}$$

Time scale:

$$dt1 := 1 \text{ ns} \quad t_{start1} := 0 \text{ ns} \quad t_{end1} := 1 \text{ } \mu\text{s}$$

$$dt2 := 1 \text{ } \mu\text{s} \quad t_{start2} := t_{end1} \quad t_{end2} := 1 \text{ ms}$$

$$dt3 := 1 \text{ ms} \quad t_{start3} := t_{end2} \quad t_{end3} := 1 \text{ s}$$

$$dt4 := 10 \text{ s} \quad t_{start4} := t_{end3} \quad t_{end4} := 72000 \text{ s} = 20 \text{ hr}$$

$$t1 := t_{start1}, t_{start1} + dt1 .. t_{end1} = \begin{bmatrix} 0 \\ \vdots \\ \vdots \end{bmatrix} \text{ ns} \quad \#t1 := \text{length}(t1) = 1001$$

$$t2 := t_{start2}, t_{start2} + dt2 .. t_{end2} = \begin{bmatrix} 1 \cdot 10^{-6} \\ \vdots \\ \vdots \end{bmatrix} \text{ s} \quad \#t2 := \text{length}(t2) = 1000$$

$$t3 := t_{start3}, t_{start3} + dt3 .. t_{end3} = \begin{bmatrix} 0.001 \\ \vdots \\ \vdots \end{bmatrix} \text{ s} \quad \#t3 := \text{length}(t3) = 1000$$

$$t4 := t_{start4}, t_{start4} + dt4 .. t_{end4} = \begin{bmatrix} 1 \\ \vdots \\ \vdots \end{bmatrix} \text{ s} \quad \#t4 := \text{length}(t4) = 7200$$

$$t_{sim} := \text{stack}(t1, t2, t3, t4) = \begin{bmatrix} 0 \\ \vdots \\ \vdots \end{bmatrix} \text{ s} \quad \#t := \text{length}(t_{sim}) = 10201$$

Set up rate model for the reaction:

start values:

$$n_{start} := \begin{bmatrix} conc_{Ru} \\ \vdots \end{bmatrix} \quad K_{reaction} := \begin{bmatrix} k_1 \\ \vdots \end{bmatrix}$$

Schätzwerte

$$Ru(0 \text{ s}) = N_1 \quad RuT(0 \text{ s}) = N_2 \quad RuC(0 \text{ s}) = N_3 \quad Ena(0 \text{ s}) = N_4 \quad BrMal(0 \text{ s}) = N_5$$

$$OrCat(0 \text{ s}) = N_6 \quad Mal(0 \text{ s}) = N_7 \quad Oct(0 \text{ s}) = N_8 \quad H2O(0 \text{ s}) = N_9 \quad AmiR(0 \text{ s}) = N_{10}$$

$$Imin(0 \text{ s}) = N_{11} \quad P(0 \text{ s}) = N_{12}$$

$$\frac{d}{dt} Ru(t) = -I_{abs} + K_5 \cdot BrMal(t) \cdot RuC(t) + K_3 \cdot RuT(t)$$

$$\frac{d}{dt} RuT(t) = I_{abs} - K_4 \cdot Ena(t) \cdot RuT(t) - K_8 \cdot AmiR(t) \cdot RuT(t) - K_3 \cdot RuT(t)$$

$$\frac{d}{dt} RuC(t) = K_4 \cdot Ena(t) \cdot RuT(t) + K_8 \cdot AmiR(t) \cdot RuT(t) - K_5 \cdot BrMal(t) \cdot RuC(t)$$

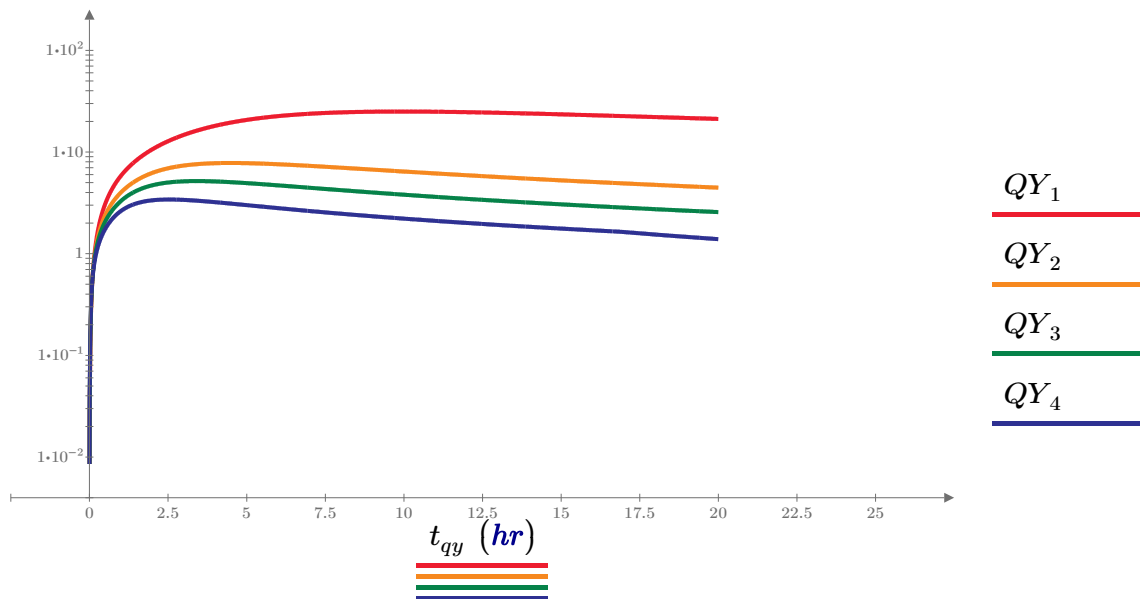
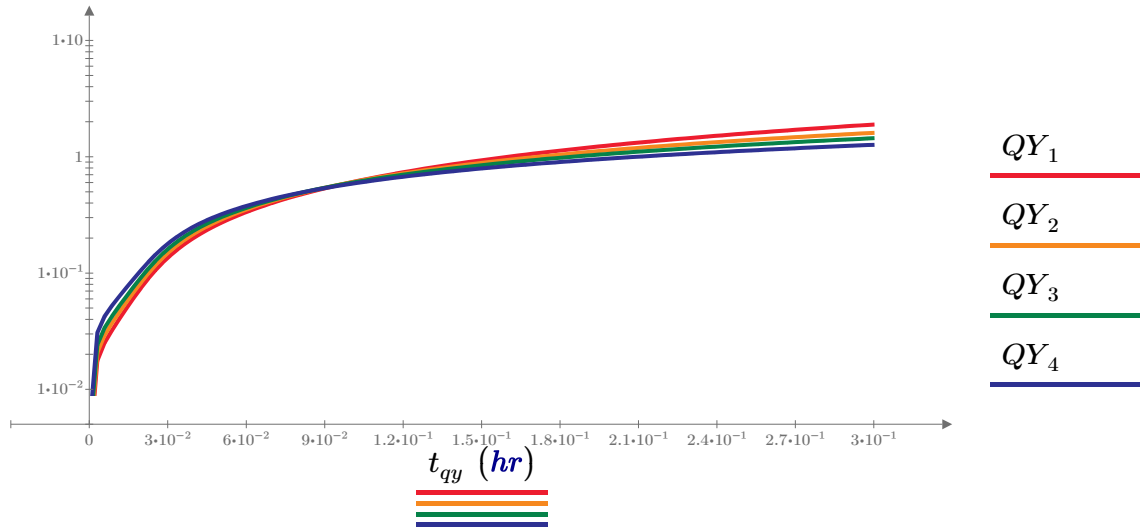
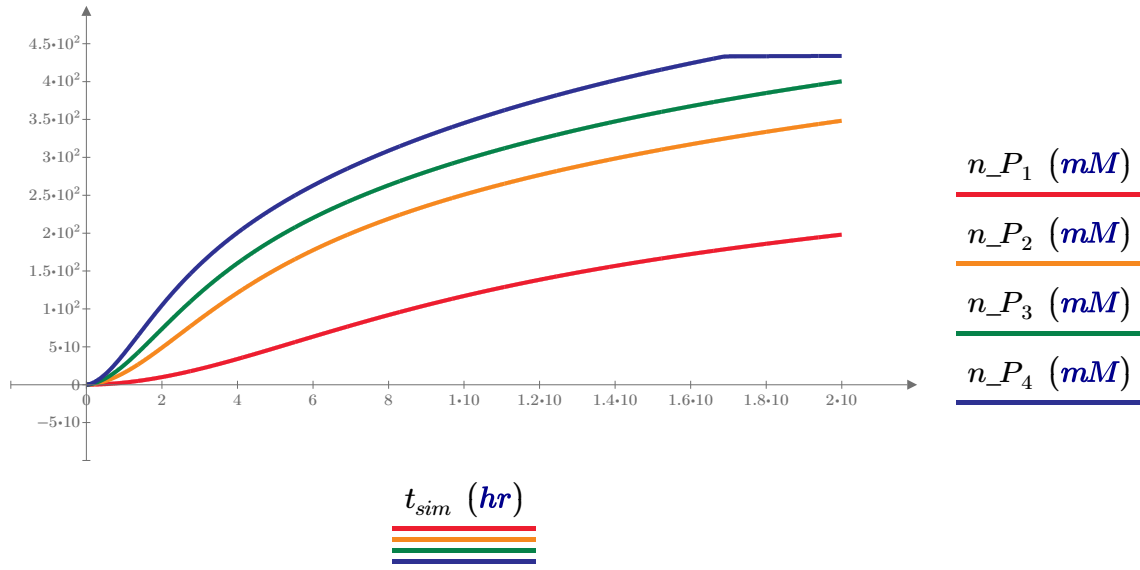
$$\frac{d}{dt} Ena(t) = -K_4 \cdot Ena(t) \cdot RuT(t) + K_1 \cdot OrCat(t) \cdot Oct(t) - K_2 \cdot Ena(t) \cdot H2O(t) - K_6 \cdot Ena(t) \cdot Mal(t)$$

Nebenbedingungen

$$\frac{d}{dt} BrMal(t) = -K_5 \cdot BrMal(t) \cdot RuC(t) - K_7 \cdot BrMal(t) \cdot AmiR(t)$$

$$\frac{d}{dt} OrCat(t) = -K_1 \cdot OrCat(t) \cdot Oct(t) + K_2 \cdot Ena(t) \cdot H2O(t) + K_9 \cdot Imin(t) \cdot H2O(t) - K_{10} \cdot P(t) \cdot OrCat(t)$$

$$\frac{d}{dt} Mal(t) = K_5 \cdot BrMal(t) \cdot RuC(t) - K_6 \cdot Ena(t) \cdot Mal(t) + K_7 \cdot BrMal(t) \cdot AmiR(t) - K_{11} \cdot Mal(t)$$



Appendix A3

MathCad Code for the intermittent illumination experiment

For estimating the average lifetime of the radical chain in the photoredox catalytic aldehyde alkylation reaction.

Determination of radical chain lifetime in the aldehyde alkylation reaction

1. Experimental data:

$$\text{period of light } (\mu\text{s}): \quad t_L := \begin{bmatrix} 10 \\ 100 \\ 1000 \end{bmatrix}$$

$$\text{(rate P)}_{av}/(\text{rate P})_c: \quad \text{Data} := \begin{bmatrix} 0.04317 \\ 0.03402 \\ 0.03294 \end{bmatrix}$$

The value $(\text{rate P})_{av}/(\text{rate P})_c = 0.0315$ at $10000\mu\text{s}$ is used as a factor in order to scale the theoretical curve.

$$\text{dark to light ratio:} \quad p := 9$$

2. Shepp's model [She56]:

$$\beta(\alpha, \tau_0) := \frac{t_L}{\tau_0} \cdot \frac{1}{1 + \alpha}$$

$$a(\alpha, \tau_0) := \exp((2 + \alpha) \cdot \beta(\alpha, \tau_0))$$

$$b(\alpha, \tau_0) := \exp(p \cdot \alpha \cdot \beta(\alpha, \tau_0))$$

$$c(\alpha, \tau_0) := \frac{(b(\alpha, \tau_0) - 1)}{\alpha}$$

$$A(\alpha, \tau_0) := \overline{(a(\alpha, \tau_0) - 1) + c(\alpha, \tau_0) \cdot (a(\alpha, \tau_0) \cdot (1 + \alpha) + 1)}$$

$$B(\alpha, \tau_0) := \overline{b(\alpha, \tau_0) \cdot (a(\alpha, \tau_0) \cdot (1 + \alpha) + 1) - c(\alpha, \tau_0) \cdot (1 + \alpha) \cdot (a(\alpha, \tau_0) - 1) - (a(\alpha, \tau_0) + 1 + \alpha)}$$

$$C(\alpha, \tau_0) := \overline{-b(\alpha, \tau_0) \cdot (1 + \alpha) \cdot (a(\alpha, \tau_0) - 1)}$$

$\alpha, \beta, a, b, c, A, B, C$:
the symbols are the same as that in paper

ratio1: M_1/M_I in paper

$$\text{ratio1}(\alpha, \tau_0) := -\frac{B(\alpha, \tau_0)}{2 \cdot A(\alpha, \tau_0)} + \sqrt{\frac{(B(\alpha, \tau_0))^2 - 4 \cdot A(\alpha, \tau_0) \cdot C(\alpha, \tau_0)}{4 \cdot A(\alpha, \tau_0)^2}}$$

ratio2: M_2/M_I in paper

$$\text{ratio2}(\alpha, \tau_0) := \frac{1}{c(\alpha, \tau_0) + b(\alpha, \tau_0) \cdot \frac{1}{\text{ratio1}(\alpha, \tau_0)}}$$

ratioM: M_hat/M_l in paper

$$ratioM(\alpha, \tau_0) := \frac{1}{p+1} \cdot \left(1 + \frac{1}{\beta(\alpha, \tau_0)} \cdot \ln \left(\frac{(ratio2(\alpha, \tau_0) + 1 + \alpha) \cdot (ratio1(\alpha, \tau_0) + \alpha)}{(ratio1(\alpha, \tau_0) + 1 + \alpha) \cdot (ratio2(\alpha, \tau_0) + \alpha)} \right) \right)$$

The ratioM for long light period is equal to $1/(p+1) = 0.1$. We assume that at $10000\mu s$ the ratioM approaches a constant. Therefore, the value 0.0315 at $10000\mu s$ is used as a factor to scale the ratioM in order to obtain the theoretically estimated (rate P)av/(rate P)c curve.

ratioRateP: (rate P)av/(rate P)c

$$ratioRateP(\alpha, \tau_0) := ratioM(\alpha, \tau_0) \cdot 0.0315 \cdot (p+1)$$

3. Least Squares Fitting:

Define the residuals and the sum of squares:

$$redis(\alpha, \tau_0) := Data - ratioRateP(\alpha, \tau_0)$$

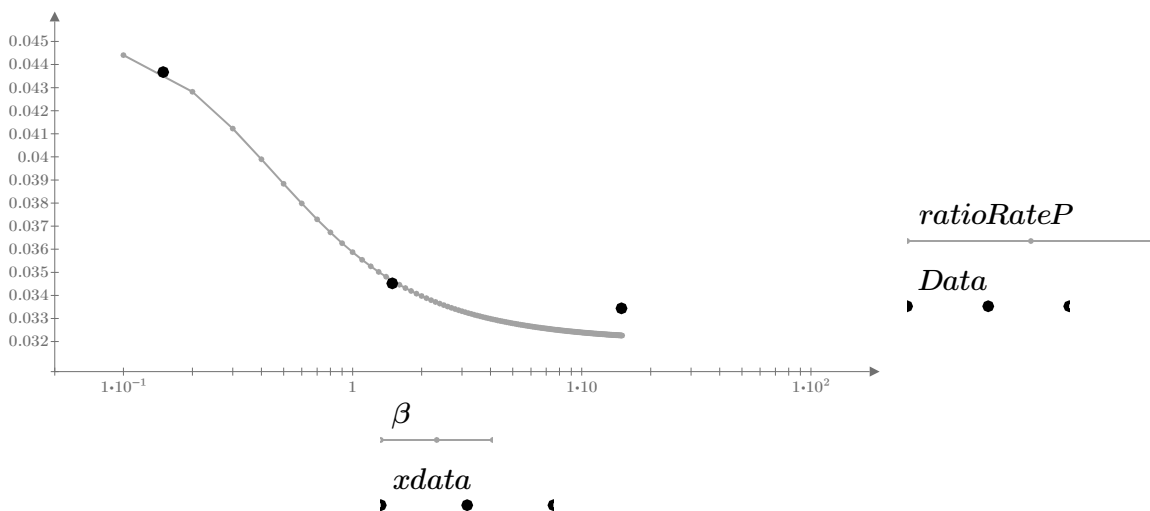
$$SSE(\alpha, \tau_0) := \sum redis(\alpha, \tau_0)^2$$

$\alpha := 1$ $\tau_0 := 40$

$\begin{bmatrix} \alpha \\ \tau_0 \end{bmatrix} := \text{minimize}(SSE, \alpha, \tau_0)$

results: $\begin{bmatrix} \alpha \\ \tau_0 \end{bmatrix} = \begin{bmatrix} 1.914 \\ 23.021 \end{bmatrix}$

Visualization:



Validation of the theoretical treatment of the intermittent illumination method

1. Unit definition: $\text{ORIGIN} := 1$ $mM := 10^{-3} \cdot \frac{\text{mol}}{L}$ $\mu M := 10^{-6} \cdot \frac{\text{mol}}{L}$

2. Parameters: $\lambda := 441 \text{ nm}$ LED light wavelength

$p := 9$ dark to light ratio

$V := 1 \text{ mL}$ volume

$P_{abs} := (p + 1) \cdot 0.5 \text{ mW}$ LED peak light pulse power

$$J_{abs} := P_{abs} \cdot \frac{\lambda}{h \cdot c} \cdot \frac{1}{N_A} \cdot \frac{1}{V} = 18.432 \frac{\mu M}{s}$$

$Q := 0.1$ Quenching fraction [Cis15], which describes the initiation of the productforming radical cycle

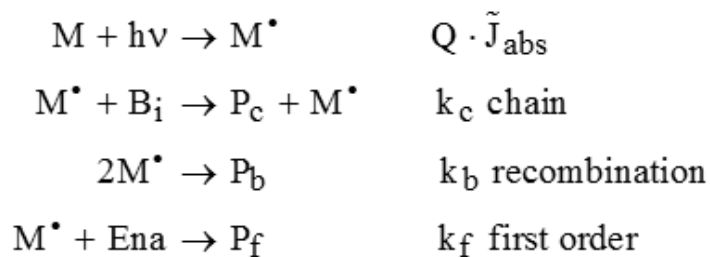
$\text{conc}_{Ena} := 23.8 \text{ mM}$ initial concentration of the enamine

$k_b := 8.3 \cdot 10^9 \frac{L}{\text{mol} \cdot s}$ hypothetical rate constant of recombination

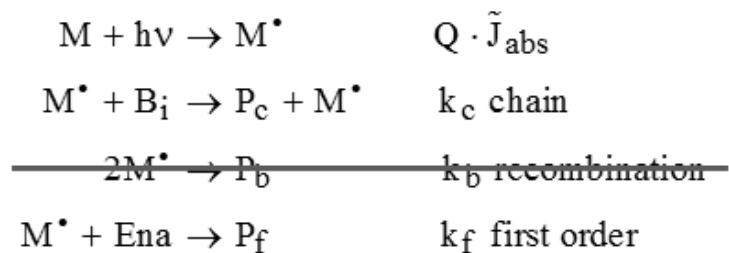
$k_f := 8.2 \cdot 10^3 \frac{L}{\text{mol} \cdot s}$ hypothetical rate constant of product formation

3. Model:

Model 1: with a bi-radical reaction



Model 2: without a bi-radical reaction



$$X(t) = \begin{bmatrix} Mr(t) \\ P(t) \end{bmatrix}$$

vector of dependent variables, Mr(t) for the concentration of radical M* and P(t) for the concentration of the product P

$$mL1(t_start, t_end, dt, n_start) := \left\| \begin{array}{l} \text{init} \leftarrow \begin{bmatrix} n_start_1 \\ n_start_2 \end{bmatrix} \\ D(t, X) \leftarrow \begin{bmatrix} Q \cdot J_{abs} - 2 \cdot k_b \cdot X_1^2 - k_f \cdot X_1 \cdot conc_{Ena} \\ k_f \cdot X_1 \cdot conc_{Ena} \end{bmatrix} \\ N \leftarrow \frac{t_end - t_start}{dt} \\ mcw \leftarrow \text{AdamsBDF}(\text{init}, t_start, t_end, N, D) \end{array} \right\|$$

for model 1: to evaluate the solution in the light period

$$mD1(t_start, t_end, dt, n_start) := \left\| \begin{array}{l} \text{init} \leftarrow \begin{bmatrix} n_start_1 \\ n_start_2 \end{bmatrix} \\ D(t, X) \leftarrow \begin{bmatrix} -2 \cdot k_b \cdot X_1^2 - k_f \cdot X_1 \cdot conc_{Ena} \\ k_f \cdot X_1 \cdot conc_{Ena} \end{bmatrix} \\ N \leftarrow \frac{t_end - t_start}{dt} \\ mD \leftarrow \text{AdamsBDF}(\text{init}, t_start, t_end, N, D) \end{array} \right\|$$

for model 1: to evaluate the solution in the dark period

$$mL2(t_start, t_end, dt, n_start) := \left\| \begin{array}{l} \text{init} \leftarrow \begin{bmatrix} n_start_1 \\ n_start_2 \end{bmatrix} \\ D(t, X) \leftarrow \begin{bmatrix} Q \cdot J_{abs} - k_f \cdot X_1 \cdot conc_{Ena} \\ k_f \cdot X_1 \cdot conc_{Ena} \end{bmatrix} \\ N \leftarrow \frac{t_end - t_start}{dt} \\ mL \leftarrow \text{AdamsBDF}(\text{init}, t_start, t_end, N, D) \end{array} \right\|$$

for model 2: to evaluate the solution in the light period

$$mD2(t_start, t_end, dt, n_start) := \left\| \begin{array}{l} \text{init} \leftarrow \begin{bmatrix} n_start_1 \\ n_start_2 \end{bmatrix} \\ D(t, X) \leftarrow \begin{bmatrix} -k_f \cdot X_1 \cdot conc_{Ena} \\ k_f \cdot X_1 \cdot conc_{Ena} \end{bmatrix} \\ N \leftarrow \frac{t_end - t_start}{dt} \\ mD \leftarrow \text{AdamsBDF}(\text{init}, t_start, t_end, N, D) \end{array} \right\|$$

for model 2: to evaluate the solution in the dark period

4. Simulation of the model 1:

Calculation for cw light

$$M_{0cw} := (6.187 \cdot 10^{-3}) \mu M \quad \text{initial concentration of the radical for cw}$$

$$n_{start0} := \begin{bmatrix} M_{0cw} \\ 0 \text{ mM} \end{bmatrix} \quad dt0 := 100 \text{ ns} \quad t_{start0} := 0 \text{ ns} \quad t_{end0} := 20 \text{ ms}$$

$$Sol_cw := mL1(t_{start0}, t_{end0}, dt0, n_{start0})$$

$$t := Sol_cw^{(1)} \quad Mrcw := Sol_cw^{(2)} \quad Pcw := Sol_cw^{(3)}$$

steady state concentration of the radical under continuous illumination:

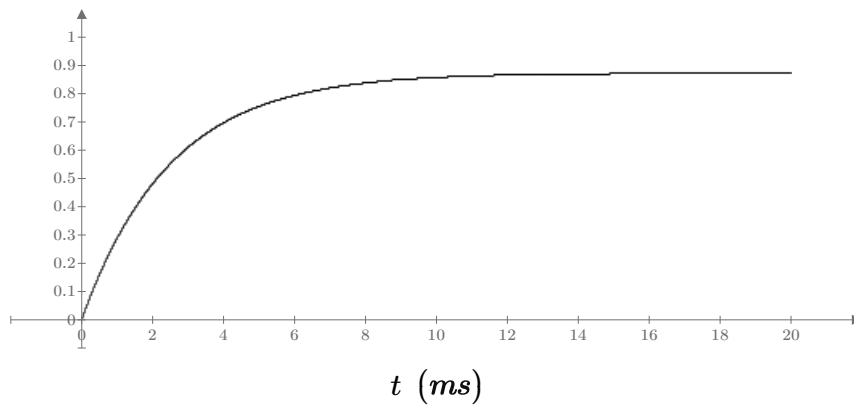
$$Mc := \max(Mrcw) = (6.188 \cdot 10^{-3}) \mu M$$

dimensionless parameter defined in [She56]:

$$\alpha := \frac{k_f \cdot conc_{Ena}}{2 \cdot k_b \cdot Mc} = 1.9$$

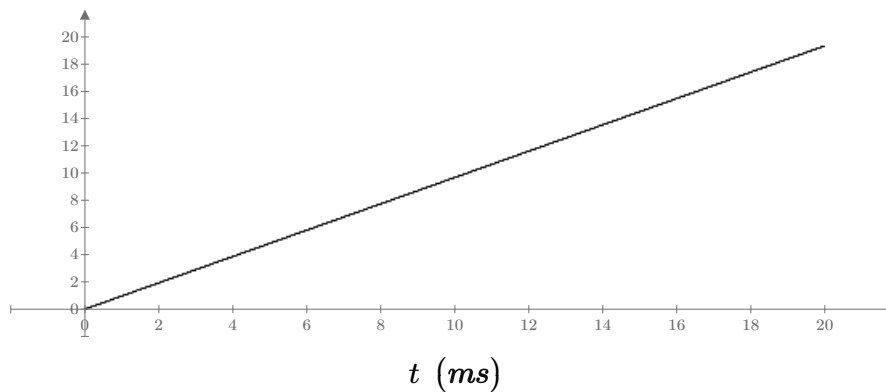
expected maximum and minimum values of the ratio Mav/Mc according to [She56]:

$$MAX := -\frac{\alpha}{2} + \left(\frac{\alpha^2}{4} + \frac{(1+\alpha)^2}{1+p} \right)^{0.5} = 0.14 \quad MIN := \frac{1}{1+p} = 0.1$$



time trace of the radical concentration

$Mrcw$ (μM)



time trace of the product concentration

Pcw (μM)

Calculation for light pulse (10kHz)

$$f_{LED} := 10 \text{ kHz} \quad M_{0P} := 8.7 \cdot 10^{-4} \text{ } \mu\text{M} \quad n_{start0} := \begin{bmatrix} M_{0P} \\ 0 \text{ mM} \end{bmatrix}$$

period of light: $t_L := \frac{1}{f_{LED} \cdot (p+1)} = 10 \text{ } \mu\text{s}$ light-off period: $t_D := t_L \cdot p = 90 \text{ } \mu\text{s}$

$$dtL := 10 \text{ ns} \quad dtD := dtL \quad t_{startL0} := 0 \text{ ns} \quad t_{endL0} := t_{startL0} + t_L$$

```

pulseout := |
| t_endL ← t_endL0
| mag ← mL1 (t_startL0, t_endL0, dtL, n_start0)
| for i ∈ 1, 2..10
| | t_startD ← t_endL
| | t_endD ← t_startD + t_D
| | l ← rows (mag)
| | n_start ← (submatrix (mag^i, 1, 1, 2, 3))^T
| | mag ← stack (mag, mD1 (t_startD, t_endD, dtD, n_start))
| | t_startL ← i · (t_D + t_L)
| | t_endL ← t_startL + t_L
| | l ← rows (mag)
| | n_start ← (submatrix (mag^i, 1, 1, 2, 3))^T
| | mag ← stack (mag, mL1 (t_startL, t_endL, dtL, n_start))
| mag

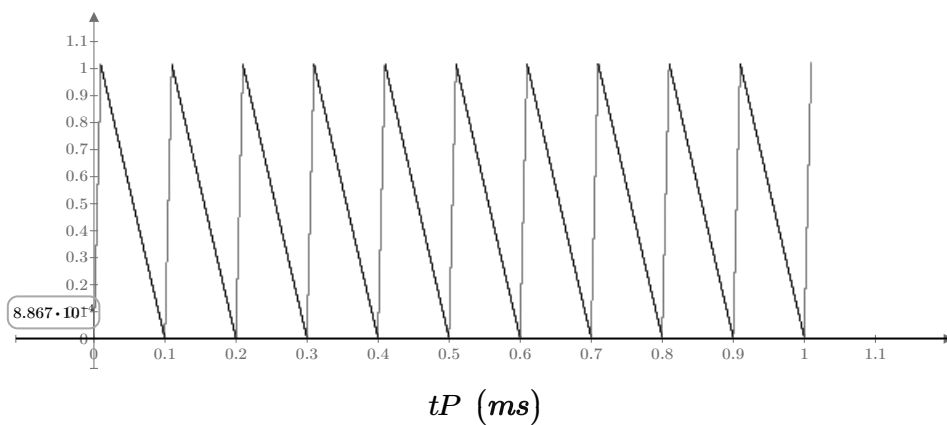
```

$Sol_pulse := pulseout$

$$tP := Sol_pulse^{(1)} \quad MrP := Sol_pulse^{(2)} \quad PP := Sol_pulse^{(3)} \quad l := rows (MrP) = 1.01 \cdot 10^5$$

average concentration of the radical under intermittent illumination:

$$Mp := mean (submatrix (MrP, 1, l - 10^3, 1, 1)) = (8.783 \cdot 10^{-4}) \text{ } \mu\text{M}$$



time trace of
the radical
concentration

MrP (μM)

tP (ms)

ratio of the average concentration of the radical under intermittent illumination over the concentration of the radical under continuous illumination, ratio M_{av}/M_{cw} :

$$ratio := \frac{M_p}{M_c} = 0.142$$

Calculation for light pulse (1Hz)

$$f_{LED} := 1 \text{ Hz} \quad M_{0P} := 0 \text{ mM} \quad n_{start0} := \begin{bmatrix} M_{0P} \\ 0 \text{ mM} \end{bmatrix}$$

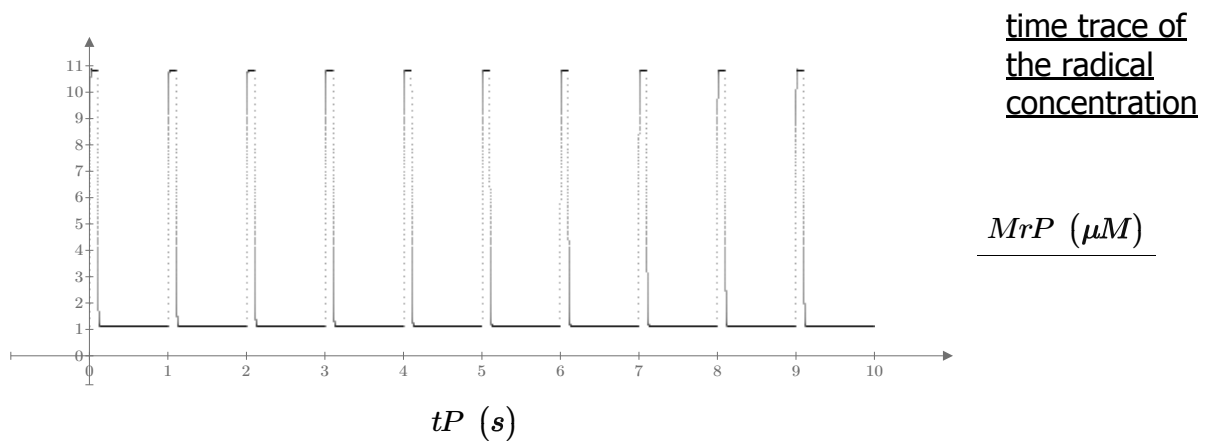
$$t_L := \frac{1}{f_{LED} \cdot (p+1)} = 100 \text{ ms} \quad t_D := t_L \cdot p = 900 \text{ ms}$$

$$dtL := 100 \text{ } \mu\text{s} \quad dtD := dtL \quad t_{startL0} := 0 \text{ ns} \quad t_{endL0} := t_{startL0} + t_L$$

```
pulseout := |
  t_endL ← t_endL0
  mag ← mL1 (t_startL0, t_endL0, dtL, n_start0)
  for i ∈ 1, 2..10
    |
      t_startD ← t_endL
      t_endD ← t_startD + t_D
      l ← rows (mag)
      n_start ← (submatrix (mag^l, 1, 1, 2, 3))^T
      mag ← stack (mag, mD1 (t_startD, t_endD, dtD, n_start))
      t_startL ← i • (t_D + t_L)
      t_endL ← t_startL + t_L
      l ← rows (mag)
      n_start ← (submatrix (mag^l, 1, 1, 2, 3))^T
      mag ← stack (mag, mL1 (t_startL, t_endL, dtL, n_start))
    |
  mag
```

$Sol_pulse := pulseout$

$$tP := Sol_pulse^{(1)} \quad MrP := Sol_pulse^{(2)} \quad PP := Sol_pulse^{(3)} \quad l := rows (MrP) = 1.01 \cdot 10^5$$



average concentration of the radical under intermittent illumination:

$$M_p := \text{mean}(\text{submatrix}(MrP, 1, l - 10^3, 1, 1)) = (6.269 \cdot 10^{-4}) \mu M$$

ratio of the average concentration of the radical under intermittent illumination over the concentration of the radical under continuous illumination, ratio M_av/M_cw:

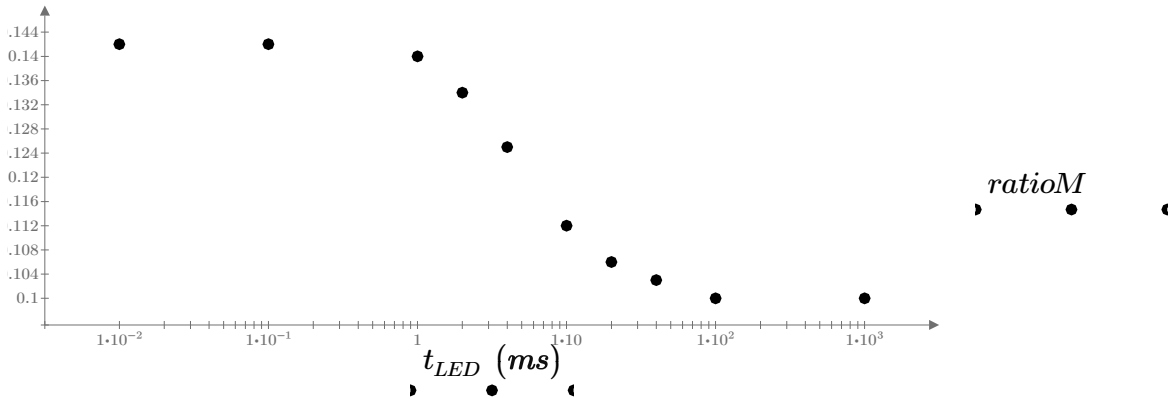
$$\text{ratio} := \frac{M_p}{M_c} = 0.1$$

4. Results of intermittent illumination simulation:

repetition frequency $f_{LED} := [10 \ 1 \ 0.1 \ 0.05 \ 0.025 \ 0.01 \ 0.005 \ 0.0025 \ 0.001 \ 0.0001]^T \text{ kHz}$

ratio M_av/M_cw $\text{ratioM} := [0.142 \ 0.142 \ 0.14 \ 0.134 \ 0.125 \ 0.112 \ 0.106 \ 0.103 \ 0.10 \ 0.10]^T$

period of light $t_{LED} := \frac{1}{f_{LED} \cdot (p+1)} = \begin{bmatrix} 10 \\ \vdots \end{bmatrix} \mu s$

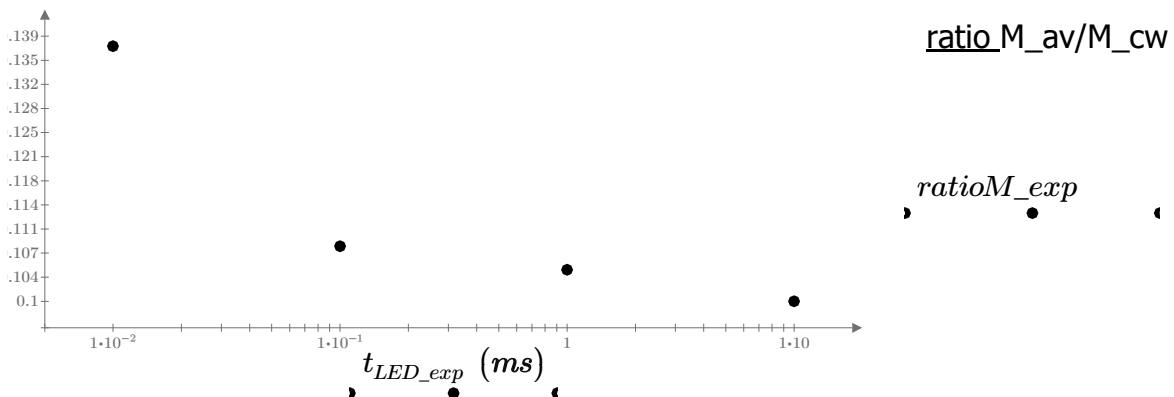


Experiment Results:

period of light $t_{LED_exp} := [10 \ 100 \ 1000 \ 10000]^T \mu s$

ratio (rate P)av/(rate P)c $\text{Data} := [0.04317 \ 0.03402 \ 0.03294 \ 0.0315]^T$

$$\text{ratioM_exp} := \frac{\text{Data}}{0.315}$$



5. Simulation of the model 2:

Calculation for cw light

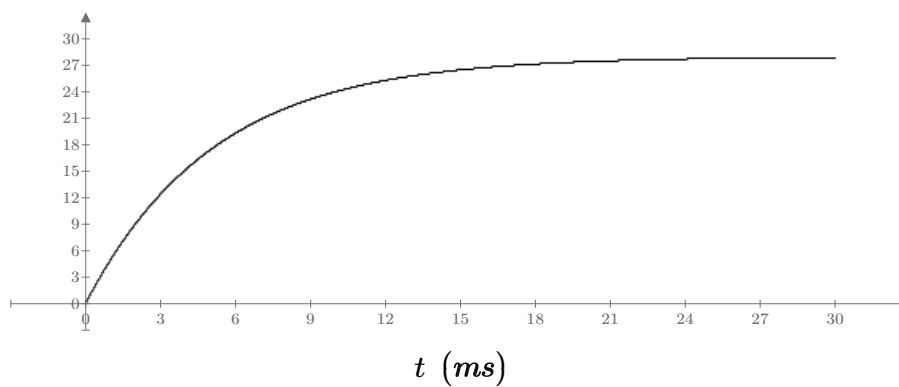
$$M_{0cw} := (9.435 \cdot 10^{-3}) \mu M \quad n_{start0} := \begin{bmatrix} M_{0cw} \\ 0 \text{ mM} \end{bmatrix} \quad dt0 := 100 \text{ ns}$$

$$t_{start0} := 0 \text{ ns} \quad t_{end0} := 30 \text{ ms} \quad Sol_cw := mL2(t_{start0}, t_{end0}, dt0, n_{start0})$$

$$t := Sol_cw^{(1)} \quad Mrcw := Sol_cw^{(2)} \quad Pcw := Sol_cw^{(3)}$$

steady state concentration of the radical under continuous illumination:

$$Mc := \max(Mrcw) = (9.445 \cdot 10^{-3}) \mu M$$



time trace of the radical concentration

Mrcw (mM)

Calculation for light pulse (10kHz)

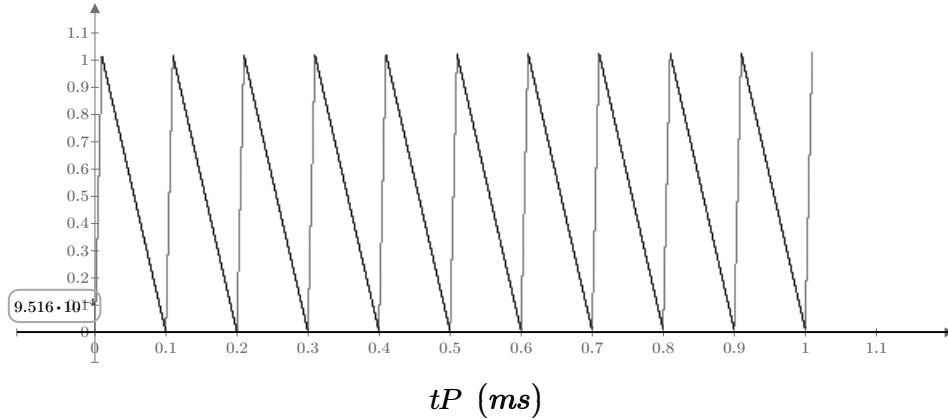
$$f_{LED} := 10 \text{ kHz} \quad M_{0P} := 9.35 \cdot 10^{-4} \mu M \quad n_{start0} := \begin{bmatrix} M_{0P} \\ 0 \text{ mM} \end{bmatrix} \quad dtL := 10 \text{ ns} \quad dtD := dtL$$

$$t_L := \frac{1}{f_{LED} \cdot (p+1)} = 10 \mu s \quad t_D := t_L \cdot p = 90 \mu s \quad t_{startL0} := 0 \text{ ns} \quad t_{endL0} := t_{startL0} + t_L$$

```
pulseout :=
  t_endL ← t_endL0
  mag ← mL2(t_startL0, t_endL0, dtL, n_start0)
  for i ∈ 1, 2..10
    t_startD ← t_endL
    t_endD ← t_startD + t_D
    l ← rows(mag)
    n_start ← (submatrix(mag, 1, 1, 2, 3))^T
    mag ← stack(mag, mD2(t_startD, t_endD, dtD, n_start))
    t_startL ← i · (t_D + t_L)
    t_endL ← t_startL + t_L
    l ← rows(mag)
    n_start ← (submatrix(mag, 1, 1, 2, 3))^T
    mag ← stack(mag, mL2(t_startL, t_endL, dtL, n_start))
  mag
```

$Sol_pulse := pulseout$

$tP := Sol_pulse^{(1)}$ $MrP := Sol_pulse^{(2)}$ $PP := Sol_pulse^{(3)}$ $l := rows(MrP) = 1.01 \cdot 10^5$



time trace of
the radical
concentration

MrP (μM)

average concentration of the radical under intermittent illumination:

$$Mp := \text{mean}(\text{submatrix}(MrP, 1, l - 10^3, 1, 1)) = (9.434 \cdot 10^{-4}) \mu M$$

ratio of the average concentration of the radical under intermittent illumination over the concentration of the radical under continuous illumination, ratio M_{av}/M_{cw} :

$$ratio := \frac{Mp}{Mc} = 0.1$$

Calculation for light pulse (1Hz)

$$f_{LED} := 1 \text{ Hz} \quad M_{0P} := 0 \text{ mM} \quad n_{start0} := \begin{bmatrix} M_{0P} \\ 0 \text{ mM} \end{bmatrix} \quad dtL := 100 \mu s \quad dtD := dtL$$

$$t_L := \frac{1}{f_{LED} \cdot (p+1)} = 100 \text{ ms} \quad t_D := t_L \cdot p = 900 \text{ ms} \quad t_{startL0} := 0 \text{ ns} \quad t_{endL0} := t_{startL0} + t_L$$

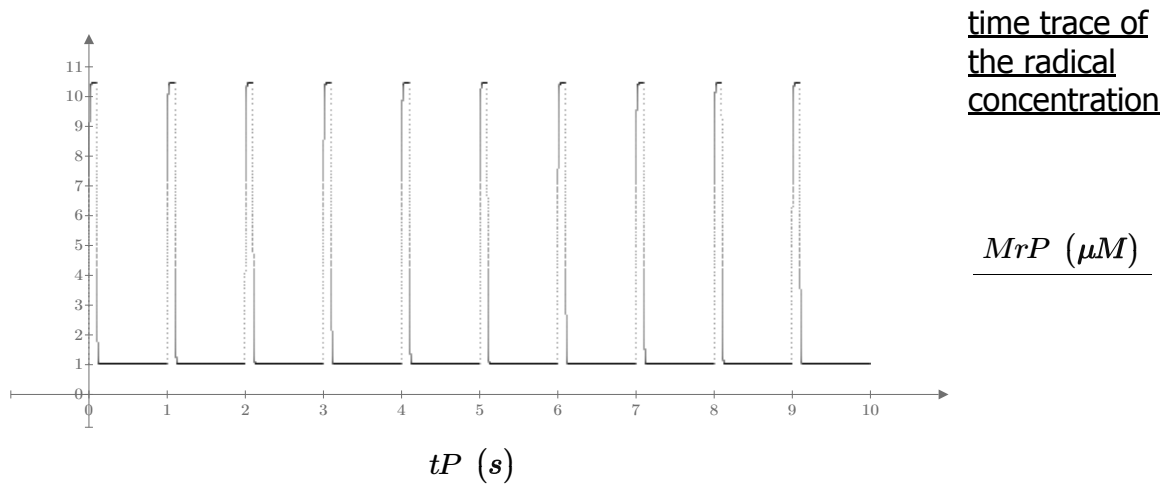
```

pulseout := ||
  t_endL ← t_endL0
  mag ← mL2(t_startL0, t_endL0, dtL, n_start0)
  for i ∈ 1, 2..10
    ||
      t_startD ← t_endL
      t_endD ← t_startD + t_D
      l ← rows(mag)
      n_start ← (submatrix(magl, 1, 1, 2, 3))T
      mag ← stack(mag, mD2(t_startD, t_endD, dtD, n_start))
      t_startL ← i · (t_D + t_L)
      t_endL ← t_startL + t_L
      l ← rows(mag)
      n_start ← (submatrix(magl, 1, 1, 2, 3))T
      mag ← stack(mag, mL2(t_startL, t_endL, dtL, n_start))
    ||
  mag

```

$Sol_pulse := pulseout$

$tP := Sol_pulse^{(1)}$ $MrP := Sol_pulse^{(2)}$ $PP := Sol_pulse^{(3)}$ $l := rows(MrP) = 1.01 \cdot 10^5$



average concentration of the radical under intermittent illumination:

$$Mp := \text{mean}(\text{submatrix}(MrP, 1, l - 10^3, 1, 1)) = (9.451 \cdot 10^{-4}) \mu M$$

ratio of the average concentration of the radical under intermittent illumination over the concentration of the radical under continuous illumination, ratio M_{av}/M_{cw} :

$$ratio := \frac{Mp}{Mc} = 0.1$$

Conclusion: The ratio M_{av}/M_{cw} in the case of model 2 is not a function of LED pulse light duration.

Appendix A4

**Steady-state spectroscopic characterizations and TA spectroscopic studies
of NDI-A in Chapter 5**

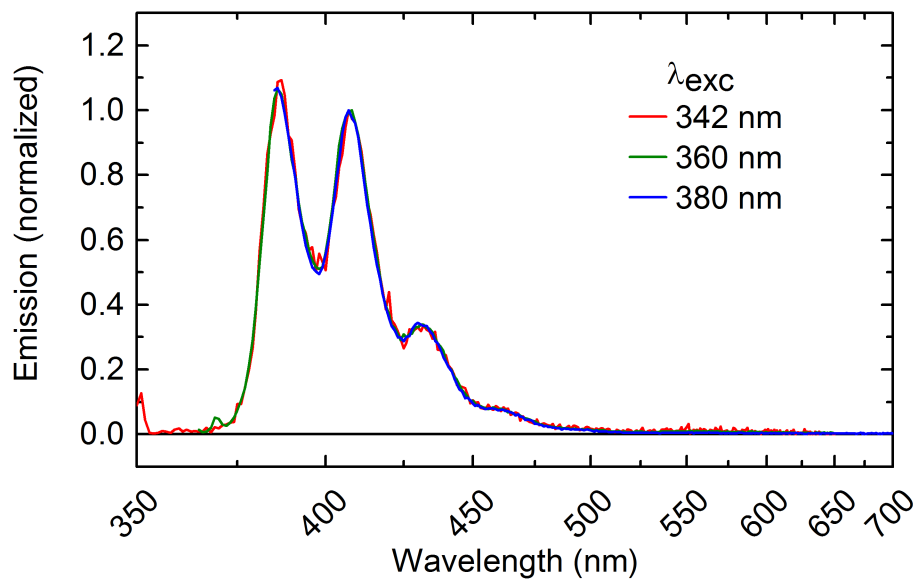


Fig. A4.1: Fluorescence spectra of 20 μM NDI-A in CH_2Cl_2 at room temperature.

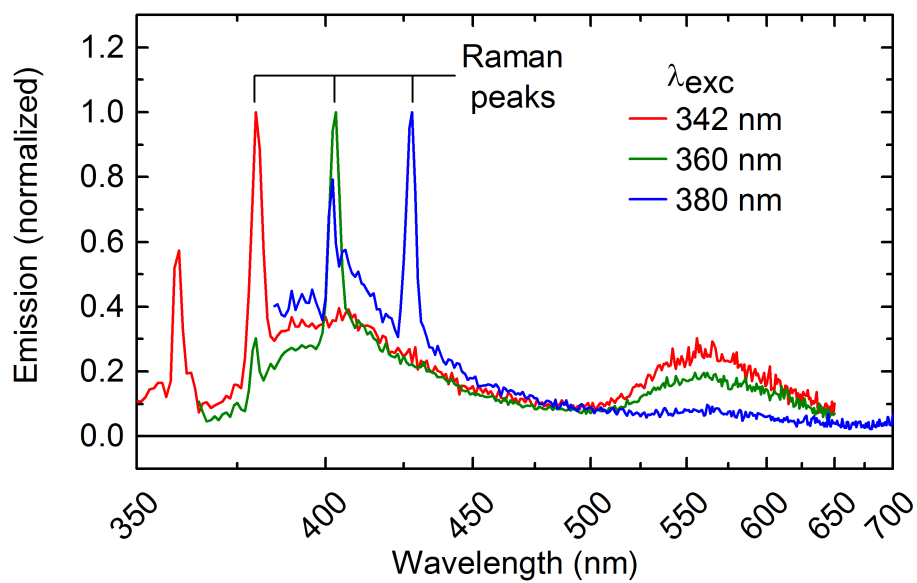


Fig. A4.2: Fluorescence spectra of 20 μM NDI-A in DMF at room temperature.

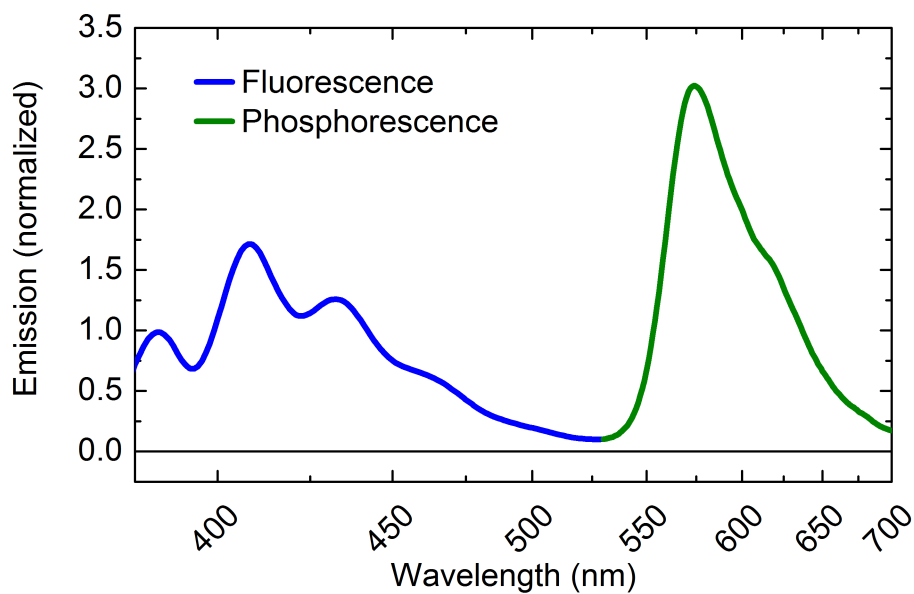


Fig. A4.3: Phosphorescence spectra of 10 μM NDI-A in CH_2Cl_2 at room temperature (10% ethyl iodide was added to induce phosphorescence).

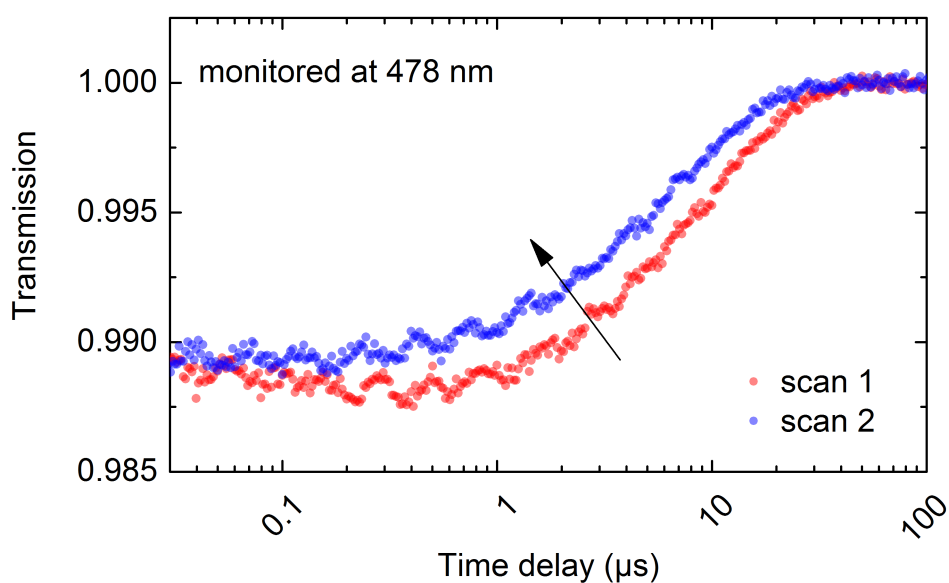


Fig. A4.4: Kinetic traces monitored at 478 nm for the TA spectroscopic study of NDI-A under catalytic conditions in the absence of DMF.

Appendix A5

**Steady-state spectroscopic characterizations and TA spectroscopic studies
of N_x-Me in Chapter 6**

Steady-state spectroscopy:

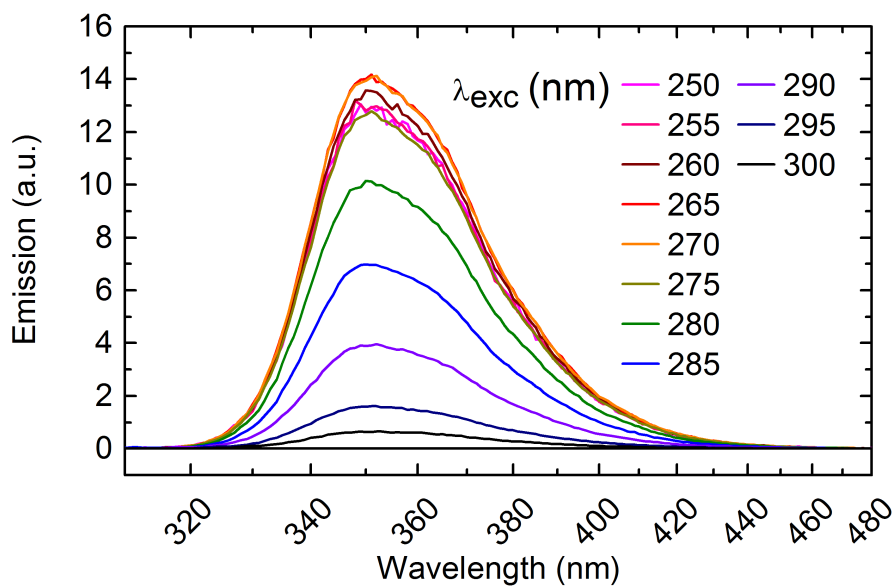


Fig. A5.1: Fluorescence spectra of 10 μM N₀-Me in CH₂Cl₂ at room temperature.

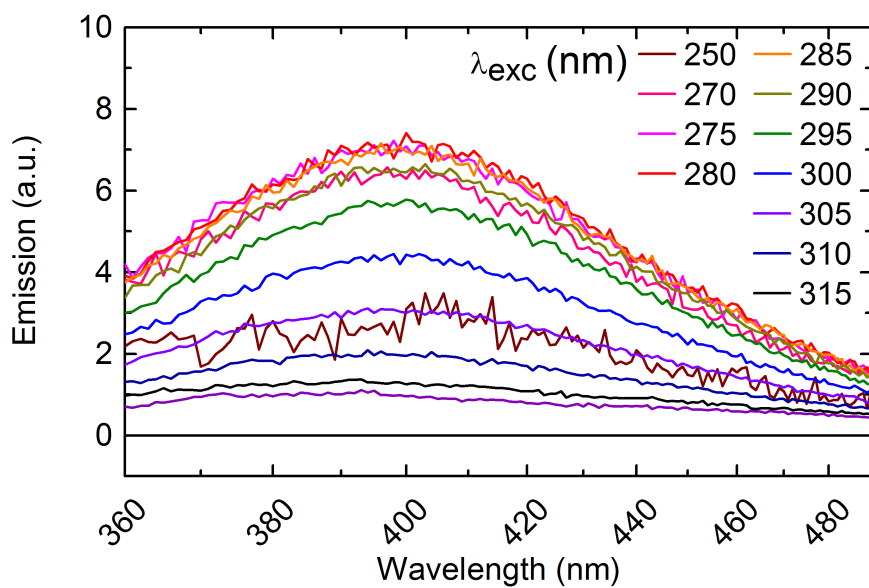


Fig. A5.2: Fluorescence spectra of 10 μM N₃-Me in CH₂Cl₂ at room temperature.

Experiment conditions of transient absorption measurements:

Table A5.1: The experiment conditions of femtosecond transient absorption measurements.

The sample is prepared in CH_2Cl_2 . The relative polarizations between the pump and probe were set to the magic angle (54.7°) by a half-wave plate in the pump-beam path. A flow cell with 100 μm thickness was used.

Sample	Concentration (mM)	Pump wavelength (nm)	Pump intensity ($\text{mJ}\cdot\text{cm}^{-2}$)	Pulse duration (fs)
N ₀ -Me	1.0	272	0.55	40
N ₁ -Me	1.0	272	0.72	40
N ₁ -Me	2.2	330	0.96	50
N ₂ -Me	1.1	272	0.61	40
N ₂ -Me	2.0	330	0.96	50
N ₃ -Me	1.2	270	0.42	27

Table A5.2: The experiment conditions of nanosecond transient absorption measurements.

The sample is prepared in CH_2Cl_2 and is excited with 3 ns pulses from an Optical Parametric Oscillator (OPO) system (Ekspla NT242).

Sample	Concentration (mM)	Pump wavelength (nm)	Pump intensity ($\text{mJ}\cdot\text{cm}^{-2}$)	Cuvette thickness
N ₀ -Me	1.0	270	0.33	1 mm
N ₁ -Me	1.0	270	0.32	100 μm
N ₁ -Me	1.0	320	0.96	100 μm
N ₂ -Me	1.1	270	0.30	100 μm
N ₂ -Me	1.1	320	0.92	100 μm
N ₃ -Me	1.2	270	0.30	100 μm

Rate constants used in the analysis of the TA measurements:

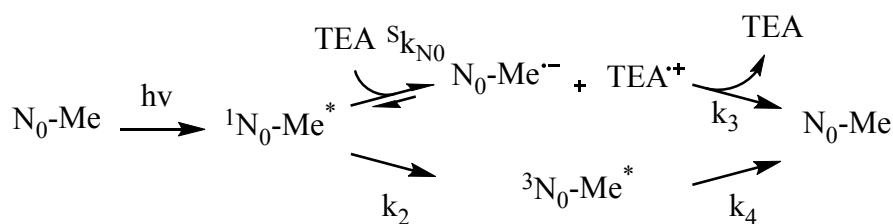


Fig. A5.3: Scheme of the reduction mechanism of the excited $\text{N}_0\text{-Me}$ in the presence of TEA.

Table A5.3: List of rate constants for the analysis of the TA measurement of $\text{N}_0\text{-Me}$ in the presence of TEA (Scheme of the mechanism in Fig. A5.3).

Rate constant	$S k_{\text{N}_0} (\text{M}^{-1}\text{s}^{-1})$	$k_2 (\text{s}^{-1})$	$k_3 (\text{s}^{-1})$	$k_4 (\text{s}^{-1})$
Value	2.5×10^9	3.1×10^7	1.5×10^8	3.3×10^6

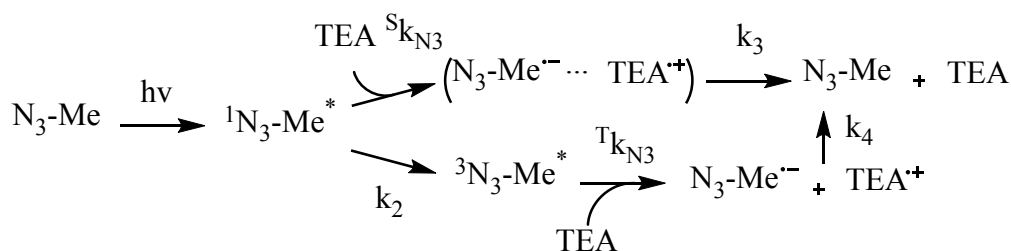


Fig. A5.4: Scheme of the reduction mechanism of the excited $\text{N}_3\text{-Me}$ in the presence of TEA.

Table A5.4: List of rate constants for the analysis of the TA measurement of $\text{N}_3\text{-Me}$ in the presence of TEA (Scheme of the mechanism in Fig. A5.4).

Rate constant	$S k_{\text{N}_3} (\text{M}^{-1}\text{s}^{-1})$	$k_2 (\text{s}^{-1})$	$k_3 (\text{s}^{-1})$	$k_4 (\text{s}^{-1})$	$T k_{\text{N}_3} (\text{M}^{-1}\text{s}^{-1})$
Value	7.0×10^9	1.7×10^{10}	3.3×10^9	2.8×10^6	1.4×10^9

Acknowledgments

This work would not have been possible in its actual form without the support of people I appreciate to have worked with during my PhD study. All the projects would not have been as successful as they were, if not conducted in the unique and inspiring atmosphere at the “Lehrstuhl für BioMolekulare Optik”. In the following, I would like to thank:

- **Prof. Dr. Eberhard Riedle** for the opportunity to work in his group on interdisciplinary and exciting research projects. I am particularly grateful for giving me the trust and freedom to develop my own ideas and giving me support where I need it. Without his advices and impressive knowledge, so many projects would lack improving aspects. The inspiring atmosphere and the enthusiastic supervision have mainly contributed to the success of this thesis.
- **Prof. Dr. Hans-Achim Wagenknecht** for the excellent cooperation in the NDI project and the possibility to work in his synthetic lab. I am grateful for the valuable ideas and many stimulating discussions. His coworker **Dr. David Rombach** is acknowledged for the steady support during my work in Karlsruhe.
- **Prof. Dr. Bettina Valeska Lotsch** for the superb collaboration on the water splitting project and many productive discussions. I also want to thank her coworker **Dr. Vijay Vyas** for providing samples.
- **Prof. Dr. Jürgen Hauer** for taking over the second supervisor position of my thesis.
- **Prof. Dr. Bernhard Dick and Prof. Dr. Wolfgang Zinth** for helping in the TA data analysis.
- **Prof. PhD. Cristina Woods** for valuable advice on the academic career.
- **Dr. Barbara Reiß** for successfully working together on the NDI project. Without her expertise and experience, the quantum yield experiments and the interpretation of the molecular dynamics would not have been such a smooth project.
- **Dr. Roger-Jan Kutta** for the great support in the TA data analysis and interpretation.
- **My colleagues:** Dr. Bastian Baudisch, Ferdinand Bergmeier, Matthias Block, Dr. Max Bradler, Dr. Richard Ciesielski, Henrietta Derondeau, Marcus Götz, Dr. Nils Krebs, Cristinna Leonado, Dr. Igor Pugliesi, Rudolf Reiel, Roland Wilcken, Dr.

Emanuel Wittmann for the extraordinarily pleasant atmosphere in the group and supporting me in many measurements. Vielen Dank!

- **Dr. Karl-Heiz Mantel and Dr. Florian Trommer** for the IT-support and poster print.
- **Christian Hausmann, Rudi Schwarz, and Alfons Stork** for the support in the technical work.
- **Alexandra Michaelis** for helping in organizational tasks.
- My wife **李翔宇 (Dr. Xiangyu Li)** and my parents **于丽 (Li Yu) and 扈立军 (Lijun Hu)**, whose support and love make it possible for me to come where I am standing now and who always take care of me.

Hiermit erkläre ich, die vorliegende Arbeit selbstständig verfasst und keine anderen als die angegebenen Quellen und Hilfsmittel verwendet zu haben.

München, den 10. Juni 2020

Qi Hu